

JOURNAL of GEOLOGICAL RESEARCH

GAS HYDRATE ON CONTINENTAL MARGINS

GUEST EDITORS: UMBERTA TINIVELLA, MICHELA GIUSTINIANI, XUEWEI LIU, AND INGO PECHER





Gas Hydrate on Continental Margins

Journal of Geological Research

Gas Hydrate on Continental Margins

Guest Editors: Umberta Tinivella, Michela Giustiniani,
Xuewei Liu, and Ingo Pecher



Copyright © 2012 Hindawi Publishing Corporation. All rights reserved.

This is a special issue published in "Journal of Geological Research." All articles are open access articles distributed under the Creative Commons Attribution License, which permits unrestricted use, distribution, and reproduction in any medium, provided the original work is properly cited.



Editorial Board

Teofilo A. Abrajano, USA
Jan H. Behrmann, Germany
Kent C. Condie, USA
M. H. Engel, USA
Steven L. Forman, USA

Michael O. Garcia, USA
Agust Gudmundsson, UK
Keiko H. Hattori, Canada
David Matthey, UK
Atle Nesje, Norway

Josep Pares, Spain
Joaquin Ruiz, USA
James R. Rustad, USA
David T. A. Symons, Canada

Contents

Gas Hydrate on Continental Margins, Umberta Tinivella, Michela Giustiniani, Xuewei Liu, and Ingo Pecher
Volume 2012, Article ID 781429, 2 pages

Gas Hydrate Formation and Dissipation Histories in the Northern Margin of Canada: Beaufort-Mackenzie and the Sverdrup Basins, Jacek Majorowicz, Kirk Osadetz, and Jan Safanda
Volume 2012, Article ID 879393, 17 pages

Thessaloniki Mud Volcano, the Shallowest Gas Hydrate-Bearing Mud Volcano in the Anaximander Mountains, Eastern Mediterranean, C. Perissoratis, Chr. Ioakim, S. Alexandri, J. Woodside, P. Nomikou, A. Dählmann, D. Casas, K. Heeschen, H. Amman, G. Rousakis, and V. Lykousis
Volume 2011, Article ID 247983, 11 pages

Seismic Expression of Polygonal Faults and Its Impact on Fluid Flow Migration for Gas Hydrates Formation in Deep Water of the South China Sea, Duanxin Chen, Shiguo Wu, Xiujuan Wang, and Fuliang Lv
Volume 2011, Article ID 384785, 7 pages

Methane Hydrate Distribution from Prolonged and Repeated Formation in Natural and Compacted Sand Samples: X-Ray CT Observations, Emily V. L. Rees, Timothy J. Kneafsey, and Yongkoo Seol
Volume 2011, Article ID 791815, 15 pages

Gas Hydrates Accumulations on the South Shetland Continental Margin: New Detection Possibilities, V. D. Solovyov, V. G. Bakhmutov, I. N. Korchagin, S. P. Levashov, N. A. Yakymchuk, and D. N. Bozhezha
Volume 2011, Article ID 514082, 8 pages

Simulation of Methane Recovery from Gas Hydrates Combined with Storing Carbon Dioxide as Hydrates, Georg Janicki, Stefan Schlter, Torsten Hennig, Hildegard Lyko, and Gorge Deerberg
Volume 2011, Article ID 462156, 15 pages

Geophysical Indicators of Gas Hydrate in the Northern Continental Margin, South China Sea, Xiujuan Wang, Shiguo Wu, Yiqun Guo, Shengxiong Yang, and Yuehua Gong
Volume 2011, Article ID 359597, 8 pages

Assessment of Marine Gas Hydrates and Associated Free Gas Distribution Offshore Uruguay, Juan Tomasini, Hector de Santa Ana, Bruno Conti, Santiago Ferro, Pablo Gristo, Josefina Marmisolle, Ethel Morales, Pablo Rodriguez, Matas Soto, and Gerardo Veroslavsky
Volume 2011, Article ID 326250, 7 pages

Early Diagenesis Records and Pore Water Composition of Methane-Seep Sediments from the Southeast Hainan Basin, South China Sea, Daidai Wu, Nengyou Wu, Ying Ye, Mei Zhang, Lihua Liu, Hongxiang Guan, and Xiaorong Cong
Volume 2011, Article ID 592703, 10 pages

Gas Hydrate System of Shenhu Area, Northern South China Sea: Geochemical Results, Nengyou Wu, Haiqi Zhang, Shengxiong Yang, Guangxue Zhang, Jinqiang Liang, Jin'an Lu, Xin Su, Peter Schultheiss, Melanie Holland, and Youhai Zhu
Volume 2011, Article ID 370298, 10 pages

Basal and Frontal Accretion Processes versus BSR Characteristics along the Chilean Margin,

I. Vargas-Cordero, U. Tinivella, F. Accaino, F. Fanucci, M. F. Loreto, M. E. Lascano, and C. Reichert

Volume 2011, Article ID 846101, 10 pages

**Natural Gas Production from Methane Hydrate Deposits Using CO₂ Clathrate Sequestration:
State-of-the-Art Review and New Technical Approaches,**

Annick Nago and Antonio Nieto

Volume 2011, Article ID 239397, 6 pages

Analysis of Water Features in Gas Leakage Area, Liu Huaishan, Wang Fengfan, Tong Siyou, Li Gaolin,
and Zhang Haiyan

Volume 2011, Article ID 525781, 10 pages

**Possible Relationships between Seep Carbonates and Gas Hydrates in the Miocene of the Northern
Apennines,** Stefano Conti and Daniela Fontana

Volume 2011, Article ID 920727, 9 pages

BSR versus Climate Change and Slides, U. Tinivella, M. Giustiniani, and D. Accettella

Volume 2011, Article ID 390547, 6 pages

Editorial

Gas Hydrate on Continental Margins

Umberta Tinivella,¹ Michela Giustiniani,¹ Xuewei Liu,² and Ingo Pecher³

¹ *Istituto Nazionale di Oceanografia e di Geofisica Sperimentale, OGS, Borgo Grotta Gigante 42/C, 34010 Trieste, Italy*

² *Institute of Geophysics and Geomatics, China University of Geosciences, 29 Xueyuan Road, Beijing 100083, China*

³ *GNS Science, 1 Fairway Drive, P.O. Box 30368, Lower Hutt 5010, New Zealand*

Correspondence should be addressed to Umberta Tinivella, utinivella@ogs.trieste.it

Received 23 November 2011; Accepted 23 November 2011

Copyright © 2012 Umberta Tinivella et al. This is an open access article distributed under the Creative Commons Attribution License, which permits unrestricted use, distribution, and reproduction in any medium, provided the original work is properly cited.

Gas hydrate is a solid crystalline material composed of water and natural gas that forms at low temperature and high pressure. Gas hydrates represent an important reservoir of natural gas, even if the current global estimate is very rough. The increasing attention to gas hydrates is arising from (1) the assessment of methane hydrates as a new relatively clean energy source, (2) the relationship between gas hydrate and global climate, (3) the geological hazards related to gas hydrates, and (4) recent programs to sequester CO₂ in gas hydrate reservoirs.

Generally, gas hydrate deposits are investigated by using several geophysical methods. The seismic technique, which is the most used, allows detecting an indicator of the hydrate and free gas accumulations, known as bottom simulating reflector (BSR). Moreover, seismic data provide information about the geometry of the main geological structures, allowing possible explanations of the presence/absence of gas hydrate on continental margins. In the last years, the scientific community has started to integrate geophysical, geochemical, and heat-flow data in order to detect and characterize gas hydrate and free gas volumes and their distribution in marine sediments. Thus, reviews of extensive geophysical surveys and direct measurements combined with geological interpretation and theoretical modelling will increase understanding on the occurrence, distribution, and concentration of gas hydrate and the underlying free gas beneath the ocean bottom, as demonstrated by the papers included in this issue.

The main topic of three of the papers is modelling. L. Huaishan et al. established sound models with hydrate and free gas in the water and sediment in order to extract information about gas bubble size, gas content, sound

velocity, attenuation, resonance frequency, and scattering cross-section from acoustic data. J. Majorowicz et al. studied the dynamic permafrost and gas hydrate history in the Northern Canadian margin using a numerical model to illustrate how changes in setting and environment, especially periodic glacial ice cover, affected gas hydrate stability. The models show that gas hydrates have persisted through interglacial episodes. The paper of V. Tinivella et al. is focussing on the relationship between gas hydrates and slope instability in polar regions. Their modelling suggests that, during the interglacial period, gas hydrate influences slope stability and climate change only at the beginning of the warming period and only if the sea bottom is affected by temperature variations.

Another part of this issue is dedicated to several geophysical methods applied to study gas hydrate reservoirs. D. Chen et al. analysed 3D seismic data to identify polygonal faults in the South China Sea. They observed that gas hydrates are located in the sediments above a polygonal fault layer. Polygonal faults can act as pathways for the migration of fluids, which can supply hydrocarbons for the formation of gas hydrates. To study physical properties of methane gas hydrate-bearing sediments, it is necessary to synthesize laboratory samples due to the limited availability of cores from natural deposits, as reported by E. V. L. Rees et al. They performed X-ray computed tomography during hydrate formation and decomposition phases. The investigation revealed the impact of water saturation on location and morphology of hydrate in both laboratory and natural sediments during repeated hydrate formations. Significant redistribution of hydrate and water in the samples was

observed over both the short-term and long-term. V. D. Solovyov et al. used short-pulsed electromagnetic field and vertical electric-resonance sounding, integrated with special technology of satellite data processing and interpretation, offshore Antarctic Peninsula. J. Tomasini et al., I. Vargas-Cordero et al., and X. Wang et al. analysed 2D seismic reflection data to determine gas hydrates and associated free gas distribution offshore Uruguay, offshore Southern Chilean margin, and in the South China sea, respectively, showing a great potential for this nonconventional resource and encouraging further research. In addition, two papers, by D. Wu et al. and N. Wu et al., are dedicated to geochemical analysis of samples acquired in the South China Sea, confirming seismic results that suggest the potential for gas hydrate resources in this area.

The multidisciplinary of gas hydrate research is emphasized by the papers by S. Conti and D. Fontana, which focused on contribution of paleogas hydrate destabilization in the Miocene in the Northern Apennines, and C. Perissotatis et al., which reported a detailed multibeam survey and a gravity coring carried out in the Anaximander Mountains, Eastern Mediterranean, detecting an active gas hydrate-bearing mud volcano named Thessaloniki.

Because carbon dioxide also forms gas hydrates, methane hydrate studies have recently been associated with CO₂ sequestration, which is the topic of other two papers. In these papers, approaches are analyzed for combining natural gas production from methane hydrate deposits and CO₂ sequestration. G. Janicki et al. modelled two scenarios: the depressurization of an area 1,000 m in diameter and a one-/two-well scenario with CO₂ injection. The performed simulations show that depressurization with or without simultaneous CO₂ injection is a practicable way to produce methane from subsea hydrate fields with assured rates over many years. A. Nago and A. Nieto reported the state-of-the-art of the CO₂ hydrate and investigated the molecular exchange between CO₂ and CH₄ that occurs when methane hydrates are exposed to CO₂, thus generating the release of natural gas while trapping carbon dioxide as a gas hydrate. Their work included laboratory studies on the synthesis, thermodynamics, phase equilibrium, kinetics, cage occupancy, and the methane recovery potential of the mixed CO₂-CH₄ hydrate, including both experimental and numerical data.

In conclusion, the fifteen papers reported here constitute a significant contribution to our knowledge on natural gas hydrates by presenting results from direct and indirect measurements on several continental margins, studying relationships between geophysical response and hydrate occurrence, and investigating geological aspects related to the gas hydrate presence. The papers also set the stage for future work to increase our knowledge on gas hydrates.

*Umberta Tinivella
Michela Giustiniani
Xuewei Liu
Ingo Pecher*

Research Article

Gas Hydrate Formation and Dissipation Histories in the Northern Margin of Canada: Beaufort-Mackenzie and the Sverdrup Basins

Jacek Majorowicz,¹ Kirk Osadetz,² and Jan Safanda³

¹Northern Geothermal and Department of Physics, University of Alberta, Edmonton, AB, Canada T6G 2R3

²Division of GSC Calgary, Geological Survey of Canada, Calgary, AB, Canada T2L 2A7

³Institute of Geophysics, Czech Academy of Science, 106 00 Praha 10, Prague, Czech Republic

Correspondence should be addressed to Jacek Majorowicz, majorowicz@shaw.ca

Received 16 June 2011; Revised 28 October 2011; Accepted 1 November 2011

Academic Editor: Ingo Pecher

Copyright © 2012 Jacek Majorowicz et al. This is an open access article distributed under the Creative Commons Attribution License, which permits unrestricted use, distribution, and reproduction in any medium, provided the original work is properly cited.

Gas hydrates (GHs) are a prominent subsurface feature on the Canadian Arctic continental margin. They occur both onshore and offshore, although they formed generally terrestrially, during the last glacial sea level low-stand, both in a region that was persistently glaciated (Queen Elizabeth Islands Group, Canadian Arctic Archipelago (QEIG)), and in a region that was not persistently glaciated (Mackenzie Delta-Beaufort Sea (MD-BS)). Parts of both regions were transgressed in the Holocene. We study the dynamic permafrost and GH history in both regions using a numerical model to illustrate how changes in setting and environment, especially periodic glacial ice cover, affected GH stability. MD-BS models represent the Mallik wellsite and these models successfully match current permafrost and GH bases observed in the well-studied Mallik wells. The MD-BS models show clearly that GHs have persisted through interglacial episodes. Lower surface temperatures in the more northerly QEIG result in an earlier appearance of GH stability that persists through glacial-interglacial intervals, although the base of GH base stability varies up to 0.2 km during the 100 ka cycles. Because of the persistent glacial ice cover QEIG models illustrate pressure effects attributed to regional ice sheet loading on the bases of both permafrost and GHs since 0.9 MYBP. QEIG model permafrost and GH depths are 572 m and 1072 m, respectively, which is like that observed commonly on well logs in the QEIG. In order to match the observed GH bases in the QEIG it is necessary to introduce ice buildup and thaw gradually during the glacial and interglacials. QEIG sea level rose 100–120 m about 10 ka ago following the most recent glaciation. Shorelines have risen subsequently due to isostatic glacial unloading. Detailed recent history modeling in QEIG coastal regions, where surface temperatures have changed from near zero in the offshore to -20°C in the onshore setting results in a model GH stability base, that is, <0.5 km. These coastal model results are significantly shallower than the inferred average GH base about 1 km in wells, Smith and Judge (1993). QEIG interisland channels are generally shallow and much of the previous shoreline inundated by the Holocene transgression was above the glacial sea level low-stand during the last ice age, resulting in a QEIG setting somewhat analogous to the relict terrestrial GH now transgressed by the shallow Beaufort Sea. It is also possible that the marine conditions were present at emergent shorelines for a shorter time or that the pretransgression subsurface temperatures persisted or were influenced by coastal settings, especially where lateral effects may not be well represented by 1D models.

1. Introduction

Natural petroleum gas hydrates (GHs) are a significant feature of Canada's continental margins and Arctic regions [1]. Two major types of gas hydrate occurrences are found on Canada's continental margins at a large range of pressure-temperature stability conditions [1, 2]. The first are essentially terrestrial GHs that formed in Arctic regions on,

or adjacent to the, continental shelf in response to low ground surface temperatures during glacial intervals in the Mackenzie Delta-Beaufort Sea (MD-BS), [3] and Queen Elizabeth Islands Group (QEIG) of the Arctic Archipelago [1], (Figure 1, areas A and B). Part of both areas were transgressed in response to Holocene sea level rise and, additionally, part of the QEIG coastline has emerged more recently as a result of isostatic uplift following ice sheet

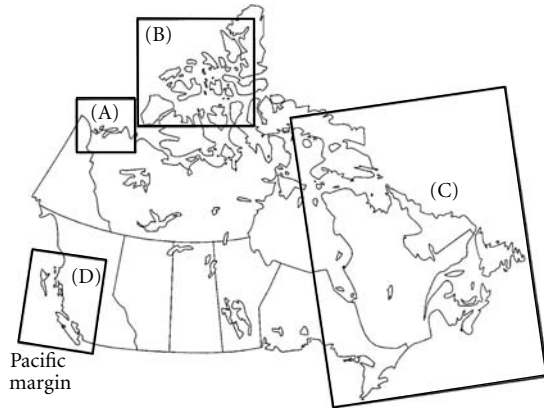


FIGURE 1: Location map for the Canadian GH study areas. (A) Mackenzie delta—Beaufort Sea, (B) Canadian Arctic Archipelago including the Queen Elizabeth Islands Group, (C) Atlantic margin, and (D) Pacific margin, west coast of Canada.

removal [4, 5]. The second type occurs on sub-Arctic continental margins, along the Pacific and Atlantic-Baffin continental shelves, where water column pressure and temperature contribute to gas hydrate stability [6–8]. The second type of GHs probably exist on the margins of the Arctic Ocean Basin, but a lack of data, other than a “BSR” from the Alpha Ridge [8] precludes current description of much of the Arctic continental margin.

Majorowicz and Osadetz [1] estimated a conservative volume of 10^{10} – 10^{12} m³ GHs with an associated methane gas potential in the range of 10^{12} – 10^{14} m³ and pointed out that large part of gas hydrate occurrences is related to deeper hydrocarbons found in the Mackenzie Delta-Beaufort Sea and Sverdrup basin (Arctic Islands). Lesser known are the biogenic deposits.

The volume of methane in hydrates in Canada is geographically distributed in the following regions (Figure 1):

- (A) the Mackenzie Delta—Beaufort Sea,
- (B) the Arctic Archipelago,
- (C) the Atlantic margin, and
- (D) the Pacific margin.

The total in situ amount of methane in Canadian hydrates is estimated to be 0.44 – 8.1×10^{14} m³, as compared to a conventional Canadian in-situ hydrocarbon gas potential of approximately 0.27×10^{14} m³. Osadetz and Chen [9] re-evaluated Mackenzie Delta-Beaufort Sea gas hydrate resources as a function of the spatial variation of pore space gas hydrate saturation (Sgh). Deterministically they mapped 8.82×10^{12} m³ raw initial natural gas in place (GIP), where, if the average Sgh is either >30% or >50%, the inferred GH resource volumes are 6.40×10^{12} m³ to 4.59×10^{12} m³ GIP, respectively. They also provided a probabilistic resource appraisal with an expected total resource = 10.23×10^{12} m³ GIP, which similarly was studied as a function of Sgh. If the average Sgh is either >30% or >50%, then the respective GH resource volumes inferred probabilistically are 6.93×10^{12} m³ and 4.20×10^{12} m³ GIP,

expected, respectively, a result comparable to the mapped deterministic estimates, and not greatly different from the regional estimate of Majorowicz and Osadetz [1].

In this study we focus on GH occurrences that are at or near the Canadian margin of the Amerasian Basin of the Arctic Ocean, its marginal seaways in the Canadian Arctic Archipelago, including the Queen Elizabeth Islands Group (QEIG), and the contiguous onshore areas (Figure 1, areas A and B). GHs occur both onshore and offshore in both regions studied. The primary difference between the two regions is that the QEIG was persistently and thickly glaciated as indicated by a strong postglacial isostatic uplift record [4, 5]; while, the MD-BS is not inferred to have been either persistently or thickly glaciated and it lacks significant postglacial isostatic uplift [5]. The QEIG is completely underlain by the upper Paleozoic to Tertiary Sverdrup Basin succession [10, 11] while the MD-BS is underlain by the largely Cretaceous and Tertiary successions of the Beaufort-Mackenzie Basin [3, 12].

Using a 1D numerical model we model geothermal regime and infer how these might affect gas hydrate stability and ice-bonded permafrost regime and distribution in both regions. Gas hydrate and ice-bonded permafrost model studies require knowledge or inference of the surface temperature history.

Majorowicz, Osadetz, and Safanda [13] developed an effective thermal history model for the analysis of GH and permafrost stability in the onshore Beaufort-Mackenzie basin constrained by Mallik project results [3] (Figure 1 area A). They showed that the formation and history of thermogenic petroleum GHs in permafrost regions can be modeled numerically using a model of surface temperature forcing due to both glacial-interglacial history and future climate change. Their model employed both a detailed Holocene history and a future climate where atmospheric CO₂ has doubled, due to the warming inferred to accompany current climate change trends. The initial model runs were constrained by deep heat flow estimates consistent with bottom-hole temperatures in deep wells and observed type I GH and permafrost thicknesses and characteristics from Mallik wells.

The models considered the pressure—depth dependence of ice and GH thawing points over the entire modeled extent of both GH and permafrost layers. Initial model results, in areas of thick permafrost, showed that expected warming in neither onshore nor offshore Beaufort Mackenzie Basin will destabilize GHs completely. In addition, where the permafrost is thick, a thinned GH stability zone is inferred to have persisted through previous interglacial periods. Previously Taylor and others [14, 15] modeled permafrost and GH stability in the present and near future environment, including both the recent glacial-postglacial history and projected future climate change for both the MD-BS (area A in Figure 1) and the offshore Pacific margin.

In this work we use the same numerical modeling approached applied by Majorowicz, Osadetz, and Safanda [13] to the MD-BS, but applying it to model the characteristics of permafrost and GH origin, growth, and persistence, as a function of temperature history and ice sheet loading

(where applicable) during the last 3 million years in order to compare and contrast cases, considering specifically: (1) MD-BS (Figure 1(A)) in the vicinity of Richards Island and the Mallik wells, an area that is inferred not to have been persistently or thickly glaciated and which lacks significant post-glacial isostatic uplift [5], versus (2) QEIG (Figure 1(B)) in Sverdrup Basin, which was persistently and thickly glaciated and where there is a strong postglacial isostatic uplift record [4, 5] such that the glacial ice sheet thermal and pressure effects were significant.

2. Method

Solution of the transient heat conduction equation gives the temporally dependent subsurface temperature change in response to surface temperature forcing:

$$C_v \frac{\partial T}{\partial t} = \frac{\partial [K(\partial T/\partial z)]}{\partial z} + A, \quad (1)$$

where T is the temperature, K is the thermal conductivity, C_v is the volumetric heat capacity, A is the rate of radiogenic heat generation per unit volume, z is the depth, and t is the time in a one-dimensional layered geothermal model. We employed a computer code to simulated temporal subsurface temperature changes in response to surface forcing by Safanda et al. [16]. Within, model (1) is solved numerically by an implicit finite-difference method [17]. The upper boundary condition is the temporally varying ground surface temperature (GST) and the lower boundary condition is a constant heat flow density at 15 km depth. The depth grid steps are: 2, 5, 10, 50, 100, 250, and 500 m in the depth layers at 0–100, 100–1500, 1500–2000, 2000–2500, 2500–5000, 5000–10000, 10000–15000 m, respectively. Time steps vary between 0.5 to 50 yrs, depending on the amplitude of GST changes. The finite-difference scheme of (1) on the depth and time grids $z_{k-1}, z_k, z_{k+1}, \dots$ and t^n, t^{n+1}, \dots , respectively, has a form:

$$C_{v,k} \frac{T_k^{n+1} - T_k^n}{t^{n+1} - t^n} = 2K_{k+1}^n \frac{T_{k+1}^{n+1} - T_k^{n+1}}{[\Delta z_{k+1}(\Delta z_k + \Delta z_{k+1})]} - 2K_k^n \frac{T_k^{n+1} - T_{k-1}^{n+1}}{[\Delta z_k(\Delta z_k + \Delta z_{k+1})]} + A_k, \quad (2)$$

where the subscript k and the superscript n denote values at the k th depth step and the n th time step, respectively, $\Delta z_k = z_k - z_{k-1}$ and $K_{k+1}^n = \Delta z_{k+1} / [\int_{z_k}^{z_{k+1}} dz/K^n(z)]$.

This difference scheme, together with the upper and lower boundary conditions leads to a system of difference equations for unknown values T_{k-1}^{n+1} , T_k^{n+1} , T_{k+1}^{n+1} (where subscript k and superscript n denote similarly the k -th depth and the n th time steps) within a tridiagonal matrix, which was solved by the forward method of Peaceman and Rachford [18].

To estimate effective thermal conductivity values and volumetric heat capacity, we consider the respective geometric and arithmetic averages of the constituent values for the rock matrix, water, ice, and GH in proportion to their fractional volumes [17]. A consumption or release of latent

heat, L , accompanying either the water/ice ($334 \text{ kJ}\cdot\text{kg}^{-1}$) or GH ($430 \text{ kJ}\cdot\text{kg}^{-1}$) transitions, accompanying thawing or freezing was included. The effects of interstitial ice and GH were accounted for using apparent heat capacity [19], when the volumetric heat capacity is increased in the model depth sections where the thawing and freezing occurs, that is, where the temperature is within the thawing range between the temperature of solidus, T_s , and liquidus, T_l , during the actual simulation time step.

The liquidus and solidus temperatures of water/ice and GH are depth and hydrostatic pressure dependent [17] and solidus temperatures were 0.2°C lower than liquidus temperatures. A contribution to the heat capacity from the latent heat $= \rho\Phi L/(T_l - T_s)$ is considered, where ρ is the density of either ice or GH and Φ is a volume fraction occupied each phase. In the ice-bonded permafrost (IBP) zone we infer the 30% rock matrix porosity to be occupied fully by water at temperatures above T_l , and by ice at temperatures below T_s . Within the GH stability zone the GH saturation in the rock matrix porosity was inferred to be 30 or 60% range for two models, where 60% is the maximum saturation found in part of the Mallik well section (Scott Dallimore, personal communication, 2011). The formation water salt concentration, 9 g/L, was considered constant with depth and the pressure-temperature phase curves were adjusted to this value. The salinity of 9 g/L was used so that the liquidus temperature at the permafrost base in Mallik (-1°C at 600 m) corresponds with the value given by formula (3):

$$T = 0^\circ\text{C} - 0.073 * \text{pressure (MPa)} - 0.064 * \text{salinity (NaCl, KCl.) (g/L)}. \quad (3)$$

This formula was taken from paper by Galushkin (1997), [17]. If there is a fresh water within Mallik sediments, the liquidus temperature would be by 0.58°C higher. If there is a sea water with 40 g/L, the liquidus would be by 1.98°C lower. For temperature gradient 20 K/km it would mean a shift of the permafrost base by 30 m downward and by 100 m upward, respectively.

Numerical code performance was tested by comparing results against the analytical solidification problem solution [19], where a molten half-space at liquidus temperature, 1300°C , is in contact with a solid half-space at zero temperature and which releases latent heat of $477 \text{ kJ}\cdot\text{kg}^{-1}$ in the temperature range $1100\text{--}1300^\circ\text{C}$. Differences between the numerical and analytical temperature profiles were found to be within $\sim 20^\circ\text{C}$. Assuming that the magnitude of the numerical/analytical difference is proportional to the temperature range the error expected for the IBP and GH numerical simulations should be about 100 times smaller (i.e., two tenths of a $^\circ\text{C}$). A similar error range was estimated by halving the time and/or depth steps.

Our model uses deep heat flow, thermal conductivity, present IBP, type I (CH4) GH thicknesses, and a surface melting temperature (-0.576°C) that also considers formation water salinities (9 g/L). It employs latent heat effects throughout the IBP and GH layers, which improves upon previous models [14, 15]. The models are constrained

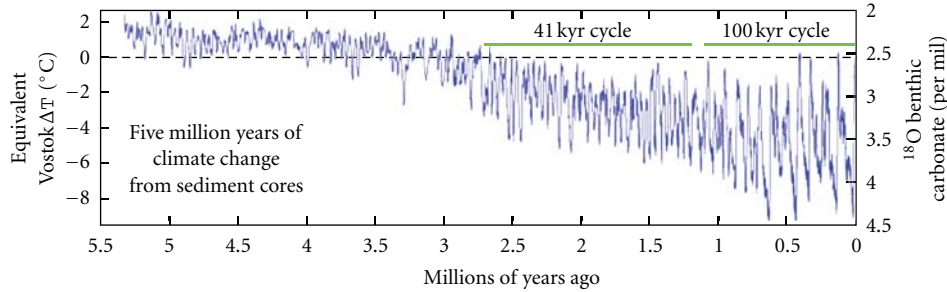


FIGURE 2: Detailed history of the last 5.5 Myr of surface forcing modified from [43].

by deep heat flow [20, 21], current IBP thickness and observed type I GH thicknesses [22, 23], as described above. The models consider the pressure-depth dependence of ice assuming hydrostatic and GH thawing points over the entire expected extent of the IBP and GH layers [24]. Previously published models have considered only a thin layer using a constant dissociation temperature [15].

In both the MD-BS and QEIG regions, it is uncommon to find GHs within the IBP, however, there are no methods that define GH within the ice-bonded layer. Logging signatures of GH and ice are similar and shallow section is not routinely logged, in large part due to drilling and hole stability problems in the IBP zone. This means we have no effective way to infer GH concentrations within the ice-bonded permafrost [25, 26]. Commonly the well surface casing is cemented in the stable indurated rock strata that occur below IBP base, but above the first GH occurrences. Rarely, GH occur in the IBP [25, 26], but the general lack of GHs in the IBP layer is consistent with models where most GHs form due to the *in situ* transformation of conventionally entrapped natural gas accumulations rather than a dynamic GH or IBP trap [1, 13]. This would appear consistent with other inferences regarding the origin of GH accumulations [1, 10]. In simulating the temporal subsurface changes in models where IBP and GH occurrences are separate and distinct, a consumption/release of the latent heat during decay/formation of IBP or GH was considered separately. In fact, GH formation/degradation occurs where the p - T field works in tandem with the complex petroleum system geological factors as illustrated by the work of Chen and Osadetz [10], and Smith and Judge [2]. Both show that rich GH accumulations are rare and the rich accumulations are commonly associated with conventional petroleum accumulations [10] as part of the thermogenic petroleum systems.

The model division into IBP and GH stability zones was prescribed explicitly. Because the IBP generally lacks GHs and the GH occur generally below the IBP only the water ice latent heat and p - T phase curve is considered in the IBP zone and that only the GH latent heat and p - T phase curve were considered in the GH stability zone.

The above conditions may not be appropriate in models where GHs are intercalated within the IBP layer. In such cases [25] at each depth point, it is prescribed which fraction of the pore space can be occupied by water ice or GH. Then the code checks independently the p - T conditions for IBP and for GH

at each depth point, in each time step, and appropriately adjusts the volumetric heat capacity. For example, in the Mallik case, where a porosity of 30% was assumed, the prescribed pore fraction of GH in the uppermost 250 m was zero and that of IBP 100%, because as the preliminary calculations had shown, IBP forms prior to hydrate, whereas GH forms first below 250 m.

3. General Paleoclimatic History

In order to model conditions for the IBP formation due to cooling of the surface and following GH formation considering latent heat “delay” effects (due to deeper formation conditions), we need to know surface conditions in the past. The evidence for past GST comes mainly from isotopic data and their analysis, especially $\delta^{18}\text{O}$ studies. Our models of surface forcing of temperature are generally based on known models of surface change [27, 28], (Figure 2). The recent and the Quaternary surface temperature forcing uses a detailed Holocene glacial-interglacial history compiled from other sources [15]. While we project the model results into the future we consider the climate effects based on a doubling of atmospheric CO_2 , that results in a local mean surface temperature increase of $2^\circ\text{C}/100$ yrs [29, 30].

The Paleocene-Eocene Thermal Maximum (PETM) could have been caused by abrupt releases of methane hydrates under the bottom of the ocean [31, 32].

During that time, the Arctic Ocean may have reached levels more typically associated with modern temperate (i.e., midlatitude) oceans. Following the Paleocene to early Eocene peak warming the climate cooled towards the Pleistocene glacial environment. However, 3 to 6 Myr ago, global average temperatures were still higher than today with surface temperature at poles higher than currently. During this interval the Northern Hemisphere likely lacked continental glaciers [27, 28]. Climate changed dramatically during the following 3 Myr before present and significant amplification of the climate response to orbital forcing (i.e., Milankovitch cycles) began. This caused changes in surface temperature forcing resulting in drastic oscillations between ice ages and warmer periods during the past 1 Myr. These resulted in cycles of glacials and interglacials marked in the Northern Hemisphere by the growth and retreat of continental ice sheets at frequencies initially 41 kyr and later 100 ky within a progressively deepening ice age. The gradual intensification

of this ice age during the last 3 Myr has been associated with declining concentrations of the CO_2 which partly influences temperatures changes. El Nino was continual rather than intermittent until 3 million years ago. The temperature change model that is applied to our study areas is shown in Figure 2.

We consider the variation between 0°C to -6°C (i.e., “warm” versus “cold” models), as a probable temperature range for the time 3 Myr ago, prior to cooling. In the “cold” model the amplitude of variations increased to 4°C by the onset of the “small” ice ages of the 41 ka period at time 2.5 Myr ago, and their mean temperature was decreasing stepwise from -8°C to -9°C and then to -9.5°C at time of the transition to the “big” ice ages of the 100 ky cycles 900 ka ago. The temperature variations during the “big” glacial cycles were 13°C . For the era prior to 2.5 Myr ago we have used a stepwise approximation of the surface temperature with a length of the step 1 Myr between 14 and 6 Myr ago and 0.5 Myr between 6 and 2.5 Myr. In the “warm” model the simulation starts at time 3 Myr ago with steady-state T - z profile corresponding to GST of 0°C . GST is decreasing linearly from 0°C at 3 Myr ago to -10°C at the beginning of the large 100 ka glacial cycles 0.9 Myr ago. The GST history during the 100 ka glacial cycles is the same in both models. Using these constraints we model the permafrost and GH thickness in the changing surface temperature environment for the MD-BS and QEIG.

It is essential to understand the origin, growth, and persistence of subpermafrost GH accumulations, as a function of temperature history, to characterize a geological natural gas resource model. Our analysis will use the characteristics of IBP and GH origin, growth, and persistence, as a function of temperature history, to constrain the models of past environments that led to the initiation, growth, and persistence of the linked occurrences of both IBP and GH accumulations in the subsurface of the Canadian Arctic. The work will also address the risks posed by global and regional temperature change, as well as providing a tool that will assist the appraisal of risks related to surface imposed changes on the GH layer.

4. Modeling of Permafrost and Gas Hydrate Stability Histories in the Mackenzie Delta-Beaufort Sea Region

Depth to GH base of type I stability in the Mackenzie Delta is well described [31] and it serves as an important constraint for the acceptance of model results. Recent analysis of the Holocene-Pleistocene temperature history using a 1D model of IBP and GH layers in an onshore Mackenzie Delta setting during the last 600 k years, Majorowicz et al. [13] showed that due to the buffering effect of the IBP and the retardation of GH dissociation due to latent heat effects GH can persist through interglacial intervals despite large variations in surface temperatures.

To better understand the formation and history of petroleum GHs in terrestrial IBP regions we have performed numerical modeling of the surface forcing due to general

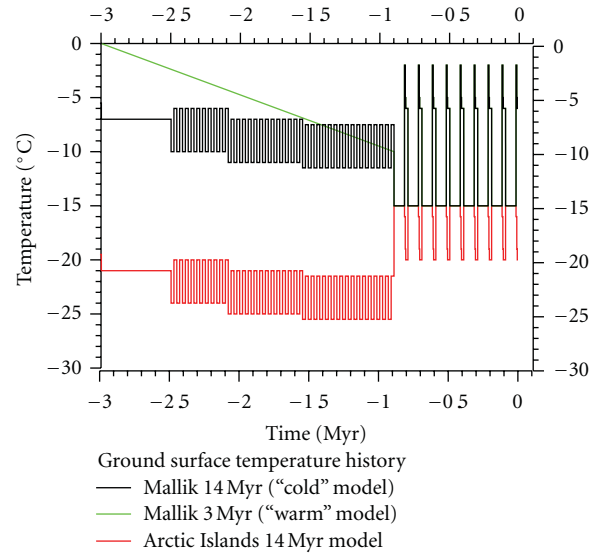


FIGURE 3: Recent 3 Myr history of surface forcing temperature (top surface) for the QEIG in comparison with previous model for Richard Island/Mallik. Ground surface temperatures are -6°C in Mallik and -20°C in QEIG at present. Two models were considered for the Mallik area, beside the 14 Myr long “cold” model also the “warm” model starting 3 Myr ago at 0°C and decreasing linearly to -10°C at 0.9 Myr ago.

cooling trend started in late Miocene and more detailed glacial-interglacial history and future climate change. Persistent GH layers in a terrestrial environment of thick IBP in cold regions sequester methane and impede its migration into the atmosphere. The Mallik site in the Mackenzie Delta is an excellent example of such GH deposits situated in the large area of deep GH type I stability in the onshore and offshore (Figure 1) under continental and continental relic IBP (accumulated during the Pleistocene marine lowstand prior to the Holocene sea level rise). More detailed descriptions of the MD-BS geothermal environment GHs and the Mallik well experiments are found elsewhere [23, 33–42].

4.1. P-T Time Envelope and Formation of Permafrost and Gas Hydrate: Preliminary Considerations. Considering the IBP and GH formation and due to the large uncertainty of surface temperature models for the remote past we used the temperature history range (“cold” versus “warm” model) shown in Figure 3 (i.e., Mallik case). Pleistocene surface history of glacials and interglacials is after Muller and MacDonald [27]. The more recent surface climate history for the end of the Wisconsinan and Holocene is after Taylor et al., [15]. The range of temperature critical for GH formation is shown in preliminary test for the steady-state in Figure 4.

Majorowicz et al. [13] showed the GH could not have formed when the GST was higher than -5°C . Before 6 Myr ago the climate was even warmer, which means that the first GH deposits might have formed around 6 Myr or later, which is different than the onset time for the IBP. The equilibrium IBP thickness is some 250 m for a GST of -5°C . It means

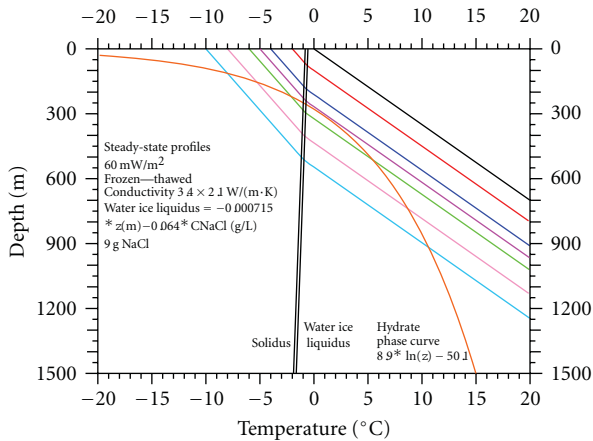


FIGURE 4: Steady-state profiles corresponding to Mallik-Richards I. area geothermal model for the range of surface temperatures varying from -10°C to 0°C which are possible in the preglacial, glacial, and interglacial periods.

that the IBP, a potentially impermeable seal for any potential gas migrating upward, existed for a long time before P - T conditions permitted the first GH formation.

4.2. Model for the 3 Myr History of Surface Temperature Change: Results. We have simulated the downward propagation of the surface warming and cooling attending the cyclical glacial and interglacial models for the eastern Richards Island/Mallik location based on the above-mentioned 2 models as shown in Figure 3.

The dependence of the thermal conductivity on water/ice content and the specific heat of the rock section on the porosity and the proportion of interstitial water and ice are important. Accounting for the effect of the latent heat necessary to thaw the interstitial ice in the IBP layer is crucial for matching observations at realistic time rates. In the absence of this heat sink provided by thawing ice in the IBP, the subsurface warming would proceed much faster.

Individual computational models use the characteristics of IBP and GH formation and dissipation, as functions of temperature history, constrained by present temperatures and observed IBP and GH layer thicknesses.

All models account for latent heat by means of the apparent specific heat, which is a standard treatment. The model also considers diffusive heat flow related to surface-subsurface coupling. GH formation can start only when the long-term GSTs drops below -5°C .

4.2.1. Case 1: Gas Hydrate Formation Controlled by the Geological Gas Entrapment Conditions. In Case 1 we allow GH occurrence only in the porous and permeable geological reservoir confined under a preexisting impermeable seal (i.e., GH formation was considered below 900 m only). At Mallik, the interbedded character of the GH bearing strata also indicates a stratigraphic and lithologic control on GH occurrence. GH layers occur in coarse-grained sandstone beds separated by thin nonhydrate-bearing, fine-grained

siltstone and claystone beds. The gas and GH at Mallik appears to be entrapped in association with the anticline structure. The fault bounding the structure is the likely conduit for migration of the gas into the GH stability zone. This is the probable situation for rich MD-BS GH in the underlying Beaufort-Mackenzie Basin (BMB). There GHs occur in close spatial association with underlying conventional petroleum accumulations, such as at the Mallik boreholes.

Two general types of gas were observed in the Mallik wells. Microbial gas is characterized by dry gas compositions (i.e., $C_1/(C_2 + C_3) > 1000$) and methane carbon isotopic ratios between -70 to -93‰ [3]. Thermogenic gas is wetter and has carbon isotopic ratios for methane of around -35 to -45‰ . The carbon isotopic ratios for thermogenic ethane and propane are -31‰ and -26‰ , respectively. Methane isotopic compositions of 12 GH samples averaged -42.7‰ and clearly indicate a thermogenic source according to Lorenson (personal comm., 2005) and [3]. Thermogenic gas likely migrated upward along listric-normal growth faults from larger depths where gas generation is possible due to availability of the source rock and higher temperatures. The deep upward migrating gas could have been trapped in the anticline and/or tilted fault blocks and converted, much later, into GH when regional cooling took place. This hypothesis is consistent with the coincidence of GH occurrences with known underlying conventional petroleum accumulations [1, 10].

We relate our model to the above findings. The division into IBP and GH stability zones was prescribed in the model explicitly such that we have vertically separated the occurrence of IBP from GHs. A consumption/release of latent heat during the decay/formation of either IBP or GH is considered separately. As mentioned above this means that only the latent heat and P - T phase curve of water ice were taken into account in IBP zone, and only GH latent heat and P - T phase curve were used in the GH stability zone. GH formation was considered below 900 m only and the maximum likely GH saturation of 60% has been used.

In the resulting models GH did not form during the coldest 41 ka cycles (from -11.5°C to -7.5°C), because the steady-state geotherm corresponding to the mean surface temperature of the cycle, -9.5°C , enters the GH stability region just above 900 m (see Figure 4) and duration of the cold phase of the cycle with surface temperature of -11.5°C is too short (20.5 ka) for the temperature to cool close to the steady-state curve corresponding to -11.5°C . The model simulates the current base of IBP and GH at 541 m, and 1060 m, respectively. These are only slightly above the observed positions of IBP and GH in the Mallik wells at 600 m and 1107 m, respectively. The surface temperatures during the glacial, -15°C , and the interglacial were the same as that used in previous including model 3 of Majorowicz et al. [13] as modified from Taylor et al. [15].

The 3 Myr “warm” history considered as an alternative to the more detailed “cold” model of the ground surface temperature used in simulations at the Mallik wells gives very similar results to that of the “cold” model for the time interval covering the second half of Pleistocene, which

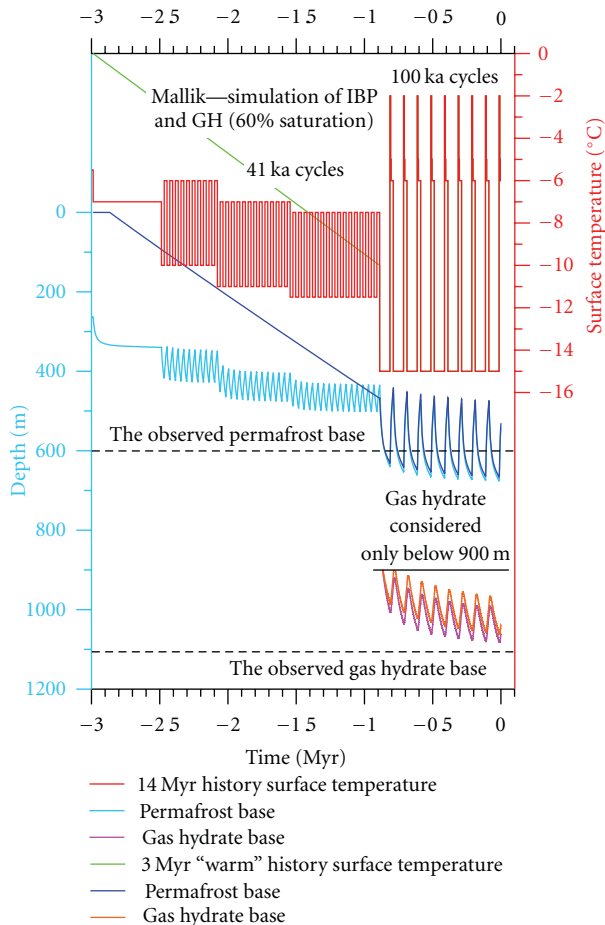


FIGURE 5: 3 Myr history of surface temperature forcing (“cold” versus “warm” models), IBP and GH base depth variation—Case 1 model (entrapment by structural cap (GH formation was considered below 900 m only)) for the high 60% GH saturation assumed as maximum case.

is characterized by 100 ka long glacial cycles (Figure 5). The simulation starts at time 3 Myr ago with a steady-state T - z profile corresponding to GST of 0°C. GST is decreasing linearly from 0°C at 3 Myr ago to -10°C at the beginning of the large 100 ka glacial cycles 0.9 Myr ago. The GST history during the more recent 100 ka glacial cycles is the same in both models. Despite the warmer temperatures of the 3 Myr history, which is up to 6°C warmer for most of the period between 3 Myr and 0.9 Myr ago, in comparison to the previous 14 Myr model, the simulated thicknesses of the IBP and the GH layer differ by at most a few tens of meters between the two models. It means that the present temperature-depth distribution is not very sensitive to the remote GST history and that the results obtained by the 14 Myr history for the end of Pleistocene and Holocene are effectively similar for the period after 3 Myr ago. Despite our use of quite general surface temperature histories, the agreement between the two model predictions and the observed bases of GH and IBP is reasonably good.

4.2.2. Case 2: Considering Simultaneous Occurrence of Permafrost and Gas Hydrate. In Case 2 we permit the simultaneous occurrence of IBP and GH. This has some geological

grounds as the geological seals are discontinuous laterally [3] and at least one such occurrence has been observed [25]. The model considered 30% porosity, with all the pore water frozen. The thermal conductivity of the frozen and thawed rock was 3.4 W/(m.K) and 2.1 W/(m.K), respectively, and the latent heat of water freezing is 0.334 MJ/kg. The numerical simulation of the subsurface temperature response to changes of the surface temperature forcing was calculated over the last 3 Myr (Figure 6). The GST history is the same as that for the Case 1 model (Figure 3).

In this case of simultaneous IBP and GH occurrence, the 3 Myr model of linear GST decrease between 3 Myr and 0.9 Myr illustrates well the interplay of the downward propagating surface cooling and the latent heat release during permafrost and gas hydrate formation. The first gas hydrate forms at the depth of 290 m, when the GST drops to -5.6°C. The latent heat of hydrate formation starts to be released, which decelerates substantially the downward propagation of the permafrost base that is, at that moment, at 250 m.

The formation of permafrost accelerates again only when the upward migrating upper boundary of hydrate meets the sediment occupied by permafrost. At that moment, the hydrate formation and therefore also its latent heat release stop there. Subsequently, the latent heat is released only at the downward-migrating bases of the IBP and GH layers.

It is questionable, what could have happened with the methane contained in the freezing rock. If all pore water had frozen, the methane could not have escaped to the surface and might have been pushed downward below the downward-migrating IBP base or escaped to the sides of the IBP body and then migrated upward. Such IBP thermokarst areas exist under water bodies of the present Mackenzie River Delta.

Figure 6 shows that depth variations of the base of both the IBP and GHs are larger in Case 2 than Case 1 during the 41 ka and 100 ka cycles. The most probable reason for the larger variations of the IBP base is a smaller damping effect of the latent heat release/consumption due to a smaller amount of freezing/melting water/ice. Most of the pore water is bounded in the GH, which is stable in this depth range. The smaller damping effect at the IBP base also means that the subsurface temperature changes propagate faster to the GH base and cause its larger depth variations compared to model—Case 1.

In order to illustrate how the simulations are sensitive to hydrate saturation, two alternative levels, 30% and 60%, were considered. The results for simultaneous IBP and GH occurrence in the Mallik geothermal model and the “warm” 3 Myr ground surface temperature history are shown in Figure 7. As expected, before hydrate formation begins, the downward propagation rate of the permafrost base does not depend on the saturation. However, since the first hydrate formation at 290 m, both the IBP and GH bases migrate downward faster when the saturation is lower due to the smaller latent heat released during less saturated hydrate formation. This deficit cannot be compensated by the latent heat of ice released in the layer of simultaneous IBP and GH occurrence from the volume occupied in the higher

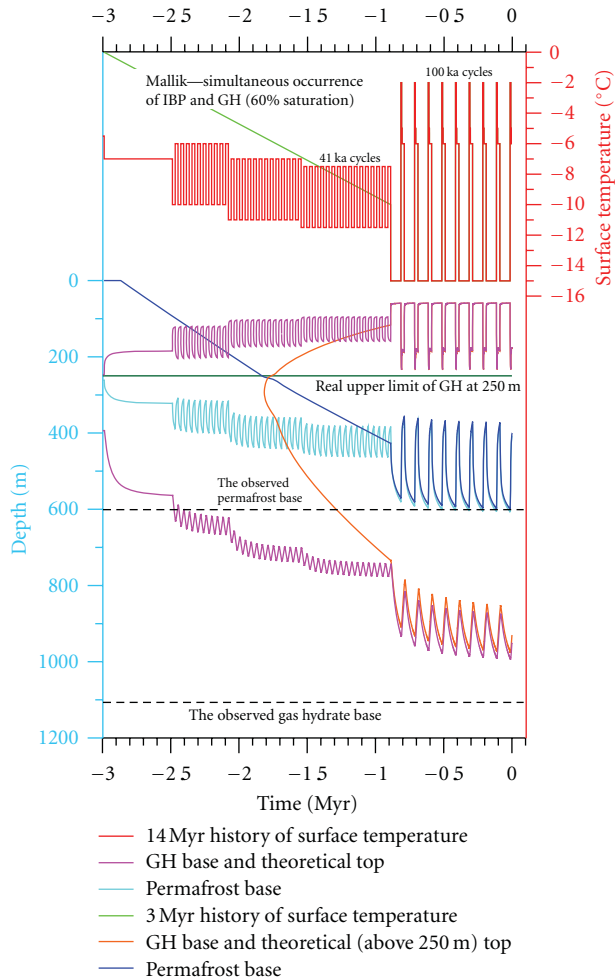


FIGURE 6: Depth variations of the IBP and GH upper and lower boundaries during the last 3 Myr for Case 2 for 60% saturation of GH. Simulation is shown for the “warm” and “cold” surface temperature forcing models.

saturation model by hydrate, because the value of latent heat of ice is lower than that of gas hydrate. During the 100 ka glacial cycles, the IBP and GH bases are by about 30 m and 40–50 m, respectively, deeper in the model with lower saturation. It is caused mostly by higher thermal conductivity within the layer of simultaneous IBP and GH occurrence, where the more conductive ice substituted for less conductive gas hydrate. The higher amplitude of the hydrate base variations in the less saturated hydrate model is caused by a smaller damping effect of the latent heat.

The Case 2 model provides no mechanism for methane to escape to the surface from below the older, but overlying IBP. This model predicts a simultaneous occurrence of IBP and GH below 250 m, which, however, is not generally observed [3]. The simultaneous occurrence also implies lower conductivity in this zone, which means a higher temperature gradient, which shifts the IBP and GH bases upward, above their currently observed position. The indicated upper GH boundary above 250 m shown in Figure 7 is a model prediction rather than an observed GH boundary. It

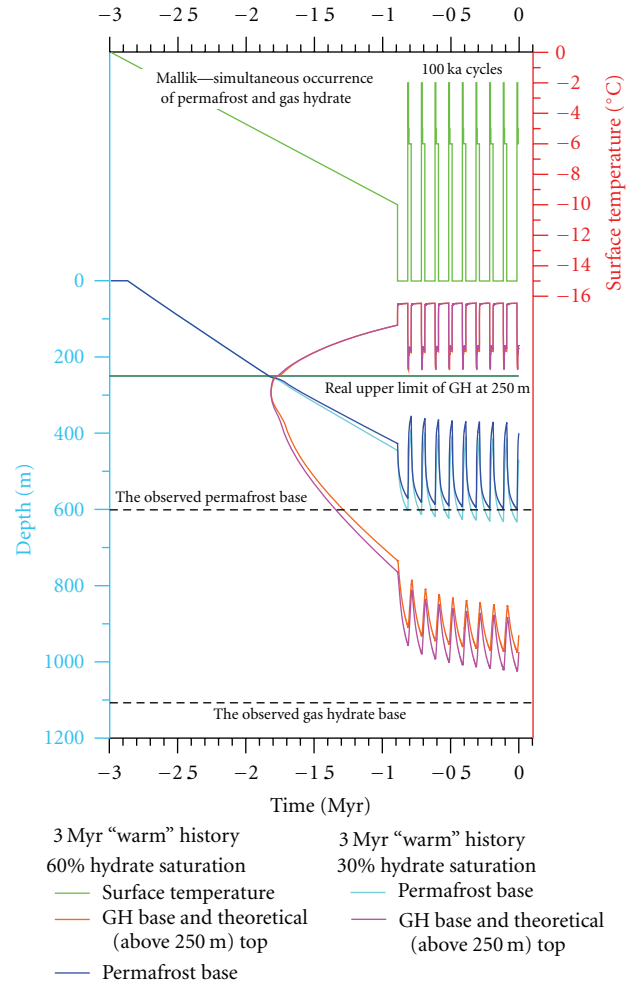


FIGURE 7: Depth variations of the IBP and GH upper and lower boundaries during the last 3 Myr for Case 2 for 30–60% saturation of GH comparison. Simulation is shown for the “warm” forcing model.

was calculated according to the P - T phase curve. In reality, no GH was considered there because all the pore space above 250 m is occupied by water ice and GH cannot displace a volume already occupied completely by ice.

5. Modeling of Permafrost: Gas Hydrate Stability History in the Queen Elisabeth Islands, Canadian Arctic

GHs are inferred to occur in only 24% of the QEIG wells. In many cases the inferred GH occur at deep depths [40] that are much deeper than the inferred depth to the base of the Type I GH stability zone determined using similar geothermal data. Permafrost thickness in the QEIG are well described [21]. There permafrost base varies with depth. In the terrestrial part it is from tens of meters to 726 m but it is only few meters under the sea offshore, based on precise temperature logs in the area [21, 34–39].

Gas hydrate thickness onshore is to a large degree controlled by the extent of the permafrost and depth to the base IBP (circa -1°C). GH occurrence in the QEIG is relatively well known although the number of wells is small for such a large region [11, 42, 44]. According to Brent [44], his study of seismic data on southern Ellef Ringnes Island indicated that the permafrost base of 470 m is directly underlain and in contact with a deep GH layer that extends down to 930 m. In some cases GH detection from well logs exceeded the projected depth interval for the methane hydrate stability [11, 42]. However, well-log-based GH detection can be uncertain. The average depth to the detected GH base is 1,020 m and it is 368 m for the top of GHs.

Heat flow in Sverdrup Basin underlying the QEIG is typical of a continental margin sedimentary basin setting and it varies mainly between 50–80 mW/m^2 [45, 46]. In such an environment of relatively high heat flow the IBP and GH stability is controlled by paleoclimate history of very low surface temperature and pressure forcing, partially due to the pressure attributed to the glacial ice sheet load.

In the QEIG area, the deepest base of subsurface terrestrial permafrost is inferred at 726 m [21]. GHs occur as deep as 1.5 km mainly a result of variable low surface temperature and past ice load history. Present occurrence of GH and overlying permafrost is not necessary in equilibrium with present P - T conditions for GH stability as derived from present knowledge of temperature depth (T - z) and formation pressure (P). The best example of this is the dependence of permafrost thickness, which is highly variable in throughout the Arctic, and which depends on the history of marine regression and shoreline emergence during the last 9 Myr [47, 48], both of which are likely due to terrestrial rebound after ice unloading.

The QEIG began to rebound following the Wisconsinan glaciation [5, 49, 50]. Change in temperature from offshore submarine to terrestrial settings was up to 20°C and this caused a gradation of permafrost onshore as thick ice permafrost is not found offshore [39]. According to Taylor, [14] thick ice-bearing permafrost is not observed currently beneath the deeper channels of the central Queen Elizabeth Islands. Analysis of a precision temperature log obtained from an offshore well near Ellef Ringnes Island [40] indicates that the thermal regime beneath the seabed is in equilibrium with today's marine environment. If thick permafrost similar to that observed on land today had existed in the Pleistocene in areas that are presently offshore, then such permafrost must have started melting no later than 25,000 years ago [14]. This suggests that the inter-island channels must have been water-filled at least by that date [14].

Currently, there are only 2-3 small ice caps from the Wisconsinan glaciations in the QEIG. There was previously a controversy, now resolved, regarding the thickness extent in space and duration in time of any glaciations of the QEIG. In spite of the substantial postglacial uplift [4, 5, 50–52], which suggested a thick and continuous ice sheet [5, 53, 54] some used geomorphic evidence to suggest that no such pervasive ice sheet existed [50, 52, 55]. However, the proponents of the discontinuous Franklinian Ice Complex have recently

acknowledged [56] presence and extent of the Innuitian Ice Sheet Model as correct.

Recent model results [57] give several important results relevant to glacial history in the Arctic: (1) an important characteristic of the 100-kyr cycle is its asymmetric structure, with long (90 kyr) fluctuating ice-growth phases followed by rapid (10 kyr) terminations; (2) 60–80% of the Laurentide Ice Sheet was cold-based (frozen to the bed) at the LGM, and therefore unable to undergo large-scale basal flow. The fraction of warm-based ice increases significantly through the ensuing deglaciation, with only 10–20% of the Laurentide Ice Sheet being cold-based by 8 kyr BP.

The study of Ice Sheet history shows that once the ice sheet formed following peak interglacial periods, at least its core remained intact through the entire glacial cycle, with ice thickness of ~ 2 km inferred for the Foxe Basin region. The volume of ice required to maintain this core of the Laurentide Ice Sheet represents at least 10 m of sea level. The Innuitian ice sheet was cold-based (comparable to or colder than Greenland Ice Sheet which is today less than -13°C according to Tarasov and Peltier [56]).

Basal temperatures in the glacial ice models are controlled by air temperatures and complex ice sheet dynamics (e.g., accumulation phase, internal sliding, etc.). Recently, Rolandone et al. [58] report data that suggests that the Laurentide Ice Sheet was not frozen to its bed along its southern margin, implying basal sliding as suggested first by Payne [59]. In such a case the glacial ice is in a completely steady state. The ice sheets do not insulate the ground from severe air temperatures, because ice has a thermal conductivity very similar to the average thermal conductivity of earth materials. This effect is often referred to as “insulating” and we will use it here. It needs to be understood though, that it refers to steady state of ice load and that more realistic is a buffering by the ice in a dynamic process of its history. The basal ice sheet temperature is the upper boundary condition for GH model temperatures.

We will use present observation of permafrost and GH base depths to constrain and the surface forcing model for the glacial-interglacial history. These models, 21 constrained by present observations, will provide insight into the past environments that led to the initiation, growth and persistence of the linked occurrences of both permafrost and GH accumulations in the subsurface of the QEIG (Canadian Arctic Archipelago) models of the surface air temperature and ice cover dynamics (base temperature and pressure).

5.1. Recent Postglacial Rebound: Gas Hydrate-Permafrost Model. According to the recent model of Taylor and Wang [60, and references therein], the cooling of the terrestrial surface of the QEIG occurred soon after coastal emergence, a result of isostatic rebound within 200 years [60]. Different portions of the islands emerged at different times before the present mainly during the interval of hundreds of years ago to several thousands of years ago. This process is well described by the relationship between elevation and time of emergence [14, 60]. This process of temperature change from subsea, -1°C , to harsh terrestrial arctic temperature

conditions, -20°C , controls, to a large extent, the subsequent IBP and GH formation. It is known from temperature-depth logs in QEIG wells (e.g., Sabine Peninsula, Melville Island, and Ellef Ringnes Island) that wells near the coasts are influenced by the recent history of emergence and some even show negative thermal gradient in the shallow section, while wells further inshore appear to have reached thermal equilibrium. Some [14] consider thick permafrost in the island interiors to be in equilibrium. In that sense, recent history would be the only factor controlling thickness of IBP and GH. We check that hypothesis with our modeling.

The QEIG model of a pure postglacial rebound considers only the effect of the islands emersion from the marine environment with a steady-state surface temperature of -1°C to the harsh terrestrial conditions of -20°C . It is assumed that similarly to [60], the cooling occurred within 200 years of emergence.

The geothermal model is:

- (1) rock porosity 30%;
- (2) gas-hydrate saturation 60% of the pore space (i.e., 18% of the total volume);
- (3) the remaining 40% of the pore space (not hydrate) is filled with either water or ice (i.e., 12% of the total volume);
- (4) conductivity of pure permafrost $3.4 \text{ W}/(\text{m}\cdot\text{K})$;
- (5) conductivity of the mixture of permafrost and GH $2.7 \text{ W}/(\text{m}\cdot\text{K})$;
- (6) conductivity of the GH $2.1 \text{ W}/(\text{m}\cdot\text{K})$;
- (7) conductivity of melted rock $2.1 \text{ W}/(\text{m}\cdot\text{K})$.

It is assumed that simultaneous occurrence of permafrost and GH is possible. The models considered the pressure-depth dependence of ice and GH thawing points over the entire expected extent of the GH and overlying permafrost. The first model assumes heat flow of $60 \text{ mW}/\text{m}^2$ [45]. This model of surface forcing and the resulting variations in the permafrost and GH below is shown in Figure 8(a).

In Figure 8(a), the yellow part of the plot marks the depth range down to 255 m, where permafrost forms before the P - T conditions for GHs are attained. If we assume that all interstitial water is frozen in permafrost, then there is no space for the hydrate formation within this interval. The P - T phase curve of hydrate is first touched by the sinking temperature curve in the depth interval 74–91 m at 1240 years, but as mentioned above, the permafrost already occupies the available pore space. The depth interval, where the actual temperature is lower than the hydrate phase curve spreads from this time both upward and downward, but no hydrate can form until 2700 years, when the model lower boundary of GH stability crosses the permafrost base at the depth of 255 m. Subsequently, the GH forms prior to permafrost below 255 m.

Due to the assumed 60% GH saturation of the pore space the remaining pore space interstitial water, 40%, can freeze and a mixture of hydrate and permafrost can form as the cooling proceeds.

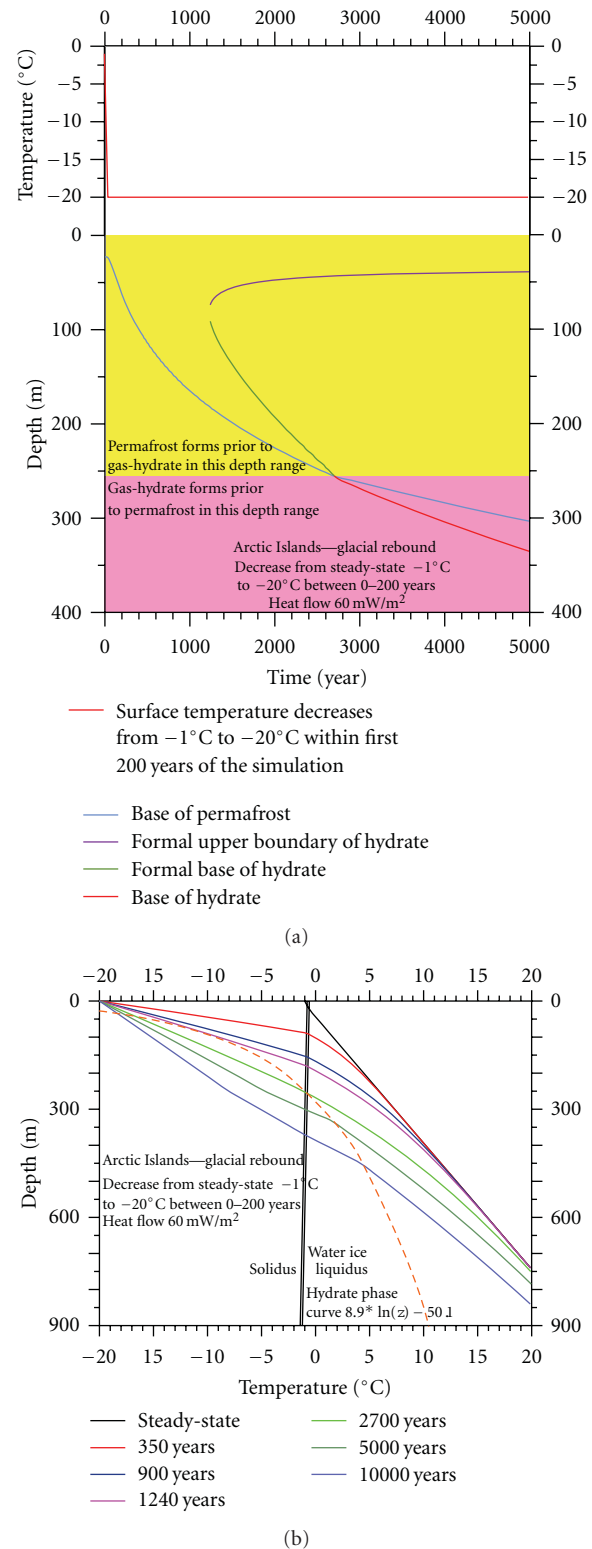


FIGURE 8: (a) History of permafrost and GH P - T stability in the early 5000 years of immersion. History of surface forcing is shown in the upper panel (from subsea -1°C to harsh terrestrial temperature condition of -20°C). (b) Corresponding modeled temperature versus depth (T - z) given for a set of times after the sea to terrestrial onset. The initial profile is a steady-state one corresponding to the marine setting conditions.

We also constructed models for heat flows values of 70 and 80 mW/m², which could be possible values in the QEIG [45] for the first 10 k years of the model runs. Comparison of the results of the emergence model shows that the results for three versions of the heat flow of 60, 70, 80 mW/m² differ only slightly due to differences in temperature gradient. The steady-state initial thickness of permafrost decreases from 23.1 m to 17.5 m with increasing heat flow. The time when the temperature curve touches the *P-T* curve of the hydrate increases with the heat flow (60, 70, 80 mW/m²) 1240 years, 1280 years, 1340 years, respectively. The time when the temperature curve drops to the crossing point of the gas/hydrate and water/ice phase curves with increasing heat flow from 2700 years via 2940 years to 3200 years. These are the times when the GH starts to form below the depth of 255 m prior to the water freezing (if the free gas is available, of course). The depth of the permafrost and the GH bases 5000 years after the land immersion decreases with increasing heat flow from 303 m and 335 m via 294 m and 319 m to 286 m and 304, respectively. Figure 8(b) shows *T-z* profiles versus stability curves for the time interval from 0 to up to 10,000 years. Time 0 equals a steady state at sea temperature -1°C; the time 1240 years equals the time when the temperature curve touched for the first time the phase curve of the hydrate; time 2700 years is the time when the temperature curve passes through the crossing of the ice/water and hydrate/water *P-T* curves.

According to these simulations, GH should not occur at sites which emerged less than 2700 years ago where the permafrost thickness should be up to 250 m. In areas, which emerged earlier than 2700 years ago, GH could occur just below the permafrost at depths greater than 250 m.

In some cases our models indicate current permafrost to a depth of 0.7 km and the hydrate layer is over 1 km [42] or close to 0.9 km deep, which is like that illustrated on Ellef Ringnes Island [44]. These depths are higher than ones possible for the models as shown above. It is possible, that marine conditions lasted only a short time and that the deep premarine subsurface temperatures could persist, at least partially. The sea level rose by some 100–120 m some 10 ka ago shortly after the end of recent glacial period. If the inundated area was above the glacial sea level during the last ice age, then the terrestrial conditions prevailed and controlled the permafrost hydrate thickness there for most of the glacial cycle. The inundation may have lasted only several thousand years. Alternatively, there may be lateral thermal effects between the exposed terrestrial setting and the inundated marine setting that are not well represented by our 1D models of coastline emergence.

5.2. Simulation of the Previous 3 Million Years

5.2.1. No Ice Insulation Case.

In the first simulations of the last 3 Myr for the QEIG two surface temperature scenarios are considered, only without considering the phase curve changes due to the ice sheet pressure. The more complicated models that consider ice sheet pressure effects are discussed below. First scenario is simply a surface model constrained

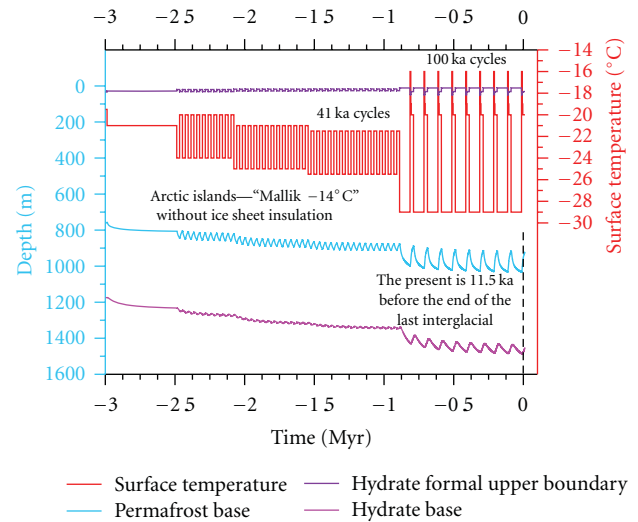


FIGURE 9: Permafrost and GH response to surface forcing considering simple surface temperature history model constrained by present -20°C terrestrial conditions in the QEIG (as in Figure 3). No ice sheet insulation effect is considered.

by the current -20°C in terrestrial conditions in the QEIG. Model 1 is shown in Figure 9.

It is apparent that assuming no ice sheet insulation, the typical heat flow results in a very thick GH stability zone base throughout the last 6 mln years and that the GH layer reaches 1.5 km in the most recent 100 ka year glacial maximum. While such base GH stability zone depths have been inferred for the Present [2, 40]; these depths are not typical and most GH in the QEIG occurs above depths of 1 km.

5.2.2. Ice Sheet Cover Case.

The second surface forcing model (2) assumes that during the last 0.9 Myr, at a time 20 ka after the beginning of each of the 100 ka glacial episodes, the area was covered by an ice sheet and that the temperature increased due to the insulation from -29°C to -15°C, which is a cold-based glacier scenario like the current Greenland ice sheet. In model 2 the interglacial temperatures are the same as those in model 1. The model 2 results for the IBP and GH layers are shown in Figure 10, where it is compared to model 1.

It is apparent that the introduction of ice sheet insulation effects, in model 2, reduces the thickness of both the IBP and Type I GH layers significantly. The IBP and the GH stability zone bases are 0.7 km and 1.1 km, respectively, which is closer to the currently observed values than the Model 1 result predicted. On the other hand, the introduction of ice sheet insulation increases the variability of permafrost and GH thickness between interglacial and glacial intervals.

5.2.3. Ice Buildup and Thaw Case.

The subsequent simulations consider the ice sheet basal temperature and thickness during the last 0.9 Myr, when the large 100 ka glacial cycles occurred. We are specifically interested to produce models that illustrate how the base of the GH stability zone responds to both ground temperature and pressure changes for

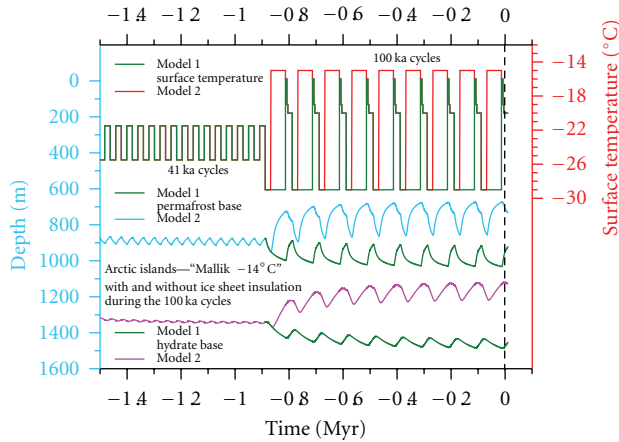
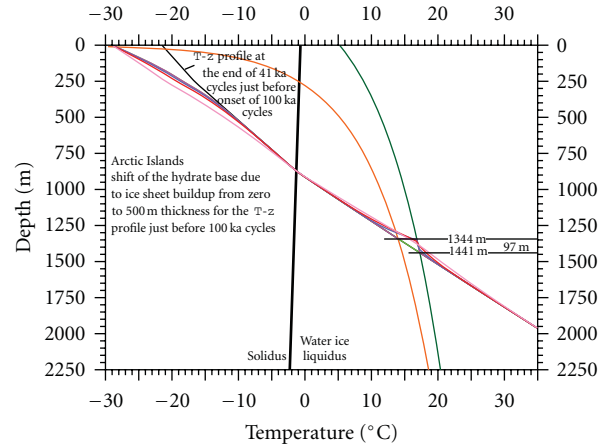


FIGURE 10: Permafrost and GH response to surface forcing considering two models (model 1 and model 2; with no ice insulation and with ice sheet insulation, resp.).



The T-z profile response to the ice sheet buildup
 Hydrate phase curve for ice sheet thickness
 — Just before
 — Just after
 — 100 years after
 — 300 years after
 — 1500 years after
 — 0 m
 — 500 m

FIGURE 12: The subsurface temperature response to the 0.5 km ice sheet buildup during the onset of the first 100 ka glacial cycle about 0.9 Myr ago.

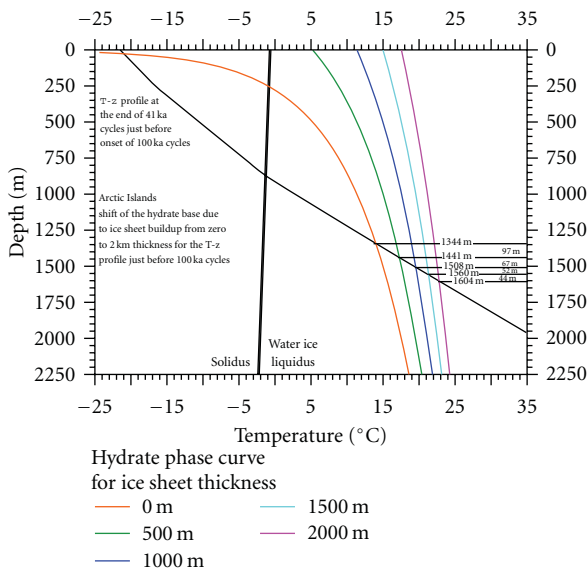


FIGURE 11: The depth migration of the base of the GH stability zone responding to ice sheet buildup (from 0 km to 2 km thickness) for the QEIG geothermal and climate model. It was assumed that the pressure increase is a hydrostatic one and that the effect of 1 km thick ice sheet corresponds to 1 km of a water column.

each of the nine 100 ka glacial-interglacial cycles assuming progressive ice sheet formation and melting. Below we show model results that illustrate ice sheet pressure effects on GH stability zone depth and history.

Figure 11 shows that the downward migration of the GH zone base decelerates with increasing ice thickness because of the steeper position of the phase curve at higher pressures. The ice sheet thickness increase from zero to 2 km by a step of 500 m means the base shifts downward from 1344 m to 1604 m by successive increases of 97 m, 67 m, 52 m, and 44 m. The maximum effect of the glaciation on GH thickness increase is therefore less than 250 m.

The modeling process that considers glaciation and ice sheet loading is illustrated in Figure 12. The sudden pressure increase due to the ice load causes the hydrate equilibrium temperature to increase at a given depth. The old and new positions of the base of the GH stability zone are given by intersections of the T-z profile with the old and new phase curves. In this case the base of the GH stability zone drops by 97 m and amounts to 1344 m and 1441 m, respectively (Figure 12).

If we assume that there is enough gas in the water-filled pores of this 97 m thick sedimentary rock layer, the process of hydrate formation within it starts immediately. Hydrate crystallization is an exothermic phase change. For the assumed porosity of 30% and the hydrate saturation of 60%, the amount of crystallization heat, that would be released by crystallization of all the possible hydrate, is by an order of magnitude larger than the heat necessary to warm the surrounding rock from the actual temperature to the equilibrium phase temperature. It means that the temperature of the rock, water, gas, and hydrate mixture in this zone reaches the equilibrium temperature long before all the possible hydrate can be formed. The fraction of the hydrate formed at a given depth by the time when the equilibrium temperature is reached is proportional to the difference between the equilibrium temperature and the original temperature. The software used for the simulations is based on the concept of apparent specific heat, where it is assumed that the crystallization heat is released or consumed during hydrate formation/decay in a temperature range constrained by the solidus (T_s) and liquidus (T_l) temperatures. In the new simulations for the ice thaw and

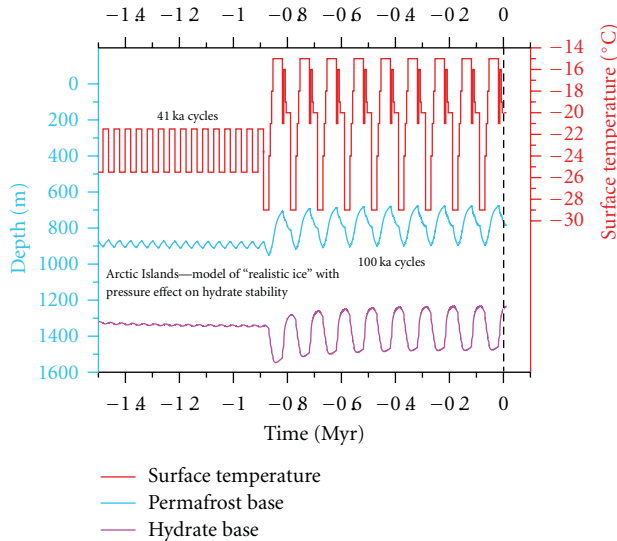


FIGURE 13: Variations of the ground surface temperature and bases of IBP and GH in a model considering ice pressure effect.

refreezing, the position of the hydrate phase curve is time dependent and it is prescribed in each time step. If the curve position changes between the two consecutive time steps, the actual temperature within the “disequilibrium” layer (in the Figure 11 between 1344 m and 1441 m) is increased to the (T_s, T_l) temperature range. The different fraction of the formed hydrate in the individual depths of the zone is taken into account by setting the temperature between (T_s, T_l) in such a distance below T_l , which is proportion to the hydrate fraction at the given depth. The (T_s, T_l) range used in the calculations was 0.2°C . An analogical process/treatment, but in a reverse direction, was considered and applied for the opposite case of ice sheet melting and dissipation.

5.2.4. “Realistic Ice” Model. Variations of ground surface temperature and the bases of IBP and GH is referred here as the “realistic ice” model including pressure effects. The model differs from the previous two surface temperature models, the “Mallik -14°C ” and the “simple ice” without pressure effect models (Figures 7 and 8) only in the last 0.9 Myr in the period of the large, 100 ka long, glacial cycles. The model is the same for each of the 9 glacial cycles, as is shown and explained in detail in Figure 13.

The Figure 13 model uses the repetition of the cycle shown in Figure 14 (last 0.9 Myr). The first 75 ka of the 100 ka cycle is the glacial part followed by 25 ka long interglacial. The upper time scale shown in that figure is the time of one 100 ka cycle and the lower time scale is that of our era. It assumes that at the present (time 0) we are 13.5 ka after the end of the last ice age and remaining 11.5 ka of the interglacial is still ahead. The model assumes the interglacial temperature course similar to the Mallik case, but shifted by -14 K . The glacial temperature at the ice sheet base depends on the thickness of the ice and was considered as:

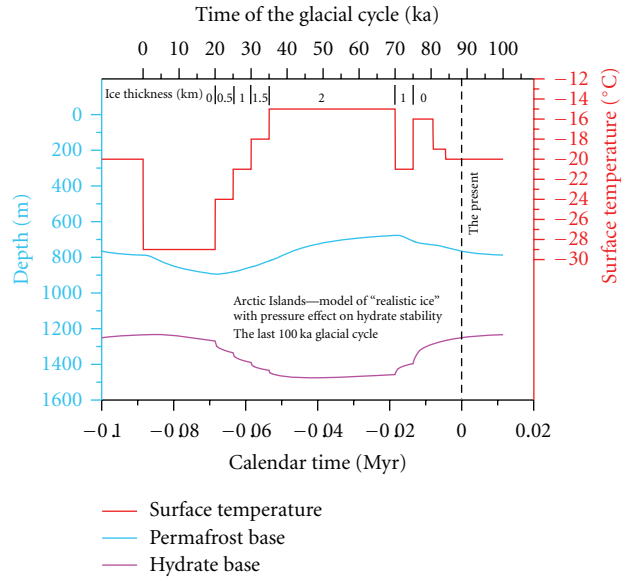


FIGURE 14: The “realistic ice” model taking into account ice thickness model, ground surface temperature model and the ice pressure effect on the hydrate stability for one 100 ka glacial cycle.

- (i) -29°C for the first 20 ka of the glacial, when no ice was assumed,
- (ii) -24°C between 20–25 ka and ice thickness 0.5 km,
- (iii) -21°C between 25–30 ka and ice 1 km,
- (iv) -18°C between 30–35 ka and ice 1.5 km, and
- (v) -15°C between 35–70 ka and ice 2 km.

At the end of the glacial, the ice thickness drops from 2 km to 1 km at the time of 70 ka and to zero at 75 ka. The pressure effect of the ice overburden on the hydrate equilibrium temperature was considered in the first approximation as a hydrostatic one, ignoring the density difference between water and ice. The depth (pressure) dependence of the equilibrium temperature $T(z)$ at depth z was given by (4):

$$T(z) = 8.9 * \ln(z + \text{ice thickness}) - 50.1. \quad (4)$$

Both, the depth and the ice thickness are given in meters. The pressure dependence of the water ice (permafrost) equilibrium temperature was not considered. Because of its very small (negative) vertical gradient, considering this dependence would influence results of the simulations negligibly.

In the model that considers ice pressure we assume that the pressure increase is hydrostatic and that the effect of a 1 km thick ice sheet corresponds to a 1 km thick water column. As can be seen, the base of the GH stability zone migration decelerates with the increasing ice thickness because of the steeper position of the phase curve at higher pressures. The ice sheet thickness increases from zero to 2 km by a step of 500 m meaning that the base moves downward from 1344 m to 1604 m by increases of 97 m, 67 m, 52 m, and 44 m. The maximum effect of the glaciation on hydrate thickness increase is therefore, less than 250 m, which is

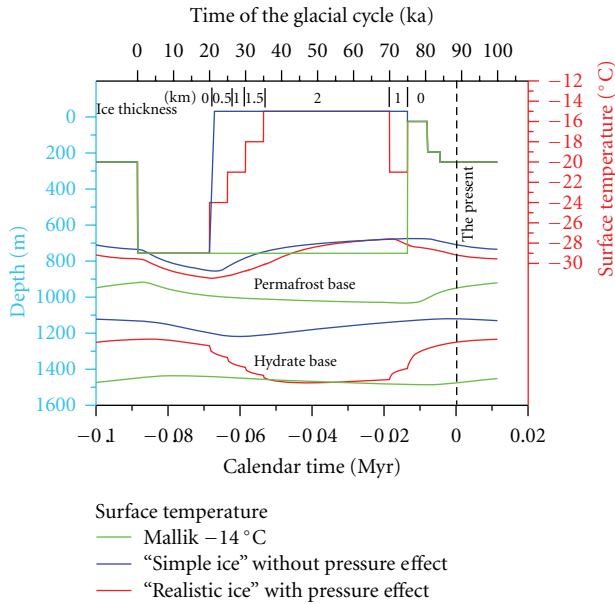


FIGURE 15: IBP and GH bases variations in the last 100 ka according to the three versions of the ground surface temperature history. For all three versions, the history of the last 6 Myr was considered and is the same for the first 5.1 Myr. It differs in the last 0.9 Myr during the 9 large 100 ka glacial cycles. The differences are shown in this figure, where each version has its own color, the same for temperature, IBP, and GH.

rather small. A variety of glacial ice models, including: no ice cover; “simple ice” cover without pressure effects and a “realistic ice” cover with pressure effects illustrated for comparison in Figure 15.

In order to bring the model GH base upward to more accurately predict the currently observed GH base of about 1 km, an alternative surface temperature history was considered. It assumed an 8°C higher temperatures during the ice free periods of the glacial cycle than those in the model “Mallik -14°C”, that is, in the periods 0–20 ka and 75–100 ka. Ground surface temperature below the ice sheet was considered -15°C, independently of the ice sheet thickness. Ground surface temperature used in the simulations and the calculated depth variations of the permafrost and GH bases during the last 100 ka are shown in Figure 16.

Currently the simulated depth of IBP and GHs occurs at 572 m and 1072 m, respectively. It is slightly more than the depths indicated by geophysical research. The ground surface temperatures can be hardly higher in the ice-free periods than those considered in the +8 K version. The simulated values could be brought closer to those observed on the seismic profile (0.9 km) by considering higher basal temperatures under the ice sheet, (-10°C). Another explanation might be that there is an overestimation of model rock thermal conductivity values, although these are only speculations.

6. Discussion and Conclusions

Historical surface temperature forcing as well as geological control have significant implications for both IBP and GHs

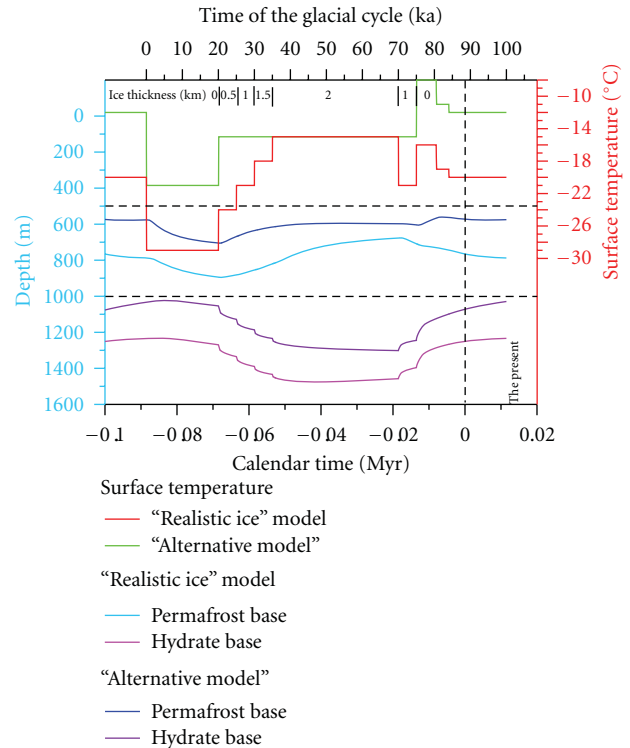


FIGURE 16: Simulation for the alternative model case where the ice-free periods are 8 K warmer than in the basic Mallik -14°C model and the periods with ice cover have a constant temperature of -15°C. The results of the “realistic ice” model (see Figure 14) are shown for comparison.

model results that consider latent heat effects of water/ice and GH formation and dissipation and the last 14 Myr of GST history. In the MD-BS (i.e., Mallik) case our model shows that the onset of GH formation always begins after the IBP layer is initiated. IBP provides a potentially impermeable seal that could entrap any upwardly migrating gas. The IBP seal is inferred to have come into existence prior to when P - T conditions permit the first GH to have formed. Therefore, if it were common for GH to form due to the IBP providing a vertical migration barrier it would be common for GH to be found intercalated with water ice within the IBP, since the IBP grows subsequently downward through the GHs. While intercalated GHs have been observed it is rare [25] and it appears more likely that most GH accumulations result from the *in situ* transformation of conventionally entrapped natural gas below a lithologic or stratigraphic seal.

The results of the Case 1 MD-BS/Mallik models permit the formation of GH from natural gas previously entrapped under a deep geological seal and the Case 2: models permit simultaneous GH and IBP formation due to a persistent gas flux into the free pore space result in two entirely different times when GHs first begin to form. For Case 1, GHs could have begun to be formed at 0.9 km only about 0.9 Myr ago. For Case 2, the first GHs formed earlier

Where the IBP layer is thick, it is likely that sub-IBP some GHs persisted through the previous interglacial intervals, nor are they expected to disappear prior to the “natural” end of

the current interglacial. In regions of thick terrestrial IBP like the Mackenzie Delta, GH layers can act as a persistent sink for methane from deep thermogenic sources and petroleum systems, and as a barrier to the migration of methane into the atmosphere. This is also likely scenario for the offshore MD-BS case where hydrates can and have probably existed under relic IBP despite marine transgression [13]. Likewise, the impact of future climate change attending a doubling of atmospheric CO₂ does not completely destabilize the GH layer. Majorowicz et al., [13] predicted that future GH layer thinning is very small, and within the range of previous natural cycle variations, in spite of the accelerated surface warming accompanying climate change. This model results appear consistent with the implications of recent observations of methane isotopic compositions from ice cores for the “clathrate gun” hypothesis of Sowers et al., [61]. However, the GHs can destabilize rapidly in response to environmental change in the marine non-IBP GHs [62, 63].

In the QEIG Sverdrup Basin case, our models show that thermal and pressure effects of the repeated formation and disappearance of the Innuitian Ice Sheet during glacial and interglacial periods is needed to successfully match the observed base of the GH stability zone at about 1020 m. Without the Innuitian Ice Sheet the exposed surface temperature would have been much lower resulting a hydrate stability zone thickness much thicker than the observed values of up 1.5 km. Detailed modeling of the recent history of coastal emergence due to isostatic uplift and the attending marine to terrestrial (−20°C) temperature changes results in a base of the GH stability zone depth that is less than 0.5 km. These are lower than the observed average depth of base of the GH stability zone of just over 1 km [42]. It is possible that marine conditions have lasted for only a very short time in the shallow interisland channels and the deep preinundation subsurface temperatures persisted, to some degree, while sea level rose by some 100–120 m some 10 ka ago, shortly after the end of the most recent glacial period. If the subsequently inundated area was above the glacial sea level during the last ice age, then those terrestrial conditions could have prevailed and controlled the permafrost and gas hydrate thickness for most of the glacial cycle. The Holocene coastal inundation lasted probably only several thousand years. Alternatively, there may be lateral thermal effects between the emergent islands and the inundated shore face that are not well represented in our 1D models.

One of the uncertainties of the model scenarios is the subice temperature. Temperatures below the ice are assumed based on the observation that current temperatures below the Greenland ice sheet may be as low as −15°C. The thickness of Greenland’s ice sheet is 2–3 km. We employed representatively lower temperatures assuming a thinner ice coverage over most of the QEIG.

Acknowledgments

This research was funded by the Geological Survey of Canada. The authors would like to make special thanks to Alan Taylor for his helpful suggestions and informed advice, which helped them to build the models and develop

their interpretation. Scott Dallimore is to be thanked for his in-depth review of the Mallik case scenario, which led to significant changes of our previous models as to surface forcing scenarios and saturation range. Other errors or omissions are the authors own.

References

- [1] J. A. Majorowicz and K. G. Osadetz, “Basic geological and geophysical controls bearing on gas hydrate distribution and volume in Canada,” *AAPG Bulletin*, vol. 85–87, pp. 1211–1230, 2001.
- [2] S. L. Smith and A. S. Judge, “Gas hydrate database for Canadian Arctic and selected east coast wells,” *Geol. Surv. Canada Open File Report 2746*, 120p., 1993.
- [3] S. R. Dallimore and T. S. Collett, Eds., “Scientific results from the Mallik 2002 gas hydrate production research well program, Mackenzie Delta, Northwest Territories, Canada,” *Geol. Surv. Canada Bull.*; 585, 140p. CD and Charts. 2005.
- [4] A. S. Dyke, “Last Glacial Maximum and deglaciation of Devon Island, Arctic Canada: support for an Innuitian ice sheet,” *Quaternary Science Reviews*, vol. 18, no. 3, pp. 393–420, 1999.
- [5] W. R. Peltier and J. T. Andrews, “Glacial-isostatic adjustment, 1. The forward problem,” *Geophysical Journal of the Royal Astronomical Society*, vol. 46, pp. 605–646, 1976.
- [6] D. C. Mosher, K. Loudon, J. Shimeld, and K. Osadetz, “Gas Hydrates Offshore Eastern Canada: Fuel for the Future?” in *Proceedings of the Offshore Technology Conference*, Houston, Tex, USA, May 2005.
- [7] J. A. Majorowicz and K. G. Osadetz, “Natural gas hydrate stability in the East Coast offshore-canada,” *Natural Resources Research*, vol. 12, no. 2, pp. 93–104, 2003.
- [8] M. Riedel, G. D. Spence, N. R. Chapman, and R. D. Hyndman, “Deep-sea gas hydrates on the northern Cascadia margin,” *Leading Edge*, vol. 20, no. 1, pp. 87–91, 2001.
- [9] K. G. Osadetz and Z. Chen, “A re-evaluation of Beaufort Sea-Mackenzie Delta basin gas hydrate resource potential: petroleum system approaches to non-conventional gas resource appraisal and geologically-sourced methane flux,” *Bulletin of Canadian Petroleum Geology*, vol. 58, no. 1, pp. 56–71, 2010.
- [10] Z. Chen and K. G. Osadetz, “Using discovery process models to improve petroleum resource assessments based on combinations of inferred accumulation reservoir parameters,” in *Arctic Petroleum Geology*, A. Spencer, A. Embry, D. Gautier, A. Stoupakova, and K. Sørensen, Eds., *Memoir of the geological Society of London No. 35*, 2011.
- [11] J. A. Majorowicz, P. K. Hannigan, and K. G. Osadetz, “Study of the natural gas hydrate “trap zone” and the methane hydrate potential in the Sverdrup Basin, Canada,” *Natural Resources Research*, vol. 11, no. 2, pp. 79–96, 2002.
- [12] K. G. Osadetz, G. R. Morrell, J. Dixon et al., “Beaufort Sea-Mackenzie Delta Basin: a review of conventional and non-conventional (gas hydrate) petroleum reserves and undiscovered resources,” in *Scientific Results from Mallik 2002 Gas Hydrate Production Research Well Program, Mackenzie Delta, Northwest Territories, Canada*, S. R. Dallimore and T. S. Collett, Eds., Geological Survey of Canada, Bulletin, 2005.
- [13] J. A. Majorowicz, K. G. Osadetz, and J. Safanda, “Modeling temperature profiles considering the latent heat of physical-chemical reactions in permafrost and gas hydrates: the Mackenzie Delta terrestrial case,” in *Proceedings of the 9th*

- International Conference on Permafrost*, D. L. Kane and K. M. Hinkel, Eds., pp. 1113–1118, 2008.
- [14] A. E. Taylor, “A constraint to the Wisconsinan glacial history, Canadian Arctic Archipelago,” *Journal of Quaternary Science*, vol. 3/1, pp. 15–18, 1988.
- [15] A. E. Taylor, S. R. Dallimore, R. Hyndman, and J. F. Wright, “Comparing the sensitivity of permafrost and marine gas hydrate to climate warming,” in *Scientific Results from the Mallik 2002 Gas Hydrate Production Research Well Program, Mackenzie Delta, Northwest Territories, Canada*, S. R. Dallimore and T. S. Collett, Eds., Geological Survey of Canada, Bulletin, 2005.
- [16] J. Šafanda, J. Szewczyk, and J. Majorowicz, “Geothermal evidence of very low glacial temperatures on a rim of the Fennoscandian ice sheet,” *Geophysical Research Letters*, vol. 31, no. 7, Article ID L07211, 4 pages, 2004.
- [17] Y. Galushkin, “Numerical simulation of permafrost evolution as a part of sedimentary basin modeling: permafrost in the Pliocene-Holocene climate history of the Urengoy field in the West Siberian basin,” *Canadian Journal of Earth Sciences*, vol. 34, no. 7, pp. 935–948, 1997.
- [18] D. W. Peaceman and H. H. Rachford, “The numerical solution of parabolic and elliptic differential equations,” *Journal of the Society for Industrial and Applied Mathematics*, vol. 3, no. 1, pp. 28–41, 1955.
- [19] H. S. Carslaw and J. C. Jaeger, *Conduction of Heat in Solids*, Oxford University Press, Oxford, UK, 2nd edition, 1959.
- [20] J. A. Majorowicz, F. W. Jones, and A. S. Judge, “Deep subpermafrost thermal regime in the Mackenzie Delta basin, northern Canada—analysis from petroleum bottom-hole temperature data,” *Geophysics*, vol. 55, no. 3, pp. 362–371, 1990.
- [21] A. E. Taylor, M. Burgess, Judge A. S., and V. S. Allen, *Canadian Geothermal Data Collection-Northern Wells 1981*, Geothermal Series Earth Physics Branch EMR, 13, 1982.
- [22] J. F. Wright, F. M. Nixon, S. R. Dallimore, J. Henniges, and M. M. Cote, “Thermal conductivity of sediments within the gas hydrate bearing interval at the Mallik 5L-38 gas hydrate production well,” in *Scientific Results from the Mallik 2002 Gas Hydrate Production Research Well Program, Mackenzie Delta, Northwest Territories, Canada*, S. R. Dallimore and T. S. Collett, Eds., vol. 585, pp. 129–130, Geological Survey of Canada, Bulletin, 2005.
- [23] J. Henniges, E. Huenges, and H. Burkhard, “In situ thermal conductivity of gas hydrate bearing sediments of the Mallik 5L-38 well,” *Journal of Geophysical Research*, vol. 110, p. B11206, 2005.
- [24] E. D. Sloan, *Clathrate Hydrates of Natural Gases*, Marcel Dekker, New York, NY, USA, 2nd edition, 1998.
- [25] T. S. Collett, “Permafrost-associated gas hydrate accumulations,” in *International Conference on Natural Gas Hydrates*, E. D. Sloan, J. Happel, and M. A. Hnatow, Eds., vol. 715, pp. 247–269, Annals of the New York Academy of Sciences, 1994.
- [26] S. R. Dallimore and T. S. Collett, “Intrapermafrost gas hydrates from a deep core hole in the Mackenzie Delta, Northwest Territories, Canada,” *Geology*, vol. 23, no. 6, pp. 527–530, 1995.
- [27] R. A. Muller and G. J. MacDonald, *Ice Ages and Astronomical Causes: Data, Spectral Analysis, and Mechanisms*, Springer, Berlin, Germany, 2000.
- [28] L. A. Frakes, J. E. Francis, and J. I. Syktus, *Climate Models of the Phanerozoic*, Cambridge Univ. Press, Cambridge, UK, 1992.
- [29] Intergovernmental Panel on Climate Change, “Fourth Assessment Report Climate Change: Synthesis Report 2007,” http://www.ipcc.ch/pdf/assessment-report/ar4/syr/ar4_syr_spm.pdf.
- [30] K. Polsson, “Climate Change - Carbon dioxide,” <http://www.islandnet.com/~kpolsson/climate/carbondioxide.htm>.
- [31] K. L. Bice and J. Marotzke, “Could changing ocean circulation have destabilized methane hydrate at the Paleocene/Eocene boundary?” *Paleoceanography*, vol. 17, no. 2, Article ID 1018, 12 pages, 2002.
- [32] M. E. Katz, B. S. Cramer, G. S. Mountain, S. Katz, and K. G. Miller, “Uncorking the bottle: What triggered the Paleocene/Eocene thermal maximum methane release?” *Paleoceanography*, vol. 16, no. 6, pp. 549–562, 2001.
- [33] J. A. Majorowicz and P. K. Hannigan, “Stability zone of natural gas hydrates in a permafrost-bearing region of the Beaufort-Mackenzie basin: study of a feasible energy source,” *Natural Resources Research*, vol. 9, no. 1, pp. 3–25, 2000.
- [34] A. S. Judge and J. A. Majorowicz, “Geothermal conditions for gas hydrate stability in the Beaufort-Mackenzie area—the global change aspect,” *Paleogeography Paleoclimatology and Paleocology, Global & Planetary Change Section*, vol. 98, pp. 251–263, 1992.
- [35] J. A. Majorowicz and S. L. Smith, “Review of ground temperatures in the Mallik field area: a constraint to the methane hydrate stability,” in *JAPEX/JNOC/GSC Mallik 2L-38 Gas Hydrate Research Well, Mackenzie Delta, Northwest Territories, Canada*, S. R. Dallimore, T. Uchida, and T. S. Collett, Eds., vol. 544, pp. 45–56, Geological Survey of Canada Bulletin, 1999.
- [36] A. E. Taylor and A. S. Judge, *Canadian geothermal data collection-Northern wells 1976-77*, Geothermal Series Earth Physics Branch, EMR, 1977.
- [37] A. E. Taylor and A. S. Judge, *Canadian geothermal data collection-Northern wells 1975*, Geothermal Series Earth Physics Branch, EMR, 1976.
- [38] A. E. Taylor and A. S. Judge, *Canadian geothermal data collection-Northern wells*, Geothermal Series Earth Physics Branch, EMR, 1974.
- [39] A. E. Taylor, A. S. Judge, and V. S. Allen, “The automatic well temperature measuring system installed at Cape Allison C-47, offshore well, Arctic Islands of Canada: 2. Data retrieval and analysis of the thermal regime,” *Journal of Canadian Petroleum Technology*, vol. 28, pp. 95–101, 1989.
- [40] A. S. Judge, A. E. Taylor, and M. Burgess, *Canadian geothermal data collection-Northern wells 1977-78*, Geothermal Series Earth Physics Branch, EMR, 1979.
- [41] A. S. Judge, A. E. Taylor, M. Burgess, and V. S. Allen, *Canadian geothermal data collection-Northern wells 1978-80*, Geothermal Series Earth Physics Branch, EMR, 1981.
- [42] A. S. Judge, S. L. Smith, and J. A. Majorowicz, “The Current Distribution and Thermal Stability of Natural Gas Hydrates in the Canadian Polar Regions,” in *Proceedings of the 4th, International Offshore and Polar Engineering Conference*, pp. 307–314, Osaka, Japan, April 1994.
- [43] L. E. Lisiecki and M. E. Raymo, “A Pliocene-Pleistocene stack of 57 globally distributed benthic $\delta^{18}\text{O}$ records,” *Paleoceanography*, vol. 20, no. 1, pp. 1–17, 2005.
- [44] T. Brent, CSPG Annual Meeting Poster, Canadian Soc. Petr. Geol. Annual Meeting, 2003.
- [45] J. A. Majorowicz and A. F. Embry, “Present heat flow and paleo-geothermal regime in the Canadian Arctic margin: analysis of industrial thermal data and coalification gradients,” *Tectonophysics*, vol. 291, no. 1–4, pp. 141–159, 1998.
- [46] D. Blackwell and M. Richards, Eds., *Heat Flow Map of North America*, SMU/AAPG, Tulsa, Okla, USA, 2004.

- [47] A. E. Taylor, A. Judge, and D. Desrochers, "Shoreline regression: its effect on permafrost and the geothermal regime, Canadian Arctic Archipelago," in *4th International Conference on Permafrost*, pp. 1239–1244, National Academy Press, 1983.
- [48] A. E. Taylor, "Modelling the thermal regime of permafrost and gas hydrate deposits to determine the impact of climate warming. Mallik field area," in *JAPEX/JNOC/GSC Mallik 2L-38 Gas Hydrate Research Well, Mackenzie Delta, Northwest Territories, Canada*, SR Dallimore, T Uchida, and T. S. Collett, Eds., vol. 544, pp. 391–401, Geological Survey of Canada Bulletin, 1999.
- [49] R. I. Walcott, "Late Quaternary vertical movements in eastern North America: Quantitative evidence of glacio-isostatic rebound," *Reviews of Geophysics*, vol. 10, pp. 849–884, 1972.
- [50] A. S. Dyke, "Holocene delevelling of Devon Island, Arctic Canada: implications for ice sheet geometry and crustal response," *Canadian Journal of Earth Sciences*, vol. 35, no. 8, pp. 885–904, 1998.
- [51] A. S. Dyke, J. Hooper, and J. M. Savelle, "A history of sea ice in the Canadian Arctic archipelago based on postglacial remains of the bowhead whale (*Balaena mysticetus*)," *Arctic*, vol. 49, no. 3, pp. 235–255, 1996.
- [52] J. England, "Postglacial isobases and uplift curves from the Canadian and Greenland high Arctic," *Arct. Alp. Res.*, vol. 8, pp. 61–78, 1976.
- [53] W. R. Peltier, "Global glacial isostasy and the surface of the ice-age earth: The ICE-5G (VM2) model and GRACE," *Annual Review of Earth and Planetary Sciences*, vol. 32, pp. 111–149, 2004.
- [54] W. R. Peltier, "Global glacial isostatic adjustment: Palaeogeodetic and space-geodetic tests of the ICE-4G (VM2) model," *Journal of Quaternary Science*, vol. 17, no. 5-6, pp. 491–510, 2002.
- [55] J. England, "Glaciation and the evolution of the Canadian high arctic landscape," *Geology*, vol. 15, no. 5, pp. 419–424, 1987.
- [56] J. England, N. Atkinson, J. Bednarski, A. S. Dyke, D. A. Hodgson, and C. Ó Cofaigh, "The Innuitian Ice Sheet: configuration, dynamics and chronology," *Quaternary Science Reviews*, vol. 25, no. 7-8, pp. 689–703, 2006.
- [57] S. J. Marshall and P. U. Clark, "Basal temperature evolution of North American ice sheets and implications for the 100-kyr cycle," *Geophysical Research Letters*, vol. 29, no. 24, Article ID 2214, 4 pages, 2002.
- [58] F. Rolandone, J. C. Mareschal, and C. Jaupart, "Temperatures at the base of the Laurentide Ice Sheet inferred from borehole temperature data," *Geophysical Research Letters*, vol. 30, no. 18, pp. 3–4, 2003.
- [59] A. J. Payne, "Limit cycles in the basal thermal regime of ice sheets," *Journal of Geophysical Research*, vol. 100, no. 3, pp. 4249–4263, 1995.
- [60] A. E. Taylor and K. Wang, "Geothermal inversion of Canadian Arctic ground temperatures and effect of permafrost aggradation at emergent shorelines," *Geochemistry, Geophysics, Geosystems*, vol. 9, no. 7, Article ID Q07019, 2008.
- [61] T. Sowers, "Late quaternary atmospheric CH₄ isotope record suggests marine clathrates are stable," *Science*, vol. 311, no. 5762, pp. 838–840, 2006.
- [62] E. G. Nisbet, "The end of the ice age," *Canadian Journal of Earth Sciences*, vol. 27, pp. 148–157, 1990.
- [63] E. G. Nisbet, "Have sudden large releases of methane from geological reservoirs occurred since the Last Glacial Maximum, and could such releases occur again?" *Philosophical Transactions of the Royal Society A: Mathematical, Physical and Engineering Sciences*, vol. 360, no. 1793, pp. 581–607, 2002.

Research Article

Thessaloniki Mud Volcano, the Shallowest Gas Hydrate-Bearing Mud Volcano in the Anaximander Mountains, Eastern Mediterranean

C. Perissoratis,¹ Chr. Ioakim,¹ S. Alexandri,² J. Woodside,³ P. Nomikou,² A. Dählmann,⁴ D. Casas,⁵ K. Heeschen,⁶ H. Amman,⁷ G. Rousakis,² and V. Lykousis²

¹Institute of Geology and Mineral Exploration, Entrance C, Spyrou Louis 1, Olympic Village, Acharne, 13677 Athens, Greece

²Hellenic Centre for Marine Research, 46th km Athens-Sounion BP712, 19013 Anavyssos, Greece

³Department of Sedimentary and Marine Geology, Vrije Universiteit Amsterdam, De Boelelaan 1085, 1081 HV Amsterdam, The Netherlands

⁴Department of Geochemistry, Faculty of Earth Sciences, Utrecht University, 80021 Budapestla-an 4, 3508 TA Utrecht, The Netherlands

⁵Institut de Sciences del Mar, Paseo Marítimo de la Barceloneta 37-49, 08003 Barcelona, Spain

⁶Bundesanstalt für Geowissenschaften und Rohstoffe Geozentrum Hannover, Stilleweg 2, D-30655 Hannover, Germany

⁷Technische Universität Berlin, Mullerv Bresslau Strasse, 10623 Berlin, Germany

Correspondence should be addressed to C. Perissoratis, perissoratis@yahoo.gr

Received 2 June 2011; Revised 16 August 2011; Accepted 12 September 2011

Academic Editor: Michela Giustiniani

Copyright © 2011 C. Perissoratis et al. This is an open access article distributed under the Creative Commons Attribution License, which permits unrestricted use, distribution, and reproduction in any medium, provided the original work is properly cited.

A detailed multibeam survey and the subsequent gravity coring carried out in the Anaximander Mountains, Eastern Mediterranean, detected a new active gas hydrate-bearing mud volcano (MV) that was named Thessaloniki. It is outlined by the 1315 m bathymetric contour, is 1.67 km² in area, and has a summit depth of 1260 m. The sea bottom water temperature is 13.7°C. The gas hydrate crystals generally have the form of flakes or rice, some larger aggregates of them are up to 2 cm across. A pressure core taken at the site contained 3.1 lt. of hydrocarbon gases composed of methane, nearly devoid of propane and butane. The sediment had a gas hydrate occupancy of 0.7% of the core volume. These characteristics place the gas hydrate field at Thessaloniki MV at the upper boundary of the gas hydrate stability zone, prone to dissociation with the slightest increase in sea water temperature, decrease in hydrostatic pressure, or change in the temperature of the advecting fluids.

1. Introduction: Purpose of This Study

The occurrence of mud volcanoes (MVs), mud diapirs, and fluid seeps has long been known in various different geological environments of the Eastern Mediterranean [1] and in the Aegean Sea [2]. They occur not only in regions of compressional stress present in subduction zones (e.g., Calabrian Arc [3], Mediterranean Ridge [4], and orogenic belts [1, 5–7]), but also on passive rifted margins such as the Egyptian offshore [8, 9] and areas of mixed tectonic signature like the ANAXIMANDER Mountains where mud volcanism is related to faults with normal and transcurrent faulting components [10–12]. Especially the accretionary prism of the Hellenic Arc (Mediterranean Ridge) is an area where a large number of mud volcanoes have been studied following

their discovery in the late 1970s [13]. Mud volcanoes are also known for their high methane fluxes, advecting methane-rich fluids at seafloor seeps, gas hydrates, and favorable environments for chemosynthetic symbiotic fauna [5, 10, 12].

The Anaximander Mountains are situated between the Hellenic and Cyprus Arcs at the junction of the African Plate with the Anatolian and the Aegean microplates, an area accommodating the relative motion between the African and Eurasian plates [6, 10, 14]. The mountains have thus undergone a complex deformation including southward directed thrusting, northeast-southwest shearing in the west (Strabo Trough trend) and northwest-southeast shearing in the east (Florence Rise trend), and cross-cutting normal faulting, all defining the current structure of the mountains [10, 12, 15, 16]. They are comprised of three

main seamounts: Anaximander, Anaximenes, and Anaxagoras (Figure 1(a)).

The setting of the Anaximander Mountains is clearly favorable for the occurrence of mud volcanoes (Figure 1) thanks to the presence of overpressured fluids and faults that act as conduits for the fluids to escape [12, 17, 18]. Discovered during the Dutch ANAXIPROBE project by multibeam surveying in 1995, seven large mud volcanoes were sampled in 1996 [6, 7, 11] when the first gas hydrates samples in the Mediterranean Sea were collected from Kula MV. By 2002 the Amsterdam and Kazan MVs were also discovered to have hydrates. Between 2003 and 2005 the EC-funded project ANAXIMANDER targeted these mud volcanoes in a study of the gas hydrates and associated deep biosphere in the area, and this was followed by the HERMES project (2005–2009). During these projects gas hydrates from Amsterdam and Kazan MVs were collected and studied, and two new mud volcanoes named Athina and Thessaloniki were also discovered, sampled, and studied (Figure 1(b) [17, 19–21]).

Since Thessaloniki MV is the shallowest known GH bearing MV in the Eastern Mediterranean, very briefly described earlier [17, 21], the purpose of this study is to carry out detailed analyses and examination of all data collected in this area and discuss the conditions and characteristics of the GH present.

2. Materials and Methods

The data examined in this study were acquired mainly during two cruises of the R/V *Aegaeo* in May 2003 and October–November 2004. During the first cruise detailed swath bathymetry and backscatter imagery of the study area was obtained using a hull-mounted SEABEAM 2120 swath system operating at 20 KHz. It has an angular sector of 150°, with 159 beams and a swath width from 7.5- to 11.5- times the water depth, for depths from 1 to 5 km respectively. Navigation was carried out with a Trimble 4000 GPS providing the ships position to within ± 10 m. The bathymetric map of Thessaloniki MV (Figure 2) was produced using a 20 m grid interval and plotted with a Mercator projection at a scale of 1 : 20,000 with 5 m contours. Sediment was sampled with a 3 m long 73 cm i.d. Benthos Instruments Gravity Corer with presplit sleeves to reduce the time needed to open and sample the cores. The time between coring the seafloor and on board sampling of cores from a depth of 2000 m was thus reduced to between 20 and 25 minutes to ensure the least possible gas hydrate dissociation and sediment distortion. As soon as the cores were opened, the temperature of the sediments was measured, and any gas hydrates were collected and placed in a freezer at -70°C . Detailed sampling of the sediment followed.

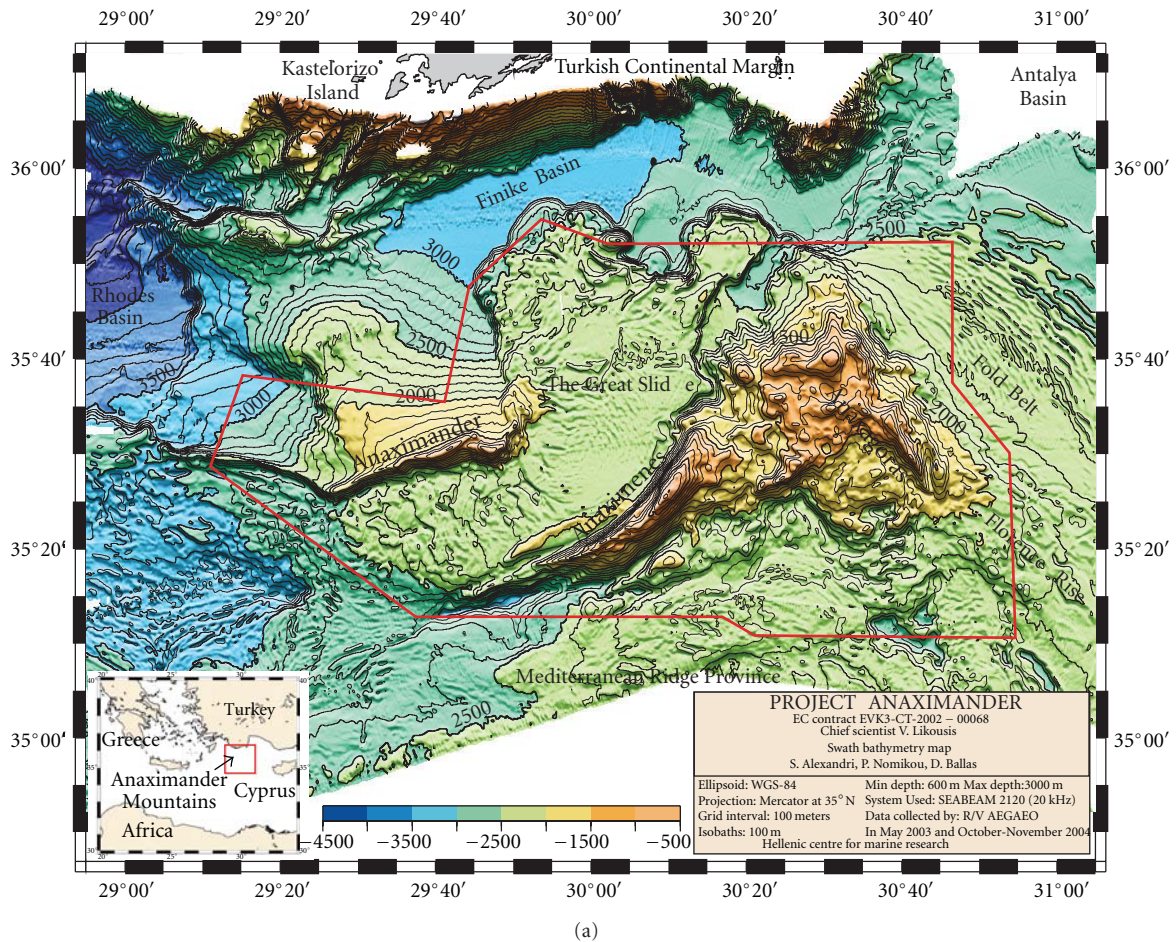
The pressure coring was carried out using the APCA (Autoclave Piston Corer Anaximander) [22] designed and fabricated by Technical University of Berlin as part of the ANAXIMANDER project. The APCA retrieves cores of 10 cm diameter and up to a length of 250 cm in water depths of up to 2500 m. It preserves the sediment cores under *in situ* pressure conditions [22]. Upon retrieval on

deck the autoclave corer was placed upright for controlled degassing and kept in an ice bath to prevent warming to deck temperatures. The degassing, gas collection, and gas-subsampling were carried out using a valve system as described by Heeschen et al. [19], a method used and described also by others [18]. The pressure was constantly monitored and the increasing volume of released gas was read off from a converted graduated cylinder. Gas subsamples were taken via a three-port valve and were stored for analysis in the laboratory [22]. A total of four gravity cores and one autoclave core were collected at Thessaloniki MV (Figure 2, Table 1). The trace and main elements were analyzed by the X-ray diffraction method using a SIEMENS D-500 instrument. The crystalline phases were determined using the Joint Committee Power Diffraction Standards and their final semiquantitative analyses by using the EVA program from Siemens/Bruker/Socabimo.

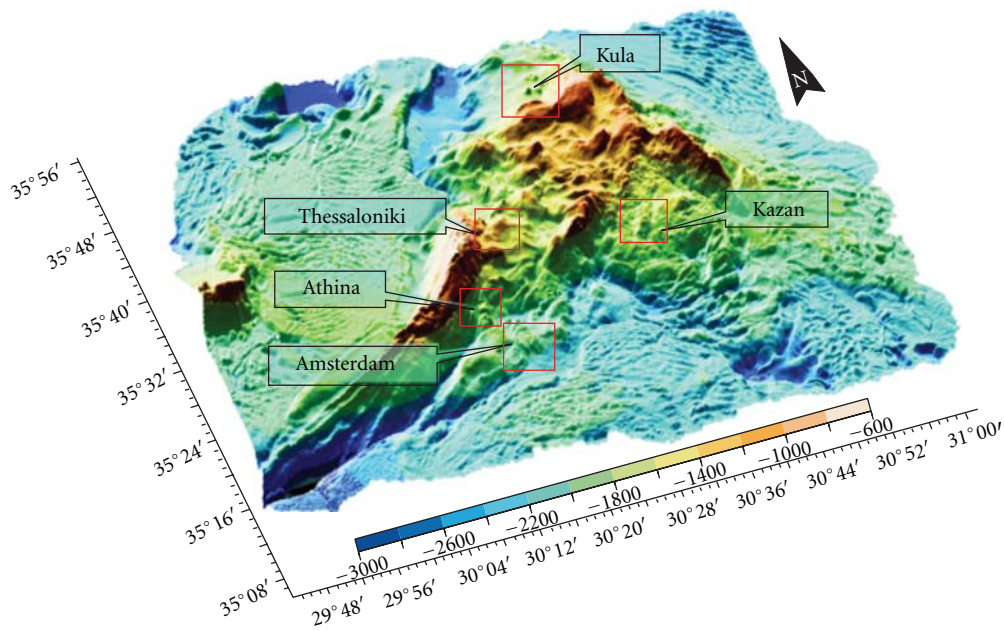
3. Results and Discussion

3.1. Bathymetry and Backscattering Imaging. Anaximenes Mountain (Figure 1) is a slightly northwestward concave feature occupying the shallowest (680 m) and smallest area in the Anaximander Complex, and therefore is characterized by steep slopes and rugged relief. To the south the Mediterranean Ridge is terminated in the form of a flat slightly wavy or folded area lying at a water depth of about 2800 m. It is separated from Anaximenes Mountain by a deep valley (>3000 m). The study of the combined 3D seabed morphology and backscatter intensity revealed in the southeastern slope of Anaximenes Mountain numerous dome-like morphological features with strong backscatter that constitute potential mud volcano sites. Following image processing of the backscatter data, a number of high backscatter areas implying potential active mud volcanism were identified. One of these sites at a depth of 1798 m was subsequently surveyed in 2003 and discovered to be a mud volcano which was named Athina MV (Figure 1, [17, 20]). In the same area, about 9 km northeast of Athina MV (at $35^{\circ} 28.60\text{ N} - 30^{\circ} 15.06\text{ E}$), and at water depths between 1320 and 1260 m the Thessaloniki MV was discovered after surveying and sampling in November 2004 (Figures 1 and 2 [17, 21]). This mud volcano had not been fully examined in previous cruises because of its small size and location at the base of a very steep sloping cliff (Figure 2), although its eastern side was crossed during the ANAXIPROBE ORETech side scan survey [7] (Figure 2). It is an oval submarine hill with its long axis about 1750 m as defined by the 1315 m isobath, with steep northern and eastern slopes and an area of about 1.67 km^2 . In the inner part, near the summit, it becomes more circular where three peaks are distinguished, two in the west outlined by the 1260 m contour and one in the east at 1265 m. Its small size and location on a steep slope made it a lower priority for investigation during earlier research projects.

3.2. Sedimentology. Five cores were collected from Thessaloniki MV: four gravity cores (AX46-GC1, AX47-GC1,



(a)



(b)

FIGURE 1: Bathymetry-physiography of the Anaximander complex (a), and swath bathymetry with locations of the five surveyed mud volcanoes ((b) from [17] supplemented with ANAXIPROBE data to outline each MV area [11]).

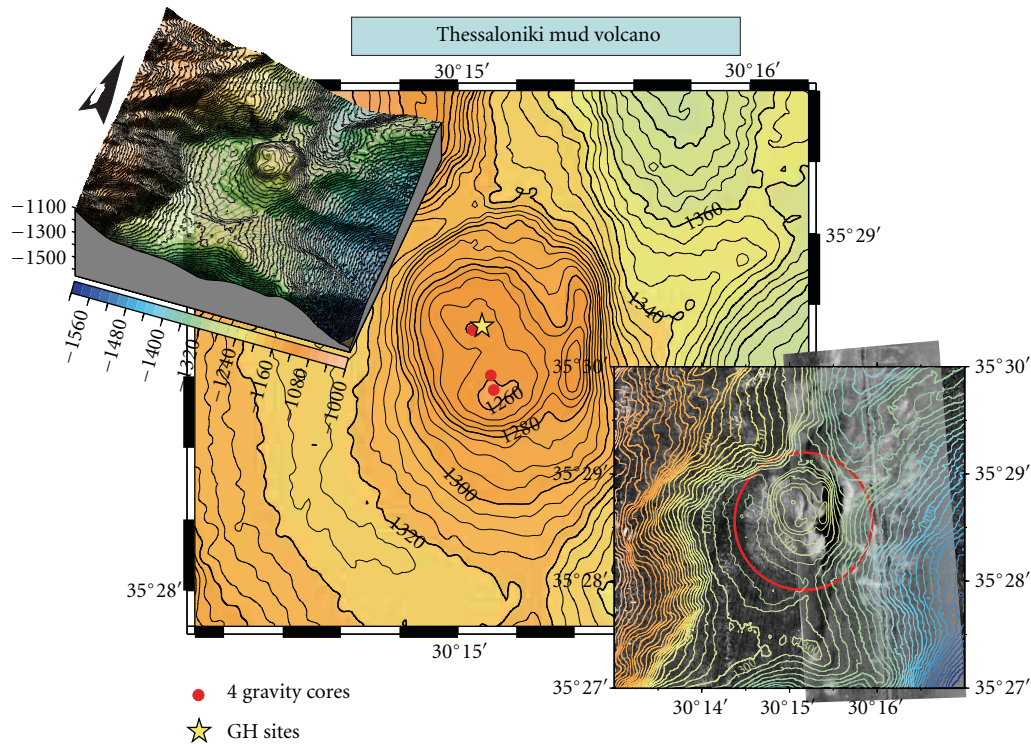


FIGURE 2: Swath bathymetry map of Thessaloniki MV and location of the collected cores (black dots). Upper left, greater swath map with the volcano at the center, lower right, ORETech side scan image from ANAXIPROBE cruise on top of SEABEAM backscatter intensity map. Gravity cores AX46-GC1, AX47-GC1, and autoclave core AX49-AP1 were retrieved from the northern peak, nearly at the same location. Gravity cores AX-48 and AX-49 were retrieved from the southern peak (from [17] supplemented with back scatter data and location of APCA core).

TABLE 1: (a) Gravity cores. (b) Autoclave core.

(a)							
Core no.	Latitude	Longitude	Water depth (m)	Sediment temperature	Length (cm)	G.H. presence (visual identification)	Smell of H ₂ S gas
AX46-GC1	35°28.603'	30°15.113'	1263	14,4° C	110	No	Yes
AX47-GC1	35°28.562'	30°15.123'	1265	12,3° C	167	No	Yes
AX48-GG1	35°28.729'	30°15.052'	1264	8.4–10.7° C	130	Yes	Yes
AX49-GC1	35°28.728'	30°15.060'	1264	No data	228	Yes	Yes

(b)							
Core no.	Latitude	Longitude	Water depth (m)	Length (cm)	Pressure (bars)	GH presence	Gas vol. (litres)
AX49-AP1	35°28.728'	30°15.060'	1.264	0.70	105	Yes	3.1

AX48-GC1, and AX49-GC1) and one autoclave core (AX49-AP1). They are located in similar sedimentary environments on the two western highs on the summit of Thessaloniki MV (Figure 2), in water depths from 1263 to 1265 m. Table 1 presents the details of the core locations and characteristics, with the initial deck observations made to determine whether there were gas hydrates (even if not actually observed; for example, with sediment temperatures below the seafloor temperature, ~13.7°C, there is likely to have

been dissociating gas hydrates present). These observations confirmed that this MV is an active gas hydrate bearing mud volcano, the fourth discovered in the Mediterranean.

The general appearance of typical mud breccia cores (Figure 3) is of a very poorly sorted sediment with muddy matrix-supported angular to subangular clasts (xenoliths) of different compositions and grain sizes (0.5 to 2.5 cm). The clasts reflect the geological units through which the overpressured sediment passed before erupting on the

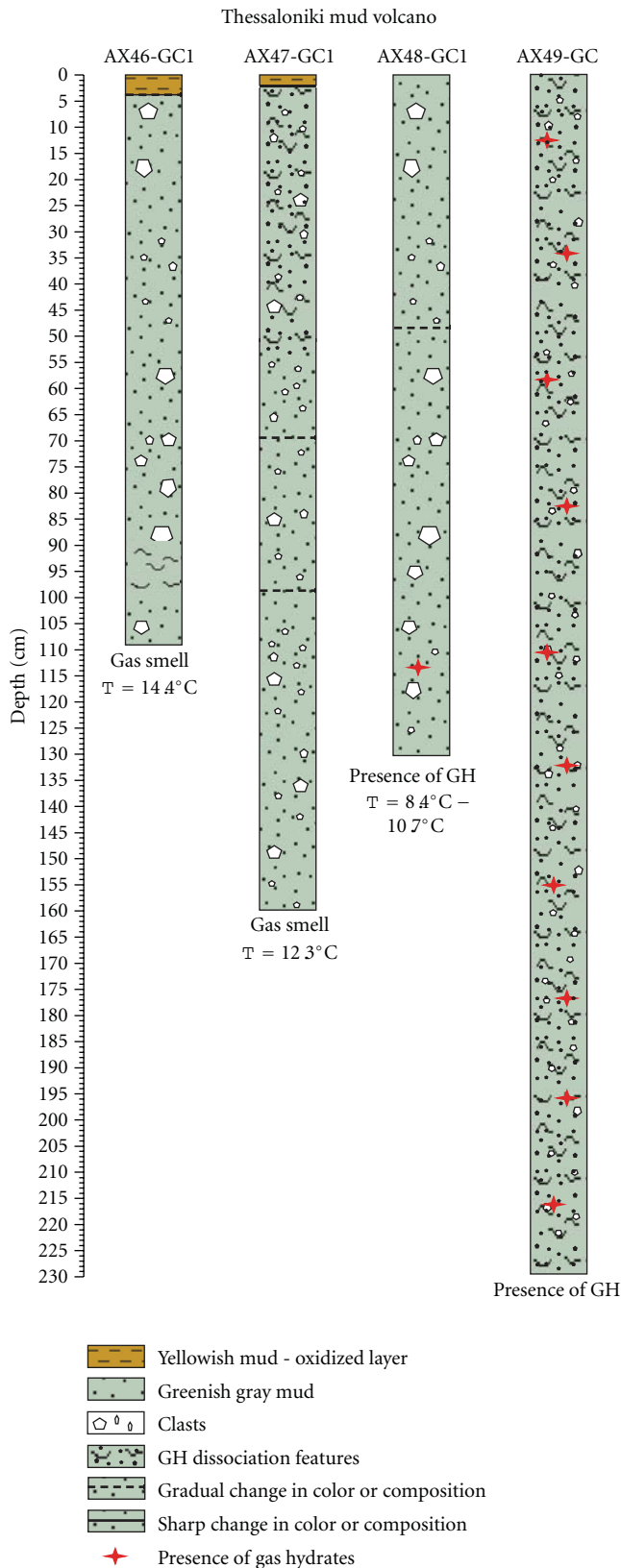


FIGURE 3: Description of the gravity cores.

seafloor as mud breccia. In this case they represent basement units associated with the Lycian Nappes and Bey Dağları to the north in Turkey [6, 7, 23–25]. Porous gas-release structures are common in the sediment we observed because much of the disseminated gas hydrates, associated with this type of sediment, dissociated during the sampling operation or minutes later onboard, where the ambient P-T conditions indicate that gas hydrates are unstable [26, 27]. Similar sediment has been described in other mud volcanoes (Amsterdam, Kula, and Kazan) in the area [17, 24, 28].

Core AX46-GC1 (Figure 3) was retrieved from the southern peak (1263 m water depth; core length of 119 cm). The top 5 cm is composed of a yellowish gray oxidized mud layer with faint laminae supporting dispersed small clasts <1.5 cm in diameter. There is a gradual change in color downwards toward the next 5 to 19 cm section which is a greenish-gray reduced mud containing a few clasts up to 3 cm in diameter. The following 19–119 section is similar in color with the overlying section but with larger clasts, up to 5 cm in diameter and increasing in the lower 10 cm. Evidence of dewatering features associated with a strong gas smell were also noted. The sediment temperature upon opening of the core was 14.4°C, roughly (actually, just above) seafloor temperature. No gas hydrates were detected.

On the same southern peak at a distance of about 80 m to the north and at a depth of 1265 m core AX47-GC1 was collected with a length of 167 cm (Figure 3). The sediment temperature upon opening was 12.3°C. At the top of the core there was a 3 cm thick yellowish gray oxidized layer followed by a 3–78 cm section of dark reduced greenish-gray mud with occasional clasts. The sediment is more soupy in the top 41 cm of the section becoming stiffer below, with faint laminae at 64 to 65 cm. The next 78 to 167 cm section contains larger rock clasts, up to 2.5 cm across, and two dark gray-colored laminated layers at 79–85 cm and at 96–99 cm. The sediment becomes stiff at the bottom of the layer. No GH were found.

On the northern peak a 130 cm long core (AX48-GC1, Figure 3) was retrieved from a water depth of 1264 m. The sediment temperature when measured on deck varied between 8.4 and 10.7°C. No oxidized layer was observed at the top of the core, indicating relatively recent mud volcanic activity in this area (because the upper part of the mud breccias had not had time to oxidize nor to be overlain by semipelagic sediment typical of the local seafloor). The sediment consists of greenish-gray mud with large rock clasts dispersed throughout the whole length of the core. The GH were observed mainly between 110 and 120 cm where their dissociation produced many degassing features resulting in the soft and sometimes soupy texture of the sediment (Figure 4). Most of the large rock clasts occur in the lower section of the core, where the sediment becomes stiffer below a core depth of 55 cm.

Core AX49-GC1 (Figure 3) was the longest core taken (228 cm) and also comes from the northern peak at the same location and water depth as core AX48-GC1. It consists of gray mud with foamy mousse-like texture and consistency,



FIGURE 4: Section 99–124 cm of core AX48-GC1. Note the soft character of section 110–120 cm which contained gas hydrates.

with many degassing features produced from the dissociation of GH dispersed throughout the whole length of the core.

3.3. Geochemical Results. A geochemical analysis was made of both the mud flow (trace element) and the rock clasts (main element) of the gravity cores.

The results of the trace element analysis in the mud flow of two gravity cores (Table 2(a)) indicate that organic carbon (C_{org}), Na_2O , Mg, Rd, Sr, and Cu do not vary down core. The total carbon (C_{tot}) is higher at the top of the cores than in the lower sections whereas the values of S and Zn are usually lower at the top of the cores than below.

Calcite is the dominant mineral in the rock clasts from gravity core AX 48-GC1 (Table 2(b)). This combined with the presence of the other main elements shown in Table 2(b), and the low dolomite content, support earlier interpretations that bedrock here is related to the Miocene flysch deposits present on land to the north ([6] see Section 3.4).

These results also indicate that the composition of the Thessaloniki MV sediments are comparable to those reported in other Mediterranean mud volcanoes like Athina [20] and even those from the Gulf of Cadiz [29].

The methane concentration was measured in both gravity cores. No gas hydrates were observed in core AX47-GC1 but the sediment was wet and in some places “soupy.” On the other hand, gas hydrates were observed throughout core AX49-GC1 when it was opened on deck (Figures 3 and 4). Methane concentrations in core AX47-GC1 were about $2800 \mu\text{mol/kg}$ wet sediment, with a maximum of $4000 \mu\text{mol/kg}$ wet sediment at a core depth below sea floor of 100 cm. In core AX49-GC1, the methane concentration was $3000 \mu\text{mol/kg}$ wet sediment, decreasing to $2000 \mu\text{mol/kg}$ wet sediment below this maximum at 100 cm down core (Figure 5). Thus the methane concentrations at both western highs on the summit of the mud volcano were high despite the apparent differences in gas hydrate content seen in the sediment. However, due to the degassing of these conventional cores during recovery, and the consequent loss of up to 90% of the methane [19], we could not determine significant differences in methane concentrations because the concentrations are far below methane saturation in the presence of gas hydrates ($\sim 100 \text{ mmol/kg}$ pore water [19]).

It is possible that observations of gas hydrates in one core, but not in another with similar concentrations of methane, can be explained by differences in the size of the gas hydrate deposits between the two cores, with the smaller GH crystals disappearing more quickly.

The *in situ* methane concentration in the autoclave core at northern site AX49 (core AX49-AP1) was calculated to be about 180 mmol/kg pore water at depths where there is no sulfate present. To calculate gas hydrate volumes from methane concentrations in relation to the core volume, the amount of collected gas ($\sum \text{CH}_4 = 3.1 \text{ L}$) is related to the core volume between the bottom of the core and the sulfate depletion depth, assuming an even distribution throughout this depth range with dissolved and hydrate-bound CH_4 to be present. The saturation concentration (c_{eq}) of CH_4 is subtracted before calculating gas hydrate volumes. For details see [30]. In core AX49-AP1 gas hydrates occupy about 0.7% of the core volume. The gas collected from the pressure core is nearly devoid of propane and butane thus allowing structure I gas hydrates to be formed [19]. No pressure corer was taken on the southern peak of this western high.

3.4. Study of the Mud Breccia Rock Clasts. The presence of a yellowish-brown oxidized layer in the upper few centimetres of the two gravity cores, where there were no gas hydrates observed, probably indicates that at these two sites mud volcano activity was low to absent during the last few hundred years. Freshly erupted mud breccia is characterised by grey reduced sediment and the lack of an oxidised hemipelagic sediment cover. An estimate of the age of eruptions can sometimes be made using the thickness of the overlying sediment and a good estimate of the rate of sedimentation, in this area about $2\text{--}5 \text{ cm/ka}$ [24]. The composition of the mud in all cores was mainly silty clays with a sand fraction between 5 to 7% and a mean grain size between 6.2 and 7.8 phi; it is consisted of terrigenous material with minor amounts of biogenic components, mainly planktonic foraminifera.

As noted previously, rock clasts that erupted through a mud volcano are comprised of a chaotic mixture of material from the overpressurized source formation and the rock units through which the eruption occurred. This material can provide significant geological information about the deeper geological units underlying the mud volcano, as well as the stratigraphy. A litho-micropalaeontological study of 39 samples of mud breccia clasts from Thessaloniki MV was undertaken.

These rock clasts of various size (2–5 cm in length) and supported in a homogeneous mud breccia matrix were sampled from the gravity cores collected during the second cruise of the ANAXIMANDER project. They were subsequently washed and classified by their general characteristics (composition, color, grain size, reaction with HCl, and roundness). Several clasts were selected then for further thin section analysis using a NIKON polarizing petrographic microscope. The most informative samples were also washed and sieved through a $150 \mu\text{m}$ sieve. This fraction is also used for analyzing the planktonic foraminifera assemblages. Typical examples of thin sections are shown in Figure 6.

TABLE 2: (a) Trace element analysis of the mud flow in cores AX48GC1 and AX49GC1. (b) Main element analysis (%) of the rock clasts from core AX48-GC1.

(a)										
Core	Sample depth (cm)	C _{tot} * %	C _{org} * %	S %	Na ₂ O %	Mg %	Sr %	Rb %	Zn ppm	Cu ppm
AX48GC1	9 cm	2,57	0,37	0,27	1,48	0,142	0,022	0,08	87	56
"	30 cm	2,05	0,35	0,44	1,75	0,146	0,019	0,10	94	78
"	65 cm	2,20	0,32	0,48	1,62	0,134	0,027	0,08	100	74
"	110 cm	1,70	0,32	0,40	1,75	0,137	0,023	0,08	104	78
AX49GC1	12 cm	2,85	0,44	0,58	1,75	0,151	0,024	0,09	89	73
"	50 cm	2,25	0,48	0,62	1,75	0,150	0,023	0,09	102	72
"	70 cm	1,45	0,39	0,48	1,75	0,158	0,016	0,08	86	69
"	105 cm	1,75	0,43	0,58	1,62	0,146	0,023	0,08	94	76

(b)	
Mineral	%
Calcite	57
Quartz	12
Montmorillonite	5
Kaolinite	8
Glaucophane	4
Albite	6
SiO ₂	5
Dolomite	3

* C_{tot} is total carbon, C_{org} is organic carbon.

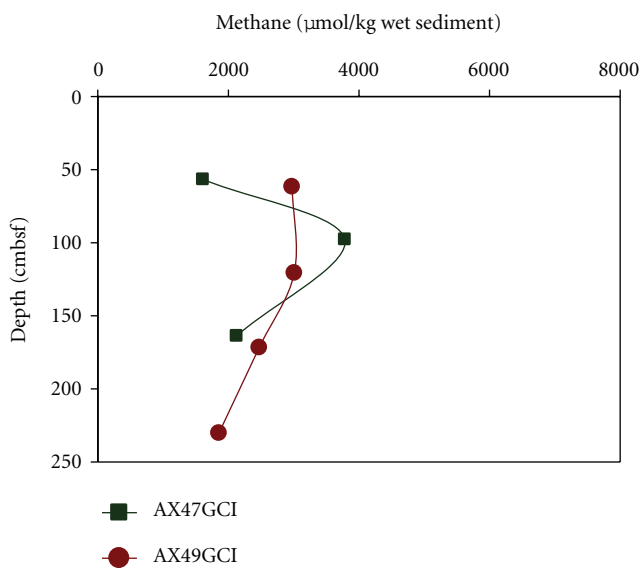


FIGURE 5: Methane concentrations of one of the southern (AX47-GG1) and northern (AX49-GG1) gravity core stations at Thessaloniki MV.

Rock clasts from the Thessaloniki MV cores (AX46GC1, AX47GC1, AX48GC1, AX49GC1, and AX49AP1) belong to two rock groups: fossiliferous micrites and detrital biomicrites. Both these two groups were recognized also in the other ANAXIMANDER mud volcanoes during this project [24, 25]. The fossiliferous micrites exhibit mainly

an angular-subangular form, are small in size, have light-gray colour, are consolidated, and contain (10–60%) well-preserved pelagic foraminifera in a micritic calcite matrix. The foram chambers are usually filled by sparitic calcite or pyrite. The planktonic species present are *Orbulina suturalis*, *Globigerinoides trilobus*, *Globigerinoides sp.*, and *Globoquadrina dehiscens*, which indicate a Lower to Middle Miocene age and an open marine environment [17, 24, 31]. The detrital biomicrites are angular-subangular in form, gray-brown in colour, contain tests and fragments of planktonic foraminifera, with fine grained aggregates of calcite and silty sized angular quartz grains in a micritic arenite matrix. Among the main fossils recognized are the species *Orbulina universa*, *Orbulina suturalis*, *Globigerinoides trilobus*, *Globoquadrina nepethens*, and *Globigerinoides obliquus*. which indicate an Upper Miocene age [31], and an open marine depositional environment.

Comparable microfaunal associations of Miocene deposits were also identified in the clasts sampled by gravity coring in the upper parts of mud flows in Amsterdam, Athina, Kazan, and Kula MVs. These data support the conclusion that part of the basement of the Anaximander Mountains in this area contains Miocene deposits that are comparable in age and facies with the geological units of the neighbouring land area of SW Turkey. Considering that these units are probably *in situ*, it can be concluded that the onshore Miocene flysch deposits of the Antalya Complex [24, 31] extend southward into the Anaximenes and Anaximander Mountains, thus supporting similar conclusions by Woodside et al. and other authors [6, 7, 12, 32, 33].

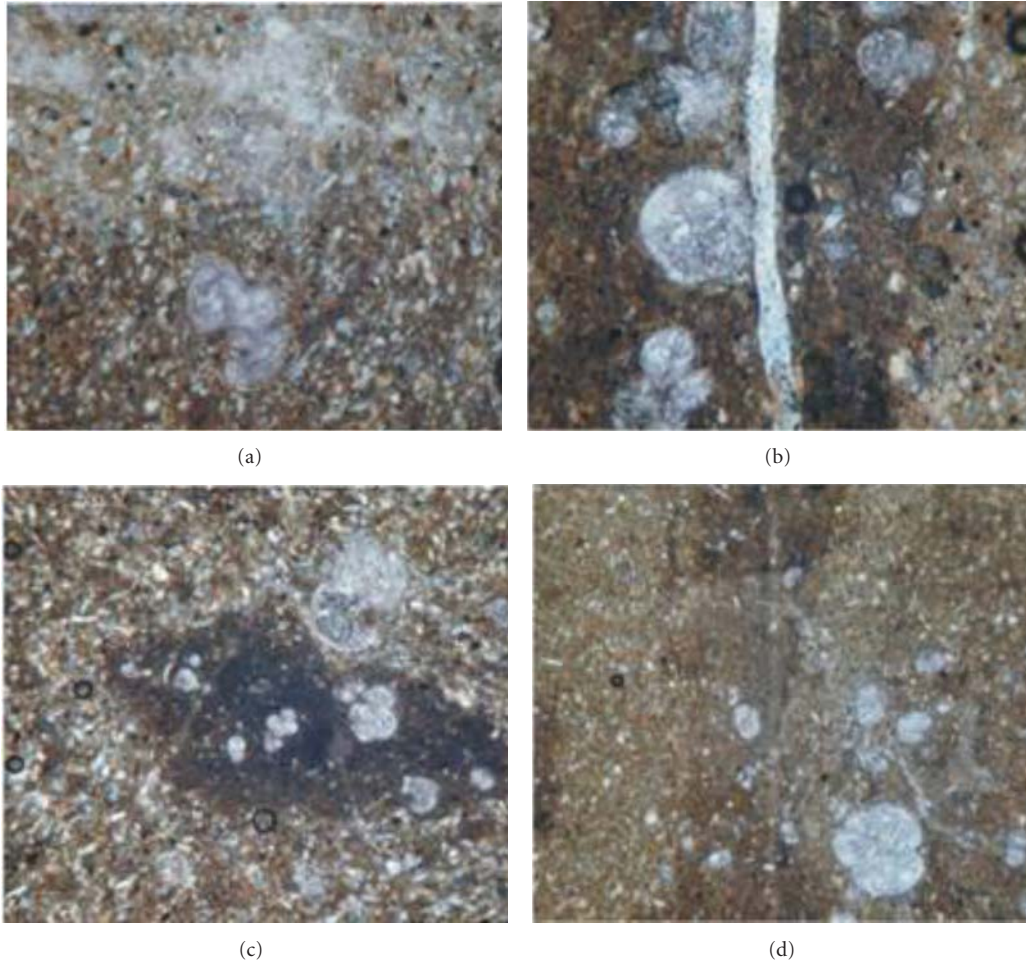


FIGURE 6: (a–d) Polarized microscope pictures of thin sections of mud breccia rock clasts; bioclastic carbonate pack/wackestones (grading into mudstones/claystones) with Globigerinidae planktonic foraminifera.

4. Gas Hydrate Stability Field

As noted above, the sediment cores with gas hydrates were all from relatively recently erupted mud breccia, as indicated by the lack of hemipelagic cover or surface oxidation of the mud flow. Thessaloniki MV is the shallowest mud volcano bearing gas hydrates in the Mediterranean (1265 m). At this depth the gas hydrates are just within, and near the edge of the gas hydrate stability zone (Figures 7(a) and 7(b)) as determined by the pressure (12.9 Mpa at 1265 m depth) and seafloor temperature ($\sim 14^{\circ}\text{C}$). The field data collected at Thessaloniki MV indicated that the GH occur at 1265 m sea floor depth and in subbottom sedimentary layers at least to 220 cm below seafloor. The sea bottom water temperature is 13.75°C and the geothermal gradient is expected to be $30\text{--}35^{\circ}\text{C}/\text{Km}$ or more, based on heat flow measurements made in the Olimpi mud diapir field [34]. During the MIMES cruise in 2004, one heat flow measurement made by Feseker and Foucher on Amsterdam Mud Volcano showed a significant warming of the sediments by over 3°C in the upper 10 m of mud [35, 36]. In other mud volcano areas the heat flow implies much higher geothermal gradients which,

for example, were as high as $2.78^{\circ}\text{C}/\text{m}$ in the active centre of Isis mud volcano [35].

A gas hydrate stability diagram, based on the parameters just described, indicates (Figures 7(a) and 7(b), [27, 36]) that the gas hydrates at Thessaloniki MV are just at the limit for the occurrence of stable methane hydrate, and do not extend more than a few meters above the known Thessaloniki MV depth. This means that with only small changes in the environmental parameters the gas hydrates could disassociate releasing water and methane. Such changes could result from a decrease in seafloor pressure (e.g., by tectonic uplift or sea level decrease) or by slight increase in the bottom water temperature (e.g., from an event like the recent increase in bottom water temperature in the Ionian Sea [37]). These small changes in temperature and sea level are both possible and sufficient to destabilize the gas hydrates at Thessaloniki MV.

Although the amount of methane produced from the autoclave core from Thessaloniki MV is minor in quantity, and the volume of gas hydrates is unlikely to be large at this site (based on the maximum depth at which gas hydrates in this area can be stable, as indicated in Figures 7(a) and 7(b)), we do not know the potential areal extent of the GH

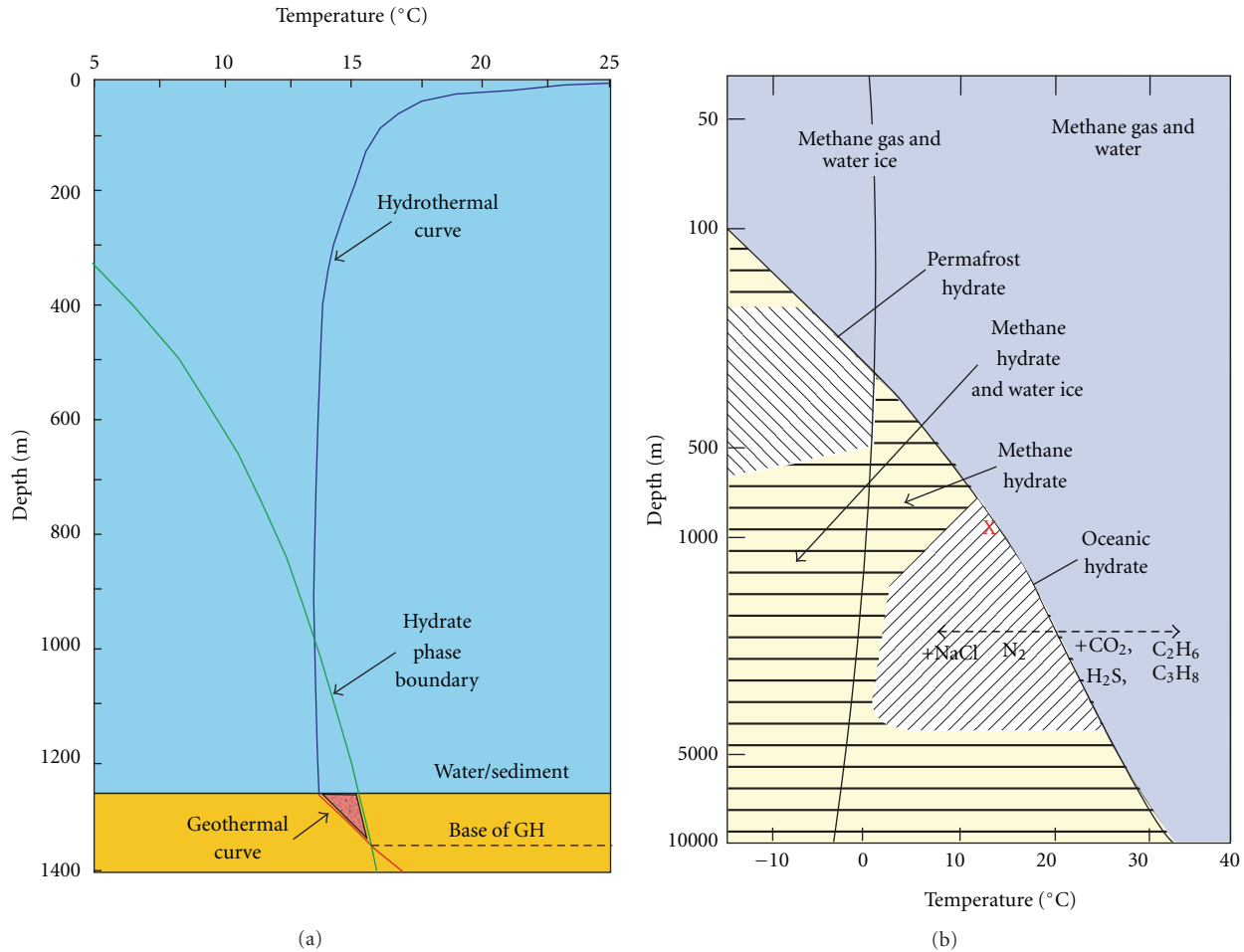


FIGURE 7: (a) Gas hydrate stability diagram for the Thessaloniki MV greater area (based on [36]), (b) gas hydrate stability diagram [27] depicting with an X the location of Thessaloniki gas hydrate field.

at these water depths in the Eastern Mediterranean. Since these GH are at the upper boundary of the GH stability diagram their distribution and presence should be studied more thoroughly.

5. Conclusion

A new gas hydrate bearing mud volcano named Thessaloniki was discovered in the Anaximander Mountains on the basis of its seafloor expression and an analysis of cores containing gas hydrates in a matrix of mud breccia typical of mud volcanoes. It is the shallowest mud volcano there, lying at depths between 1315 and 1260 m, with an areal extend of about 1.67 km² and comprising three peaks on its summit. GH were collected from three cores (two conventional gravity cores and one autoclave core). The GH crystals have the form of flakes or rice. The degassing of the 228 cm long autoclave core provided 3.1 liters of gas (mostly methane). Rock clasts from the mud breccias indicate a lower middle Miocene age for the source rock formation. The sea bottom temperature (13.7°C) and the pressure (12.9 MPa)

at Thessaloniki MV indicate that the GH there are at the upper limit of the stability zone, and prone to dissociation with the slightest temperature increase or pressure decrease. Therefore it could be a particularly suitable site for studying not only the mud volcano activity, but also the stability of natural gas hydrates and their potential environmental impact should they dissociate.

Acknowledgments

The field and office work was supported by the EC-funded projects ANAXIMANDER (EVK-CT-2002-20068) and HERMES (GOCE-CT-2005-511234-1) which the authors greatly appreciate. The authors thank the officers and the crew of the R/V *Aegaeo* for their important and effective contribution during the field work. They also thank the anonymous reviewers for the useful comments and suggestions.

References

[1] A. H. F. Robertson and A. Kopf, "Tectonic setting and processes of mud volcanism on the Mediterranean Ridge

- accretionary complex: evidence from Leg 160," in *Proceedings of the Ocean Drilling Program, Scientific Results*, A. H. F. Robertson, K.-C. Emeis, C. Richter, and A. Camerlenghi, Eds., vol. 160, pp. 665–680, 1998.
- [2] C. Perissoratis, G. Papadopoulos, and E. Zimianitis, "Occurrence of mud diapirism in the marine sector between Kos and Kalimnos islands, SE Aegean : preliminary Results," *Bulletin of the Geological Society of Greece*, vol. 32, no. 2, pp. 217–222, 1998.
 - [3] C. W. Holland, G. Etiope, A. V. Milkov, E. Michelozzi, and P. Favali, "Mud volcanoes discovered offshore Sicily," *Marine Geology*, vol. 199, no. 1-2, pp. 1–6, 2003.
 - [4] C. Huguen, J. Mascle, E. Chaumillon, A. Kopf, J. Woodside, and T. Zitter, "Structural setting and tectonic control of mud volcanoes from the Central Mediterranean Ridge (Eastern Mediterranean)," *Marine Geology*, vol. 209, no. 1–4, pp. 245–263, 2004.
 - [5] A. V. Milkov, "Worldwide distribution of submarine mud volcanoes and associated gas hydrates," *Marine Geology*, vol. 167, no. 1-2, pp. 29–42, 2000.
 - [6] J. Woodside, "Neotectonic Deformation of the Anaximander Mountains observed from EM12D multibeam data," in *Sedimentary Basins of the Mediterranean and Black Seas. TTR, 4th Post-Cruise Meeting UNESCO Report*, pp. 11–12, 1996.
 - [7] J. M. Woodside, M. K. Ivanov, and A. F. Limonov, "Shallow gas and gas hydrates in the Anaximander Mountains region Eastern Mediterranean Sea," in *Gas Hydrates: Relevance to World Margin Stability and Climate Change*, J. P. Henriot and J. Mienert, Eds., Sp. Publ. 137, pp. 177–193, Geological Society, London, UK, 1998.
 - [8] L. Loncke and J. Mascle, "Mud volcanoes, gas chimneys, pockmarks and mounds in the Nile deep-sea fan (eastern Mediterranean); geophysical evidences," *Marine and Petroleum Geology*, vol. 21, pp. 669–689, 2004.
 - [9] J. Mascle, T. Zitter, G. Bellaiche, L. Droz, V. Gaullier, and L. Loncke, "The Nile deep sea fan: preliminary results from a swath bathymetry survey," *Marine and Petroleum Geology*, vol. 18, pp. 471–477, 2001.
 - [10] J. H. ten Veen, J. M. Woodside, T. A. C. Zitter, J. F. Dumont, J. Mascle, and A. Volkonskaia, "Neotectonic evolution of the Anaximander Mountains at the junction of the Hellenic and Cyprus arcs," *Tectonophysics*, vol. 391, no. 1–4, pp. 35–65, 2004.
 - [11] J. M. Woodside and S. Dupre, "Cruise Report MIMES: an Expedition on Pelagia 13 June 2004—July 2004 (a contribution to the MEDIFLUX project of EUROMARGINS)," NWO-ALW project 855.01.031, 2004.
 - [12] T. A. C. Zitter, C. Huguen, and J. M. Woodside, "Geology of mud volcanoes in the eastern Mediterranean from combined sidescan sonar and submersible surveys," *Deep-Sea Research Part I*, vol. 52, no. 3, pp. 457–475, 2005.
 - [13] M. B. Cita, W. F. B. Ryan, and I. Paggi, "Prometheus mud breccia: an example of shale diapirism in the western Mediterranean ridge," *Annales Géologiques des Pays Helleniques*, vol. 3, pp. 543–570, 1981.
 - [14] T. A. C. Zitter, J. M. Woodside, and J. Mascle, "The Anaximander Mountains: a clue to the tectonics of southwest Anatolia," *Geological Journal*, vol. 38, no. 3–4, pp. 375–394, 2003.
 - [15] A. E. Aksu, J. Hall, and C. Yaltirak, "Miocene—recent evolution of Anaximander Mountains and Finike Basin at the junction of Hellenic and Cyprus Arcs, eastern Mediterranean," *Marine Geology*, vol. 258, no. 1–4, pp. 24–47, 2009.
 - [16] S. McClusky, S. Balassanian, A. Barka et al., "Global positioning system constraints on plate kinematics and dynamics in the eastern Mediterranean and caucasus," *Journal of Geophysical Research B*, vol. 105, no. 3, pp. 5695–5719, 2000.
 - [17] V. Lykousis, S. Alexandri, J. Woodside et al., "Mud volcanoes and gas hydrates in the Anaximander mountains (Eastern Mediterranean Sea)," *Marine and Petroleum Geology*, vol. 26, no. 6, pp. 854–872, 2009.
 - [18] T. Pape, S. Kasten, M. Zabel et al., "Gas hydrates in shallow deposits of the Amsterdam mud volcano, Anaximander Mountains, northeastern Mediterranean Sea," *Geo-Marine Letters*, vol. 30, no. 3-4, pp. 187–206, 2010.
 - [19] K. Heeschen, A. Dahlmann, H.-J. Hohnberg et al., "Pressurized near-surface sediment cores of Anaximander mud volcanoes," in *Eastern Mediterranean, EGU General Assembly*, vol. 8 of *Geophysical Research Abstracts*, Vienna, Austria, April 2006, 07005. SRef-ID: 1607-7962/gra/EGU06-A-07005.
 - [20] V. Lykousis, S. Alexandri, J. Woodside et al., "New evidence of extensive active mud volcanism in the Anaximander mountains (Eastern Mediterranean): the "ATHINA" mud volcano," *Environmental Geology*, vol. 46, no. 8, pp. 1030–1037, 2004.
 - [21] C. Perissoratis, Chr. Ioakim, V. Lykousis et al., "Characteristics of the Thessaloniki Mud Volcano, a recently discovered gas hydrate bearing area in the Anaximander Mountains," in *Eastern Mediterranean, EGU General Assembly*, vol. 8 of *Geophysical Research Abstracts*, Vienna, Austria, April 2006, 03874, SRef-ID: 1607-7962/gra/EGU06-A-03874.
 - [22] H. Amann, J. Baraza, C. Marx et al., "HYACE, an Autoclave coring equipment for systematic offshore sampling, measurement and ground truthing," in *Eurocean*, pp. 670–673, 2000.
 - [23] C. Huguen, J. Benkheilil, P. Gresse et al., "Échantillons rocheux provenant de "volcans de boue" de Méditerranée orientale," *Oceanologica Acta*, vol. 24, no. 4, pp. 349–360, 2001.
 - [24] Chr. Ioakim, St. Tsaila-Monopolis, C. Perissoratis, and V. Lykousis, "The examination of the gas hydrates hosting environment at the Anaximander Mud Volcanoes, Eastern Mediterranean: stratigraphy and Sedimentary successions at the mud beacia clasts," in *CIESM Workshop Monograph*, vol. 29, pp. 87–96, Bologna, Italy, 2005.
 - [25] Chr. Ioakim, St. Tsaila-Monopolis, C. Perissoratis, V. Lykousis, S. Alexandri, and J. Woodside, "Deciphering the deep geology of the Anaximander Mountains area (Eastern Mediterranean)," in *Proceedings of the 3rd Geological Congress*, 2008, abstract.
 - [26] K. A. Kvenvolden, "Gas hydrates-geological perspective and global change," *Reviews of Geophysics*, vol. 31, no. 2, pp. 173–187, 1993.
 - [27] R. E. Pellenberg and D. Max, "Introduction, physical properties, and natural occurrences of hydrate," in *Natural Gas Hydrate: in Oceanic and Permafrost Environments*, D. Max, Ed., vol. 5, pp. 1–8, Kluwer Academic Publishers, Dordrecht, The Netherlands, 2000.
 - [28] D. Casas, G. Ercilla, V. Lykousis, Chr. Ioakim, and C. Perissoratis, "Physical properties and their relationship to sedimentary processes and texture in sediments from mud volcanoes in the Anaximander Mountains (Eastern Mediterranean)," *Scientia Marina*, vol. 70, no. 4, pp. 643–659, 2006.
 - [29] V. H. Magalhaes, J. Bobos, L. Gaspar, L. M. Pinheiro, J. H. Monteiro, and M. K. Ivanov, "Mineralogy and geochemistry of carbonate chimneys from the Gulf of Cadiz: preliminary results," IOC Workshop Report no. 183, 2002.

- [30] K. U. Heeschen, H. J. Hohnberg, M. Haeckel, F. Abegg, M. Drews, and G. Bohrmann, "In situ hydrocarbon concentrations from pressurized cores in surface sediments, Northern Gulf of Mexico," *Marine Chemistry*, vol. 107, no. 4, pp. 498–515, 2007.
- [31] H. Bolli and J. Saunders, "Oligocene to Holocene low latitude planctonic foraminifera," in *Planctonic Stratigraphy*, H. Bolli, J. Saunders, and G. Perch-Nielsen, Eds., pp. 155–263, Cambridge University Press, Cambridge, UK, 1985.
- [32] M. Gutnic, O. Monod, A. Poisson, and J. F. Dumont, "Geologie des Taurides Occidentales (Turquie)," *Mémoires de la Société Géologique de France*, vol. 137, pp. 1–112, 1979.
- [33] T. A. C. Zitter, *Mud volcanism and fluid emissions in Eastern Mediterranean neotectonic zones*, Ph.D. thesis, Vrije University, 2004.
- [34] A. Camerlenghi, M. B. Cita, B. Della Vedova, N. Fusi, L. Mirabile, and G. Pellis, "Geophysical evidence of mud diapirism on the Mediterranean Ridge accretionary complex," *Marine Geophysical Researches*, vol. 17, no. 2, pp. 115–141, 1995.
- [35] T. Feseker, A. Dählmann, J. P. Foucher, and F. Harmegnies, "In-situ sediment temperature measurements and geochemical porewater data suggest highly dynamic fluid flow at Isis mud volcano, eastern Mediterranean Sea," *Marine Geology*, vol. 261, no. 1–4, pp. 128–137, 2009.
- [36] E. D. Sloan, "Natural gas hydrate phase equilibria and kinetics: understanding the state-of-the-art," *Revue de l'Institut Français du Pétrole*, vol. 45, no. 2, pp. 245–266, 1990.
- [37] B. Klein, W. Roether, B. B. Manca et al., "The large deep water transient in the Eastern Mediterranean," *Deep-Sea Research Part I*, vol. 46, no. 3, pp. 371–414, 1999.

Research Article

Seismic Expression of Polygonal Faults and Its Impact on Fluid Flow Migration for Gas Hydrates Formation in Deep Water of the South China Sea

Duanxin Chen,^{1,2} Shiguo Wu,¹ Xiujuan Wang,¹ and Fuliang Lv³

¹Key Laboratory of Marine Geology and Environment, Institute of Oceanology, Chinese Academy of Sciences, Qingdao 266071, China

²Graduate University of Chinese Academy of Sciences, Beijing 100049, China

³Hangzhou Institute of Geology, PetroChina, Hangzhou 310023, China

Correspondence should be addressed to Shiguo Wu, swu@qdio.ac.cn

Received 31 May 2011; Revised 2 September 2011; Accepted 12 September 2011

Academic Editor: Ingo Pecher

Copyright © 2011 Duanxin Chen et al. This is an open access article distributed under the Creative Commons Attribution License, which permits unrestricted use, distribution, and reproduction in any medium, provided the original work is properly cited.

Polygonal faults were identified from three-dimensional (3D) seismic data in the middle-late Miocene marine sequences of the South China Sea. Polygonal faults in the study area are normal faults with fault lengths ranging from 100 to 1500 m, fault spaces ranging from 40 to 800 m, and throws ranging from 10 to 40 m. Gas hydrate was inferred from the seismic polarity, the reflection strength, and the temperature-pressure equilibrium computation results. Gas hydrates located in the sediments above the polygonal faults layer. Polygonal faults can act as pathways for the migration of fluid flow, which can supply hydrocarbons for the formation of gas hydrates.

1. Introduction

Polygonal faults are a network of layer-bound, mesoscale (throws from 10 to 100 m) extensional faults arranged in a polygonal structure developing in deep-water sequence [1]. The term “polygonal fault” was named by Cartwright [2] when he analyzed the shale sedimentary throughout the 3D seismic data obtained from North Sea basin. Up to now, more than 50 basins have found the existence of polygonal faults. Some geologists presented different formation mechanisms, including density inversion [3, 4], gravity sliding or collapse [5], episodic hydrofracturing [6], “volumetric contraction” [7], and low coefficients of friction [8].

In the South China Sea (SCS), polygonal faults were for the first time identified in the Qiongdongnan basin (QDNB) in 2009 [9]. Sun et al. [10] mentioned the migration of hydrocarbon through polygonal faults in QDNB. However, there is no document about reservoirs of gas hydrates associated with polygonal faults in SCS.

In this paper, we will show the seismic geometry and distribution of polygonal faults and investigate the geophysical characters of gas hydrates in deep water of QDNB

and Zhongjiannan basin (ZJNB) (Figure 1). We use high-resolution 2D and 3D seismic data integrated with local sedimentary history to study the function of polygonal faults in acting as conduits of gas hydrate provinces.

2. Geological Backgrounds

Sedimentary basins in northern South China Sea margin underwent an early syn-rifting stage in Paleogene and a postrifting thermal subsidence stage in Neogene and Quaternary [11]. The separation for syn-rifting and postrifting stage is a breakup unconformity T60 (stratigraphic frames listed in Figure 2) between Oligocene and Miocene. Sedimentary facies in syn-rifting stage chiefly evolved from alluvial, delta, and lacustrine facies to shallow marine facies, whereas shallow, bathyal, and abyssal facies occupied the postrifting stage [11]. Sediments in lower Huangliu formation and upper Meishan formation of Miocene sequence consist of fine-grained claystone and limestone-hosting polygonal faults based on wireline log interpretations from wells drilled in QDNB.

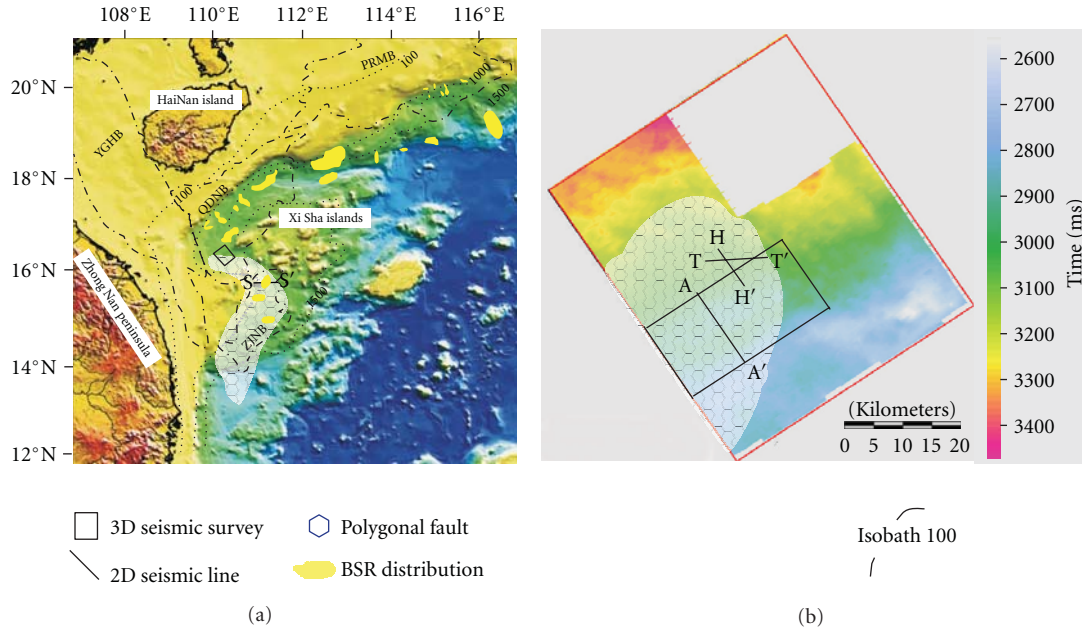


FIGURE 1: (a) The schematic map of South China Sea. The map shows the distribution of polygonal faults and prospective gas hydrate zones in QDNB and ZJNB. (b) The 3D seismic survey in deep water of QDNB. The basemap is the time depth of the sequence boundary of the base of upper Miocene. Lines plotted in the map will be discussed below.

3. Data and Methodology

This study is based on an integrated analysis of seismic data including a 3D survey and 2D lines acquired by BGP Inc., (China National Petroleum Corporation (CNPC)), processed by Liaohe Petroleum (CNPC, PetroChina). The 3D seismic data covers an area of 1480 km² with a bin size of 12.5 m × 25 m and water depth ranging from 1120 m to 1275 m in west of Xisha Islands, while 2D seismic data covers the deepwater of the southern depression of QDNB and the overall ZJNB with the common depth point (CDP) interval of 25 m (Figure 1(a)). We used the coherency slice and sequence flattening technique to study the 3D and partial 2D seismic data. With estimated geothermal gradient values and proper formation velocities, the study utilizes temperature-pressure equilibrium to compute the base of GHSZ.

4. Results

4.1. Seismic Imaging to Identify Polygonal Faults. Polygonal faults were identified in deep water of the southern depression of QDNB and northeastern of ZJNB over an area of about 6000 km² (Figure 1(a)). 3D seismic data from QDNB indicated that the polygonal faults pervasively occur in the lower Huangliu formation and upper Meishan formation and are limited by layer-bound strata of the base of Pliocene (T30) and Meishan formation (T50), as seen in Figure 3. Polygonal faults in northern SCS are extensional faults with fault lengths ranging from 100 to 1500 m, fault spaces ranging from 40 to 800 m, and throws ranging from 10 to 40 m (Figures 3 and 4). The view of the coherence slice from the 3D seismic data shows the

irregular polygonal map geometry (Figure 4). The deformed interval is generally subdivided into two tiers. The upper tier lies in the layer of 2.5–2.7 s two-way travel time (TWT)- and the lower one is in the layer of 2.7–3.0 s (TWT), manifesting the stratigraphically delimited subunits within the deformed interval. However, faults with longer vertical slip may connect the two tiers, piercing the base of Pliocene and Meishan formation. Smaller faults could be found dim among distinct polygonal faults (Figure 4). It might indicate the existence of smaller scale of polygonal faults.

4.2. BSRs Occurrence in Deep Water of SCS. Distributions and characteristics of BSRs in deep water of QDNB have been delineated (Figure 1(a)) [12–16]. Most of the BSRs with middle- to- high amplitude develop in Neogene and Quaternary strata which are paralleling to the seafloor.

We calculated the base of GHSZ and plotted it in seismic profile SS' in Figure 5 using the geothermal gradient and water depth obtained from this basin. The geothermal gradient was 0.045°Cm⁻¹ suggested by Ma et al. [17]. The water depth was acquired in accordance with multibeam data.

Temperature-pressure equilibrium equation was given by Miles [18]

$$P = 2.8074023 + a \cdot T + b \cdot T^2 + c \cdot T^3 + d \cdot T^4, \quad (1)$$

where P (MPa) is the formation pressure; T (°C) is formation temperature; $a = 1.559574 \times 10^{-1}$; $b = 4.8275 \times 10^{-2}$; $c = -2.78083 \times 10^{-3}$; $d = 1.5922 \times 10^{-4}$. And values of parameters (a – d) were used by Wang et al. [19].

In (1), the input water depth is 1100 m and the geothermal gradient is 0.045°C m⁻¹. The thickness of base of GHSZ

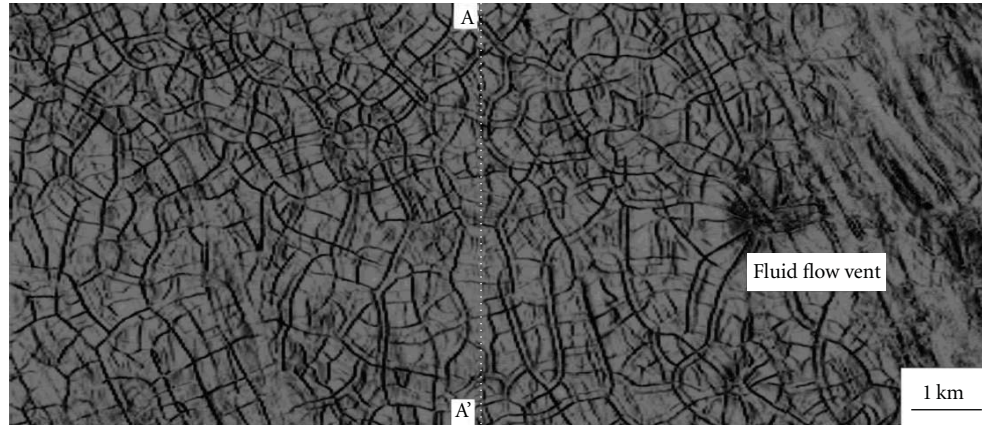


FIGURE 4: Coherence slice through the T40 horizon. The polygonal geometry is visible in the map. The rectangle boundary and vertical seismic profile of line AA' are displayed in Figure 1(b). The vent may have formed as a result of expelled fluid flow.

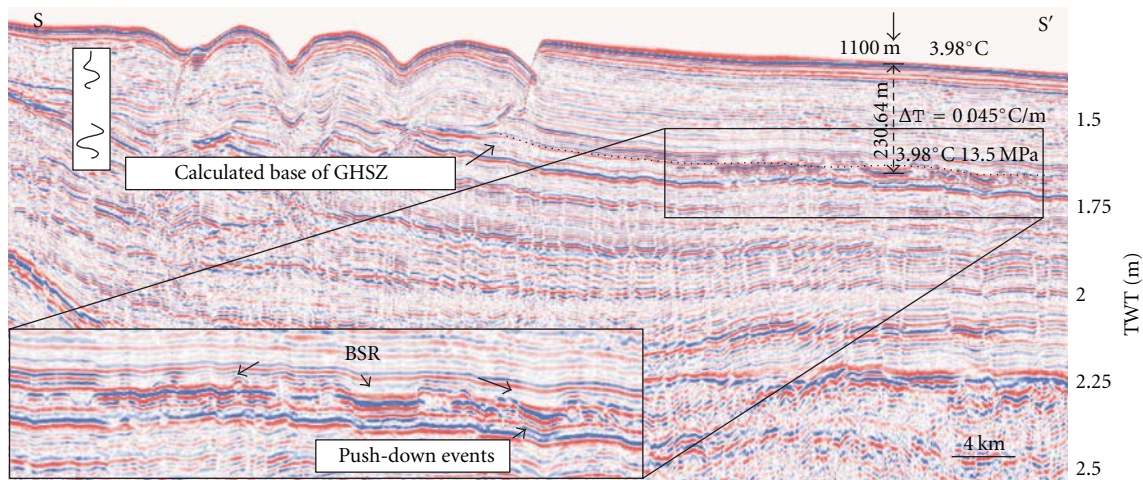


FIGURE 5: The calculated depth of GHSZ, and heat flow values in seismic profile SS'.

is 230.64 m and the pressure of the BSR is about 13.53 MPa. The conductivity is $1.18792 \text{ Wm}^{-1}\text{C}^{-1}$, and heat flow value at the BSR is 53.456 mWm^{-2} . The result is plotted in Figure 5. Heat flow value is in accordance with He et al. [20], who proposed that the average heat flow was about 59 mWm^{-2} which was caused by the high rate of sedimentation. The estimated thickness of GHSZ also coincides with the values given by Jin et al. [21] and Shi et al. [22] in this area.

5. Discussions

5.1. Focused Fluid Flow Associated with Polygonal Fault. Many people have reported the existence of pockmarks, gas chimneys, mud diapirs, slides, and channels and discussed their relationship to the fluid flow in northern South China Sea [14, 16, 19, 23, 24]. However, the polygonal faults may provide an additional pathway for the fluid flow, and the relationship has also been documented in the Lower Congo Basin [25], Norway continental margin [26, 27], and Scotian slope of the eastern Canada continental margin [28].

In QDNB and ZJNB, a large volume of source rocks and syn-rift faults were well developed in the Paleogene

sequences, whereas few faults occurred in the postrifting stage in deep water, which limited deep hydrocarbon in syn-rifting strata to migrate upward into the post-rifting strata. Therefore, polygonal faults developing in the lower Huan-gliu formation and the upper Meishan formation provide enhanced permeability for the fine-grained claystone and act as a pathway linking source rock in the syn-rifting strata to the reservoir in the post-rifting strata which may release more hydrocarbons migrating upwards the base of GHSZ.

Fluid flow involved in mud diaper, upwelling along a polygonal fault, indicates that polygonal faults may serve as fluid flow conduits, as shown in Figure 6. In the section, fluid flow commenced its migration through the lower tier of polygonal faults. Acoustic blanking zones and strong reflectors above sacking structures indicate the presence of gas. A small amount of fluid could also flow upwards via the upper tier. Polygonal faults display a radiant shape, as shown in Figure 4.

The model of low coefficient of friction raised by Gouly [8] may support the function of conduits of polygonal faults as well as conventional faults. It was demonstrated that low coefficients of residual friction in fine-grained sediments

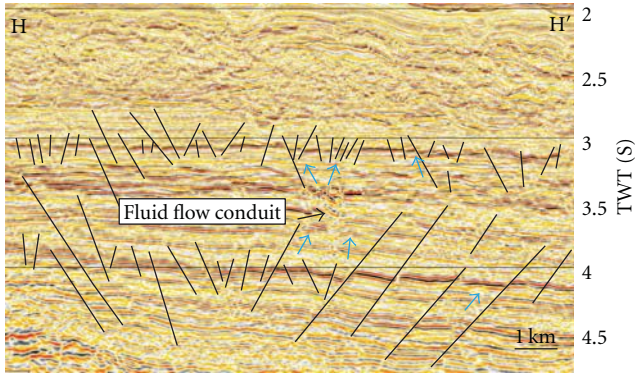
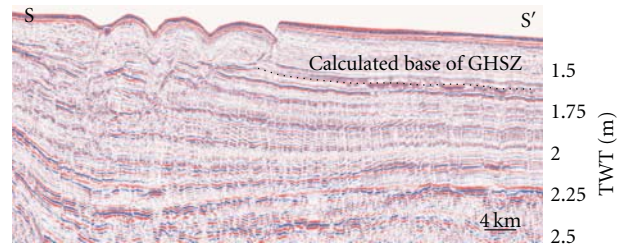


FIGURE 6: Interpretation of seismic profile HH', which describes the migration of fluid flow through polygonal faults. The dim seismic reflectors and fluid flow pipes are visible. See position in Figure 1(b).

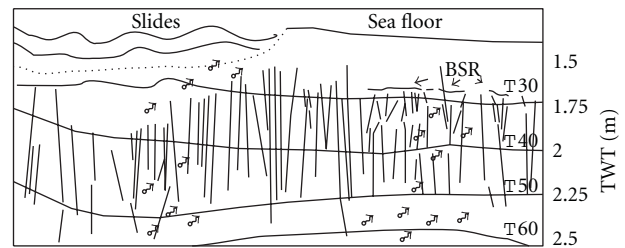
might be key to the formation of the polygonal system, and there was no evidence that nucleation of those faults that evolve into polygonal systems differs fundamentally from the processes involved in the nucleation of conventional faults in soft sediments [8]. Previous studies show that polygonal faults often initiate at shallow burial depth [2, 7, 29]. With increasing buried depth, compacted dewatering continuously occurs in layers underlying polygonal faults, and expelled fluids migrate up through polygonal faults and rock porosities to arrive at the seabed. However, with relation to different formation models of polygonal faults, the transporting mechanisms of fluid flows through polygonal faults are controversial [6, 8]. The preferred way of fluid flows may be episode eruptions provided by Cartwright [6]. Roberts and Nunn (1995) also conducted numerical simulations showing that a vertical fracture opened for 20–50 years in the seal and provided a permeable pathway from the geopressured sediments into the overlying section when the fluid pressure exceeds 85% of the lithostatic pressure. Then Fluid pressure in the seal decreased, and the fracture closed until fluid pressure increased to the fracture criteria, which took 10,000–500,000 years [30].

5.2. Gas Hydrate Occurrence with Polygonal Faults. The fact that deep fluid flows upwell through polygonal faults to produce gas hydrates is confirmed in several basins. The relationship between the polygonal fault and gas hydrate has been discussed on the continental margin of Norway, the Lower Congo basin, and the Scotian margin of the east coast of Canada [23, 24, 26]. On the mid-Norwegian margin, the polygonal fault system is located in the fine-grained hemipelagic sediments of the Kai formation, showing that fluid flow related to polygonal fault in this area is an ongoing process since the early Miocene in the mid-Norwegian [26, 27].

Besides tectonic faults, diapirs, and gas chimney act as conduits for the reservoir of gas hydrates in the South China Sea; the polygonal fault system is considered to be a new pathway linking to the GHSZ. The BSRs locate at the base of GHSZ which may indicate the presence of gas hydrates. The distribution of BSRs is shown in Figure 1(a). The BSRs



(a)



(b)

FIGURE 7: (a) The seismic profile SS'. (b) The interpretation of line SS'. The figure shows fluid flow migrated into the GHSZ through the polygonal faults. BSRs are distinctly visible overlying the polygonal faults. See the position in Figure 1(a).

are discontinuous and occur overlying the polygonal faults. The negative relieves are discovered below the BSRs, which may result from pushing down seismic events due to high concentration of free gas below GHSZ (Figures 5 and 7).

Biogenic gas migration may occupy partial gas component in gas hydrate in and above middle Miocene, while thermogenic hydrocarbon source rocks host in early Oligocene Yacheng formation, late Oligocene Lingshui formation, and Miocene Sanya formation [31]. Zhu et al. [32] tested gases released from acid hydrocarbon on 127 shallow sediment samples in QDNB, and indicated the existence of thermogenic gases with methane concentration $10 \sim 243.5 \mu\text{Lkg}^{-1}$, carbon isotope $-43.8\% \sim -26.6\%$, and $\text{C1}/(\text{C2} + \text{C3})_{10} \sim 30$. It is inferred that focus fluid flows with large volume of thermogenic gas from the source rocks, together with shallow biogenic gas, may mix and migrate upward along the polygonal fault system and form gas hydrates in locations of appropriate temperature and pressure. Hence, polygonal faults serve as a pathway linking thermogenic gas and shallow biogenic gas to the reservoirs of gas hydrates.

6. Conclusions

Researches based on high resolution 3D and 2D seismic data show that polygonal faults are tensional normal faults with fault lengths from 100 to 1500 m, fault spaces from 40 to 800 m, and throws from 10 to 40 m. The layer-bound sequence surfaces, two or more tiers, and polygonal geometry view pattern in plane can be recognized. Occurrence of gas hydrates in deep water of South China Sea is considered to be related to fluid flow through the polygonal fault system. Polygonal faults link thermogenic gas and shallow biogenic

gas to GHSZ, serving as pathways to migrate gas upwards to form gas hydrates.

Acknowledgments

The authors thank the Hangzhou Institute of Geology of PetroChina for permission to release these data in this paper. They gratefully acknowledge the reviewers for further suggestions and grammar revision. The research work was supported by the National Natural Science Foundation of China (no. 40930845), International Science & Technology Cooperation program of China (no. 2010DFA21740), and the National Basic Research Program (no. 2009CB219505).

References

- [1] J. A. Cartwright and D. N. Dewhurst, "Layer-bound compaction faults in fine-grained sediments," *Bulletin of the Geological Society of America*, vol. 110, no. 10, pp. 1242–1257, 1998.
- [2] J. A. Cartwright, "Episodic basin-wide hydrofracturing of overpressured Early Cenozoic mudrock sequences in the North Sea Basin," *Marine and Petroleum Geology*, vol. 11, no. 5, pp. 587–607, 1994.
- [3] J. P. Henriët, M. de Batist, and W. van Vaerenbergh, "Seismic facies and clay tectonic features of the Ypresian clay in the Southern North Sea," *Bulletin van de Belgische Vereniging voor Geologie*, vol. 97, pp. 457–472, 1989.
- [4] J. P. Henriët, D. Batist, and M. Verschuren, "Early fracturing of Palaeogene clays, southernmost North Sea: relevance to mechanisms of primary hydrocarbon migration," in *Generation, Accumulation and Production of Europe's Hydrocarbons*, A. M. Spencer, Ed., pp. 217–227, Oxford University Press, Oxford, 1991.
- [5] W. G. Higgs and K. R. McClay, "Analogue sandbox modeling of Miocene extensional faulting in the Outer Moray Firth," *Geology Society of London*, vol. 71, pp. 141–162, 1993.
- [6] J. A. Cartwright, "Episodic basin-wide fluid expulsion from geopressed shale sequences in the North Sea Basin," *Geology*, vol. 22, no. 5, pp. 447–450, 1994.
- [7] J. A. Cartwright and L. Lonergan, "Volumetric contraction during the compaction of mudrocks: a mechanism for the development of regional-scale polygonal fault systems," *Basin Research*, vol. 8, no. 2, pp. 183–193, 1996.
- [8] N. R. Goult, "Geomechanics of polygonal fault systems: a review," *Petroleum Geoscience*, vol. 14, no. 4, pp. 389–397, 2008.
- [9] S. Wu, Q. Sun, T. Wu, S. Yuan, Y. Ma, and G. Yao, "Polygonal fault and oil-gas accumulation in deep-water area of Qiongdongnan Basin," *Shiyou Xuebao/Acta Petrolei Sinica*, vol. 30, no. 1, pp. 22–26, 2009 (Chinese).
- [10] Q. Sun, S. Wu, F. Lü, and S. Yuan, "Polygonal faults and their implications for hydrocarbon reservoirs in the southern Qiongdongnan Basin, South China Sea," *Journal of Asian Earth Sciences*, vol. 39, no. 5, pp. 470–479, 2010.
- [11] X. N. Xie, R. D. Müller, S. Li, Z. Gong, and B. Steinberger, "Origin of anomalous subsidence along the Northern South China Sea margin and its relationship to dynamic topography," *Marine and Petroleum Geology*, vol. 23, no. 7, pp. 745–765, 2006.
- [12] B. C. Yao, "Gas hydrates in the South China Sea," *Journal of Tropical Oceanography*, vol. 20, no. 2, pp. 20–28, 2001 (Chinese).
- [13] B. C. Yao, "The forming condition and distribution characteristics of the gas hydrate in the South China Sea," *Marine Geology & Quaternary Geology*, vol. 25, no. 2, pp. 81–90, 2005 (Chinese).
- [14] D. F. Chen, X. X. Li, and B. Xia, "Distribution of gas hydrate stable zones and resource prediction in the Qiongdongnan basin of the South China Sea," *Chinese Journal of Geophysics*, vol. 47, no. 3, pp. 483–489, 2004.
- [15] S. Wu, G. Zhang, Y. Huang, J. Liang, and H. K. Wong, "Gas hydrate occurrence on the continental slope of the northern South China Sea," *Marine and Petroleum Geology*, vol. 22, no. 3, pp. 403–412, 2005.
- [16] X. J. Wang, S. G. Wu, D. D. Dong, Y. H. Gong, and C. Chai, "Characteristics of gas chimney and its relationship to gas hydrate in Qiongdongnan basin," *Marine Geology & Quaternary Geology*, vol. 28, no. 3, pp. 103–108, 2008 (Chinese).
- [17] Q. Ma, S. Chen, Q. Zhang, S. Guo, and S. Wang, *Overpressure Basins and Hydrocarbon Distribution*, Geological Press, Beijing, China, 2000.
- [18] P. R. Miles, "Potential distribution of methane hydrate beneath the European continental margins," *Geophysical Research Letters*, vol. 22, no. 23, pp. 3179–3182, 1995.
- [19] X. Wang, S. Wu, S. Yuan et al., "Geophysical signatures associated with fluid flow and gas hydrate occurrence in a tectonically quiescent sequence, Qiongdongnan Basin, South China Sea," *Geofluids*, vol. 10, no. 3, pp. 351–368, 2010.
- [20] L. He, K. Wang, L. Xiong, and J. Wang, "Heat flow and thermal history of the South China Sea," *Physics of the Earth and Planetary Interiors*, vol. 126, no. 3–4, pp. 211–220, 2001.
- [21] C. S. Jin, J. Y. Wang, and G. X. Zhang, "Factors affecting natural gas hydrate stability zone in the South China Sea," *Mineral Deposits*, vol. 24, no. 5, pp. 388–397, 2005 (Chinese).
- [22] X. Shi, X. Qiu, K. Xia, and D. Zhou, "Characteristics of surface heat flow in the South China Sea," *Journal of Asian Earth Sciences*, vol. 22, no. 3, pp. 265–277, 2003.
- [23] L. Chen and H. B. Song, "Research progress on seismic detection methods of natural gas seepage on the seabed," *Natural Gas Industry*, vol. 26, no. 7, pp. 35–39, 2006 (Chinese).
- [24] J. X. He, B. Xia, S. L. Zhang, P. Yan, and H. L. Liu, "Origin and distribution of mud diapirs in the Yinggehai basin and their relation to the migration and accumulation of natural gas," *Geology in China*, vol. 33, no. 6, pp. 1336–1344, 2006 (Chinese).
- [25] A. Gay, M. Lopez, P. Cochonat, M. Séranne, D. Levaché, and G. Sermondadaz, "Isolated seafloor pockmarks linked to BSRs, fluid chimneys, polygonal faults and stacked Oligocene-Miocene turbiditic palaeochannels in the Lower Congo Basin," *Marine Geology*, vol. 226, no. 1–2, pp. 25–40, 2006.
- [26] S. Hustoft, J. Mienert, S. Bünz, and H. Nouzé, "High-resolution 3D-seismic data indicate focussed fluid migration pathways above polygonal fault systems of the mid-Norwegian margin," *Marine Geology*, vol. 245, no. 1–4, pp. 89–106, 2007.
- [27] C. Berndt, S. Bünz, and J. Mienert, "Polygonal fault systems on the mid-Norwegian margin: a long term source for fluid flow," in *Subsurface Sediment Mobilization*, P. Rensbergen, R. R. Hillis, A. J. Maltman, and C. K. Morley, Eds., pp. 283–296, Geology Society of London, London, UK, 2003.

- [28] J. Cullen, D. C. Mosher, and K. Loudon, "The mohican channel gas hydrate zone, scotian slope: geophysical structure," in *Proceedings of the 6th International Conference on Gas Hydrates*, Vancouver, Canada, 2008.
- [29] J. Watterson, J. Walsh, A. Nicol, P. A. R. Nell, and P. G. Bretan, "Geometry and origin of a polygonal fault system," *Journal of the Geological Society*, vol. 157, no. 1, pp. 151–162, 2000.
- [30] S. J. Roberts and J. A. Nunn, "Episodic fluid expulsion from geopressed sediments," *Marine and Petroleum Geology*, vol. 12, no. 2, pp. 195–204, 1995.
- [31] J. X. He, B. Xia, D. S. Sun, S. L. Zhang, and B. M. Liu, "Hydrocarbon accumulation, migration and play targets in the Qiongdongnan Basin, South China Sea," *Petroleum Exploration and Development*, vol. 33, no. 1, pp. 53–58, 2006 (Chinese).
- [32] Y. H. Zhu, B. H. Wu, X. R. Luo, and G. X. Zhang, "Geochemical characteristics of hydrocarbon gases and their origin from the sediments of the South China Sea," *Geoscience*, vol. 22, no. 3, pp. 407–414, 2008 (Chinese).

Research Article

Methane Hydrate Distribution from Prolonged and Repeated Formation in Natural and Compacted Sand Samples: X-Ray CT Observations

Emily V. L. Rees,¹ Timothy J. Kneafsey,¹ and Yongkoo Seol²

¹Earth Sciences Division, Lawrence Berkeley National Laboratory, 1 Cyclotron Road, Berkeley, CA 94720, USA

²Office of Research and Development, National Energy Technology Laboratory, 626 Cochran Mill Road, P.O. Box 10940, Pittsburgh, PA 15236, USA

Correspondence should be addressed to Emily V. L. Rees, evrees@lbl.gov

Received 16 June 2011; Revised 12 August 2011; Accepted 13 August 2011

Academic Editor: Xuewei Liu

Copyright © 2011 Emily V. L. Rees et al. This is an open access article distributed under the Creative Commons Attribution License, which permits unrestricted use, distribution, and reproduction in any medium, provided the original work is properly cited.

To study physical properties of methane gas hydrate-bearing sediments, it is necessary to synthesize laboratory samples due to the limited availability of cores from natural deposits. X-ray computed tomography (CT) and other observations have shown gas hydrate to occur in a number of morphologies over a variety of sediment types. To aid in understanding formation and growth patterns of hydrate in sediments, methane hydrate was repeatedly formed in laboratory-packed sand samples and in a natural sediment core from the Mount Elbert Stratigraphic Test Well. CT scanning was performed during hydrate formation and decomposition steps, and periodically while the hydrate samples remained under stable conditions for up to 60 days. The investigation revealed the impact of water saturation on location and morphology of hydrate in both laboratory and natural sediments during repeated hydrate formations. Significant redistribution of hydrate and water in the samples was observed over both the short and long term.

1. Introduction

Gas hydrates (herein called “hydrate” or “hydrates”) are non-stoichiometric inclusion compounds formed from a network of hydrogen bonded water molecules encapsulating small gas molecules [1]. Hydrates typically form at high pressures and low temperatures in the presence of water and the hydrate-forming compound (e.g., methane, ethane, propane, or carbon dioxide). When formed naturally in sediments, hydrates strongly affect the sediment’s mechanical, geophysical, and hydrologic behavior [2]. Methane hydrate has been observed in nature in a wide variety of sediment types, in accumulations ranging from veins and massive nodules of hydrate [3–6] to dispersed and disseminated hydrate in the pore space of sediments [7–10]. There are numerous hypotheses as to the control of gas hydrate formation in sediments and whether they will form as a pore filling or cementing component of the sediment [5, 11, 12] or as a grain displacing component

resulting in veins, nodules, and layers [13]. Hydrate distributions in natural sediments are attributed to variations in chemistry, lithology, local tectonic activity, and nature of the gas supply in a hydrate-bearing region [1].

Hydrate redistribution in porous media following initial hydrate formation has been observed at the grain scale in a number of visualization experiments [14–16]. This reconfiguration of hydrate crystal shape was typically observed over relatively short timescales (up to several days); however, changes in hydrate distribution over several weeks have not been examined before. The observations from such tests as those conducted by Katsuki et al. [15, 16] and Tohidi et al. [14] are important because changes in hydrate distribution in a sample (e.g., by dissociating at one location and reforming at another) will result in changes in the physical properties of the sediment. Observations of long-term hydrate redistribution under stable conditions are also

important for understanding natural gas hydrate deposits and how they may change over time.

Repeated hydrate formation has often been reported to yield a “memory effect.” This is a phenomenon whereby water molecules retain a “memory” of their previous clathrate structure after dissociation at moderate temperatures. This retention of structure means that hydrate crystals can nucleate more easily from the same water body than when it was originally formed [1]. There have been numerous investigations into the memory effect of gas hydrates [17–23], most of which focus on the changes in the induction time for hydrate reformation after a dissociation event. Evidence from such experiments shows that the induction time for hydrate nucleation reduces significantly if the components have been used to make hydrate previously. There are, however, limitations on the persistence of the memory effect, related to the decomposition state of the previous hydrate and how long the components have been out of the stability zone. The general consensus is that the memory effect can be removed from a system by keeping the system out of the stability zone for longer than 24 hours or by heating the system to a temperature sufficiently above the stability zone for a given pressure [1]. To date, the hydrate memory effect has not been observed directly in sediment-hosted gas hydrate systems nor investigated with regard to its control on the location of hydrate nucleation in a porous media during reformation events.

To understand the formation and growth patterns of methane hydrate in natural sediments, a number of experiments have been performed using a core sample from the Mount Elbert Stratigraphic Test Well located in the Alaskan permafrost. In addition, hydrates were also formed in packed sand samples to allow comparison of hydrate formation in natural and reformed sediments. The aim of the experiments on the two sediment samples was to observe repeated hydrate formation and dissociation using X-ray computed tomography (CT) scanning, investigating the evolving distribution patterns of methane hydrate and also the behavior of hydrate during prolonged time inside the hydrate stability zone. The tests also provided a unique opportunity to investigate whether the memory effect can control the location of hydrate within sediments.

2. Experimental Methods

2.1. Mount Elbert Core

2.1.1. Sample Origin. The natural sediment used in the test sequence was recovered from the BPXA-DOE-USGS Mount Elbert Gas Hydrate Stratigraphic Test Well. The Mount Elbert well is located in the Milne Point oil field, on the north slope of the Brooks Range in Northern Alaska. The core used in this series of tests came from 660 m below surface level, part of Unit “C” of the reservoirs sands prevalent in the Milne Point region (Sample HYPV3 in Kneafsey et al. [24]). Descriptions of the geology and hydrate in this permafrost region can be found in Boswell et al. [25], Collett et al. [26], and Rose et al. [27].

2.1.2. Sample Preparation and CT Scanning. After collection, the hydrate-bearing sample was placed in a pressure vessel and pressurized with methane to maintain hydrate stability. The vessel was stored under pressure outdoors in the arctic winter and later moved to a freezer. Prior to shipment, the pressure vessel was rapidly vented and the sample was removed and placed in liquid nitrogen (LN; normal boiling point -196°C). Once received at the laboratory, the core was removed from LN and the ends of the core were rapidly cut flat. A belt sander was used to remove the outer layer of the sample in many steps, with sequential cooling by submersion in LN to keep the sample cold. Similarly, holes were drilled in the ends of the sample to accommodate thermocouples.

The core sample was encased in a custom-manufactured nitrile butadiene rubber sleeve. Poly-vinyl chloride caps were placed on the ends of the sample inside the sleeve and secured with wire to ensure a snug fit. Thermocouples were inserted into the sample from each end through the end caps to obtain temperature readings from locations inside the sample. A thermocouple was attached to the outside of the rubber sleeve to monitor confining fluid temperature. The core was then placed inside the pressure vessel, and confining pressure was applied.

The pressure vessel used was an X-ray transparent 8.9 cm outside diameter aluminum tube with threaded stainless steel end caps (Figure 1). The inlet port to the pressure vessel was connected to a high-pressure syringe pump (Teledyne Isco, Lincoln, Neb) and a fixed-volume methane bottle. The outlet of the sample was connected to another high-pressure syringe pump and could also be vented to the atmosphere. Pore pressure in the core was measured at both the inlet and outlet ports. In addition to the thermocouples inside the sample and in the confining fluid, temperature measurements were also made at the methane bottle. Temperature in the system was controlled by flowing temperature-controlled water/propylene glycol through a fluid jacket over the outside of the pressure vessel. Once the pressure cell/fluid jacket assembly was fully connected, it was placed on the CT scanner bed and insulated.

CT scanning was performed using a modified Siemens Somatom HiQ medical X-ray CT scanner. The X-ray CT scanning produced axial (x - y) cross-sections through the cylindrical vessel that could then be assembled to give a three-dimensional volume. Slice thickness was 3 mm, and 54 slices were needed to cover the length of the sample (Figure 2). Resolution of each scan resulted in voxel dimensions of $195\ \mu\text{m} \times 195\ \mu\text{m} \times 3000\ \mu\text{m}$ (x - y - z). The CT scanner was calibrated with known standards (air, water, Lucite, glass, nylon, and aluminum) in order to convert X-ray attenuation data into density.

Prior to the tests described here, the original natural hydrate in the sample had been dissociated by depressurization (the results of this dissociation are described in Kneafsey and Moridis [28]). Following the depressurization, the sample was CT scanned to obtain a baseline for later comparison. The initial scan showed the core to have two distinct regions with different densities (Figure 2). The left 70 mm of the core in Figure 2 (Part A) has a lower average density than the remaining 92 mm (Part B). Initial water

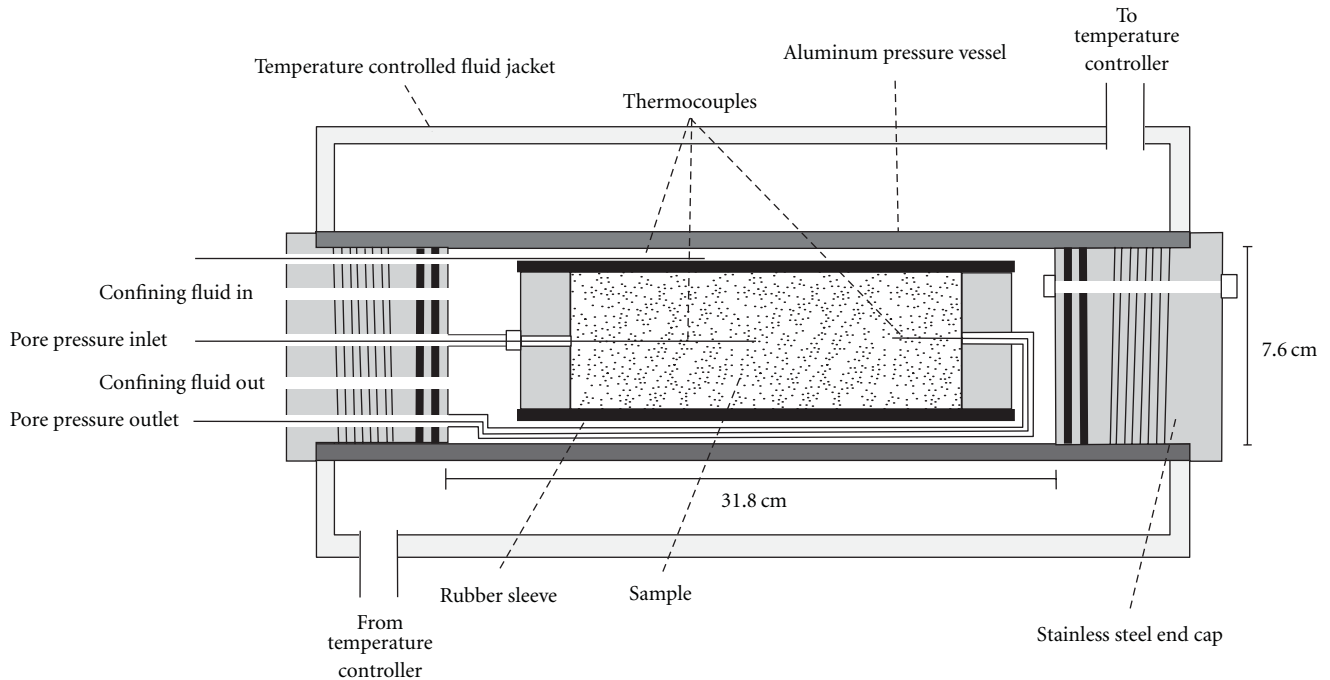


FIGURE 1: Schematic of the pressure vessel used in the Mount Elbert core tests.

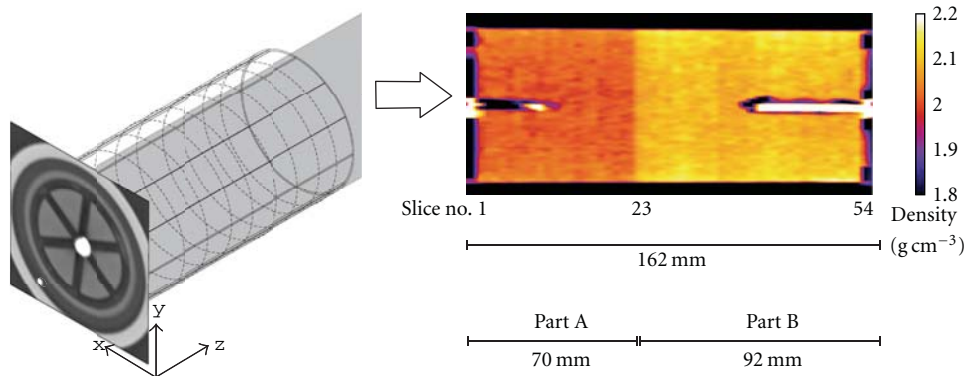


FIGURE 2: CT scanning image presentation for Mount Elbert core section. 54 x - y slices are obtained from the scanning process which are 3 mm deep in the z direction (left). It takes 2.7 seconds to scan each slice, with an additional 10-second processing time per slice. The 54 slices are reconstructed to produce a y - z slice showing the length of the core (right) and calibrated to give density values. Scan shown here is of the Mount Elbert core after original hydrate has been dissociated, but before laboratory hydrate formation. Parts A and B of the core are indicated.

saturations of each section of the core were also slightly different: Part A had an initial water saturation of 0.59, whereas Part B had an initial saturation of 0.75. Water saturations were calculated from calibrated CT scans of the core by comparing density values from the core in a fully water saturated state and a fully dry state. The calculated porosities of Parts A and B based on CT images are 0.29 and 0.28, respectively. Grain size analysis (Figure 3) shows Part A to have a larger average grain size than Part B. This analysis also showed that the average grain size was larger than $10\ \mu\text{m}$ for all sediment particles, indicating that the equilibrium conditions for methane hydrate would not be significantly shifted due to pore size inhibition [29]. In addition, XRD

analysis shows the mineral content of each part of the core to be similar, with the largest difference being a slightly larger amount of kaolinite in Part A than Part B.

2.1.3. Test Sequence. The test sequence consisted of two phases, each with two tests. In the first phase, the aim was to examine changes in the distribution of methane hydrate in the Mount Elbert core during repeated formation of the hydrate after only a couple of days in the stability zone. Prior to this first test, the Mount Elbert core had been out of the hydrate stability zone for over 24 hrs. The first hydrate formation (Test ME1.1) was initiated by increasing the pore pressure to 4.4 MPa (confining pressure to 5.4 MPa). Hydrate

TABLE 1: Summary of tests conducted on the Mount Elbert core.

Sample phase no.	Test no.	Formation method	Pressure start (MPa)	Pressure end (MPa)	Temp (°C)	Time in hydrate stability zone	Time to hydrate formation	Hydrate saturation
1	ME1.1	Pressurization	4.36 *(5)	4.14 *(4.6)	3.34	2 days	13 minutes	60.3%
	ME1.2	Cooling	4.41 *(5.2)	4.16 *(4.6)	3.50	3 days	95 minutes	59.3%
2	ME2.1	Pressurization	4.83 *(6.1)	4.58 *(5.6)	3.99	60 days	9 minutes	59.5%
	ME2.2	Cooling	*a	*a	~4	>42 days	*a	60%*b

* Equilibrium temperature for methane hydrate at given pressure (°C).

*a A power failure temporarily stopped data logger.

*b Estimated from CT scans.

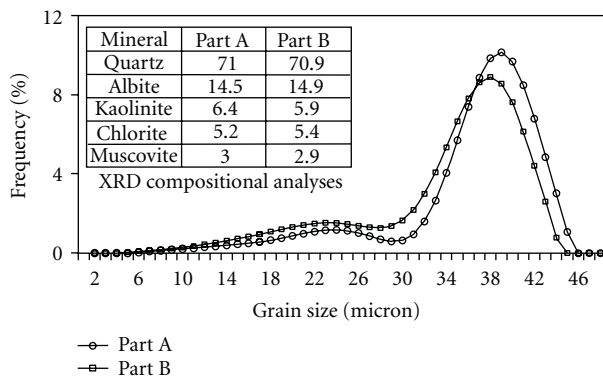


FIGURE 3: Grain-size and XRD analysis for Parts A and B of the Mount Elbert core.

formation began after 13 minutes in the stability zone, marked by an increase in temperature inside the sample. Temperature returned to the set value after ~15 hours, and hydrate formation was assumed to be complete. The sample was kept in the hydrate stability zone for 2 days before dissociation by increasing the temperature to 10°C. The sample was then held out of the stability field for another 24 hours before hydrate was reformed by decreasing the temperature to 4°C (Test ME1.2). Once inside the stability zone, hydrate formation did not occur for 80 minutes, with temperature and pressure stabilizing after 11 hours. The sample was held in the stability zone for 3 days before dissociation by allowing temperatures and pressures to be equilibrated to ambient conditions.

The second phase of the Mount Elbert core test sequence aimed to maintain hydrate in the core under stable conditions for extended periods of time. Hydrate was first made via pressurization at a cool temperature. Initially, the temperature of the core was lowered from laboratory ambient temperature to 4°C, with the pore pressure of the system at 2.9 MPa (confining fluid pressure at 4 MPa). These initial conditions were outside the methane hydrate stability zone. Hydrate formation was initiated by increasing the pore pressure to 4.8 MPa (confining pressure 5.5 MPa). Hydrate formation began after only 9 minutes inside the stability

zone, indicated by an increase in internal temperature of more than 1°C. After 10 hours, the temperature inside the core returned to the applied temperature (~4°C), and hydrate formation was considered complete. The core sample remained in the hydrate stability zone for 60 days, during which pressure and temperature were monitored and X-ray CT scans were conducted at intervals of 3 to 10 days (Test ME2.1).

After ~60 days, the hydrate was dissociated. The pressure inside the vessel remained at ~4.8 MPa, since the produced methane vented to a large, pressurized bottle. These conditions are outside of the stability zone for methane hydrate. After several days, the temperature of the system returned to 4°C, thereby reforming methane gas hydrate in the core via cooling. X-ray CT scanning revealed that hydrate had formed inside the core, and the sample was allowed to remain under hydrate stable conditions for 41 days for continued observation (Test ME2.2). Table 1 gives a summary of the tests in both phases of the testing sequence.

2.1.4. Determination of Hydrate Saturation. During each test the system remained isolated so that the amount of methane consumed by hydrate formation could be calculated from the pressure drop inside the sample and methane bottle. Knowing the temperature of the bottle and sample, the measured pressure drop could be converted to moles of methane consumed by hydrate formation, assuming a constant water to methane molecular ratio of 6 and the methane hydrate density to be 0.917 g cm⁻³ [1]. This measurement gave a bulk hydrate volume for the whole core (Table 1). The porosity was computed using CT scans from the water saturated and dry conditions obtained after the hydrate formation tests. The amount of water in the samples was determined by comparing the CT scans prior to a test to the CT scans of the samples when water saturated and was dry (obtained after the test). Comparing the predicted number of moles of methane to be consumed by the all of the water present with the measured methane consumption yielded a 70% conversion of water to methane hydrate.

The spatial distribution of hydrate saturation was calculated through analysis of the CT data combined with

the mass balance [30]. Part B had a higher average hydrate saturation by $\sim 10\%$ over Part A, corresponding to the varying initial water saturations, and irregular hydrate distribution (described in more detail in Section 3).

2.2. Packed Sand Sample. A predetermined volume of water and fine silica sand (F-110: 99.8% silica, rounded to subangular grains, $120\ \mu\text{m}$ average grain size, used as received [31]) was mixed thoroughly in a sealed container. The volume of water added was calculated to produce the desired water saturation (26 and 37%) once the sample was packed. The sand and water mixture was kept at room conditions for 12 hours to allow water distribution equilibration before being remixed and packed into a 19.8 cm long rubber sleeve having an outside diameter of 5.1 cm. The packed rubber sleeve was then placed in a pressure vessel, allowing the application of triaxial confining pressure. Thermocouples at both ends were inserted into the sand pack to monitor temperature. The pressure vessel was enclosed with a water jacket that provided constant temperature conditions over the course of the experiments. Methane hydrate was formed in the sand by raising pore methane gas pressure to 8.3 MPa (confining pressure to 10.3 MPa), while the system was maintained at 8°C . The sand sample was continuously monitored for hydrate formation as in the Mount Elbert core tests, using pressure and temperature data and X-ray CT scans. Initiation of hydrate formation was detected by declining pressure and rising temperature inside the sand core.

Experiments were performed to observe hydrate distribution during formation and dissociation within two sand packs (SP1 and SP2). The first tests examined the impact of differing time periods between the end of dissociation for preexisting hydrate and the start of new hydrate formation (Tests SP1). The time periods were varied from 19 hours to 48 hours. The second tests with SP2 were performed to check the repeatability of hydrate distribution patterns (Tests SP2). The time gap between the first dissociation and the second formation was 15.3 hrs. SP1 and SP2 had similar initial water saturations (37% and 26%, resp.) and porosity (34%), which was uniform throughout the cores (Table 2). Hydrate formation and dissociation were induced by controlling pore pressure with a syringe pump. During repetitive formation and dissociation tests (Tests SP1), the gas within the sample was kept in the syringe pump to maintain a constant total volume of methane gas and water. During the second tests on SP2, the core was monitored more often while hydrate formation was occurring, to capture evolution of hydrate distribution during formation.

3. Results

3.1. Short-Term Test Results. As described in Section 2.1.3, methane hydrate was formed twice in the Mount Elbert core sample to observe whether the hydrate formation was repeatable and to examine the distribution of the hydrate across the natural sediment (Tests ME1.1 and ME1.2). Similar tests were conducted in a sand pack with four consecutive hydrate formations in the sample, SP1, and

TABLE 2: Measured properties of packed sand cores.

Parameter	SP1	SP2
Cylinder dimensions:		
Diameter, d (mm)	51	51
Length, L (mm)	188	188
Pressure (MPa)	8.3	8.3
Temperature ($^\circ\text{C}$)	8	8
Porosity, ϕ	0.34	0.34
Initial water saturation, S_w	0.37	0.26
* Hydrate saturation, S_H	0.38	0.28

* 100% water-to-hydrate conversion is assumed.

with two more tests on a second sand pack, SP2. Hydrate formation was documented in each experiment by taking periodic CT scans at specific locations in the cores at frequent intervals. Scanning was started once the onset of hydrate formation was detected in the pressure-temperature data for all the tests. Hydrate formation was indicated in the CT scans by an increase in density, which in this case refers to the mass per voxel volume in g cm^{-3} . Because the voxel size in these scans ($\sim 195\ \mu\text{m} \times 195\ \mu\text{m} \times 3000\ \mu\text{m}$) was larger than the grain size of the core sediment (less than $45\ \mu\text{m}$ for the Mount Elbert sample (Figure 3) and $120\ \mu\text{m}$ for the sand packs), each voxel contained sand, gas, hydrate (under proper conditions), and water. The increase in mass caused by the inclusion of methane molecules to the hydrate structure resulted in an increase in density of a voxel in a CT scan since the voxel size was large enough to encompass the volume change of water when it formed hydrate.

Hydrate began to form 13 minutes after pressurizing the core in Test ME1.1 (Table 1), but it did not start for 80 minutes after the sample was cooled into the stability zone in Test ME1.2. Figure 4 compares CT scan data at a single location in the Mount Elbert core (111 mm from the end) over the duration of both tests. Figure 4(a) shows hydrate developing as several concentrated masses within the sediment early in Test ME1.1. These masses spread outwards as hydrate formation continues to 170 minutes after initial onset. Figure 4(b) shows hydrate formation during Test ME1.2. Even though hydrate formation has started elsewhere in the core (seen by an increase in temperature and drop in pressure), hydrate formation does not occur at location 111 mm until 80 minutes after initial onset. In contrast to Test ME1.1, it can be seen in Figure 4(b) that hydrate starts forming at the edge of the core, spreading towards the center as formation continues.

In the packed sand sample SP1, hydrate started forming within 60 minutes after application of pressure and temperature (8.3 MPa and 8°C) in each of the formation events. It was found, however, that hydrate formation initiated faster after hydrate had once been formed in the core. Subsequent hydrate formation began almost instantaneously as the pressure inside the core reached stability conditions, regardless of the time period left between consecutive dissociation and reformation events. Because of this, no relationship could be determined between induction time and the time

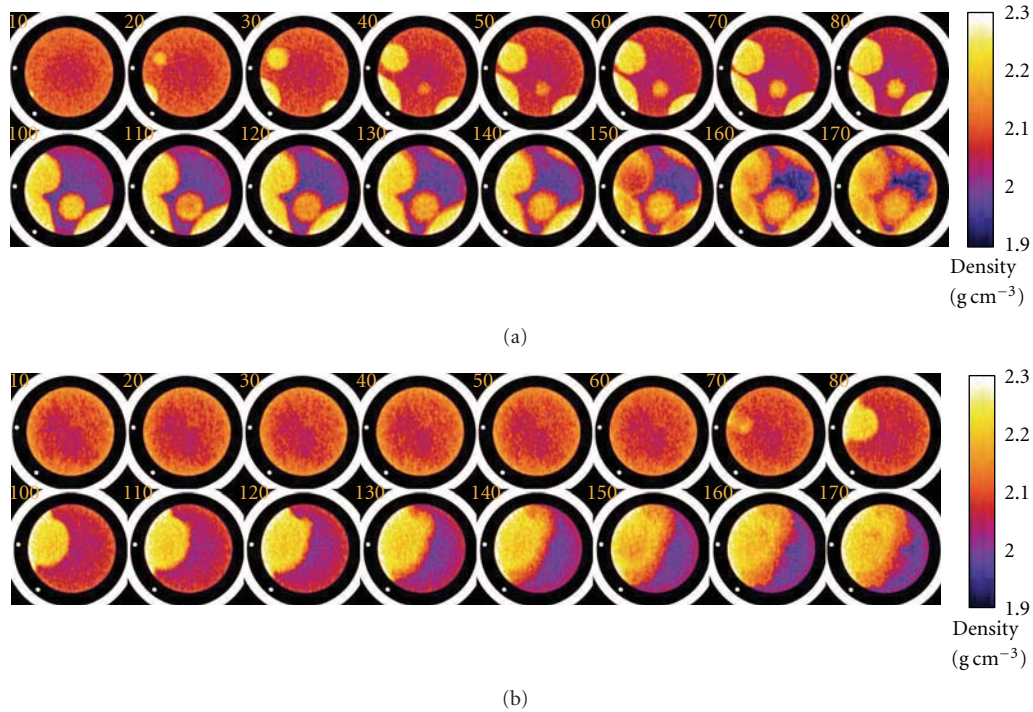


FIGURE 4: Methane hydrate formation at location 111 mm in the Mount Elbert core. (a) Test ME1.1—pressurization. (b) Test ME1.2—cooling. Slices in both figures were taken at 10-minute intervals after the initial onset of hydrate formation was observed in the pressure/temperature data for each test.

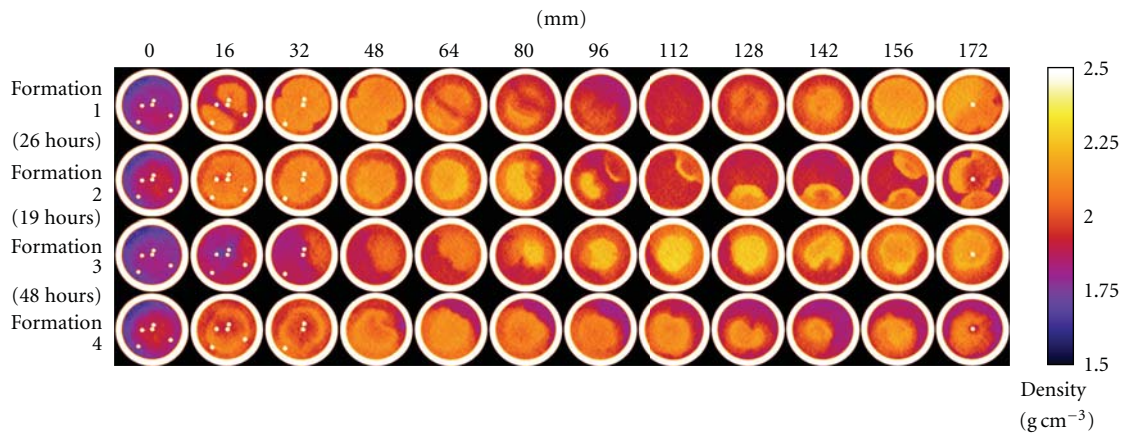


FIGURE 5: Hydrate formation distribution patterns on four consecutive formation events in packed sand sample SP1 at 8.3 MPa and 8°C. The time periods between dissociation and consecutive formation were varied: 26 hrs between 1 and 2; 19 hrs between 2 and 3; 48 hrs between 3 and 4.

period between hydrate dissociation and reformation in the same core. Figure 5 shows the four hydrate distribution patterns in SP1, imaged following completion of hydrate formation. This figure shows that the hydrate distributions among consecutive formation events do not show a repetitive hydrate formation pattern.

Two additional hydrate formation events were conducted in SP2. Figure 6 shows the two hydrate formation events. As with the tests on the Mount Elbert core, observation time began when the pressure and temperature conditions

inside the pack pass into the phase equilibrium boundary for methane hydrate. The first hydrate formation (Figure 6(a)) shows hydrate forming quickly in highly concentrated localities, but then growing outward over time. In Figure 6(b), hydrate formation occurs immediately through the entire core, but without further redistribution over the time observed (about 24 hours). In Figure 6(a), hydrate formation began at a number of locations near the gas injection point (32 and 50 mm) as seen in the 44 minutes column. At 99 minutes, hydrate forms throughout

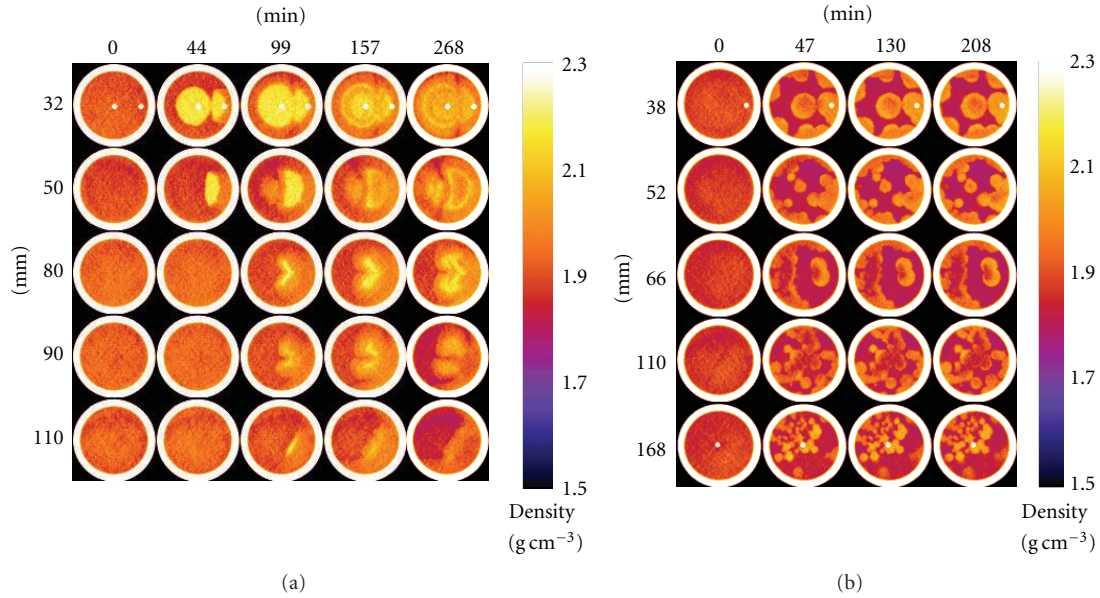


FIGURE 6: Methane hydrate formation in sample SP2. (a) First hydrate formation in SP2. (b) Second hydrate formation in SP2 after previous hydrate dissociation from (a).

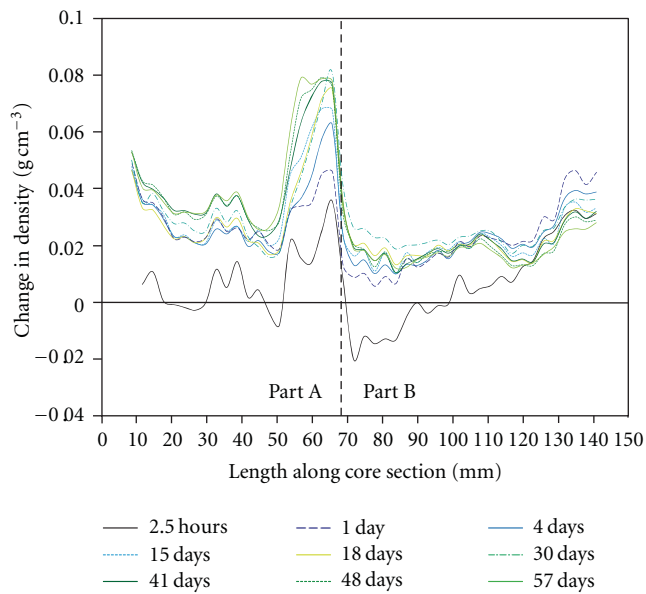


FIGURE 7: Profile of the average change in density of each slice at various times, from slices 5 to 48.

the sample while further hydrate accumulation occurs at the 32 and 50 mm locations. During the test, as shown in Figure 6(a), the initial hydrate formation occurs soon after the application of pressure to the sand pack, indicated by the rise in temperature inside the sample and the continuous drop in pressure. At ~140 minutes, the temperature inside the sand pack increased by 0.5°C , suggesting further hydrate formation in the sample.

Figure 6(b) shows a contrasting hydrate distribution pattern to that in Figure 6(a). Hydrate formation appears to

start in many locations throughout the entire core, forming numerous separated spherical masses. Unlike the hydrate in Figure 6(a), no redistribution is detected after the initial formation pattern (47 minutes in Figure 6(b)). The pressure and temperature data also suggest that no further hydrate formation occurred after 47 minutes since no fluctuations were observed.

3.2. Long-Term Test Results. The first phase of this test sequence (Test ME2.1) showed hydrate formation initiating after only 9 minutes in the stability zone. A scan was taken 2.5 hours after the onset of hydrate formation and showed hydrate forming in localized regions throughout the core. Another scan performed after 24 hours in the stability zone, showed that hydrate formation had evened out across the core. These first scans showed that, when hydrate formed at specific locations, other areas were depleted of water, lowering the density locally in those areas. After 24 hours, hydrate formation had spread throughout the core. Figure 7 shows the density change throughout 57 days of the ~60 day time span of the test, by plotting the average density of each x - y cross-section along the core length with the density obtained from the prehydrate scan subtracted. The plot for 2.5 hours shows an increase in density in the center of the core, in Part A, and an adjacent decrease in Part B, suggesting early hydrate formation depleting Part B of water. Between 2.5 hours and 1 day, hydrate continues to form and moisture redistributes itself resulting in density increase in both parts of the core, but the density in Part A close to the boundary with Part B remains higher. From 1 day to 57 days, density increases at this boundary (50 mm to 70 mm in Figure 7), even though density change is minimal in the locations adjacent to this region. Note also that a decrease

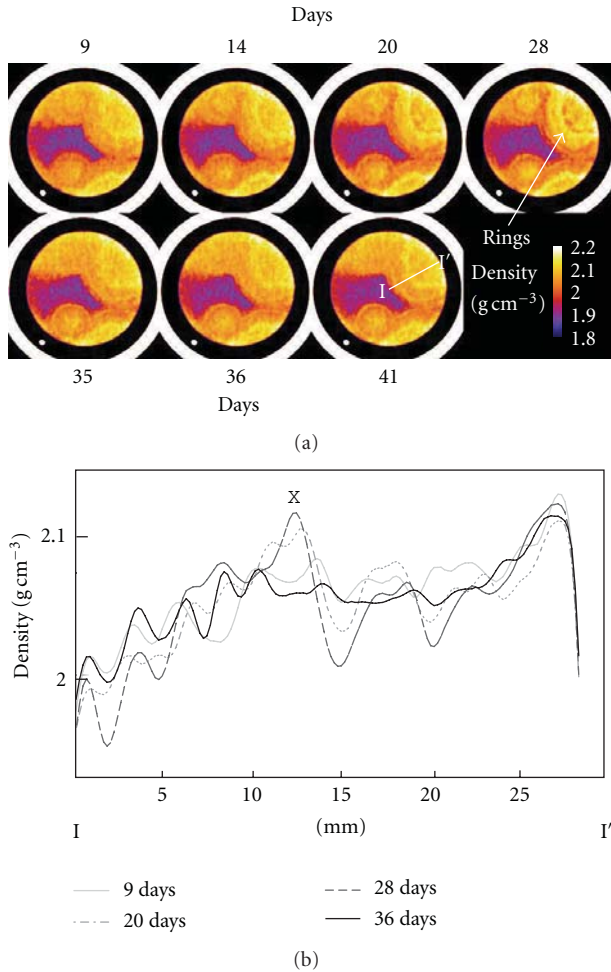


FIGURE 8: (a) X-Y cross-sections at location 63 mm in the Mount Elbert core showing the development of “rings” inside a hydrate mass. (b) Density profile along the line I-I’ in (a) for 4 times during Test ME2.2. X-axis represents millimeters along line I-I’.

in density occurs in Part B of the core between 130 mm and 140 mm. It is likely that moisture from this part of the core is redistributing over this period to the center of the core.

Over the course of Test ME2.1, temperature fluctuations $\sim 0.5^\circ\text{C}$ consistently occurred due to the daily ambient temperature changes in the laboratory. These fluctuations were well within the hydrate stability zone and were not accompanied by unexpected increases or decreases in pressure, which would indicate hydrate dissociation or formation, respectively. To investigate this further, the temperature in the control bath was dropped by 0.9°C , corresponding to a drop in pore pressure of 0.07 MPa on day 33 of the test sequence. The temperature was maintained at this lower value for the remainder of the test, placing the hydrate under more stable conditions. The scans from before and after this change (days 30 and 41 in Figure 7) show the higher density region between 60 and 70 mm in the 30 day scan thickens so that a band of higher density can be seen from 50 to 70 mm in the 41-day scan. This change is not greatly different from

the progressive redistribution seen throughout the test and so may not be caused by the applied temperature drop.

The first CT scan in Test ME2.2 was taken ~ 9 days after the core returned to hydrate-stable conditions. After 9 days, methane hydrate was clearly present in distinct patches across the core. In this test, hydrate appeared to form in a more heterogeneous manner in Part A of the core than in Part B, as well as forming concentrated hydrate masses, in contrast to the relatively dispersed nature in Test ME2.1. Over the 41 day duration of Test ME2.2, systematic CT scans were taken to monitor any changes in distribution. Over the first 28 days, several hydrate masses appeared to increase in density into distinct “ring” structures (Figure 8(a)). Between the scans at 28 days and 35 days the sharp density variations disappear, with the rings becoming less evident. Figure 8(b) highlights this change by showing a plot of density change across one of the patches. From 9 to 28 days density differences become more pronounced with a peak and trough evident between 10 and 16 mm. The final trace at 36 days, shows the peak and trough to have disappeared, and the average density across the length of the plot to have increased slightly. At 33 days, an increase in temperature and decrease in pressure, consistent with hydrate formation, were detected inside the core. Pore pressure inside the sample (and attached bottle) dropped by 0.07 MPa, and the internal temperature of the core increased by 0.9°C before returning to ambient temperatures after 3 hours. The changes seen in the pressure-temperature conditions suggest further hydrate formation during the redistribution evident in the CT scans. After the scan at 36 days, the ring structures again began to become more distinct. The test sequence was ended after 42 days.

4. Discussion

4.1. Repeated Hydrate Formation. The first phase of testing was conducted to investigate repeated hydrate formation in a natural core sample and in a sand pack. Figure 4 compares the hydrate formation at a single location in Mount Elbert Tests ME1.1 and ME1.2. The hydrate does not display the same formation morphology between the two tests. Hydrate formed in numerous discrete, highly localized masses in Test ME1.1, while it formed in much larger clusters in Test ME1.2. These results compare favorably with the results from the packed sand sample (Figures 5 and 6), where repeated hydrate formation also yielded poor repeatability in hydrate morphology. The results from both the Mount Elbert tests and the packed sand tests would suggest that the mechanisms for repeated hydrate formation in sediments are complex and may include a number of factors.

One factor possibly controlling the varying hydrate morphology in the repeated tests could be the water distribution following hydrate dissociation. To examine this effect, water saturation in the cores was analyzed before and after hydrate formation. In both the natural sediment core and the hand-packed sample, water was more concentrated in certain areas after hydrate dissociation. When this water saturation variation was compared to subsequent hydrate formation in each

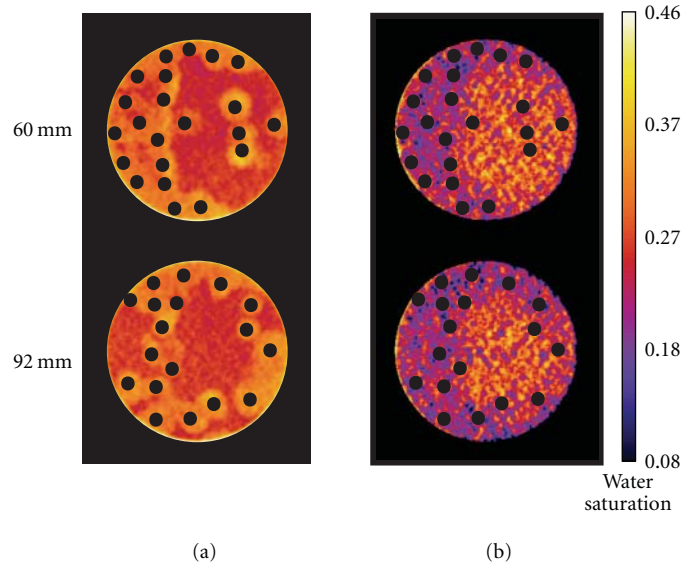


FIGURE 9: A comparison of hydrate nucleation locations with water saturation; (a) hydrate saturation distribution after the second hydrate formation in SP2 with black dots for the center of high hydrate saturation area indicating hydrate nucleation locations and (b) water distribution before the second hydrate formation with the black dots of hydrate nucleation superimposed.

sample, no correlation was observed in the Mount Elbert core from the end of test ME1.1 to the hydrate formation in ME1.2. However, the comparison in SP2 showed that hydrate formed more predominantly in areas where there was lower water saturation following hydrate dissociation. Figure 9 highlights this correlation by showing slices from two parts of the sample before and after hydrate formation. Figure 9(a) shows the sample with hydrate already formed (second formation in SP2), with black dots indicating locations of higher hydrate saturation in the sample. Figure 9(b) shows the same location for the sample prior to hydrate formation (after first hydrate dissociation in SP2), with the same black dots for hydrate formation superimposed. It can be seen from this figure that hydrate preferentially occurred in areas of lower water saturation ($< \sim 20\%$) in this case.

Hydrate nucleation is thought to be a process with a significant random component [1, 32], with the probability for nucleation increasing as the driving force of the reaction is higher, that is, the further into the hydrate stability zone the sample is placed prior to formation. All the tests described here have a relatively low driving force, defined as where the sample temperature and pressure conditions are approximately 1 MPa above the three-phase equilibrium for methane hydrate [22]. At this low driving force, the probability of hydrate nucleation has a substantial random element. Factors such as salinity, grain size distribution, and grain composition will alter the likelihood of nucleation in one region or another [1]. Sample SP2 was formed from uniform sand with distilled water in the pore space. The hydrate formation would therefore not be affected by salinity or grain size disparities across the sample. The differences in water saturation compounded by the random nucleation are therefore likely to be the main controlling factors in distribution within sample SP2. Figure 9 shows

hydrate preferentially growing in areas of lower initial water saturation, adjacent to areas where the water saturation is higher. This would suggest that small accumulations of water at grain contacts promote hydrate formation over large accumulations, which could be due to the influence of the surface of the sand grains on the structure of the water.

When water is in contact with a hydrophilic surface such as silica, water molecules will orientate in response to the charge on the surface of the mineral [33]. This “ordering” of the water molecules, called a hydration shell, is transmitted into the bulk of the water, becoming less ordered with increasing distance away from the mineral surface [34]. Hydration shells may provide an order to the water molecules that increases the probability of hydrate nucleation in porous media when water saturation is low. Although the hydration shells around the sand grains in SP2 would be considered relatively large at the nanometer scale, the variation in grain roughness might provide thinner films at the “peaks” of protrusions on rough grains, which could supply ordered nucleation sites for hydrate. Once water saturations become higher, the distance from the mineral surface to the gas/water interface is increased, and the effect of ordering from the hydration shells may not contribute as much to nucleation probability. Stevens et al. [35] and Bagherzadeh et al. [36] also observed that hydrate formation in low water saturation sandstone cores was faster than in high water saturation samples.

Although the hand-packed sand samples appear to show a correlation between water saturation and the location of reformed hydrate, the natural sediment samples did not show the same relationship. Distribution of water before and after each hydrate formation event was analyzed, with no correspondence seen throughout the core. Other factors affecting the nucleation probability in the Mount Elbert core

must therefore be considered, such as salinity variations, grain distribution, and thermal history.

The original salinity of the pore water in the Mount Elbert core was ~ 4 ppt [37]. Nevertheless, the inclusion of salts into water alters the stability conditions of methane hydrate, requiring higher pressures and lower temperatures for stability and making it slightly harder for hydrate to nucleate in certain regions. Variable salinity across the core, caused by dissociation of hydrate yielding fresh water in certain areas, but leaving others with a higher salinity, may have predestined some areas of the core to subsequent hydrate formation. This would imply that hydrate would tend to reform in the same locations it previously occupied. Once again, however, analysis of the scans does not suggest any control from potential salinity variations.

It is also possible that thermal history may play a role in influencing the nucleation of hydrate across a sediment core, in addition to salinity variability and saturation variations. Tests ME1.1 and ME1.2 do not share the same thermal history with regard to applied conditions for methane hydrate stability. Test ME1.1 began by cooling the sediment to 4°C at a pressure outside the stability zone and once temperature had stabilized, increasing the pressure to within the stability zone (4.4 MPa). Alternatively, Test ME1.2 started with the core at 4.4 MPa pressure but at 10°C , before instigating hydrate formation by cooling the core to 4°C . The induction times for these two tests may indicate the difference in thermal history experienced in the core. Hydrate began forming 13 minutes after application of stability conditions in Test ME1.1 but took 80 minutes to begin forming in Test ME1.2. In addition, in Test ME1.2, the outer regions of the core would have been in the hydrate stability zone longer than the inner regions because of heat transfer.

When considering whether the thermal gradient inside the core could be a factor, examination of the temperature data from the outside and inside the core shows that it takes ~ 14 minutes for temperatures on the outside of the core to be transmitted to the center. Temperature data from Test ME1.2 also shows that internal temperatures had equilibrated with the outer edge of the core prior to hydrate formation, so it would seem that temperature gradients do not directly affect formation of hydrate here. However, they may contribute to the water distribution. Analysis of the CT scans gives no indication of thermal history control on distribution, with hydrate forming both at the edges and inside of the core in equal measure.

One observation that can be made from the repeated tests on the Mount Elbert core is the significance of the random aspect of hydrate nucleation. Sloan and Koh [1], Parent and Bishnoi [32], and Servio and Englezos [22] all stress that, at low driving forces, hydrate nucleation is a random process influenced by grain characteristics, salinity, and thermal history of the pore water [1]. It can be determined from these tests that, in a system with no salinity and a consistent thermal history, water saturation has the most influence on hydrate nucleation probability. However, in a natural system where there are several aspects in conflict, no one factor seems to control hydrate nucleation, and the probabilities are not altered to favor specific locations.

4.2. Memory Effect. The memory effect can have a strong influence on the induction time of hydrate nucleation [17–23]. The memory effect was observed to influence hydrate formation in the hand-packed sand samples SP1 and SP2, as subsequent hydrate formation occurred almost instantaneously after hydrate had been formed and decomposed inside the sand once. In the Mount Elbert core, the memory effect did not appear to occur between ME1.1 and ME1.2 (recall test ME1.2 formed hydrate by cooling, and the sample remained at 10°C for 24 hours prior to hydrate formation) since the induction time increased between the two tests instead of decreasing. The changing induction times seen in tests ME1.1 and ME1.2 may result from the varying thermal history between the cores. Test ME1.1 on the Mount Elbert core sample formed hydrate through pressurization, but the core was maintained at 4°C for at least 12 hours prior to hydrate formation. These differences in thermal history could be responsible for the differences in induction time seen between the tests, as Ohmura et al. [19] have shown that induction times for methane hydrate formation increase as the temperature at which the system was held after dissociation increases.

The memory effect has been linked to the timing of hydrate formation, but not to its location. The memory effect does not affect the location of hydrate formation in repeated tests. Water distribution is shown to have the most control over hydrate location in the packed sand samples. In the Mount Elbert core, no correlation can be seen between old and new hydrate formation in the cores, indicating that prior hydrate formation has no effect on location of hydrate nucleation.

4.3. Density Redistribution. Because the sand in our samples was held in place by a combination of cementation and effective stress, density changes were caused by (1) incorporation of methane into water, resulting in hydrate increasing the mass in a voxel of fixed volume or (2) the change in location of water or hydrate within the pore space. Density redistribution was seen to occur over two timescales: (1) short term, over the hours it takes for hydrate to fully form (Tests ME1.1, 1.2, 2.1, and SP2), and (2) long term, over several weeks (Tests ME2.1 and ME2.2).

4.3.1. Short-Term Density Redistribution. In Test ME2.1 (pressurization), hydrate formation during the initial 2.5 hours produced patchy and localized regions of elevated hydrate saturation in the sediment, which became more homogeneous over 24 hours and with full hydrate formation. Early and more localized density redistribution was also seen in the hydrate formed in Tests ME1.1 and ME1.2 and in the packed sand sample SP2. Two processes need to be considered with regard to the density redistribution observed across these tests: capillarity and recrystallization.

Capillarity will cause water to be drawn towards the hydrate formation front. The physical presence of water-wetting hydrate in the pore space (1) reduces pore sizes, thus strengthening capillary suction, and (2) changes surface energy, increasing the capillary suction locally [38–40]. This

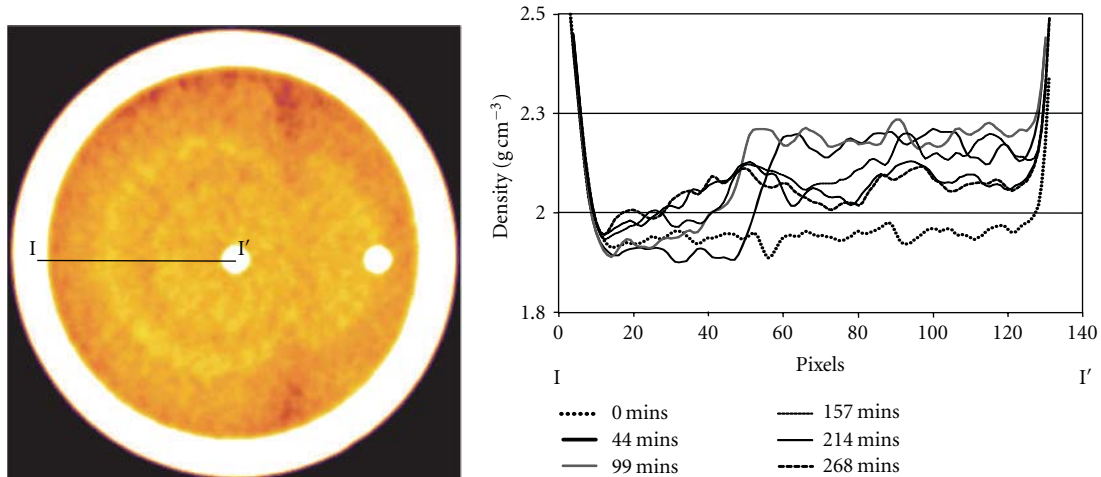


FIGURE 10: Cross-sectional profiles of density in the core (I to I' at 32 mm from the injection point) showing the evolution of density distribution patterns.

change in capillary pressure results in water being drawn towards the forming hydrate and therefore in an increase in local density due to water accumulation (in addition to hydrate formation) seen in the CT scans. This also creates areas of lower density nearby where water is depleted, such as in the plot for 2.5 hours over the region 70 to 90 mm in Figure 7 from Test ME2.1. Rapid placement of samples into the hydrate stability zone caused fast nucleation (as described in earlier sections). Visual inspection of fast hydrate growth [14, 15, 22] has shown that hydrate forms in dendritic crystals with high surface areas. Over time, these dendritic crystals recrystallize into more energy-efficient configurations [14, 15, 22]. The presence of these more compact, energy-efficient configurations in the porous medium results in a lower capillary suction than when the dendritic hydrate previously occupied the pore space.

Figure 10 shows the change in density during the first hydrate formation in SP2 over time for a single slice of the sample. Initial hydrate formation caused a high-density region (highly hydrate- and water-saturated) in the center of the sample (see also Figure 6). The initial rapid nucleation of hydrate in the sample would have likely created dendritic hydrate crystals with high surface areas and unstable surface energies. As time progresses ($t > 157$ minutes), the density in the center decreases, while the density outside the center increases and an outer circular band forms. This change in distribution is consistent with the dendritic hydrate crystals reconfiguring into more energy-efficient shapes [40] and the resulting water movement. The dendritic hydrate holds the water that was initially present and draws water towards itself due to capillarity. As the hydrate recrystallizes into more compact forms, the heightened capillary suction around the reformed crystals is reduced and water redistributes away from the early hydrate growth area. The same effect is seen in the hydrate growth patterns in Figure 4. As hydrate reconfigures and continues to form across the core, a density increase can be seen everywhere (plot for 1 day in Figure 7).

The observations of Servio and Englezos [22] regarding hydrate crystal reconfiguration may help explain why this dispersive nature is not seen in the second hydrate formation in SP2. In Figure 6b, hydrate forms in concentrated masses that do not disperse as formation matures. Servio and Englezos [22] show that, when repeating hydrate formation in droplets of water, dendritic crystals do not form during the second hydrate nucleation phase if the time between decomposition and reformation is short (< 24 hrs). It is possible that the time period between hydrate formations in SP2 was short enough in this case (< 16 hrs) to allow the water to retain a memory of the hydrate formation.

4.3.2. Long-Term Density Redistribution. The long-term tests conducted with the Mount Elbert Core sample, ME2.1 and ME2.2, show density redistribution over several weeks. In Test ME2.1, density was redistributed over the scale of several centimeters, with a large increase in density occurring near the interface between the two regions in the sample, primarily on the higher porosity and larger grain size side. This redistribution is particularly apparent with the changing peak in density between 50 mm and 70 mm in Figure 7. In Test ME2.2, rings of adjacent high and low density can be seen to form in areas of hydrate formation over a period of 28 days (Figure 8(a)). These changes can be attributed to two processes: (1) hydrate dissociation in one location and reformation in another; (2) water migration due to capillary pressure gradients caused by the hydrate formation and configuration changes.

Hydrate dissociation and reformation in equal amounts could occur if either water or gas was available in a limiting quantity. Since gas was present in excess (macroscopically), water can be considered as the limiting reagent. Under equilibrium conditions, some hydrate is dissociating while forming in equal amounts in other areas. Over long timescales, more hydrate would dissociate in less energetically favorable locations and more would form in more favorable locations

(much like ice in a non-frost-free freezer sublimates from the ice cube tray and precipitates on the freezer wall).

The second process, water migration caused by hydrate formation and configuration changes, could also be responsible for the density changes observed. Calculations of initial water content and gas uptake during hydrate formation indicate only a 70% conversion of total water to hydrate in Tests ME2.1 and ME2.2. The remaining water could be considered to be bound to grain surfaces and unavailable for hydrate formation due to its low chemical potential [40, 41], or some water may be completely occluded from the methane gas by hydrate. Water bound to surfaces is still mobile and can move in response to capillary pressure changes in the sediment as long as the phases are interconnected at grain contacts [42]. Because the sample was heterogeneous on many scales, capillary pressure would result in different water saturations throughout the core under prehydrate equilibrium conditions. Hydrate formation changed these equilibrium conditions and resulted in water migration. Because of the randomness of the resulting hydrate configuration, the hydrate is not likely to be in its lowest energy equilibrium configuration and will continue to reduce its surface area to minimize energy. These changes in the hydrate configuration impact the capillary suction of the sediment, resulting in further water migration.

Over the first 57 days in Test ME2.1 and 9–28 days in Test ME2.2, the pressure and temperature measurements inside the sample showed no anomalous decreases or spikes, respectively, indicating that neither of the processes described above caused additional hydrate formation in the core. Note that slight thermal gradients occurred in the sample from daily temperature changes in the laboratory impacting the temperature-controlled bath, tubing, and jacket. In addition, slight pressure fluctuations occurred from room temperature changes affecting the external gas bottle, causing the pressure to increase when the room temperature increased. In spite of these oscillations in pressure and temperature, the sample was maintained well within the stability zone for the test duration.

Density redistribution from the above processes can be seen in Test ME2.1 (Figure 7). The peak in hydrate content localized between 50 and 70 mm after 1 day in Test ME2.1 (Figure 7) would have caused a capillary pressure gradient to have developed between Parts A and B. Water slowly moved toward that location in response to this gradient resulting in density increases in the region between 50 and 70 mm. The overall density in Part A increased whereas the overall density of Part B decreased. Part A therefore had a larger hydrate content than Part B following initial hydrate formation (1 day in Figure 7). This higher hydrate content caused Part A to have a larger capillary suction than that of Part B after 1 day, and water was drawn to Part A over the next 57 days as a result.

Density changes seen in the first 28 days of Test ME2.2 could also be caused by the movement of free water due to capillary pressure gradients. A number of hydrate patches formed predominantly in Part A of the core during Test ME2.2. Within these masses, slight variations in hydrate content would draw water towards certain areas, increasing

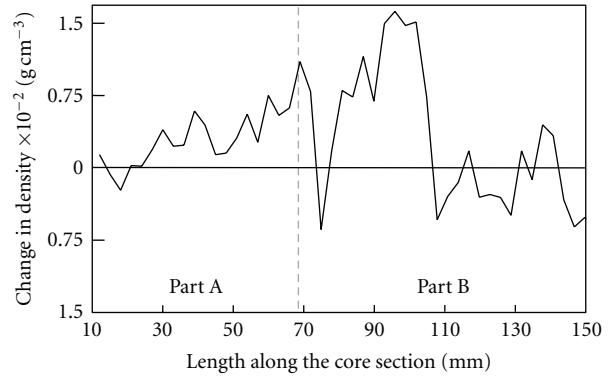


FIGURE 11: Density change along the length of the core between day 28 and day 35 in Test ME2.2. New hydrate formation was indicated by a temperature spike on day 33 of the test.

the density locally. In adjacent areas, the density would decrease where water was depleted. These regions can be seen as ring structures in Figure 8(a).

4.3.3. Additional Hydrate Formation in ME2.2. A hydrate formation event occurred on the 33rd day of Test ME2.2, resulting in a drop in pressure (0.07 MPa) and spike in temperature (0.9°C). The temperature spike was observed in Part A of the core 10 minutes before the Part B side, indicating that the location of hydrate formation was closer to the A side thermocouple. CT scans show that density increased in both parts, with the largest increase occurring between 80 and 110 mm (Part B, see Figure 11). The CT data also shows the disappearance of the rings of density variation (Figure 8(b)). The density equilibration over the region between 10 and 16 mm along line I-I' indicates that the redistribution in this region was most likely from moisture movement. If hydrate had reconfigured in this ring, the density would not have decreased (for a hydrate formation event) at Point X in Figure 8(b).

The most likely explanation for additional hydrate forming in Test ME2.2 after 33 days in the stability zone is that water that had been isolated from the methane gas in the pore space during initial hydrate formation became exposed. Instances of exposure of isolated water have been indicated in previous hydrate formation tests [39, 43], where initial hydrate formation isolates gas and water from each other, ceasing hydrate formation until there is a “punch-through” and water and methane components come into contact once more. Kneafsey et al. [39] observed punch-through over 24 hours during the early stages of hydrate formation, and Linga et al. [43] saw several temperature spikes over a period of 75 hours during hydrate formation in a sand pack, indicating a new hydrate formation event. This punch-through phenomena has not been observed over longer time periods.

A punch-through occurrence during Test ME2.2 would be a localized event. However, the disappearance of the ring structures and redistribution of density across the core occur sample wide. There are a number of possibilities for this

global redistribution of density. We assume that the change in density seen in Figure 11 is due to water movement, in addition to new hydrate formation. With this in mind, three hypotheses can be made with regard to the cause of the water movement during this time: (1) expansion of trapped gas due to pressure decrease, (2) gas coming out of solution due to temperature changes during hydrate formation, and (3) local redistribution of moisture due to capillary pressure changes because of the presence of new hydrate formation.

First, water could have been redistributed by the expansion of trapped gas inside hydrate masses. This would account for a reduction in density in the rings (as seen in Figure 8) in addition to the increase in density caused by hydrate formation. This hypothesis assumes, however, that there was trapped gas in each of the ring regions.

The second hypothesis accounts for the global change in density observed across the core by considering the change in temperature that resulted from the new hydrate formation. If liquid water was accumulating in regions of higher hydrate saturation due to capillary pressure gradients, the rings would have higher unconverted water saturations than the adjacent areas. The 0.9°C increase in temperature caused by hydrate formation (temperature in the sample was 0.9°C above bath temperature for 60 minutes) may have caused more methane to dissolve into solution in the residual water in the rings, as methane solubility increases with temperature when in the presence of hydrate [44–46]. Once hydrate formation was over and the temperature returned to the previous conditions (3 hours after initial temperature increase), the dissolved methane exsolved from solution forming bubbles and pushing water out of the higher density regions, causing a drop in density in those regions. This density change is consistent with the disappearance of the peak at Point X in Figure 8(b). Formation of bubbles in such small pore spaces under these conditions may not be possible however.

The third hypothesis assumes that the new hydrate formation that occurred on day 33 of the test altered the capillary pressures in the core and caused moisture redistribution as a result. New hydrate formation in certain pores would increase capillary suction by reducing pore size locally. The increased capillary suction in these areas would draw residual water away from previous accumulations (rings) and redistribute density in the core. Interpretation of the results discussed in previous sections agrees with this hypothesis; however it would occur locally to where hydrate formed, and density redistribution was seen globally in each ring structure not just in isolated regions.

It is possible that a combination of processes is responsible for the density changes seen throughout the core between days 28 and 35 of test ME2.2. The global nature of the redistribution indicates that a response to the temperature and/or pressure changes during new hydrate formation may be responsible; however, the results from tests ME1.1, 1.2, and 2.1 suggest that the capillary pressure alterations caused by additional hydrate presence should not be discounted.

Between 35 and 41 days in Test ME2.2, the ring structures began to appear once again in the hydrate masses. The higher

local capillary suction that caused the rings to occur between days 9 and 28 would not have changed significantly during the hydrate formation event at 33 days. Even if new hydrate formed elsewhere, the larger accumulations of hydrate in the masses in Part A would still impart capillary pressure gradients that would draw the water into ring-like structures again. In addition, more hydrate could form around the new gas bubbles, increasing capillary suction further and drawing water into those regions once again.

This study has a number of implications regarding forming hydrate in the laboratory, as well as our understanding of natural hydrate deposits. Previous assumptions that methane hydrate is an immobile mass in porous media must be reconsidered. Short-term redistribution of methane hydrate as it grows in a sediment must be accounted for by those making physical measurements because the changing morphology will impact physical characteristics until complete hydrate formation has been achieved. In addition, long-term observation of hydrate-bearing sediments has shown that the capillary suction differences imposed in a sediment due to hydrate formation can cause moisture and/or hydrate to redistribute weeks after initial hydrate formation has been completed.

5. Conclusions

Methane hydrate was repeatedly formed and dissociated in a natural sediment core from the Mount Elbert Stratigraphic Test Well, as well as in laboratory sand packs, to investigate hydrate redistribution in sediments over time and the growth patterns of hydrate when made repeatedly in the same material. CT scanning was employed in both sets of experiments to directly observe hydrate structure within the cores.

Results from repeated hydrate formation experiments showed that hydrate formed randomly across the cores indicating that numerous factors affect hydrate formation. Hydrate nucleation is a random process, with salinity, saturation of the pore water, grain size distribution, and mineralogy each altering the probability of nucleation under the low driving force formation conditions. In the samples with no pore water salinity and uniform grain-size, water saturation variation was the dominant control on the location of reformed hydrate, with hydrate forming preferentially in areas of lower water saturation adjacent to regions of higher water saturation. In the natural sample with varying pore water salinity and grain size distribution, no correlation between previous hydrate formation and water saturation, salinity or mineralogy changes could be found to affect the location of hydrate formation in the core. The random nature of hydrate formation dominates nucleation location in this case. The memory effect did not control the location of nucleation events in reforming hydrate in these samples in spite of reducing the time needed for hydrate to begin forming.

Density redistribution was observed in both short- and long-term tests. Over the time period of hydrate formation (hours), density variations occurred whereby hydrate masses went from being concentrated to disperse. This change is

attributed to early rapid hydrate formation in dendritic, high surface energy morphologies, then recrystallizing as hydrate formation progressed into more energy-efficient crystal configurations. Over the long-term tests, density redistributions were observed over periods of up to 60 days, which we attribute to mobile free water in the samples being drawn to areas of high capillary suction causing areas of higher density. We believe this moisture redistribution also caused renewed hydrate formation in one test by exposing previously trapped water so that it became available for more hydrate formation.

The results from the tests described in this paper suggest that in natural hydrate-bearing deposits, hydrate and residual moisture may not be stagnant phases and are likely to redistribute in response to stimuli. These stimuli include the thermal gradient changes that could occur from wells or pipelines carrying fluid at a different temperature than that of the ambient conditions.

Acknowledgments

This work was supported by the Assistant Secretary for Fossil Energy, Office of Oil and Natural Gas, Gas Hydrate Program, through the National Energy Technology Laboratory of the US Department of Energy under Contract no. DE-AC02-05CH11231. The authors would also like to thank Kelly Rose and Kyle Littlefield of NETL for providing the grain size distributions and mineralogy of the Mount Elbert core sample.

References

- [1] E. D. Sloan and C. A. Koh, *Clathrate Hydrates of Natural Gases*, CRC Press, New York, NY, USA, 3rd edition, 2008.
- [2] W. F. Waite, J. C. Santamarina, D. D. Cortes et al., "Physical properties of hydrate-bearing sediments," *Reviews of Geophysics*, vol. 74, no. 4, p. RG4003, 2009.
- [3] K. Kvenvolden and T. McDonald, "Gas hydrates of the Middle America Trench, deep sea drilling project Leg 84," in *Initial Reports of the Deep Sea Drilling Project*, R. Von-Huene and J. Aubouin, Eds., pp. 664–682, U.S. Government Printing Office, Washington, DC, USA, 1985.
- [4] P. G. Brewer, F. M. Orr, G. Friederich et al., "Deep-ocean field test of methane hydrate formation from a remotely operated vehicle," *Geology*, vol. 25, no. 5, pp. 407–410, 1997.
- [5] T. Collett, M. Riedel, and J. Cochran, "Indian national gas hydrate program expedition 01 initial reports," Tech. Rep., Indian Directorate General of Hydrocarbons, 2008.
- [6] A. M. Trehu, F. R. Rack, and M. Chapman, "Drilling gas hydrates on hydrate ridge, cascadia continental margin," in *Proceedings of the Ocean Drilling Program Scientific Results Leg 204*, Ocean Drilling Program, College Station, Tex, USA, 2006.
- [7] G. K. Westbrook et al., "Proceedings ocean drilling program, initial reports," Ocean Drilling Program, 146, 1994.
- [8] L. M. Kraemer, R. M. Owen, and G. R. Dickens, "Lithology of the upper gas hydrate zone, blake outer ridge: a link between diatoms, porosity and gas hydrate," in *Proceedings of the Ocean Drilling Program Results*, C. Paull, R. Matsumoto, and P. Wallace, Eds., pp. 229–236, Ocean Drilling Program, 2000.
- [9] M. Riedel, T. S. Collett, M. J. Malone, and The Expedition 311 Scientists, "Cascadia margin gas hydrates," in *Proceedings of the Integrated Ocean Drilling Program Expedition Reports*, Integrated Ocean Drilling Program Management International, 2006.
- [10] S. R. Dallimore, T. Uchida, and T. Collett, "Results from Japex/Jnoc/Gsc mallik 2l-38 gas hydrate research well, mackenzie delta, northwest Territories, Canada," *Geological Survey of Canada Bulletin*, no. 544, 1999.
- [11] W. F. Waite, W. J. Winters, and D. H. Mason, "Methane hydrate formation in partially water-saturated Ottawa sand," *American Mineralogist*, vol. 89, no. 8-9, pp. 1202–1207, 2004.
- [12] W. J. Winters, I. A. Pecher, W. F. Waite, and D. H. Mason, "Physical properties and rock physics models of sediment containing natural and laboratory-formed methane gas hydrate," *American Mineralogist*, vol. 89, no. 8-9, pp. 1221–1227, 2004.
- [13] M. Holland, P. Schultheiss, J. Roberts, and M. D. Geotek, "Observed gas hydrate morphologies in marine sediments," in *Proceedings of the 6th International Conference on Gas Hydrates*, Vancouver, Canada, 2008.
- [14] B. Tohidi, R. Anderson, M. B. Clennell, R. W. Burgass, and A. B. Biderkab, "Visual observation of gas-hydrate formation and dissociation in synthetic porous media by means of glass micromodels," *Geology*, vol. 29, no. 9, pp. 867–870, 2001.
- [15] D. Katsuki, R. Ohmura, T. Ebinuma, and H. Narita, "Formation, growth and ageing of clathrate hydrate crystals in a porous medium," *Philosophical Magazine*, vol. 86, no. 12, pp. 1753–1761, 2006.
- [16] D. Katsuki, R. Ohmura, T. Ebinuma, and H. Narita, "Methane hydrate crystal growth in a porous medium filled with methane-saturated liquid water," *Philosophical Magazine*, vol. 87, no. 7, pp. 1057–1069, 2007.
- [17] P. Buchanan, A. K. Soper, H. Thompson et al., "Search for memory effects in methane hydrate: structure of water before hydrate formation and after hydrate decomposition," *The Journal of Chemical Physics*, vol. 123, no. 16, p. 164507, 2005.
- [18] J. D. Lee, R. Susilo, and P. Englezos, "Kinetics of structure H gas hydrate," *Energy and Fuels*, vol. 19, no. 3, pp. 1008–1015, 2005.
- [19] R. Ohmura, M. Ogawa, K. Yasuoka, and Y. H. Mori, "Statistical study of clathrate-hydrate nucleation in a water/hydrochlorofluorocarbon system: search for the nature of the 'memory effect,'" *Journal of Physical Chemistry B*, vol. 107, no. 22, pp. 5289–5293, 2003.
- [20] P. M. Rodger, "Methane hydrate: melting and memory," *Annals of the New York Academy of Sciences*, vol. 912, pp. 474–482, 2000.
- [21] J. P. Schroeter, R. Kobayashi, and M. A. Hildebrand, "Hydrate decomposition conditions in the system H₂S-methane-propane," *Industrial & Engineering Chemistry Fundamentals*, vol. 22, no. 4, pp. 361–364, 1983.
- [22] P. Servio and P. Englezos, "Morphology of methane and carbon dioxide hydrates formed from water droplets," *AIChE Journal*, vol. 49, no. 1, pp. 269–276, 2003.
- [23] T. Uchida, T. Ebinuma, and H. Narita, "Observations of CO₂-hydrate decomposition and reformation processes," *Journal of Crystal Growth*, vol. 217, no. 1, pp. 189–200, 2000.
- [24] T. J. Kneafsey, L. Hailong, W. William et al., "Examination of core samples from the mount Elbert gas hydrate stratigraphic test well, Alaska North Slope: effects of retrieval and preservation," *Marine and Petroleum Geology*, vol. 28, no. 2, pp. 381–393, 2011.
- [25] R. Boswell, K. Rose, T. S. Collett et al., "Geologic controls on gas hydrate occurrence in the Mount Elbert prospect:

- Milne Point Unit, Alaska North Slope," *Marine and Petroleum Geology*, vol. 28, no. 2, pp. 589–607, 2010.
- [26] T. S. Collett, M. W. Lee, W. F. Agena et al., "Permafrost associated natural gas hydrate occurrences on the Alaska North Slope," *Marine and Petroleum Geology*, vol. 28, no. 2, pp. 279–294, 2009.
- [27] K. Rose, R. Boswell, and T. Collett, "BPXA-DOE-USGS Mount Elbert gas hydrate stratigraphic test well: coring operations, core sedimentology and lithostratigraphy," *Marine and Petroleum Geology*, vol. 28, no. 2, pp. 311–331, 2010.
- [28] T. J. Kneafsey and G. J. Moridis, "Methane hydrate dissociation by depressurization in a mount Elbert Sandstone sample: experimental observations and numerical modeling," in *Proceedings of the Arctic Technology Conference*, Houston, Tex, USA, 2011.
- [29] T. Uchida, S. Takeya, E. M. Chuvilin et al., "Decomposition of methane hydrates in sand, sandstone, clays and glass beads," *Journal of Geophysical Research: B*, vol. 109, no. 5, pp. B05206–12, 2004.
- [30] Y. Seol and T. J. Kneafsey, "Methane hydrate induced permeability modification for multiphase flow in unsaturated porous media," *Journal of Geophysical Research*, vol. 116, no. B8, Article ID B08102, 15 pages, 2011.
- [31] G. C. Cho, J. Dodds, and J. C. Santamarina, "Particle shape effects on packing density, stiffness, and strength: natural and crushed sands," *Journal of Geotechnical and Geoenvironmental Engineering*, vol. 132, no. 5, pp. 591–602, 2006.
- [32] J. S. Parent and P. R. Bishnoi, "Investigations into the nucleation behaviour of methane gas hydrates," *Chemical Engineering Communications*, vol. 144, pp. 51–64, 1996.
- [33] J. Israelachvili, *Intermolecular and Surface Forces*, Academic Press, New York, NY, USA, 2nd edition, 1992.
- [34] D. Grasso, K. Subramaniam, M. Butkus, K. Strevett, and J. Bergendahl, "A review of non-DLVO interactions in environmental colloidal systems," *Reviews in Environmental Science and Biotechnology*, vol. 1, no. 1, pp. 17–38, 2002.
- [35] J. C. Stevens, B. A. Baldwin, A. Graue, G. Erslund, J. Husebo, and J. J. Howard, "Measurements of hydrate formation in sandstone," *Petrophysics*, vol. 49, no. 1, pp. 67–73, 2008.
- [36] S. A. Bagherzadeh, I. L. Moudrakovski, J. A. Ripmeester, and P. Englezos, "Magnetic resonance imaging of gas hydrate formation in a bed of silica sand particles," *Energy and Fuels*, vol. 25, no. 7, pp. 3083–3092, 2011.
- [37] M. E. Torres, T. Collett, K. Rose, J. C. Sample, W. Agena, and E. Rosenbaum, "Pore fluid geochemistry from the Mount Elbert gas hydrate stratigraphic test well, Alaska North Slope," *Marine and Petroleum Geology*, vol. 28, no. 2, pp. 332–342, 2009.
- [38] A. Gupta, T. J. Kneafsey, G. J. Moridis, Y. Seol, M. B. Kowalsky, and E. D. Sloan, "Composite thermal conductivity in a large heterogeneous porous methane hydrate sample," *Journal of Physical Chemistry: B*, vol. 110, no. 33, pp. 16384–16392, 2006.
- [39] T. J. Kneafsey, L. Tomutsa, G. J. Moridis et al., "Methane hydrate formation and dissociation in a partially saturated core-scale sand sample," *Journal of Petroleum Science and Engineering*, vol. 56, no. 1–3, pp. 108–126, 2007.
- [40] M. B. Clennell, M. Hovland, J. S. Booth, P. Henry, and W. J. Winters, "Formation of natural gas hydrates in marine sediments 1. Conceptual model of gas hydrate growth conditioned by host sediment properties," *Journal of Geophysical Research: B*, vol. 104, no. 10, pp. 22985–23003, 1999.
- [41] T. R. Carlisle and G. W. Hodgson, "The formation of natural-gas hydrates in sedimentary rock," *Chemical Geology*, vol. 49, no. 1–3, pp. 371–383, 1985.
- [42] P. Hoekstra and R. D. Miller, "On the mobility of water molecules in the transition layer between ice and a solid surface," *Journal of Colloid And Interface Science*, vol. 25, no. 2, pp. 166–173, 1967.
- [43] P. Linga, C. Haligva, S. C. Nam, J. A. Ripmeester, and P. Englezos, "Gas hydrate formation in a variable volume bed of silica sand particles," *Energy and Fuels*, vol. 23, no. 11, pp. 5496–5507, 2009.
- [44] Y. P. Handa, "Effect of hydrostatic pressure and salinity on the stability of gas hydrates," *Journal of Physical Chemistry*, vol. 94, no. 6, pp. 2652–2657, 1990.
- [45] P. Servio and P. Englezos, "Measurement of dissolved methane in water in equilibrium with its hydrate," *Journal of Chemical and Engineering Data*, vol. 47, no. 1, pp. 87–90, 2002.
- [46] Y. S. Kim, B. D. Lim, J. E. Lee, and C. S. Lee, "Solubilities of carbon dioxide, methane, and ethane in sodium chloride solution containing gas hydrate," *Journal of Chemical and Engineering Data*, vol. 53, no. 6, pp. 1351–1354, 2008.

Research Article

Gas Hydrates Accumulations on the South Shetland Continental Margin: New Detection Possibilities

V. D. Solovyov,¹ V. G. Bakhmutov,² I. N. Korchagin,³ S. P. Levashov,⁴
N. A. Yakymchuk,⁴ and D. N. Bozhezha⁴

¹ Department of Seismometry and Physical Properties of the Earth, Institute of Geophysics of National Academy of Science of Ukraine, Palladin Avenue 32, 03680 Kyiv, Ukraine

² Department of Geomagnetism, Institute of Geophysics of National Academy of Science of Ukraine, Palladin Avenue 32, 03680 Kyiv, Ukraine

³ Department of Geothermy and Modern Geodynamics, Institute of Geophysics of National Academy of Science of Ukraine, Palladin Avenue 32, 03680 Kyiv, Ukraine

⁴ Institute of the Applied Problems of Ecology, Geophysics and Geochemistry, Laborator Street 1, 03133 Kyiv, Ukraine

Correspondence should be addressed to V. D. Solovyov, valera@igph.kiev.ua

Received 19 April 2011; Revised 26 July 2011; Accepted 27 July 2011

Academic Editor: Umberta Tinivella

Copyright © 2011 V. D. Solovyov et al. This is an open access article distributed under the Creative Commons Attribution License, which permits unrestricted use, distribution, and reproduction in any medium, provided the original work is properly cited.

The results of investigations in 2006–2010 for hydrocarbon and gas hydrates on the Antarctic Peninsula continental margin are given. In 2004 and 2006, the marine geoelectric researches by methods of forming a short-pulsed electromagnetic field (FSPEF) and vertical electric-resonance sounding (VERS) had been conducted in this region. The “deposit” type anomaly was mapped by FSPEF survey, and anomalous polarized layers of “hydrocarbon deposit” type were chosen by VERS sounding within this anomaly on Antarctic margin in the region of UAS “Academician Vernadsky.” Anomalous zones of “gas hydrate deposit” type were detected on the South Shetland margin due to the special technology of satellite data processing and interpretation using. These results confirm the high gas hydrates potential of the West Antarctica region. Some practical results of the experimental approbation of these original technologies for the “direct” prospecting and exploration of hydrocarbon (HC) and gas hydrates accumulations in different oil-and-gas bearing basins of Russia and Gulf of Mexico are proposed. The integration of satellite data processing and materials of FSPEF-VERS methods enable improving their efficiency for different geological and geophysical problems solving.

1. Introduction

Previous studies have revealed the real possibilities of new mobile geophysical technologies using for hydrocarbon (HC) accumulations prospecting [1–6]. One of this technologies, method of forming a short-pulsed electromagnetic field (FSPEF) and vertical electric-resonance sounding (VERS), makes possible the efficient and accurate determination of a stratigraphic (geologic) model beneath a sounding site. The first publications about this technology as a whole had appeared in Russian (in 2001), in English—in 2003 [1, 2]. The basic physical principles that underlie the method of VERS probing described in English in the patent nos. 7227362, 7248052 (USA, 2007). On the basis of this patent in the United States was elaborated the power imaging (PI)

geophysical prospecting method to aid in the exploration for hydrocarbons. PI technology is used to confirm the thickness and depth of expected hydrocarbon zones and provides a means for the direct detection of hydrocarbons [7].

Express technology of “direct” prospecting of the HC accumulations by geoelectric methods (FSPEF-VERS) was developed by experiments on the known oil and gas fields within the largest gas and condensate fields of Ukraine and once again showed the working capacity and economic efficiency of the FSPEF-VERS technology [1–6]. The geoelectric researches on some oil and gas fields allow finding out new perspective sites and horizons and may be used for operative prospects estimation of the deep productive horizons. The FSPEF-VERS technology has passed approbation on more than 55 known oil and gas fields. The “deposit” type

anomalies were fixed by the FSPEF survey on all oil and gas fields. The anomalous polarized layers (APL) of “oil” and “gas” type were chosen by VERS soundings in cross-section within the mapped anomalies. The “deposit” type anomalies were mapped also by FSPEF method within 70 perspective structures and separate areas from the 97 examined.

The second used technology for mobile HC accumulation prospecting is based on the satellite special data processing and interpretation and on the selection and processing of the resonance frequencies of the electromagnetic field data for each type of hydrocarbons' compounds. New (nonclassical) methods of geophysical research focused on direct search for specific physical substances with a characteristic set of properties: oil, gas, gas hydrates, water, various minerals, and rocks. The first method of satellite data interpretation is connected with electromagnetic fields structure of definite substance studying [8, 9].

“Spatial-frequency electromagnetic fields structure of any substance is determined by the chemical composition and spatial structure of molecules or the crystal lattice of the substance. A large number of homogeneous matters will create a collective characteristic of the substance in the electromagnetic field radiation power which is proportional to the substance concentration in a given direction. We can assume that the linear-polarized wave with a given frequency response carries information about the structure of the substance and is not absorbed by the medium, and the wave intensity does not decrease with distance. The homogeneous substance at any depth would create a field as if the substance was on the surface. It turned out that the characteristic electromagnetic wave of a large quantity of oil and gas is fixed in a certain way in satellite images. In most cases the technology of the quantum-optical satellite imagery filtration allows to identify the boundaries of oil and gas projected fields anywhere in the world and to record the density of stocks distribution” [5]. There are also the method of the distance-controlled discovery of HC deposits [6] and InfoScan technology, which is based on processing of analog photo material [9]. Accuracy of object location detecting directly depends on the scale of the investigated photograph.

This original satellite data processing technology may be integrated also with the traditionally used methods of HC accumulations and gas hydrates prospecting as well as with nonclassical geophysical technologies.

2. Some Results of Proposed Technologies Practical Using

The first successful approbation of this technology was conducted on the known hydrocarbon fields and gas hydrates occurrences.

2.1. Continental Margin of Antarctica. First approbation of these special methods was realized for the area situated not far from the Ukrainian Antarctic station (UAS) “Academic Vernadsky” (Figure 1).

The HC-potential experience has shown that oil and gas deposits may be associated with large zones of tectonic

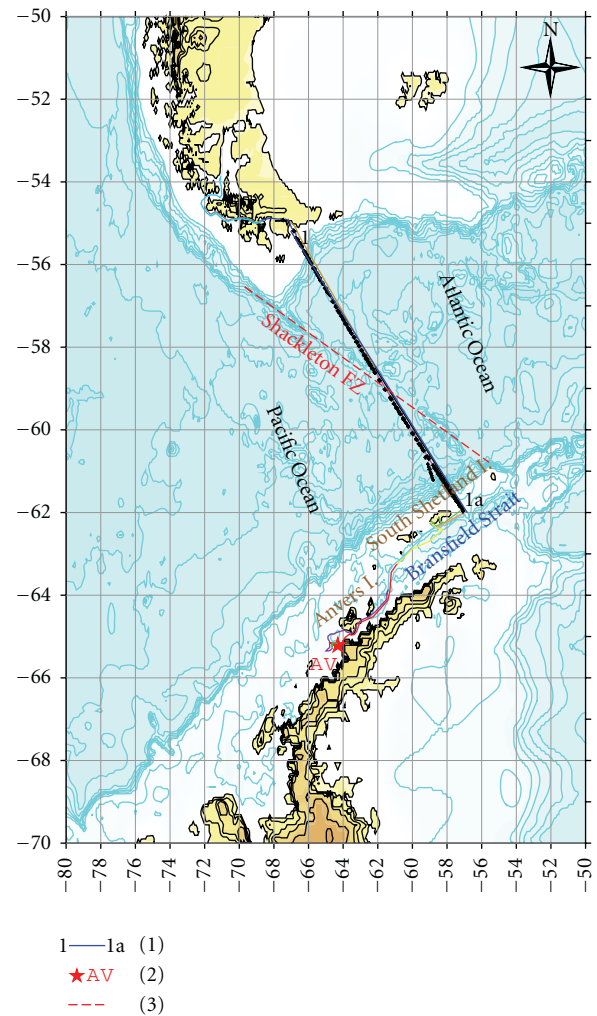


FIGURE 1: The scheme of the ship motion and location of the FSPEF-VERS-profiles in 11th UAE (2006). Legend: (1) sounding profile through Drake Passage; (2) UAS “Academician Vernadsky” (Galindez Island); (3) Shackleton fracture zone.

fractures and rift structures of the continental margin of Antarctica. There are necessary conditions to generate and for the inorganic synthesis of HC of different types. The HC formation may be connected with the presence of subglacial drainage network which helps the crustal fluids and gases to move in Antarctic continental shelf direction.

Marine researches with FSPEF-VERS technology were fulfilled during the seasonal works of the Ukrainian Antarctic expeditions (UAE) with the aim of studying the crustal structure of Drake Passage and Bransfield Strait down to depth of >30 km [4]. This method was also used for the hydrocarbon accumulations prospecting on the Antarctic Peninsula continental margin near Anvers Island. One “deposit” type anomaly (DTA) zone was mapped by VERS sounding in depth interval up to 3500 m (Figure 2).

We applied the special method of satellite data processing and used only reconnaissance character which was carried out on the investigated sites (Figure 3).

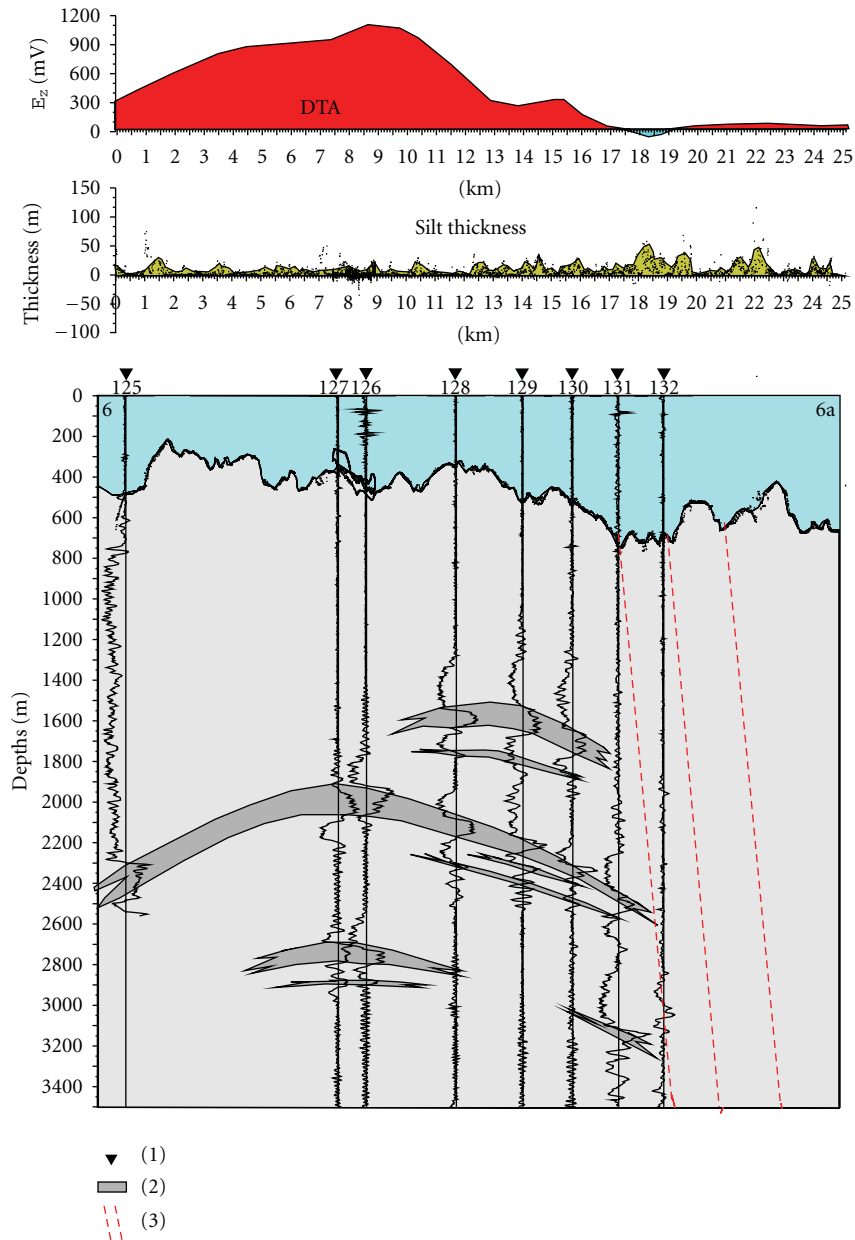


FIGURE 2: The VERS sounding data over geoelectric anomalous zone of the “hydrocarbon deposit” type in the Antarctic Peninsular region. (1) Sounding points (125–132); (2) anomalous polarized layers of “hydrocarbon deposit” type; (3) tectonic fracture zone.

It means that a number of small and possibly medium-sized objects (fields) could be omitted. However, during the larger-scale data processing they can be identified and mapped. The points of anomalous response values determination are shown on figure. The accuracy and detail of the anomalous objects mapping can be increased substantially when the concentration of points will be raised.

2.2. Experiments on Gas Hydrate and Oil Fields. Traditional energy sources deficiency arouses scientific and practical interest to nontraditional sources and the gas hydrates deposits. Gas hydrates are solid compounds of the gas molecules and water that exist under certain values of pressure and temperature.

The Messoyakh field in Russia was the first deposit with gas hydrate concentrations. It is located in the north-eastern part of Western Siberia and was discovered in 1967 [10, 11].

The deposits of natural gas and gas hydrates are installed there in dome trap of Cenomanian productive stratum (Dolgan formation) at 800–900 m depth. There are several hypotheses of Dolgan deposits structure. By one of them the gas hydrate deposits are located in the structure roof, and the gas reservoir is underlain by water at the structure base [10].

The satellite data processing for the Messoyakh gas hydrates deposits area (Figure 4) was carried out to verify the correctness of these parameters determined in order to find the anomalous zones of “gas hydrates deposit” type in the Antarctic region.

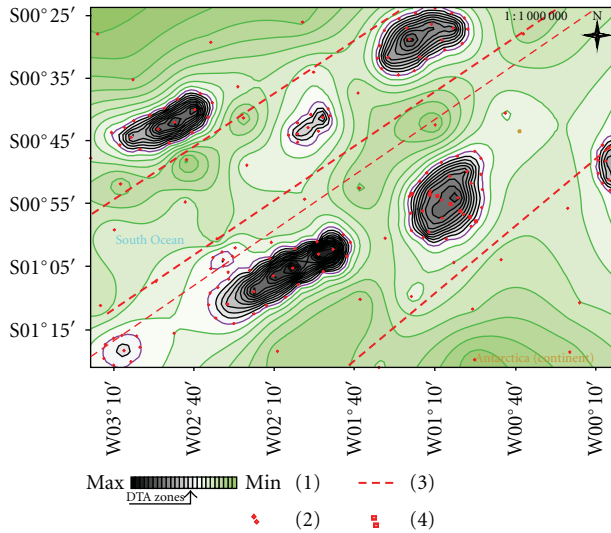


FIGURE 3: Map of anomalous zones of “oil deposit” type in the Antarctic region (relative coordinates, area of the “Academician Vernadsky”), allocated by the satellite data special processing and interpretation results. (1) The anomalous response intensity scale; (2) points of the anomalous response values; (3) predicted tectonic fractures; (4) points of “deposit” type anomalies registration by marine geoelectric methods FSPEF and VERS (2006).

The anomalous zones of “gas hydrates deposit” type were discovered and mapped only within two hydrocarbons deposits, and with the parameters of satellite data processing and interpretation, as in the Antarctic region. The anomalous zones of “gas hydrates deposit” and “gas deposit” types have been discovered and mapped with the satellite data processing in the southern part and anomalous zones of “gas deposit” and “oil deposit” types—in the northern part of the surveying area.

2.3. Pechora Sea Arctic Region of Russia. Six deposits are discovered on the Pechora Sea offshore: 4 oilfields (Prirazlomnoye, Varandey-More, Medynskoye-More 2, and Dolginskoye), North-Gulyaevskoe oil, gas, and gas-condensate field and Pomorskoye gas-condensate field. Oil pools are installed on the Medynskoye-More 2 field in the upper and lower Devonian and Silurian sediments. The area of Medynskaya-More 1 structure is located to south from Medynskoye-More 2 field (Figure 5).

The satellite data for this structure area were processed and interpreted. Large-scale anomalous zone of “hydrocarbon reservoir” type of high intensity was identified and mapped within the structure contours. The borehole, projected according to seismic and other geological and geophysical data, falls almost into the anomalous zone center. Nevertheless, the anomaly maximum is shifted slightly to the north-west of the project well point (Figure 6). Four small anomalous zones of low intensity and different scale were mapped to the east from anomalous zone over the Medynskaya-More 1 structure. The area of these anomalies location can be recommended for detailed study by other geophysical methods. Two anomalous zones of small area

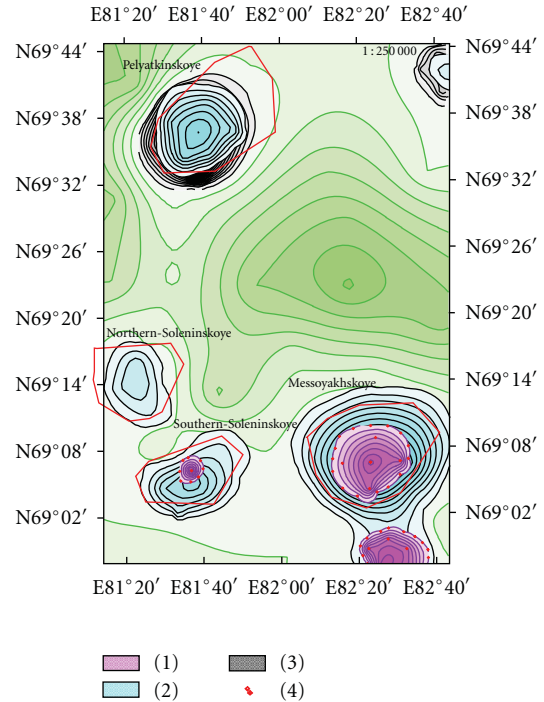


FIGURE 4: Map of hydrocarbon accumulations zones, produced on the satellite data processing results for the “Messoyakh” gas-hydrate deposit area (Western Siberia, Russia). (1) Zone of gas-hydrate deposits, (2) zone of gas deposits; (3) zone of oil deposits; (4) points of the anomalous responses registration from gas-hydrate deposits.

were identified also to the west of the Medynskaya-More 1 structure, and another—to the north. A large scaled anomalous zone of high intensity was fixed in the north-eastern part of the satellite data processing and interpretation area.

This anomaly is even more large-scale than anomalous zone over the Medynskaya-More 1 structure. This area deserves high priority when the further exploration was carried out in this region. It is possible to suggest the fracture zones presence within the investigated site on the satellite data processing results. The possible fractures positions are also shown (Figure 6).

The received results indicate that the special technology of satellite data processing and interpretation may be applied for hydrocarbon accumulations prospecting and exploration in the Arctic and Antarctic regions of Earth.

2.4. Gulf of Mexico. This technology was used for the hydrocarbon deposits detection and possible risk determination of oil production at one of the Gulf of Mexico (GOM) local areas [11].

The intensive anomaly of “oil deposit” type has been isolated and mapped by the results of satellite data processing in the area of emergency drilling platform in the Gulf of Mexico (Figures 7 and 8).

The relative values of reservoir pressure were determined within most of the anomalies also. The dependence of the values of the anomalous response from the reservoir pressure

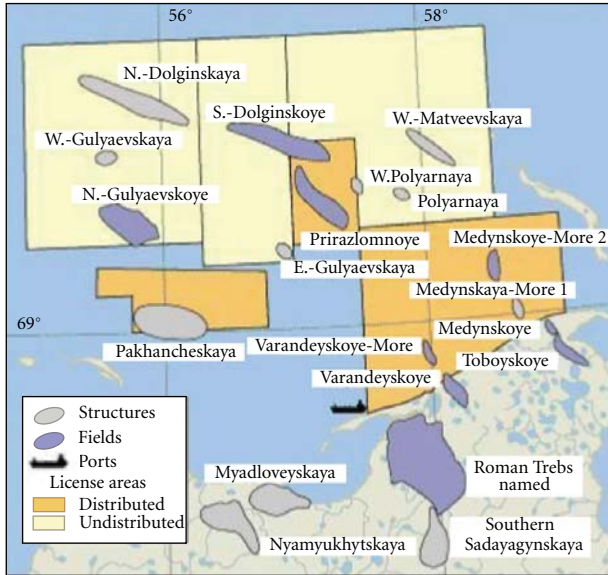


FIGURE 5: Sketch map of the structures and oilfields location in Pechora Sea, Arctic, Russia.

for gas has been installed by experimental measurements earlier. The scale of relative values of the pressure in the range from 0 to 6 has been formed by these data using. The relative value of reservoir pressure has been defined equal to 6; that is, the pressure in the wells is highest in comparison with those at other surveyed sites. In principle, this high values may be used to indicate the higher probability of commercial fluid inflow receiving. But too high expenses and risks that are related to gas hydrates production are reasons for terms transfer of these resources future mastering.

Satellite data from this region were also processed for the gas hydrates deposits detection and mapping (Figure 8). The same values of gas hydrates parameters, as in the Antarctic region and Messoyakh field, have been used satellite for data processing in this area. The results of satellite data processing showed that the “Deepwater Horizon,” an emergency drilling platform had been situated in the center of “oil deposit” type anomaly with high-intensity values of reservoir pressure and in the anomalous zone of “gas-hydrate deposits” type with relative high intensity values of the response too. Such combination of anomalous areas promotes technological risks during drilling works in this place to a great extent. There are also another “oil deposit” type anomaly in north-western part of district (Figure 7) with low layer pressure and anomaly of “gas-hydrate deposits” type with the higher intensity of anomalous response. Such combination of parameters specifies on relatively small potential of this deposit and promoted level of danger at his possible early development. These data also show the wide occurrences of the anomalous zones of “gas-hydrate deposits” type with relative high intensity values of the response.

On April 20, 2010 an explosion and fire racked the “Deepwater Horizon,” a drilling platform operating in the Gulf of Mexico, in Mississippi Canyon. It may be assumed that the explosion of giant bubble of methane was one of the reasons of the “Deepwater Horizon” platform destruction.

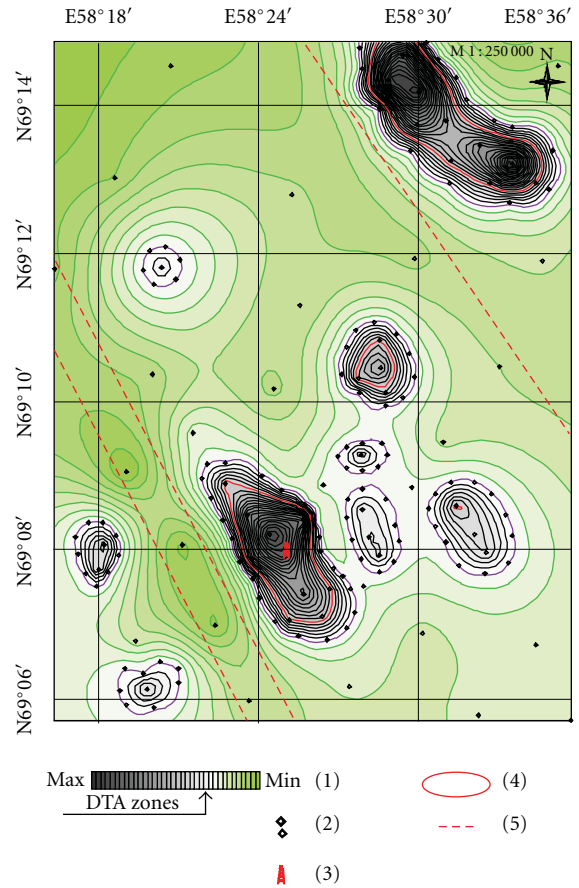


FIGURE 6: Sketch map of anomalous zones of “hydrocarbon deposit” type (DTA) in the “Medynskaya-More 1” structure region. (1) Scale of anomalous response intensity; (2) points of anomalous response determination; (3) location of projected well on the “Medynskaya-More 1” structure; (4) prognostic areas of oil-saturation maximum; (5) tectonic fracture zones.

The results of searching and mapping of hydrocarbon and gas hydrates accumulations in different regions show the necessity of this technology application especially on the early stages of researches when appears the possibility not only to detect the perspective on the different types of minerals areas but also to estimate possible risks during their future industrial development.

3. Gas Hydrate Reservoir on the South Shetland Continental Margin (SSCM) Finding

In some parts of the Antarctic Peninsula margin there are available all necessary thermobaric conditions for gas hydrates existence and their deposits formation that is proved by their distribution and concentration detection and mapping on South Shetland continental margin. The multichannel seismic data acquired on the South Shetland margin show that bottom simulating reflectors (BSR-s) are widespread at water depths ranging from 1000 to 4800 m, implying large volumes of gas hydrates (Figure 9) [10–12].

According to sights of many researchers, this area represents “two distinct and superimposed tectonic regimes:

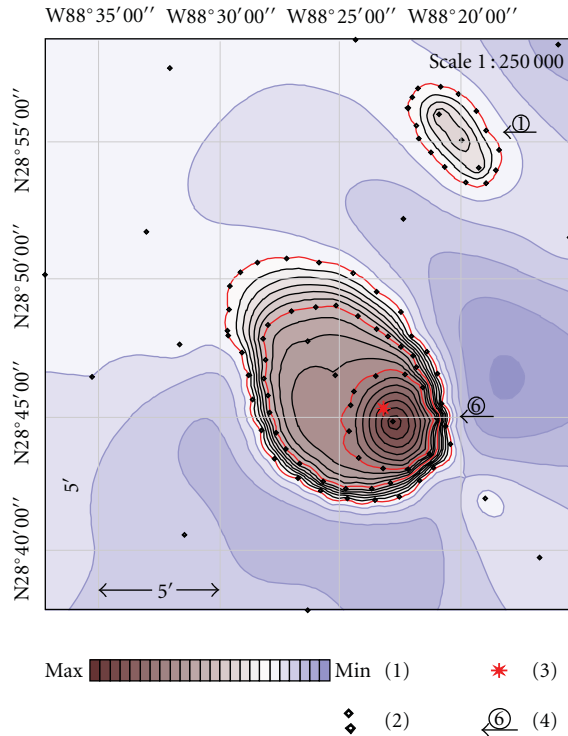


FIGURE 7: Map of the “oil deposit” type anomalies in the area of the “Deepwater Horizon” drilling platform in the Gulf of Mexico, based on the satellite data processing results. (1) Scale of the reservoir pressure relative values; (2) points of the anomalous response registration; (3) emergency platform location; (4) relative values of reservoir pressure in the anomalous zone.

an older regime is related to Mesozoic-Middle Cenozoic subduction-related tectonism of Gondwana margin; a younger one is associated with a mainly extensional tectonic phase, and related to the Oligocene development of the Western Scotia Sea” [11]. This part of continental margin is limited by two fracture zones, Shackleton (NE) and Hero (SW), the South-Shetland trench in a southeast and South Scotia Ridge in the East. The region of the triple junction between the Shackleton Fracture Zone, the South Shetland trench, and the South Scotia Ridge is an area where the BSR-zones are the strongest [12–14].

Assumptions of researchers about other processes of bottom structures tectonic development of this region are quite proved. Geodynamic features of this region may be defined also as complex interaction of different age’s continental and oceanic structures and are the result of active breaking which is connected with regional rifting processes [13, 15]. It is possible to consider that numerous deep tectonic fractures assist to formation of natural gas migration ways towards the surface, creating the necessary conditions for stable BSR-zones appearance.

Satellite data over the BSR zones extension area, identified by seismic studies [10–12], have been processed and interpreted. The various processing parameters were analyzed for revealing and mapping the anomalous zone of “gas hydrates deposit” type within the surveying area (Figure 10).

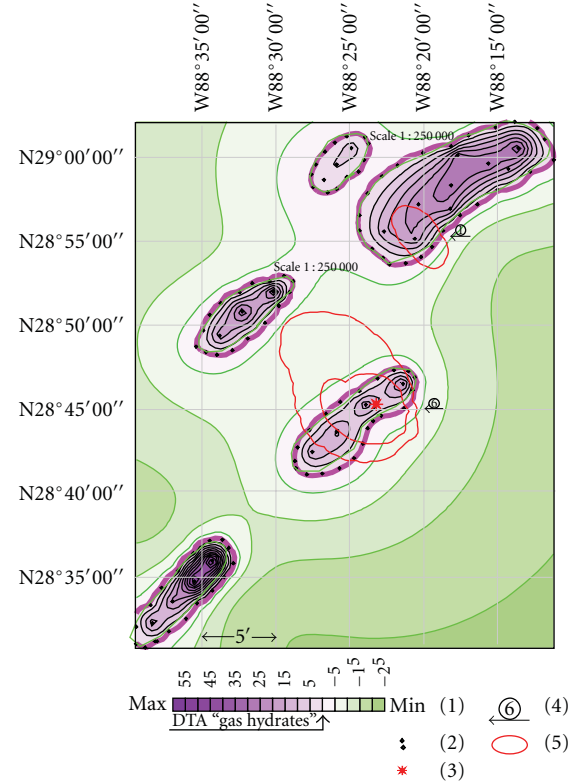


FIGURE 8: Map of anomalies of “gas-hydrate deposits” type in the area of the “Deepwater Horizon” drilling platform in the Gulf of Mexico. (1) Scale of intensity values of the anomalous response; (2) points of the anomalous response registration; (3) platform location; (4) relative values of the reservoir pressure in the anomalous zone; (5) contours of the anomalous zone of “oil pool” type, based on satellite data.

The contours of identified anomalous zones (Figure 10) are superimposed on the bottom topography map and the scheme of seismic profiles [12–14]. In general, the revealed and mapped anomalous zones of “gas hydrates deposit” type correlate satisfactory with BSR zones defined by seismic data.

The anomalous zones of “gas deposit” and “oil deposit” types were not detected within the surveyed sites. It was rather unexpected because the thickness of the free-gas zone was estimated on average to be about 50 m, with local increases of as much as 400 m but variable average concentration [13, 14].

Possibly, free gas between the BSR and the Base of Gas Reflector accumulates in amounts that are insufficient for detection by this satellite method.

4. Conclusions

The results of the FSPEF-VERS technology obtained during the Ukrainian Antarctic expeditions have confirmed high efficiency of the separate methods of technology for different geological-geophysical problems decision.

- (1) The “deposit” type anomaly was mapped by FSPEF survey in the Antarctic margin structure, and the

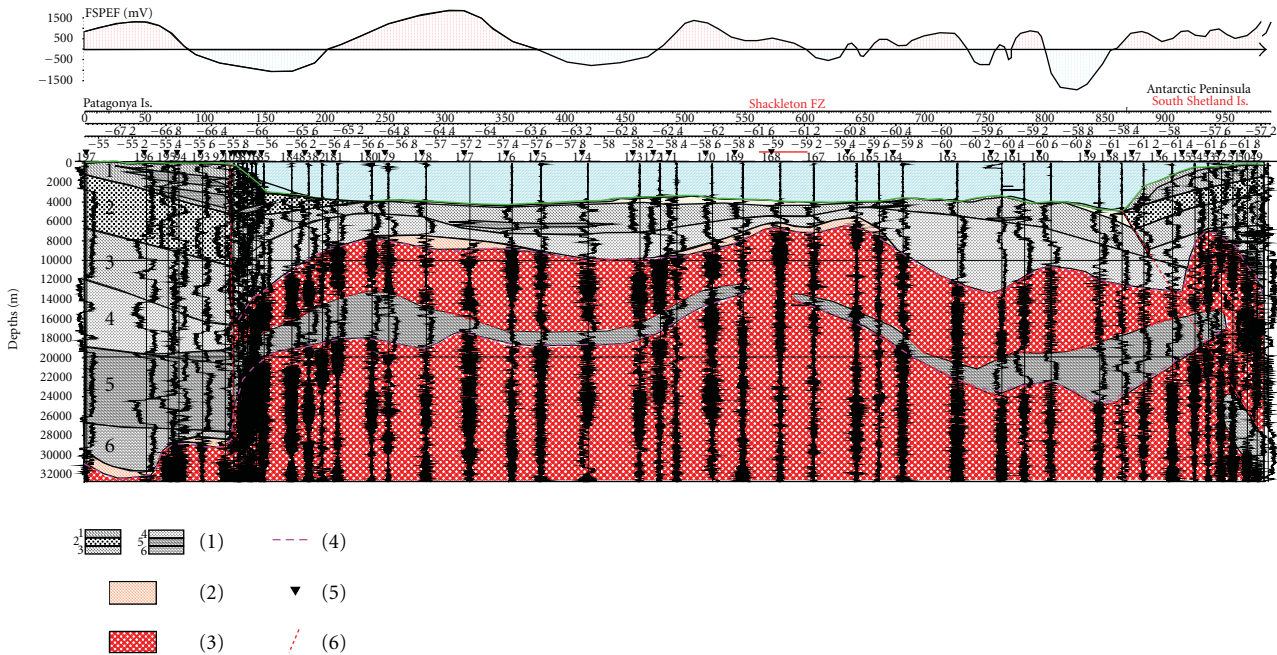


FIGURE 9: Interpreted geoelectrical cross-section of the crust and upper mantle along the profile through Drake Passage and the South Shetland Trench. Legend: (1) complex of volcanic and crystalline rocks; (2) rocks of crust-mantle transition layer; (3) upper mantle; (4) Moho boundary; (5) VERS points; (6) fracture zones.

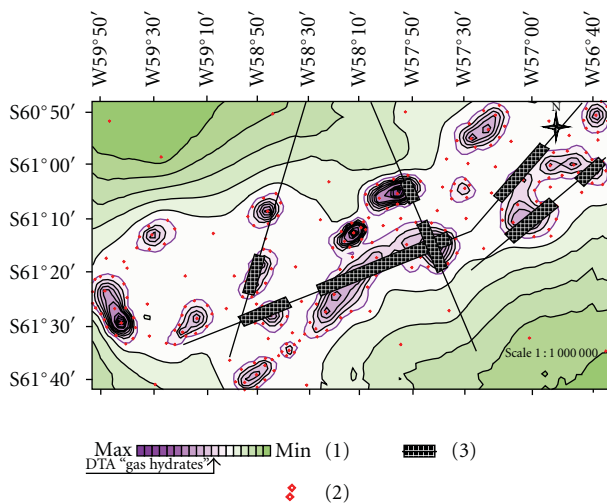


FIGURE 10: Map of the anomalous zones of “gas hydrates deposits” type, produced by the special satellite data processing results (Antarctic Peninsula region). (1) Anomalous responses intensity scale; (2) points of the anomalous response values; (3) BSR zones defined by seismic data.

anomalous polarized layers of “hydrocarbon deposit” type were chosen by VERS sounding within this anomaly. This indicates the possibility of the FSPEF-VERS technology using for hydrocarbon accumulation prospecting.

- (2) Investigations have demonstrated high efficiency of the VERS method using for studying of the Earth’s crust and upper mantle deep structure.

- (3) First approbation of satellite special data processing and interpretation original technology was conducted on the known hydrocarbon fields and gas hydrates occurrences. This technology may be integrated also with the traditionally used methods of HC accumulations and gas hydrates prospecting as well as with nonclassical geophysical technologies. Our practical experiments testify that integration of satellite data processing and materials of FSPEF-VERS methods enable improving their efficiency for different geological and geophysical problems solving. Obtained results confirm the high HC and gas hydrates potential of Antarctic Peninsula region.

References

- [1] S. P. Levashov, N. A. Yakymchuk, I. N. Korchagin, and K. M. Taskynbaev, “Geoelectric investigations in Kenbye oilfield in Western Kazakhstan,” in *Proceedings of the 65th EAGE Conference and Technical Exhibition*, vol. 2, p. 4, Stavanger, Norway, June 2003, Extended abstracts book, Poster Presentations, Absr. P154.
- [2] V. P. Bokovoy, S. P. Levashov, N. A. Yakymchuk, I. N. Korchagin, and J. N. Yakymchuk, “Mudslide area and moistening zones mapping with geophysical methods on the slope of the Dniپر river in Kyiv,” in *Proceedings of the 65th EAGE Conference and Technical Exhibition*, vol. 2, p. 4, Stavanger, Norway, June 2003, Extended abstracts book, Poster presentations, Absr. P208.
- [3] S. P. Levashov, N. A. Yakymchuk, I. N. Korchagin et al., “Electric- resonance sounding method and its application

- for the ecological, geological-geophysical and engineering-geological investigations,” in *Proceedings of the 66th EAGE Conference & Exhibition*, 2004, Extended Abstracts P035.
- [4] V. Bakhmutov, V. Solovyov, I. Korchagin et al., “Drake passage: crustal structure, tectonic evolution and new prognosis for local HC accumulations along the Antarctic Peninsula margin,” *Geophysical journal*, vol. 32, no. 4, pp. 12–15, 2010.
- [5] N. A. Yakymchuk, S. P. Levashov, and I. N. Korchagin, “Express-technology for direct searching and prospecting of hydrocarbon accumulation by geoelectric methods,” in *Proceedings of the International Petroleum Technology Conference*, p. 11, Kuala Lumpur, Malaysia, December 2008, Paper IPTC-12116-PP. CD-ROM.
- [6] S. P. Levashov, N. A. Yakymchuk, and I. N. Korchagin, “Drake passage and bransfield Strait—new geophysical data and modelling of the crustal structure,” in *Proceedings of Antarctica: A Keystone in a Changing World—Online Proceedings for the 10th International Symposium on Antarctic Earth Sciences (ISAES '07)*, A. K. Cooper, C. R. Raymond et al., Eds., 2007, USGS Open-File Report 2007-1047.
- [7] Direct Hydrocarbon Detection, <http://www.wavetechnology-group.com/>.
- [8] N. Kovalev, V. Goh, S Soldatova, and I. Lyamtseva, “Using of geogologographical complex “Search” for hydrocarbons detecting,” *Geoinformatika*, no. 3, pp. 83–87, 2009.
- [9] V. V. Rostovtsev, V. N. Rostovtsev, and B. B. Laynveler, “To great oil deposits of Russia,” *Geomatics*, no. 1, pp. 60–63, 2011 (Russian), <http://www.geomatica.ru/eng/>.
- [10] Y. F. Makogon, F. A. Trebin, A. A. Trofimuk, and V. P. Cherskii, “Detection of a pool of natural gas in a solid hydrate state,” *Doklady Akademii Nauk SSSR*, vol. 196, no. 1, pp. 197–200, 1971.
- [11] K. A. Kvenvolden and T. D. Lorenson, “The global occurrence of natural gas hydrate,” in *Natural Gas Hydrates: Occurrence, Distribution, and Detection*, C. K. Paull and W. P. Dillon, Eds., vol. 124 of *Geophysical Monograph*, pp. 3–18, American Geophysical Union, Washington, DC, USA, 2001.
- [12] Y. K. Jin, M. W. Lee, Y. Kim, S. H. Nam, and K. J. Kim, “Gas hydrate volume estimations on the South Shetland continental margin, Antarctic Peninsula,” *Antarctic Science*, vol. 15, no. 2, pp. 271–282, 2003.
- [13] E. Lodolo, A. Camerlenghi, G. Madrussani, U. Tinivella, and G. Rossi, “Assessment of gas hydrate and free gas distribution on the South Shetland margin (Antarctica) based on multichannel seismic reflection data,” *Geophysical Journal International*, vol. 148, no. 1, pp. 103–119, 2002.
- [14] U. Tinivella, F. Accaino, and A. Camerlenghi, “Gas hydrate and free gas distribution from inversion of seismic data on the South Shetland margin (Antarctica),” *Marine Geophysical Researches*, vol. 23, no. 2, pp. 109–123, 2002.
- [15] H. W. Schenke and G. B. Udintsev, “The central scotia sea-floor—is it an paleo-oceanic plate, an young rifted plate or an paleo-land Scotia?” *Ukrainian Antarctic Journal*, no. 8, pp. 36–45, 2009.

Research Article

Simulation of Methane Recovery from Gas Hydrates Combined with Storing Carbon Dioxide as Hydrates

Georg Janicki, Stefan Schlüter, Torsten Hennig, Hildegard Lyko, and Gorge Deerberg

Fraunhofer Institute for Environmental, Safety, and Energy Technology UMSICHT, Osterfelder Strasse 3, 46047 Oberhausen, Germany

Correspondence should be addressed to Georg Janicki, georg.janicki@umsicht.fraunhofer.de

Received 15 June 2011; Accepted 1 August 2011

Academic Editor: Michela Giustiniani

Copyright © 2011 Georg Janicki et al. This is an open access article distributed under the Creative Commons Attribution License, which permits unrestricted use, distribution, and reproduction in any medium, provided the original work is properly cited.

In the medium term, gas hydrate reservoirs in the subsea sediment are intended as deposits for carbon dioxide (CO₂) from fossil fuel consumption. This idea is supported by the thermodynamics of CO₂ and methane (CH₄) hydrates and the fact that CO₂ hydrates are more stable than CH₄ hydrates in a certain *P-T* range. The potential of producing methane by depressurization and/or by injecting CO₂ is numerically studied in the frame of the SUGAR project. Simulations are performed with the commercial code STARS from CMG and the newly developed code HyReS (hydrate reservoir simulator) especially designed for hydrate processing in the subsea sediment. HyReS is a nonisothermal multiphase Darcy flow model combined with thermodynamics and rate kinetics suitable for gas hydrate calculations. Two scenarios are considered: the depressurization of an area 1,000 m in diameter and a one/two-well scenario with CO₂ injection. Realistic rates for injection and production are estimated, and limitations of these processes are discussed.

1. Introduction

Gas hydrates are ice-like solid compounds of water and gas molecules (clathrates) which are stable at low temperature and elevated pressure [1]. The water molecules build out cages by hydrogen bonds in which gas molecules are embedded. Generally, gas hydrates can contain different guest molecules in different cages, depending on their sizes and the availability of guest molecules under given thermodynamic conditions, but methane is the prevalent gas in natural gas hydrates. The exploitation of natural gas hydrate deposits that are known in various permafrost regions and submarine sediments all over the world is in the focus of several research groups because the amount of methane to be recovered could overcome future energy shortages. The greenhouse gas CO₂ is able to build hydrates too, and these hydrates are thermodynamically more stable than methane hydrates. The possibility to destabilize methane hydrate by injecting CO₂ as pressurized gas or in liquid form was verified in several small-scale experiments carried out by different research groups (see [2–6]). Thus, the combination of both processes offers the opportunity to open up new energy resources as well as

to combat climate change by reducing CO₂ emissions. However, the technical realization of this combination of processes has to face various challenges. Besides the technical and economic efforts for drilling in submarine sediments or in deep layers in permafrost regions, these challenges concern the reaction kinetics and transport resistances within the sediments in which methane hydrates are embedded in natural deposits.

Thus, to find the best strategy for methane recovery from a specific deposit with or without CO₂ sequestration, a large variety of parameters describing the properties of the particular layer as well as the time- and location-dependent thermodynamic conditions have to be considered. Within the framework of the German SUGAR (Submarine GAs Hydrate Reservoirs) project, strategies to produce natural gas from marine methane hydrates and simultaneously store CO₂ as hydrates are explored. Before undertaking drilling tests, numerical simulations of the local processes are necessary and helpful. For this purpose, a new scientific simulation model called UMSICHT HyReS was developed to describe the methane production from submarine hydrate layers and the exchange of methane by carbon dioxide. In addition,

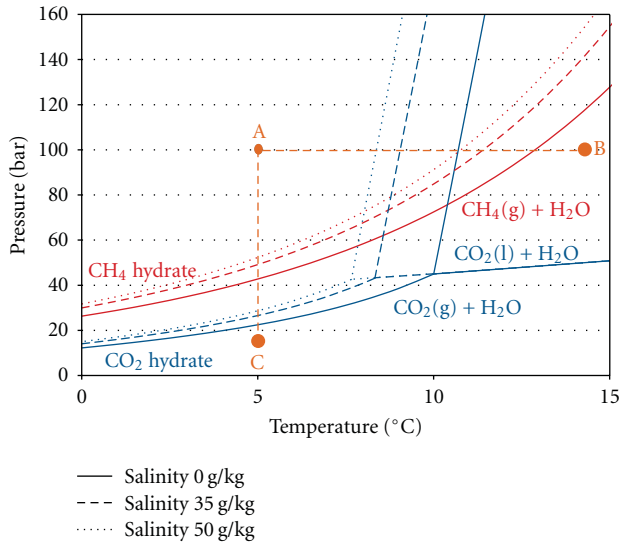


FIGURE 1: Equilibrium curves of methane hydrate and carbon dioxide hydrates for different salinities (stability curves calculated after Tishchenko et al. [7] and with NIST data [8]).

the commercially available simulation tool STARS (CMG Ltd., Canada) was used. In the following, the new simulation tool is described, and the results of the calculations based on particular reservoir parameters, reaction kinetics, and extraction techniques are outlined.

2. Principles of Methane Extraction with CO₂ Sequestration

2.1. Exploitation Strategies and Their Limitations. All strategies to destabilize methane hydrate are aimed to change the thermodynamic and/or chemical properties within the reservoir in order to overcome the preconditions for stability. The thermodynamic equilibrium curves for methane and carbon dioxide hydrates given in Figure 1 reveal that either thermal stimulation (A-B), depressurization (A-C), or a combination of both approaches may be the best choice to destabilize a hydrate and to recover the pure gas.

The variety of measures to supply heat into a hydrate layer for thermal destabilization ranges from injecting warm water or steam into a well over injecting fuel and oxygen to especially designed on-site combustion chambers up to electromagnetic heating of a particular region around a well. Recently, Schicks et al. [9] suggested the in situ catalytic oxidation of methane to supply the heat that is needed to decompose the hydrate.

Depressurization of a hydrate-bearing region is achieved by suction through one or more wells. According to the equilibrium curve (Figure 1), lowering the pressure will shift the equilibrium to lower temperatures. However, the release of methane gas from its hydrate consumes heat (e.g., Goel [10]) so that the reaction only continues until the temperature reaches the new equilibrium point. Su et al. [11] reported on depressurization experiments that were carried out in a high-pressure reactor in which methane hydrate

had been built within a layer of natural sand. It was shown that the gas production rate does not only depend on the driving force (expressed as the difference of actual and equilibrium pressure). Reaction kinetics, heat and mass transfer limitations, and multiphase flow effects are also important. In addition, the possible formation of ice that may hamper mass and heat transfer must be considered.

2.2. Classification of Hydrate Deposits. In recent years, the classification of natural gas hydrate deposits in three classes according to their geologic and reservoir conditions has become accepted. According to Moridis and Collet [12], class 1 deposits comprise a hydrate layer and an underlying two-phase fluid zone with free gas and formation water. They describe class 2 deposits as a hydrate layer with an underlying mobile water zone with no free gas, and single-hydrate layers without underlying mobile fluids are characterized as class 3 accumulations. Class 1 deposits are the most attractive deposits with respect to exploitation strategies because the bottom of such a layer that is in contact with mobile gas must be in or near thermodynamic equilibrium. Therefore, the energy needed to destabilize the hydrate is minimal compared to classes 2 and 3 in which the hydrate interval may be far within the stability zone. In addition, an underlying layer of mobile water and/or gas provides a better conductivity within the sediment and supplies additional heat. This expands the reaction area where hydrates decompose. Besides these three classes, a fourth class of deposits, that is to say disperse, low-saturated hydrate accumulations in oceanic sediments, was also investigated by Moridis and Sloan [13]. They evaluated an exploitation of such deposits as non-economic.

Structural properties of geological formations also comprise the conditions for the injection of CO₂ and the building up and stability of CO₂ hydrates. Uddin et al. [14] used the thermal reservoir simulator STARS to initially simulate the CO₂ hydrate formation in four simplified geological formations that were classified with respect to their mean porosity and initial permeability. The parameters (mean porosity 0.25–0.35, permeability 10–1,000 mD) were chosen according to geological formations identified in the Mallik deposit in Canada's Mackenzie Delta which is a permafrost region. The SUGAR project is explicitly aimed at submarine gas hydrates. Hester and Brewer [15] showed over 70 different locations of subaquatic deposits all over the world that had been identified by 2009, with less than half of them being actually known deposits, the others described as inferred deposits that had been identified with indirect markers so far. Some data on the structural properties like mean porosities and intrinsic permeabilities of hydrate-bearing sediments are available for some sites that have been investigated so far (see [14, 16, 17]). Thus mean porosities reported so far range from 0.2 to 0.5 (e.g., [16, 17]), permeabilities range from 0.1 [17] to 1,000 mD [18].

2.3. Simplified Reservoir Model. For simulations, a simplified reservoir model built of layers with homogeneous properties for porosity, permeability, and initial hydrate saturation was

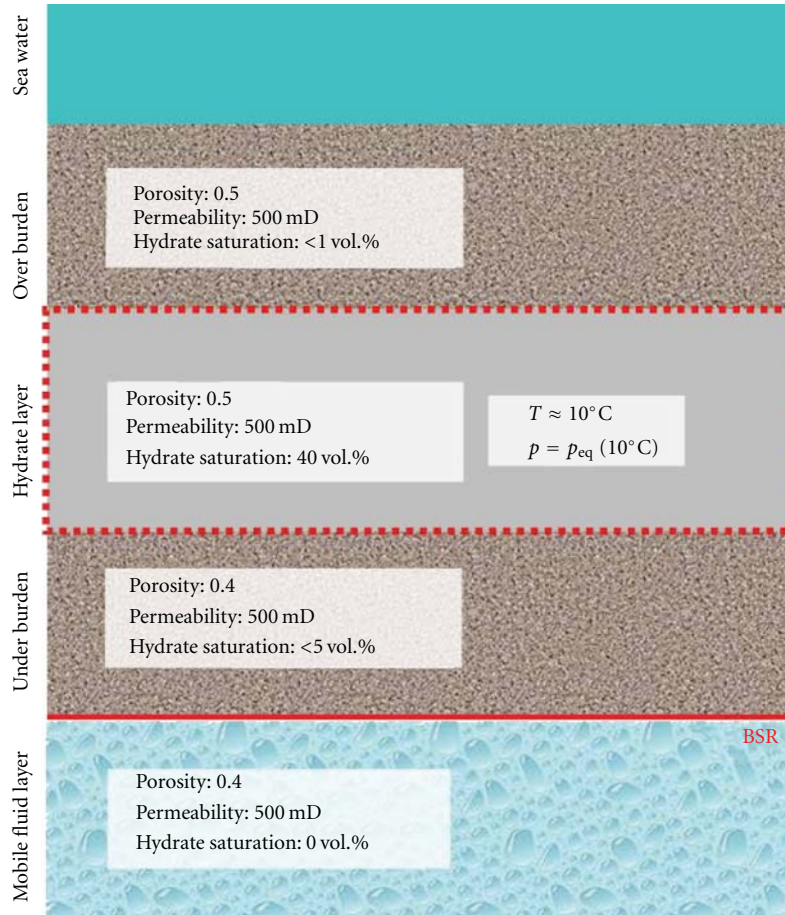


FIGURE 2: Reservoir model for simulations.

used (see Figure 2). According to the classification of Moridis and Collet [12], the reservoir corresponds to class 1 type.

In the simulations presented, the focus is on scenarios where only the hydrate layer with no-flow boundaries for mass and/or heat is considered. The initial conditions are shown in Table 2. As initial pressure, the equilibrium pressure at a given temperature was chosen in order to avoid artificial hydrate formation or decomposition during the simulation run.

3. Simulation Tools

Within the frame of the SUGAR research project, two simulation programs are used:

- (i) the simulator STARS (Steam, Thermal and Advanced Processes Reservoir Simulator, Computer Modeling Group Ltd. (CMG), Canada), an oil and gas industry standard reservoir simulator,
- (ii) the simulation code UMSICHT HyReS, a newly developed in-house code.

STARS was primarily developed to model oil and gas flow through 3-dimensional sediments, but it can be set up to deal with hydrate formation and decomposition as well. Due

to the complexity of subsea hydrate systems and several restrictions in using STARS regarding full thermodynamics of gas hydrate physics, a second in-house code called UMSICHT HyReS was developed within the project to achieve full flexibility.

3.1. Model Concept. The underlying operation scenario for the development of a new model is methane production from subsea gas hydrate accumulations by depressurization, thermal stimulation, or injection of liquid/soluted CO_2 . The latter can result in an exchange of methane by carbon dioxide in the hydrate lattice or in a two-step decomposition/formation process with gaseous methane and hydrate-stabilized CO_2 in the end [5, 6, 19, 20]. Conservation laws for such a complex situation must be formulated for a gas and a liquid phase flowing through sediment partially blocked by hydrates. Assuming a stable nonmoving sediment phase, only sediment porosity will be constant, whereas the saturation of gas, liquid, and hydrates is free variables. Therefore, the flow within the sediment strongly depends on the time-dependent distribution of phase saturations within the calculated volume, and this is a fundamental feature of the UMSICHT HyReS model. The second fundamental concept is the perception of decomposition/formation kinetics within the hydrates. According to works of Haeckel et al. [21, 22], gas

hydrate formation is controlled by a liquid phase formation equilibrium. Conceptually this means that hydrate formation is a two-step process of solution of the gas component in the liquid and formation of hydrate within the liquid. From a thermodynamic point of view, this is more complicated than the well-known kinetics of the *Kim-Bishnoi* type. The third remarkable feature of the new model is the distinct formulation of energy balances for gas, liquid, hydrate, and sediment phase which was made for dealing with special operation situations in thermally stimulated gas production.

3.2. Flow Models. The velocity of a fluid phase α in the multiphase system is given by *Darcy's* law:

$$\mathbf{u}_\alpha = -\frac{k_{\text{rel},\alpha} K_{\text{abs}}}{\eta_\alpha} (\nabla P_\alpha - g\rho_\alpha). \quad (1)$$

Equations of the Carman-Kozeny type are widely used as permeability models for subsea sediments. In UMSICHT HyReS, formulations of *Brooks-Corey*, *van Genuchten*, and the model used in STARS are implemented. In this work, the *Brooks-Corey* model (which is also used by Sun and Mohanty [23]) is applied:

$$k_{\text{rel},\alpha} = k_{\text{rel},\alpha}(S_G, S_L), \quad (2)$$

$$K_{\text{abs}} = K_0(S_G + S_L) \left(\frac{(1-\phi)(S_G + S_L)}{1-\phi(S_G + S_L)} \right)^{2\kappa}, \quad (3)$$

$$k_{\text{rel},G} = k_{\text{rel},G}^0 (S_{G,\text{eff}}^*)^{\sigma_G}, \quad k_{\text{rel},L} = k_{\text{rel},L}^0 (S_{L,\text{eff}}^*)^{\sigma_L}, \quad (4)$$

$$S_{G,\text{eff}}^* = \frac{(S_G/S_G + S_L) - S_{G,\text{res}}^{\text{eff}}}{1 - S_{G,\text{res}}^{\text{eff}} - S_{L,\text{res}}^{\text{eff}}}, \quad S_{L,\text{eff}}^* = \frac{(S_L/S_G + S_L) - S_{L,\text{res}}^{\text{eff}}}{1 - S_{G,\text{res}}^{\text{eff}} - S_{L,\text{res}}^{\text{eff}}}. \quad (5)$$

With (3), the blocking of the flow path by solid gas hydrates is included. A similar formulation for the absolute permeability is used in STARS:

$$K_{\text{abs}} = K'_0 \left(\frac{S_G + S_L}{S_G^0 + S_L^0} \right)^\gamma \left(\frac{1 - \phi(S_G^0 + S_L^0)}{1 - \phi(S_G + S_L)} \right)^2. \quad (6)$$

Here, K'_0 is the permeability under starting conditions including initial hydrate saturation, whereas in (3) K_0 is the permeability under pure conditions without hydrates. Parameterization of these equations is given later in Table 2. The parameters for (6) used in STARS are set to give equal flow as (3) in UMSICHT HyReS. With the concept of relative permeability, the flow-model includes the time-dependent progress of gas, liquid, and hydrate phase saturations and is able to describe subsea sediment flow under changing conditions during methane gas production.

3.3. Kinetic Model. Decomposition and formation of gas hydrates are modelled by a linear driving force approach.

For methane and carbon dioxide hydrate formation, the following gross kinetic is assumed:

$$\begin{aligned} R_{\text{MH}} &= \frac{1}{V} \frac{\partial N_{\text{MH}}}{\partial t} = k_{\text{MH}} a_{\text{MH}} (c_{M,L} - c_{M,L}^{*(H)}), \\ R_{\text{CH}} &= \frac{1}{V} \frac{\partial N_{\text{CH}}}{\partial t} = k_{\text{CH}} a_{\text{CH}} (c_{C,L} - c_{C,L}^{*(H)}). \end{aligned} \quad (7)$$

As mentioned before, the kinetic model assumes that the formation process is controlled by the liquid phase concentrations of the hydrate-forming gas. Within this approach, the concentrations $c_{M,L}^{*(H)}$, $c_{C,L}^{*(H)}$ are liquid phase concentrations of the gas components in thermodynamic equilibrium with the hydrates present in the volume. These equilibrium concentrations are different from the solution equilibria between gas and liquid phase (solubility). The hydrate formation from a component present in the gas phase can be modelled as a two-step mechanism of gas solution (step one) and hydrate formation by (7) (step two). Decomposition is modelled by the same equations, but in opposite direction. A formulation for the thermodynamic equilibrium of solution and hydrate formation of methane and carbon dioxide is given by Tishchenko et al. [7]; kinetic constants k_α are adapted from data given by Haeckel et al. [21, 22], and inter-phase areas for methane and carbon dioxide hydrate formation/decomposition are calculated according to Sun and Mohanty [23] by

$$a_\alpha = \sqrt{\frac{(\phi(S_G + S_L))^3}{2K_{\text{abs}}}} (S_L S_\alpha)^{2/3}, \quad \alpha = (\text{MH}, \text{CH}). \quad (8)$$

Equation (8) ensures that the hydrate decomposition results in a hydrate-free environment; in case of hydrate formation in a hydrate-free environment, a small initial saturation is a prerequisite. Calculations with the STARS code are done with the well-known *Kim-Bishnoi* kinetic approach:

$$\begin{aligned} R'_{\text{MH}} &= \frac{1}{V} \frac{\partial N_{\text{MH}}}{\partial t} = k'_{\text{MH}} a'_{\text{MH}} (P_{M,G} - P_{M,G}^{*(H)}), \\ R'_{\text{CH}} &= \frac{1}{V} \frac{\partial N_{\text{CH}}}{\partial t} = k'_{\text{CH}} a'_{\text{CH}} (P_{C,G} - P_{C,G}^{*(H)}). \end{aligned} \quad (9)$$

Here, the distance to thermodynamic equilibrium given in gas phase partial pressures is used as the driving force for hydrate formation and decomposition. In this approach, liquid phase concentrations of the hydrate forming gas have no influence on hydrate formation.

3.4. Other Submodels and Property Data. Within the scope of UMSICHT HyReS, a large number of submodels for capillary pressure, property data, thermal and diffusional conductivity, and for heat and mass transfer between coexistent phases are used. Most submodels depend on one or more free solution variables (like temperature, pressure, concentration, or saturation), resulting in a strong numerical coupling of balance equations. In the following, the most relevant models are presented.

Capillary pressure is given by a modified *Brooks-Corey* approach also used in [23]:

$$P_c = P_c^0 \left(\frac{(1 - \phi)(S_G + S_L)}{1 - \phi(S_G + S_L)} \right)^{-\kappa} (S_{L,\text{eff}}^*)^{-\sigma_c}. \quad (10)$$

Additionally, the *van Genuchten* equation is available:

$$P_c = 2 \cdot 10^5 \left((S_{L,\text{eff}}^*)^{-1/0.771} - 1 \right)^{1/4.37}. \quad (11)$$

The effective saturation $S_{L,\text{eff}}^*$ is given by (5). Mass transfer of gaseous components to liquid and vice versa is modelled by a two-film theory linear approach

$$\dot{n}_{i,GL} = \beta_L a_{GL} (c_{i,G}^* - c_{i,G}). \quad (12)$$

The mass transfer coefficient β_L is set equal to $2.0 \cdot 10^{-8}$ m/s for all components, gas-liquid interphase area is calculated from

$$a_{GL} = \phi S_G \frac{6}{d_B} \quad (13)$$

with a constant bubble diameter of $d_B = 10^{-4}$ m. Property data of gas phase components are taken from *NIST Standard Reference Database* [8] and are molar-weighted; for the gas phase density, the *Peng-Robinson* equation is used. Liquid phase property data are also taken from NIST and other available sources; special corrections for saline seawater are used for density (UNESCO Standard Reference Equation), thermal conductivity [24], viscosity [25], and diffusion coefficients [26]:

$$\begin{aligned} \lambda_{\text{SW}} &= 0.57153(1 + 0.0039 - 1.025 \cdot 10^{-5} \vartheta^2 \\ &\quad + 6.53 \cdot 10^{-10} P_L - 0.29 s_L), \\ \eta_{\text{SW}} &= (1.7910 - 6.144 \cdot 10^{-2} \vartheta_L + 1.4510 \cdot 10^{-3} \vartheta_L^2 \\ &\quad - 1.6826 \cdot 10^{-5} \vartheta_L^3 - 1.5290 \cdot 10^{-9} P_L \\ &\quad + 8.3885 \cdot 10^{-18} P_L^2 + 2.4727 s_L + \vartheta_L \\ &\quad (6.0574 \cdot 10^{-11} P_L - 2.6760 \cdot 10^{-19} P_L^2) \\ &\quad + s_L (4.8429 \cdot 10^{-2} \vartheta_L - 4.7172 \cdot 10^{-3} \vartheta_L^2 \\ &\quad + 7.5986 \cdot 10^{-5} \vartheta_L^3)) \cdot 10^{-3}. \end{aligned} \quad (14)$$

Overall liquid phase heat conductivity and viscosity are calculated with volumetric and molar-weighted functions:

$$\begin{aligned} \lambda_{\text{eff}} &= (1 - \phi) \lambda_S + \phi \sum_{\alpha \neq S} S_\alpha \lambda_\alpha, \\ \ln \eta_L &= \sum_i y_i^L \ln \eta_i^L. \end{aligned} \quad (15)$$

Diffusion coefficients are calculated from *IFM-GEOMAR* data functions [26]:

$$\begin{aligned} \delta_M^{\text{SW}} &= 4.72 \cdot 10^{-14} \frac{T_L}{\eta_{\text{W}}(37.7)^{0.6}} \left(\frac{\eta_{\text{W}}}{\eta_{\text{SW}}} \right), \\ \delta_C^{\text{SW}} &= 10^{-9} \left(0.1959 + 5.089 \cdot 10^{-6} \frac{T_L}{\eta_{\text{W}}} \right) \left(\frac{\eta_{\text{W}}}{\eta_{\text{SW}}} \right), \end{aligned} \quad (16)$$

and the *Boudreau* tortuosity correction [27]:

$$\delta_{i,L}^{\text{eff}} = \frac{\delta_i^L}{1 - 2 \ln \phi}. \quad (17)$$

Other property data for sediment and hydrates are given in Table 1.

3.5. Governing Equations System. Conservation laws are formulated for a two-phase fluid flow through a stable sediment matrix as a heterogeneous continuum model with advection-diffusion type equations for component mass conservation. In UMSICHT HyReS, there are five coexistent phases:

- (i) gas phase (consists of methane, water, and carbon dioxide),
- (ii) liquid phase (consists of water, salt, methane, and carbon dioxide),
- (iii) methane hydrate phase,
- (iv) carbon dioxide hydrate phase,
- (v) sediment.

The unsteady conservation conditions to describe the submarine layer flow of gas and liquid lead to a system of partial differential equations. The solution variables of the model are

- (i) pressure of gas and liquid phase,
- (ii) saturation of gas, liquid, methane hydrate, and carbon dioxide hydrate,
- (iii) temperature of gas, liquid, hydrate, and sediment phase,
- (iv) concentrations of methane, water, and carbon dioxide in the gas phase,
- (v) concentrations of water, salt, methane, and carbon dioxide in the liquid phase.

Based on these assumptions and settings, the conservation equations used in the UMSICHT HyReS code are given as follows.

TABLE 1: Property data of hydrates and sediment.

Parameter	Value	Parameter	Value
Hydrate number CH ₄ hydrate	5.90	Hydrate number CO ₂ hydrate	7.67
Molar mass CH ₄ hydrate	122.3 g/mole	Molar mass CO ₂ hydrate	174.3 g/mole
Density CH ₄ hydrate	7,522 mol/m ³	Density CO ₂ hydrate	6,350 mol/m ³
Specific heat CH ₄ hydrate	256.8 J/(kg*K)	Specific heat CH ₄ hydrate	362.5 J/(kg*K)
Thermal conductivity CH ₄ hydrate	0.5 W/(m*K)	Thermal conductivity CH ₄ hydrate	0.5 W/(m*K)
Dissociation enthalpy CH ₄ hydrate	-54 kJ/mole	Dissociation enthalpy CO ₂ hydrate	-65 kJ/mole
Sediment density	2,600 kg/m ³	Sediment thermal conductivity	3.9 W/(m*K)
Sediment specific heat	1,000 J/(kg*K)		

Mass conservation of fluid and hydrate phases.

$$\begin{aligned} \frac{\partial}{\partial t} (\phi S_G \tilde{\rho}_G) + \nabla \cdot (\tilde{\rho}_G \mathbf{u}_G) &= \frac{1}{V} \sum_i \frac{\partial N_{i,G}}{\partial t}, \\ \frac{\partial}{\partial t} (\phi S_L \tilde{\rho}_L) + \nabla \cdot (\tilde{\rho}_L \mathbf{u}_L) &= \frac{1}{V} \sum_i \frac{\partial N_{i,L}}{\partial t}, \\ \frac{\partial}{\partial t} (\phi S_{MH} \tilde{\rho}_{MH}) &= \frac{1}{V} \frac{\partial N_{MH}}{\partial t}, \\ \frac{\partial}{\partial t} (\phi S_{CH} \tilde{\rho}_{CH}) &= \frac{1}{V} \frac{\partial N_{CH}}{\partial t}. \end{aligned} \quad (18)$$

Mass conservation of components.

$$\begin{aligned} \frac{\partial}{\partial t} (\phi S_G c_{i,G}) + \nabla \cdot (\mathbf{u}_G c_{i,G}) - \nabla \cdot (\phi S_G \delta_{i,G} \nabla c_{i,G}) &= \frac{1}{V} \frac{\partial N_{i,G}}{\partial t}, \\ \frac{\partial}{\partial t} (\phi S_L c_{i,L}) + \nabla \cdot (\mathbf{u}_L c_{i,L}) - \nabla \cdot (\phi S_L \delta_{i,L} \nabla c_{i,L}) &= \frac{1}{V} \frac{\partial N_{i,L}}{\partial t}. \end{aligned} \quad (19)$$

Energy conservation for gas, liquid, hydrate, and sediment.

$$\begin{aligned} \frac{\partial}{\partial t} (\phi S_G \tilde{\rho}_G \tilde{e}_G) + \nabla \cdot (\mathbf{u}_G \tilde{\rho}_G \tilde{h}_G) - \nabla \cdot (\phi S_G \lambda_G \nabla T_G) &= \dot{q}_G, \\ \frac{\partial}{\partial t} (\phi S_L \tilde{\rho}_L \tilde{e}_L) + \nabla \cdot (\mathbf{u}_L \tilde{\rho}_L \tilde{h}_L) - \nabla \cdot (\phi S_L \lambda_L \nabla T_L) &= \dot{q}_L, \\ \frac{\partial}{\partial t} (\phi (S_{MH} \tilde{\rho}_{MH} \tilde{e}_{MH} + S_{CH} \tilde{\rho}_{CH} \tilde{e}_{CH})) \\ - \nabla \cdot (\phi (S_{MH} \lambda_{MH} + S_{CH} \lambda_{CH}) \nabla T_H) &= \dot{q}_H, \\ \frac{\partial}{\partial t} ((1 - \phi) \tilde{\rho}_s \tilde{e}_s) - \nabla \cdot ((1 - \phi) \lambda_s \nabla T_s) &= \dot{q}_s. \end{aligned} \quad (20)$$

Fluid velocity \mathbf{u}_α of phase α is given by Darcy's law as stated in Section 3.2. The conservation laws given above are completed by two equations-of-state:

$$\tilde{\rho}_G = \tilde{\rho}_G(P_G, T_G, c_{i,G}), \quad \tilde{\rho}_L = \tilde{\rho}_L(P_L, T_L, c_{i,L}), \quad (21)$$

a capillary pressure condition,

$$P_L = P_G - P_c, \quad (22)$$

$$\frac{\partial P_L}{\partial t} = \frac{\partial P_G}{\partial t} - \frac{\partial P_c}{\partial t} = \frac{\partial P_G}{\partial t} - \left(\frac{\partial P_c}{\partial S_G} \right)_{S_L} \frac{\partial S_G}{\partial t} - \left(\frac{\partial P_c}{\partial S_L} \right)_{S_G} \frac{\partial S_L}{\partial t}, \quad (23)$$

respectively, and the phase closing condition:

$$S_G + S_L + S_{MH} + S_{CH} = 1, \quad (24)$$

$$\frac{\partial S_G}{\partial t} + \frac{\partial S_L}{\partial t} + \frac{\partial S_{MH}}{\partial t} + \frac{\partial S_{CH}}{\partial t} = 0, \quad (25)$$

respectively.

3.6. *Boundary Conditions.* Boundary conditions (BCs) are necessary to solve the PDE system given above under specific physical constraints. Generally, two types of BC are used in UMSICHT HyReS,

- (i) "no-flow" conditions at boundaries impermeable for mass and/or heat flow,
- (ii) "flow" conditions at boundaries permeable for mass and/or heat flow.

Both BC can be mixed, for example, if a boundary is permeable for heat, but impermeable for mass. If j_c are convective and j_d are diffusive fluxes at a boundary, the general form of these BC is

$$j_c + j_d = 0 \rightarrow j_d = 0, \quad (26)$$

for "no-flow" boundaries, and

$$j_c + j_d = (j_c + j_d)_{\text{out}}, \quad (27)$$

for "flow" boundaries where flow conditions at the point behind the boundary are indexed by "out." With the general equations (26) and (27), boundary conditions for the solution vector and its derivatives can be set up for a special physical scenario. In UMSICHT HyReS, all boundaries are outer boundaries of the calculated volume and there exist no inner BC.

3.7. *Numerical Solution.* The system of partial differential equations given in Section 3.5 has the general form

$$\mathbf{A} \frac{\partial \mathbf{u}}{\partial t} = f \left(t, x, \frac{\partial \mathbf{u}}{\partial x}, \frac{1}{x^{c_x}} \frac{\partial}{\partial x} \left(x^{c_x} \mathbf{D}_x \frac{\partial \mathbf{u}}{\partial x} \right), y, \frac{\partial \mathbf{u}}{\partial y}, \frac{1}{y^{c_y}} \frac{\partial}{\partial y} \left(y^{c_y} \mathbf{D}_y \frac{\partial \mathbf{u}}{\partial y} \right) \right), \quad (28)$$

in which \mathbf{u} is the vector of solution variables and both the mass matrix \mathbf{A} and the generalized diffusion coefficient matrices $\mathbf{D}_x, \mathbf{D}_y$ may depend on \mathbf{u} . The variable c can take values of $c = 0, 1$, or 2 indicating the coordinate system in the respective spatial direction ($c = 0$: Cartesian, $c = 1$: cylindrical, $c = 2$: spherical). Equation (28) exhibits the typical structure of a system of convection-diffusion equations. In UMSICHT-HyReS, the well-established (vertical) method of lines is applied for solving: spatial derivatives are approximated by finite differences on a structured rectangular grid in the (x, y) plane, whereas temporal derivatives are left in their continuous form. The result of this semidiscretization is a large system of ordinary differential equations for the values of the solution variables in each grid point. Highly efficient solvers are available for such systems with banded Jacobian matrix, for example, the differential-algebraic integrator RADAU [28].

Below, the discretization schemes used for the first and (generalized) second-order derivatives in x direction are specified. The expressions in y direction are treated analogously. As will be discussed later in Section 4, the transport of the conserved quantities is strongly convection-dominated. For this reason, special care must be taken in the choice of the discretization scheme for the first-order spatial derivatives in order to avoid unphysical oscillations in the solution variables. In UMSICHT HyReS, a second-order upwind scheme combined with a flux-limiter method as described in [29] is used.

On the interface between cell i and cell $(i+1)$ (indexed $(i+1/2)$), flux-limited left (L) and right (R) states of the solution variables are defined by

$$\begin{aligned} u_{i+1/2}^L &= u_i + \frac{u_i - u_{i-1}}{x_i - x_{i-1}} \cdot \frac{x_{i+1} - x_i}{2} \cdot B(r_i), \\ u_{i+1/2}^R &= u_{i+1} - \frac{u_{i+2} - u_{i+1}}{x_{i+2} - x_{i+1}} \cdot \frac{x_{i+1} - x_i}{2} \cdot B\left(\frac{1}{r_{i+1}}\right), \end{aligned} \quad (29)$$

with

$$\begin{aligned} B(r_i) &= \frac{r_i + |r_i|}{1 + |r_i|} \quad (\text{van Leer-Limiter}), \\ r_i &= \frac{(u_{i+1} - u_i)/(x_{i+1} - x_i)}{(u_i - u_{i-1})/(x_i - x_{i-1})}. \end{aligned} \quad (30)$$

The first-order spatial derivatives are then approximated by

$$\left. \frac{\partial u}{\partial x} \right|_{x=x_i} = \begin{cases} \frac{u_{i+1/2}^L - u_{i-1/2}^L}{x_{i+1/2} - x_{i-1/2}}, & \text{if } (x - \text{velocity})_i \geq 0, \\ \frac{u_{i+1/2}^R - u_{i-1/2}^R}{x_{i+1/2} - x_{i-1/2}}, & \text{if } (x - \text{velocity})_i < 0. \end{cases} \quad (31)$$

The (generalized) second-order spatial derivatives are discretized by standard central differences:

$$\begin{aligned} \frac{1}{x^c} \frac{\partial}{\partial x} \left(x^c D \frac{\partial u}{\partial x} \right) \Big|_{(t, x_i)} &= \frac{c+1}{x_{i+1/2}^{c+1} - x_{i-1/2}^{c+1}} \\ &\cdot \left[x_{i+1/2}^c D_{i+1/2} \left(\frac{u_{i+1} - u_i}{x_{i+1} - x_i} \right) - x_{i-1/2}^c D_{i-1/2} \left(\frac{u_i - u_{i-1}}{x_i - x_{i-1}} \right) \right]. \end{aligned} \quad (32)$$

For the calculation of the generalized diffusion coefficients at the cell interfaces, there is a choice whether the arithmetic mean or the flux-limited left/right state of the respective solution variable is used:

$$D_{i+1/2} = D(x_{i+1/2}, u_{i+1/2}), \quad (33)$$

or

$$D_{i+1/2} = \begin{cases} D(x_{i+1/2}, u_{i+1/2}^L), & \text{if } (x - \text{velocity})_i \leq 0, \\ D(x_{i+1/2}, u_{i+1/2}^R), & \text{if } (x - \text{velocity})_i > 0. \end{cases} \quad (34)$$

4. Operation Scenarios and Simulation Results

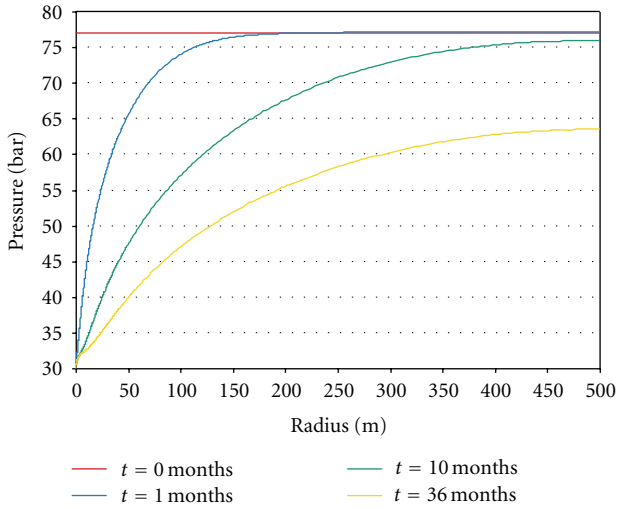
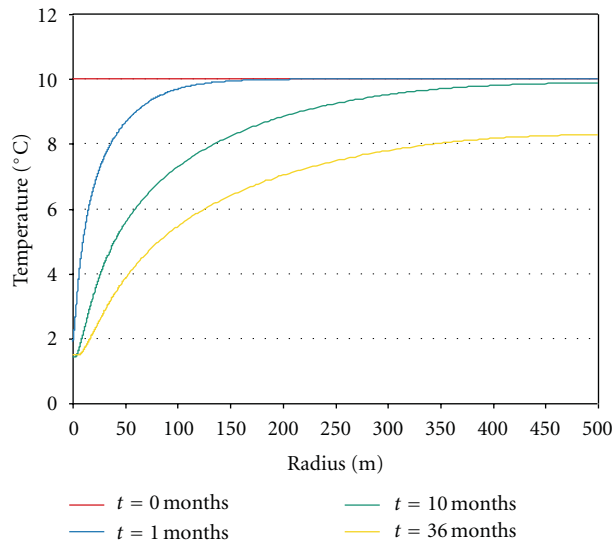
As mentioned earlier, depressurization and the supply of heat or a combination of both methods are the most obvious strategies to destabilize methane hydrate and to recover the emerging gas. An alternative means is to change the methane concentration in the hydrate-building phase by supplying a methane-free substance to the reservoir, for example, water or carbon dioxide. If carbon dioxide is supplied and the operating conditions are chosen properly, it may even be possible to substitute methane by carbon dioxide in hydrate form.

After conforming the relevant inputs in STARS to those of UMSICHT HyReS, two scenarios were set up for simulation:

- (1) first scenario: pure depressurization of a reservoir with closed boundaries,
- (2) second scenario: depressurization combined with CO_2 injection.

In the first scenario, the pressure in the centre of a cylindrical reservoir with a diameter of 1,000 m is reduced from equilibrium conditions by approximately 50 bars, and methane gas is produced for a period of three years (Case 1). STARS and UMSICHT HyReS are used to study the effect of a variation in model parameters on methane production. The results obtained from both simulators are compared and found in close agreement (see Figure 6).

The second scenario is a continuation of the first and was simulated with STARS. After three years of methane recovery at a bottom hole pressure of 30 bars, CO_2 is injected at the same well for another three years at a maximum rate of 8,000 STD m^3/day (Case 2.1).

FIGURE 3: Liquid phase pressure P_L history for Case 1.FIGURE 4: Liquid phase temperature T_L history for Case 1.

A variation of the second scenario is the simultaneous production of methane at one well and CO_2 storage at a second well in a Cartesian reservoir (Case 2.2). The distance between the two wells is 500 m, and the maximum rate of injection is 8,000 STD m^3/day . Both reservoirs (radial and Cartesian) almost have the same volume so that the same initial amount of methane is present.

4.1. First Scenario: Depressurization of a Closed Reservoir (Case 1). The reservoir volume for the depressurization scenario is a cylindrical region with a diameter of 1,000 m and a height of 20 m. The well is situated in the centre of the region and has a diameter of 1 m. Starting from CH_4 hydrate equilibrium conditions at about 77 bars and 10°C , the liquid pressure at the well is lowered to 30 bars. Methane hydrate is dissolved and a flow is induced in the direction to the well.

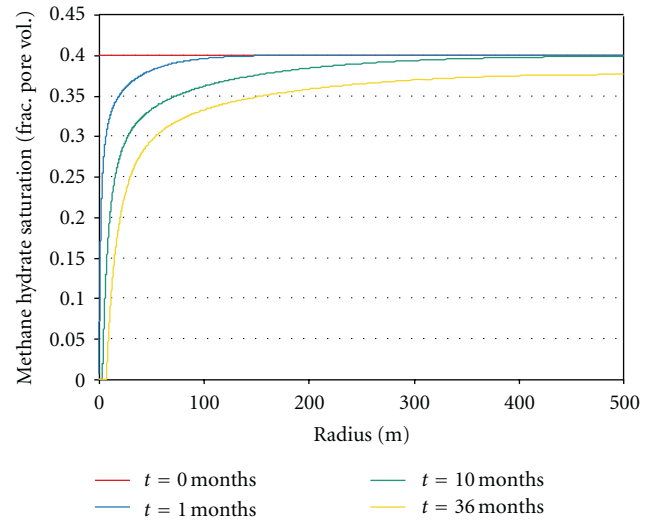
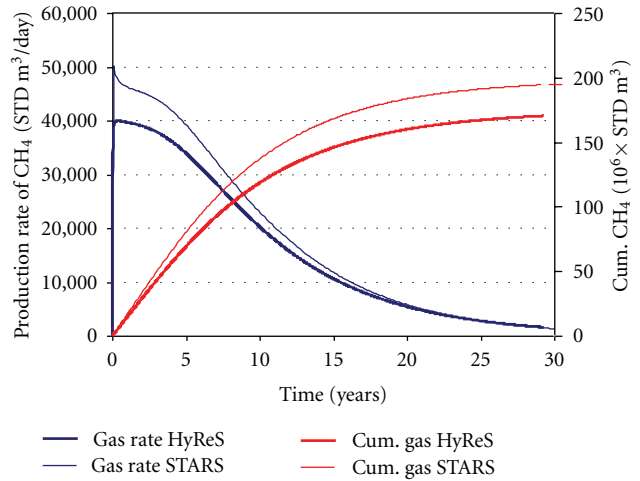
FIGURE 5: Methane hydrate saturation S_{MH} history for Case 1.

FIGURE 6: Production rate and cumulative production of methane for Case 1, comparison of simulators.

Main initial values and model parameters are given in Table 2.

Figures 3, 4, and 5 show the history of pressure, temperature, and methane hydrate saturation over the radius of the reservoir. Pressure decreases slowly from 77 bars to 30 bars within the reservoir because of the restricted permeability of the hydrate formation. Temperature starts at 10°C and decreases to 1°C (the equilibrium temperature corresponding to 30 bars); in the same period of time, the methane hydrate saturation decreases due to methane production in the volume. The process will finally stop at a lower temperature in equilibrium conditions. The overall simulation time was three years (corresponds to the lowest curve in all diagrams). The curves in all diagrams correspond to times $t = 0, 1, 10,$ and 36 months.

The production curves for methane gas obtained with UMSICHT HyReS (bold lines) and STARS (thin lines) are

TABLE 2: Basic parameters and settings for the depressurization scenario.

Parameter	Value	Parameter	Value
Diameter of area	1,000 m	Intrinsic permeability K_0	500 mD
Height of area	20 m	Brooks-Corey parameter k	2,0
Porosity of sediment	0.50	Brooks-Corey parameter σ_G	1.75
Initial gas saturation	0.05	Brooks-Corey parameter σ_L	4.0
Initial liquid saturation	0.55	Effective resident gas saturation	0
Initial methane hydrate saturation	0.40	Effective resident liquid saturation	0.20
Initial pressure	77 bars	Entry capillary pressure	2.8×10^4 Pa
Initial temperature	10°C	Capillary pressure exponent σ_C	0.50
Initial salinity (std. sea salt composition)	35 g/kg		

shown in Figure 6. To get a better impression of the curve progression, the production period was set to 30 years instead of 3 years. The maximum production rate of about 40,000 STD m³/day is quickly reached right at the beginning of the depressurization. For the next five years, methane production only slightly decreases; after five years, nearly 70 million STD m³ have been produced at the well (UMSICHT HyReS). Thereafter, the supply of gas from the outer part of the reservoir slows down because the pressure gradient towards the well becomes increasingly smaller. Thus, although after 30 years of production, the gas saturation in the reservoir is still at a level of about 12%, the lack of the pressure gradient driving force prevents the free methane gas from being recovered.

Bearing in mind that the models used in UMSICHT HyReS and STARS are of high complexity and differ slightly, the production rate and cumulative gas amount after thirty years are in close agreement. The deviation is mainly caused by different kinetic approaches (see (7)–(9)) and various thermodynamic parameters which are P, T, s -dependent (as in UMSICHT HyReS) instead of constant values (as in STARS).

Taking the above scenario as the base case, model parameters are varied in order to study the strength of their influence on methane gas production. Table 3 shows the parameters that are varied together with the resulting cumulative methane production after three years. The column in the middle represents the parameter settings of the base case. For the parameter study, the values of the base case are lowered (upper row) and increased (lower row), and the respective cumulative methane production is reported for simulations carried out with UMSICHT HyReS. As can be seen, mass transfer and kinetics are fast enough not to hinder gas recovery. The permeability of the reservoir is found to be the bottleneck of the process as it controls the overall performance of methane production.

In addition to the variation of parameters, the boundaries of the reservoir have been extended to include the over and under burdens in the simulation. Both zones are set free of hydrate and gas. As the temperature increases with the depth of the reservoir, a vertical thermal gradient of 30°C/km is assumed. The initial pressure in each layer is taken as the equilibrium pressure corresponding to the given temperature. The values for pressure and temperature listed in Table 4 are set at the uppermost layer of each zone.

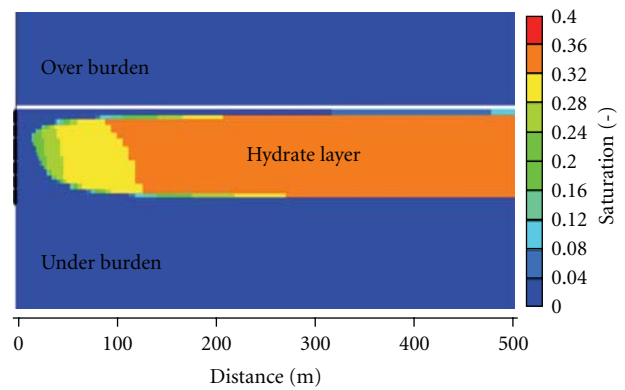


FIGURE 7: Effect of over and under burdens on hydrate decomposition.

As mentioned before, due to the depressurization and the endothermic decomposition of hydrates, the reservoir cools down until a new equilibrium is reached. At this state, no more gas is released from the hydrate, and the production rate decreases. The inclusion of the over and under burdens in the simulation leads to an enhanced gas production: after three years, 132 million STD m³ have been recovered, whereas only 50 million STD m³ are extracted for the base case. The reason is the supply of additional heat from the upper and lower layers. Figure 7 shows that more hydrate decomposes in the vicinity of the layer boundaries than in the middle of the hydrate layer. In order to reproduce that effect in the simulations, the grid near the layers has to be refined. Additionally, a thin impermeable layer was added just above the hydrate layer to avoid the rising of free gas from the hydrate to the upper layers.

4.2. Second Scenario: Depressurization Combined with CO₂ Injection (Case 2.1). The same reservoir geometry and model parameters as for Case 1 are used to simulate CO₂ storage after methane production at a single well. The results are obtained with the simulator STARS.

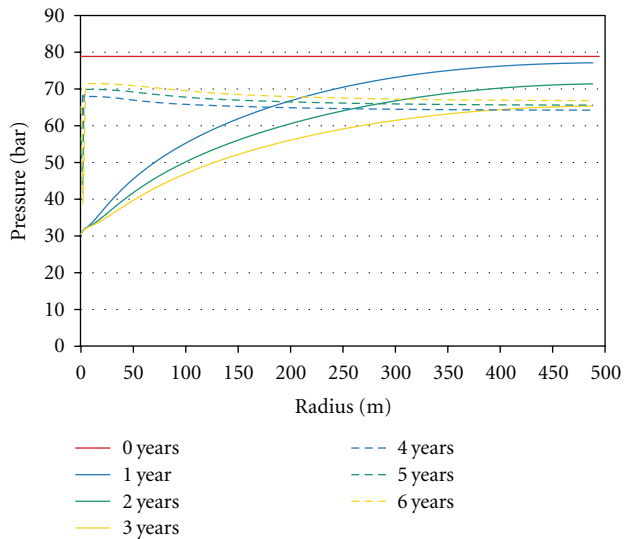
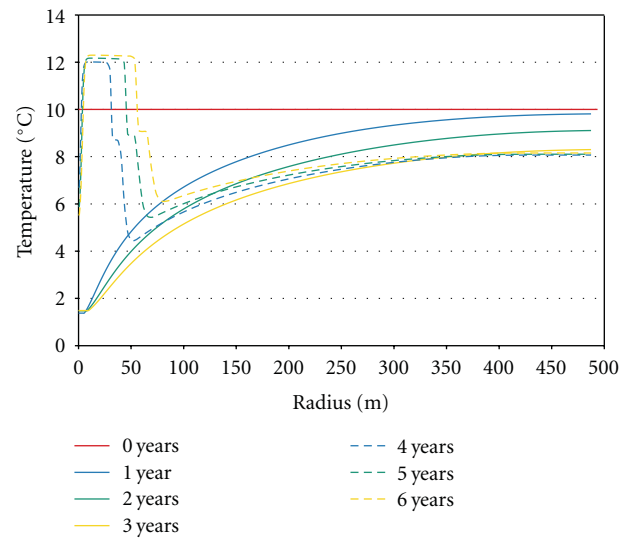
Within the three years of methane production at a well pressure of 30 bars, pressure and temperature in the volume decrease. This pressure decline propagates into the reservoir and causes a decomposition of methane hydrate around the well (see Figure 10). After three years, the well is closed for

TABLE 3: Influence of transport parameters on methane production (after 3 years).

Case	Mass transfer coefficient (m/s)	Cumulative production (STD m ³)	Kinetic constant methane dissociation (m/s)	Cumulative production (STD m ³)	Intrinsic permeability (mD)	Cumulative production (STD m ³)
–	2.0E – 9	3.88E + 07	2.00E – 10	4.17E + 07	250	2.22E + 07
Normal	2.0E – 8	4.27E + 07	2.00E – 9	4.27E + 07	500	4.27E + 07
+	2.0E – 6	4.33E + 07	2.00E – 8	4.29E + 07	750	6.30E + 07

TABLE 4: Basic parameters for simulation of layered reservoir.

	Over burden	Hydrate layer	Under burden
Porosity of sediment	0.5	0.5	0.4
Intrinsic permeability K'_0	500 mD	500 mD	500 mD
Permeability parameter γ	5.8	5.8	5.8
Initial gas saturation	0	0.05	0
Initial liquid saturation	1	0.55	1
Initial methane hydrate saturation	0	0.40	0
Initial pressure	52 bars	72 bars	77 bars
Initial temperature	7°C	10°C	10.6°C
Initial salinity	35 g/kg	35 g/kg	35 g/kg
Thickness	100 m	20 m	100 m

FIGURE 8: Liquid phase pressure P_L history for Case 2.1.FIGURE 9: Temperature T_L history for Case 2.1.

production and starts to function as an injection well for another three years. CO₂ is injected at 5°C at a maximum rate of 8,000 STD m³/day. As can be seen in Figures 8 and 9, pressure and temperature again start to increase close to the well due to the injection process and the exothermic formation of CO₂ hydrate.

After the three years of depressurization, methane hydrate is decomposed completely in a radius of approximately 10 m around the well (see Figure 10). As CO₂ is injected at

5°C into the reservoir, methane hydrate continues decomposing within a larger area. In the region of CO₂ hydrate formation, the P - T conditions are below the methane hydrate stability curve. The driving force for methane hydrate decomposition is even larger than in the case of simple depressurization. After the injection phase, the volume free of methane hydrate has a radius of approximately 60 m. In addition, while CO₂ is injected, the gaseous methane is pushed away from the well into the (closed) reservoir, and

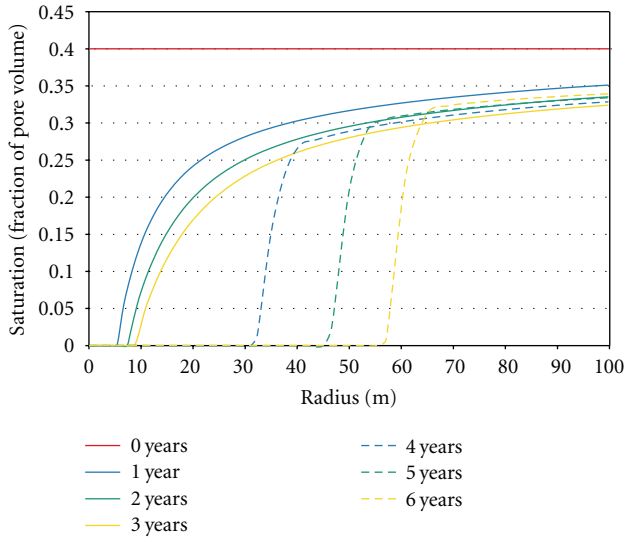


FIGURE 10: Methane hydrate saturation S_{MH} history for Case 2.1.

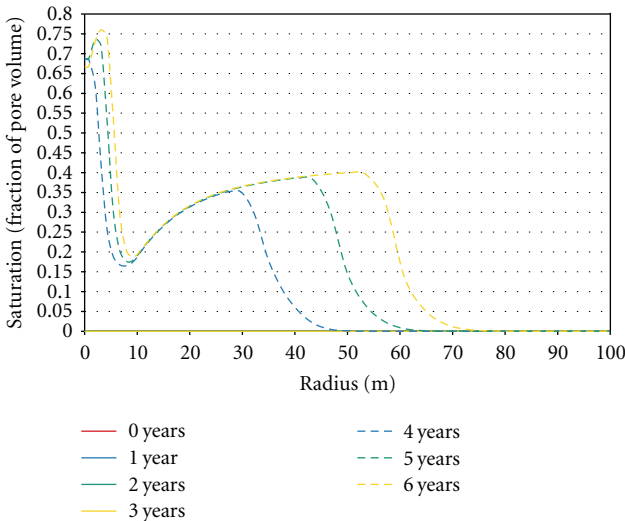


FIGURE 11: Carbon dioxide hydrate saturation S_{CH} history for Case 2.1.

secondary methane hydrate formation occurs because of an increase of pressure due to gas compression.

Figure 11 illustrates the development of CO_2 hydrate saturation for the period of injection. Within the first few meters, the saturation reaches values of about 75% after three years of injection. At a distance of more than 10 m away from the well, the formation of CO_2 hydrate is strongly limited due to the governing pressure and temperature conditions. As CO_2 migrates into the reservoir, CO_2 hydrate forms up to 40% within a radius of 55 m around the injection well.

Figure 12 illustrates the production and injection curves for Case 2.1 after three years.

4.3. *Second Scenario: Depressurization Combined with CO_2 Injection (Case 2.2).* To simulate production of methane and storage of CO_2 at two different wells, a Cartesian grid with

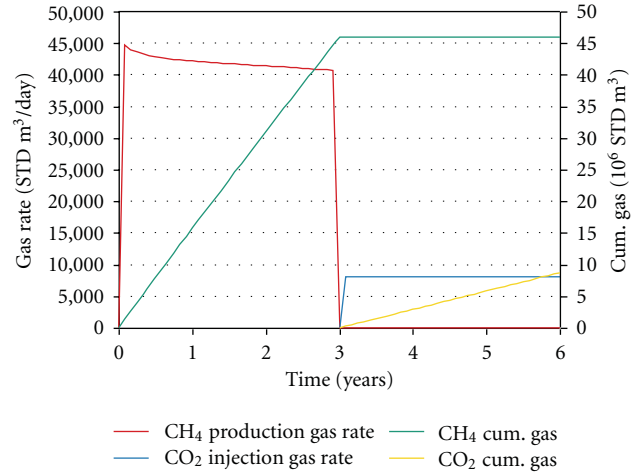


FIGURE 12: Gas production/injection rates and cumulated gas for Case 2.1.

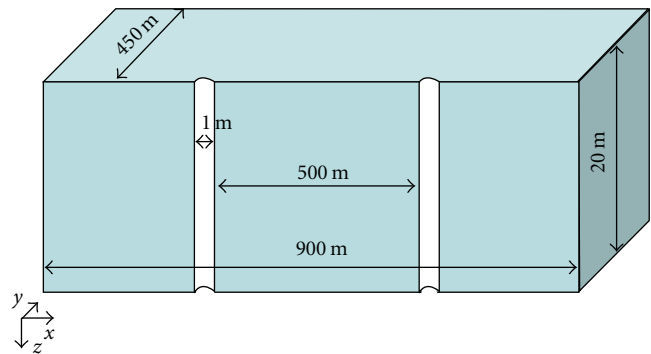
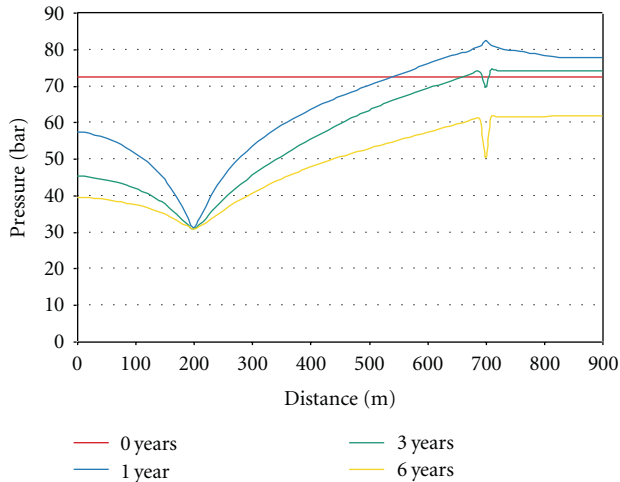
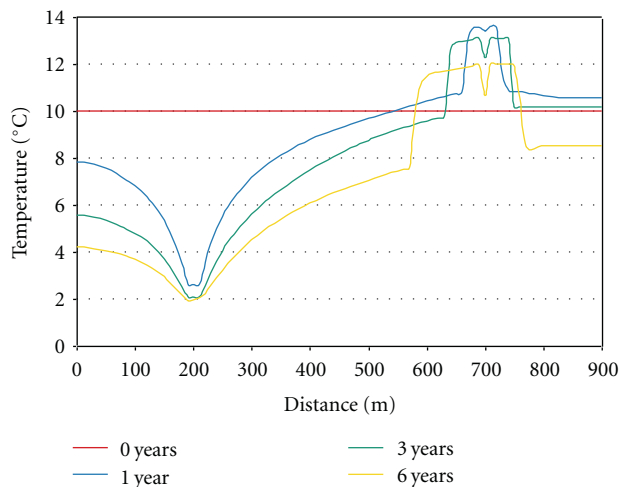


FIGURE 13: Reservoir geometry in a Cartesian grid (Case 2.2); half size.

an edge length of 900 m and a height of 20 m is used. The model parameters and initial conditions are the same as before (see Table 2). All simulations were performed with STARS. Starting from methane hydrate equilibrium at 72 bars (salinity is neglected) and $10^\circ C$, the bottom hole pressure in the production well is lowered to 30 bars. *Simultaneously*, CO_2 at $10^\circ C$ is injected at a maximum rate of $8,000 \text{ STD m}^3/\text{day}$ at the injection well which is located 500 m apart from the production well. Both wells have a diameter of 1.0 m. The geometric configuration is shown in Figure 13.

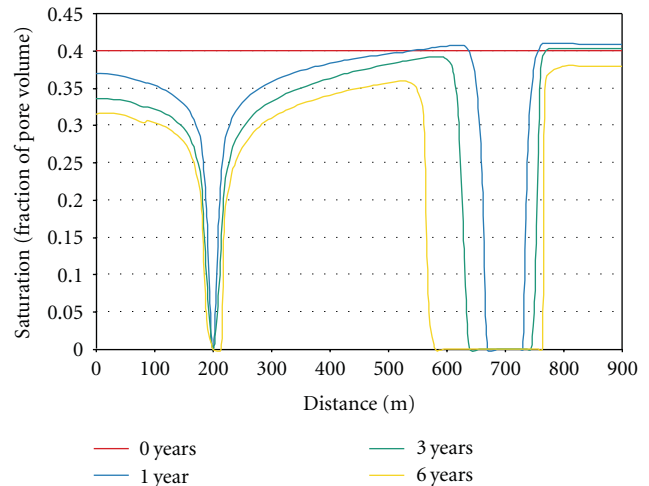
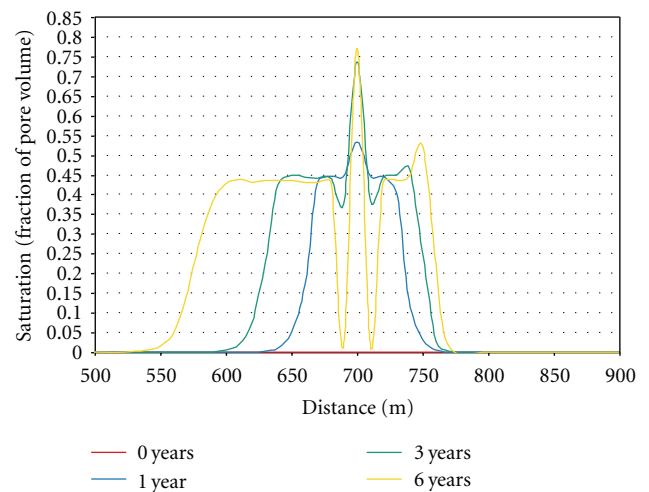
The distributions of pressure, temperature, and hydrate saturations along the x -axis of the grid in the middle layer in z -direction are illustrated in Figures 14, 15, 16, and 17, respectively, for a period of six years. As far as the production well (left hand side) is concerned, the situation is the same as for Case 1. The pressure decrease (Figure 14) causes a decomposition of CH_4 hydrate and therefore a temperature decline (Figure 15). A front propagates into the reservoir, and gas is produced from hydrates as long as the system is not at equilibrium conditions and a pressure gradient exists. The higher pressure at the injection well (right hand side) leads

FIGURE 14: Liquid phase pressure P_L history for Case 2.2.FIGURE 15: Temperature T_L history for Case 2.2.

to the exothermic formation of CO_2 hydrate and thus to an increase in temperature around the well (see Figure 15).

The decomposition of methane hydrate takes place at both wells (see Figure 16): at the production well because of the depressurization and at the injection well because of heat supply by the injection of CO_2 and the heat release due to CO_2 hydrate formation. As discussed for Case 2.1, the methane hydrate saturation declines due to depressurization within a smaller radius (10 to 20 m) than due to CO_2 injection (approximately 100 m).

After six years, a maximum peak in CO_2 hydrate saturation of about 75% is reached near the CO_2 injection well. Due to unfavourable P, T conditions for CO_2 hydrate formation near the injection, the saturation decreases significantly within a few meters apart from the well. At a distance of about 20 m, hydrate has only been formed up to a saturation of 45%. The radius within which CO_2 hydrate is formed is up to 150 m (see Figure 17).

FIGURE 16: Methane hydrate saturation S_{MH} history for Case 2.2.FIGURE 17: Carbon dioxide hydrate saturation S_{CH} history for Case 2.2.

An effect which can be seen in Figure 17 is clarified in Figure 18. Due to the fact that pressure is lowered at the production well, CO_2 is sucked towards it. Therefore, more CO_2 hydrate forms between the wells than to the right of the injection well.

In addition to the production rate for Case 2.2 (bold lines), Figure 19 shows the results for a depressurization case without CO_2 injection (dashed lines; simulated with the same grid). After 1.5 years, the production rate with CO_2 injection slightly exceeds the results for the case without CO_2 injection. The reason might be that methane is pushed towards the production well while CO_2 is injected. CO_2 is also sucked towards the production well, but within the simulated period, the amount reaching the production well is almost zero.

5. Conclusions and Outlook

First, a pure depressurization scenario for a reservoir with 1,000 m in diameter was simulated both with STARS and

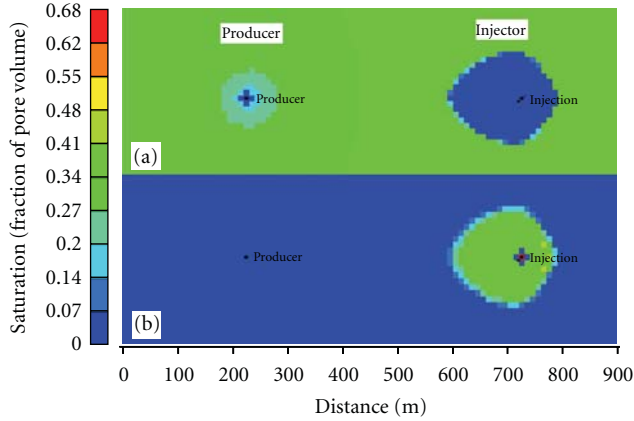


FIGURE 18: Hydrate profile after production and injection period of six years: (a) CH₄ hydrate; (b) CO₂ hydrate.

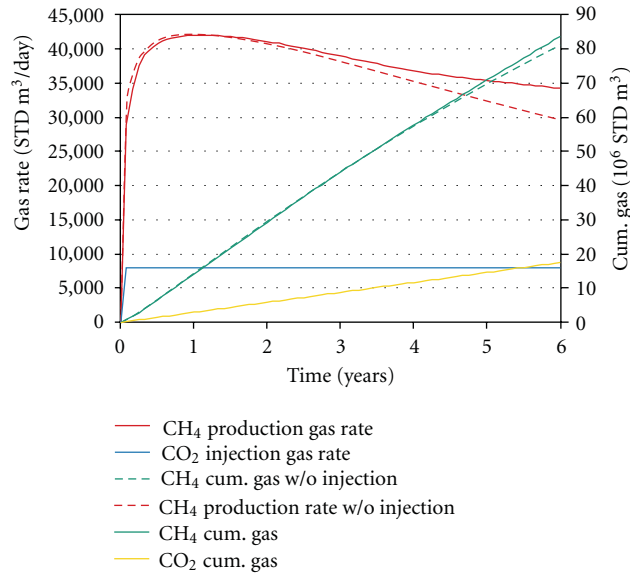


FIGURE 19: Gas rates and cumulated gas for Case 2.2.

UMSICHT HyReS. For the given reservoir settings (see Table 2), permeability turns out to be the most important parameter for methane gas production, whereas decomposition kinetics and gas-liquid mass transfer are of lower relevance. A production rate of nearly 40,000 STD m³/day can be achieved over a period of 5 years; over 10 years, the production rate decreases to half of its initial value. The reported rates can be enhanced by means of extended simulation boundaries (including over and under burdens). The results predicted by both simulators are in close agreement because the differences of the models for decomposition kinetics and gas-liquid mass transfer are of lower importance in the cases under consideration. As shown above (see Section 3.3-3.4), the enhanced hydrate formation/decomposition model used in UMSICHT HyReS depends on the concentration of the dissolved gas in the liquid phase and therefore strongly on gas-liquid mass transfer effects. Further simulation cases

will be carried out with reservoir data which make mass transfer characteristics more relevant, for example, restricted gas-liquid interphase area. In such cases, model differences between STARS and UMSICHT HyReS will become more obvious.

The second simulation case aims at the industrially relevant CO₂ sequestration problem and is set up as a one-well scenario with two consecutive steps (CH₄ hydrate decomposition with methane production/CO₂ hydrate formation) and as a two-well scenario with simultaneous methane production and CO₂ sequestration. These simulations were carried out with STARS in a 2-D radial and 3-D Cartesian volume, respectively. In continuation of the pure depressurization scenario, CO₂ is injected with a constant rate of 8,000 STD m³/day in a partially depleted radial reservoir for three years. Within this period, CH₄ hydrate has decomposed further due to unfavourable *P-T* conditions during the injection of CO₂. Simultaneously, CO₂ hydrate has formed around the well. At the end of the operation period, substitution of methane hydrate by carbon dioxide hydrate has occurred only within a radius of about 60 m around the well. The saturation of CH₄ hydrate has decreased to zero, and CO₂ hydrate saturation has increased up to 40% and 75% just next to the well, respectively.

In the case of simultaneous CH₄ production and CO₂ storage in a two-well setting with a Cartesian grid, the same effects can be observed as mentioned before. Since the productivity depends on the pressure gradient driving force towards the production well, a local increase of pressure due to injection of CO₂ leads to an enhanced gas rate (compared to the case without CO₂ injection). A maximum rate of more than 40,000 STD m³/day at the beginning of the production decreases to 35,000 STD m³/day after a period of six years. Within this period, the produced amount of injected CO₂ is almost zero.

The performed simulations show that depressurization with or without simultaneous CO₂ injection is a practicable way to produce methane from subsea hydrate fields with assured rates over many years. Thermal stimulation is an alternative from a thermodynamic point of view, but there is a lack of appropriate technology to heat up subsea sediment in a wider range around a production well. Some promising ideas (as methane-driven point heaters, e.g.) will be investigated in subsequent work.

Symbols

- a*: Volumetric interphase area (m²/m³)
- B*: van Leer limiter (1)
- c*: Molar concentration (mole/m³)
- \tilde{c}_p : Molar heat capacity (J/(mole K))
- D*: Generalized diffusion coefficient (specific)
- \tilde{e} : Molar total energy (J/mole)
- g*: Gravity constant (m/s²)
- \tilde{h} : Molar enthalpy (J/mole)
- j*: Molar flux (mol/(m²*s))
- k*: Dissociation constant (m/s)
- k_{rel}*: Relative permeability (1)

K: Absolute/intrinsic permeability (m^2)
L: Length of hydrate layer (m)
N: Molar mass (mole)
ni: Molar flow per unit volume ($\text{mole}/(\text{m}^3\text{s})$)
P: Pressure (Pa)
PC: Capillary pressure (Pa)
q̇: Heat flow per unit volume ($\text{W}/(\text{m}^3\text{s})$)
R: Volumetric molar conversion rate ($\text{mole}/(\text{m}^3\text{s})$)
S: Saturation = fraction of pore volume (m^3/m^3)
s: Salinity = mass of salt/mass of pure water (kg/kg)
T: Absolute temperature (K)
t: Time (s)
u: Velocity (volume flow per unit area), solution vector (m/s)
V: Volume (m^3)
x: Axial coordinate (m)
y: Molar fraction (mol/mol)
z: Vertical coordinate (m)
 β : Mass transfer coefficient (m/s)
 δ : Diffusion coefficient (m^2/s)
 ϵ : Volume fraction per unit volume (m^3/m^3)
 ϕ : Porosity (1)
y: Permeability model parameter in STARS code (1)
 η : Dynamic viscosity ($\text{Pa}\cdot\text{s}$)
 κ : Brooks-Corey permeability model parameter (1)
 λ : Heat conductivity ($\text{W}/(\text{m}\cdot\text{K})$)
 ν : Hydrate number (1)
 ϑ : Celsius temperature (deg C)
 ρ : Specific density (kg/m^3)
 $\tilde{\rho}$: Molar density (mole/m^3)
 σ : Brooks-Corey permeability model parameter (1).

Indices

*: In equilibrium condition
 0: Intrinsic/entry condition
 α : Phase α
 abs: Absolute
 C: Capillary
 C: Carbon dioxide
 CH: Carbon dioxide hydrate
d: Diffusive
 eff: Effective
 G: Gas phase
 H: Hydrate phase
i: Component *i*
 L: Liquid phase

M: Methane
 MH: Methane hydrate
 rel: Relative
 res: Resident
 S: Sediment phase
 SW: Sea water
 W: Pure water
x: In axial direction
z: In vertical direction.

Acknowledgments

The support of our research activities by the German Federal Ministry of Economics and Technology and the German Federal Ministry of Education and Research within the framework of the SUGAR project is gratefully acknowledged.

References

- [1] E. D. Sloan, "Clathrate hydrates: the other common solid water phase," *Industrial and Engineering Chemistry Research*, vol. 39, no. 9, pp. 3123–3129, 2000.
- [2] M. Ota, Y. Abe, M. Watanabe, R. L. Smith, and H. Inomata, "Methane recovery from methane hydrate using pressurized CO_2 ," *Fluid Phase Equilibria*, vol. 228–229, pp. 553–559, 2005.
- [3] M. Ota, K. Morohashi, Y. Abe, M. Watanabe, R. Lee Smith, and H. Inomata, "Replacement of CH_4 in the hydrate by use of liquid CO_2 ," *Energy Conversion and Management*, vol. 46, no. 11–12, pp. 1680–1691, 2005.
- [4] X. Zhou, S. Fan, D. Liang, and J. Du, "Replacement of methane from quartz sand-bearing hydrate with carbon dioxide-in-water emulsion," *Energy and Fuels*, vol. 22, no. 3, pp. 1759–1764, 2008.
- [5] G. Ersland, J. Husebø, A. Graue, B. A. Baldwin, J. Howard, and J. Stevens, "Measuring gas hydrate formation and exchange with CO_2 in Bentheim sandstone using MRI tomography," *Chemical Engineering Journal*, vol. 158, no. 1, pp. 25–31, 2010.
- [6] H. Lee, Y. Seo, Y. T. Seo, I. L. Moudrakovski, and J. A. Ripmeester, "Recovering methane from solid methane hydrate with carbon dioxide," *Angewandte Chemie*, vol. 42, no. 41, pp. 5048–5051, 2003.
- [7] P. Tishchenko, C. Hensen, K. Wallmann, and C. S. Wong, "Calculation of the stability and solubility of methane hydrate in seawater," *Chemical Geology*, vol. 219, no. 1–4, pp. 37–52, 2005.
- [8] NIST Chemistry Webbook, <http://webbook.nist.gov/chemistry/>.
- [9] J. M. Schicks, E. Spangenberg, R. Giese, B. Steinhauer, J. Klump, and M. Luzi, "New approaches for the production of hydrocarbons from hydrate bearing sediments," *Energies*, vol. 4, no. 1, pp. 151–172, 2011.
- [10] N. Goel, "In situ methane hydrate dissociation with carbon dioxide sequestration: current knowledge and issues," *Journal of Petroleum Science and Engineering*, vol. 51, no. 3–4, pp. 169–184, 2006.
- [11] K. Su, C. Sun, X. Yang, G. Cgen, and S. Fan, "Experimental investigation of methane hydrate decomposition by depressurizing in porous media with 3-Dimension device," *Journal of Natural Gas Chemistry*, vol. 19, pp. 210–216, 2010.

- [12] G. R. Moridis and T. S. Collet, "Strategies for gas production from hydrate accumulations under various geological and reservoir conditions," in *Proceedings Tough Symposium*, 2003.
- [13] G. J. Moridis and E. D. Sloan, "Gas production potential of disperse low-saturation hydrate accumulations in oceanic sediments," Tech. Rep. LBNL-5268, Lawrence Berkeley National Laboratory, Berkeley, Calif, USA, 2006.
- [14] M. Uddin, D. Coombe, and F. Wright, "Modeling of CO₂-hydrate formation in geological reservoirs by injection of ² Gas," *Journal of Energy Resources Technology, Transactions of the ASME*, vol. 130, no. 3, Article ID 032502, pp. 032502-1–032502-11, 2008.
- [15] K. C. Hester and P. G. Brewer, "Clathrate hydrates in nature," *Annual review of marine science*, vol. 1, pp. 303–327, 2009.
- [16] S. Hustoft, S. Bünz, J. Mienert, and S. Chand, "Gas hydrate reservoir and active methane-venting province in sediments on < 20 Ma young oceanic crust in the Fram Strait, offshore NW-Svalbard," *Earth and Planetary Science Letters*, vol. 284, no. 1-2, pp. 12–24, 2009.
- [17] Z. Chen, W. Bai, W. Xu, and Z. Jin, "An analysis on stability and deposition zones of natural gas hydrate in Dongsha Region, North of South China Sea," *Journal of Thermodynamics*, vol. 2010, Article ID 185639, 6 pages, 2010.
- [18] B. J. Anderson, M. Kurihara, M. D. White et al., "Regional long-term production modeling from a single well test, Mount Elbert Gas Hydrate Stratigraphic Test Well, Alaska North Slope," *Marine and Petroleum Geology*, vol. 28, no. 2, pp. 493–501, 2011.
- [19] B. A. Baldwin, J. Stevens, J. J. Howard et al., "Using magnetic resonance imaging to monitor CH₄ hydrate formation and spontaneous conversion of CH₄ hydrate to CO₂ hydrate in porous media," *Magnetic Resonance Imaging*, vol. 27, no. 5, pp. 720–726, 2009.
- [20] J. W. Jung, D. N. Espinoza, and J. C. Santamarina, "Properties and phenomena relevant to CH₄-CO₂ replacement in hydrate-bearing sediments," *Journal of Geophysical Research B*, vol. 115, no. 10, Article ID B10102, 2010.
- [21] M. Haeckel, E. Suess, K. Wallmann, and D. Rickert, "Rising methane gas bubbles form massive hydrate layers at the seafloor," *Geochimica et Cosmochimica Acta*, vol. 68, no. 21, pp. 4335–4345, 2004.
- [22] M. Haeckel, A. Reitz, and I. Klauke, "Methane budget of a large gas hydrate province offshore Georgia, Black Sea," in *Proceedings of the 6th International Conference on Gas Hydrates (ICGH '08)*, Vancouver, British Columbia, Canada, 2008.
- [23] X. Sun and K. K. Mohanty, "Kinetic simulation of methane hydrate formation and dissociation in porous media," *Chemical Engineering Science*, vol. 61, no. 11, pp. 3476–3495, 2006.
- [24] D. R. Caldwell, "Thermal conductivity of sea water," *Deep-Sea Research and Oceanographic Abstracts*, vol. 21, no. 2, pp. 131–137, 1974.
- [25] D. J. Kukulka, B. Gebhart, and J. C. Mollendorf, "Thermodynamic and transport properties of pure and saline water," *Advances in Heat Transfer*, vol. 18, pp. 325–363, 1987.
- [26] M. Haeckel, K. Wallmann et al., "Main equations for gas hydrate modeling," *SUGAR Internal Communication*, 2010.
- [27] B. P. Boudreau, *Diagenetic Models and Their Implementation: Modelling Transport and Reaction in Aquatic Sediments*, Springer, Berlin, Germany, 1997.
- [28] S. V. Pennington and M. Berzins, "New NAG library software for first-order partial differential equations," *ACM Transactions on Mathematical Software*, vol. 20, no. 1, pp. 63–99, 1994.
- [29] E. Hairer and G. Wanner, *Solving Ordinary Differential Equations II. Stiff and Differential-Algebraic Problems*, Springer Series in Computational Mathematics 14, Springer, 2nd edition, 1996.

Research Article

Geophysical Indicators of Gas Hydrate in the Northern Continental Margin, South China Sea

Xiujian Wang,^{1,2} Shiguo Wu,¹ Yiqun Guo,³ Shengxiong Yang,³ and Yuehua Gong³

¹*Institute of Oceanology, Chinese Academy of Sciences, Qingdao 266071, China*

²*Key Laboratory of Marine Hydrocarbon Resources and Environmental Geology, Ministry of Land and Resources, Qingdao 266071, China*

³*Guangzhou Marine Geological Survey, MLR, Guangzhou 510760, China*

Correspondence should be addressed to Xiujian Wang, wangxiujian@qdio.ac.cn

Received 7 April 2011; Revised 11 August 2011; Accepted 11 August 2011

Academic Editor: Umberta Tinivella

Copyright © 2011 Xiujian Wang et al. This is an open access article distributed under the Creative Commons Attribution License, which permits unrestricted use, distribution, and reproduction in any medium, provided the original work is properly cited.

Gas hydrate drilling results show that gas hydrate has a close relationship with strong bottom-simulating reflectors (BSRs) identified from seismic data in the Baiyun sag, South China Sea. The BSRs observed on seismic profiles at the crests of submarine canyons indicate the likely existence of gas hydrate. We calculate the acoustic impedance using constrained sparse spike inversion (CSSI), the interval velocity, and the seismic reflection characteristics such as reflection strength, instantaneous frequency, blanking, and enhanced reflection to demonstrate the presence of gas hydrate. Higher acoustic impedance and P-wave velocity were identified above the BSR. A remarkable low impedance, low frequency, and acoustic blanking indicated the presence of gas below gas hydrate stability zone. The occurrence of gas hydrate at the crests of canyons suggests that the abundance of gas hydrate in Baiyun sag may be due to the migrating submarine canyons providing the structural reliefs and the topographic ridges.

1. Introduction

Gas hydrates are ice-like crystalline solids and are composed of water molecules and hydrocarbon gas (usually methane). They are distributed worldwide in the continental margin sediments and beneath permafrost [1, 2]. Bottom simulating reflectors (BSRs) identified from seismic reflection profiles are conventionally interpreted as indicators for gas hydrate beneath seafloor [3]. Gas hydrates-associated BSRs have been recognized from the seismic data of other geophysical studies, and their presences have been validated by drilling or coring either in accretionary wedges [4–7] or in the continental margin of the world [8–11]. The Hikurangi Margin, east of New Zealand's North Island, is a large marine gas hydrate province. The BSRs were identified on the multichannel seismic data and there is a strong correlation between BSR strength and geological features indicating the fluid migration [12, 13]. Geophysical parameters show that gas hydrate-bearing sediments have high elastic impedance, high P-impedance, and high P-wave velocity; and the sediments containing free gas have low elastic impedance, low P-impedance, and low P-wave velocity [14]. The anomalous

velocity and the variation in amplitude and polarity of reflectors at the base of gas hydrate-bearing stability zone were used to indicate the presence of gas hydrate [15, 16]. The acoustic impedance inversion of seismic data, log to seismic correlation, and seismic attribute analyses were combined to delineate gas hydrate zone [17].

In China, eight sites were drilled in 2007 in Shenhu area, Pearl River Mouth basin (PRMB), the northern slope of South China Sea [18]. Gas hydrate samples were recovered from pressure cores at sites SH2, SH3, and SH7 in silt and silty-clay sediments with a maximum value of 47% of pore space. High-resolution multichannel 2D and 3D seismic surveys have been carried out for gas hydrate resource studies in the northern SCS. BSRs have been identified in the Xisha Trough [19], Qiongdongnan (QDN) Basin [11], in Pearl River Mouth basin (PRMB) [20] and in the Taixinan Basin of the northern SCS [21, 22]. In the PRM basin, modern submarine canyons have been identified, which are sublinear, subparallel, regularly-spaced extending from the shelf-break at 450 m water depth to their terminations at 1500 m water depth on the north flank [23]. These canyons have lengths of 30–60 km and have widths of 1–5.7 km, while the relief

ranges from 50 to 300 m. Gas hydrates have been drilled in higher relief of the ridges in one of the canyons in 2007. High-amplitude anomalies or bright spots have been observed in the Miocene sequences on the seismic profiles in the deep-water areas [24]. Faults and gas chimneys acted as pathways for upward migration of gas from source rocks to the shallower sediments [25].

The main objective of this study is to use the P-impedance profile obtained from Constrained Sparse Spike Inversion (CSSI) and geophysical attributes computed from 3D seismic data to show the presence of gas hydrate.

2. Geological Setting

The SCS is the largest marginal sea in the western Pacific and covers an area of $3.5 \times 10^6 \text{ km}^2$ [27]. PRMB and QDN basins located on the northern slope of SCS are Cenozoic rift basins developed on Mesozoic basement, and gas hydrates have been drilled in this basin (Figure 1). The structural evolution of basins can be divided into two stages: an Eocene-Oligocene rift and a Neogene-Quaternary postrift thermal subsidence [24]. In response to the structural evolution, the sedimentary deposition environment changed from paleolakes in the early stage to an open-marine setting in the late stage. The Wenchang and Enping formations in this basin are the source rocks of the Eocene rift stage with a total thickness of 3000 m. During the postrifting stage, the SCS entered into a period of subsidence. The thickness of marine facies in this stage came up to 6000 m because Baiyun sag located at the downdip direction of paleo-Pearl River and the sea level decreased. In the QDN basin, the Yacheng Formation was deposited during the early Oligocene consisting mainly of neritic mudstones and coastal plain coal-bearing strata which was the main hydrocarbon source rock in this basin [25].

The SCS has the favorable temperature and pressure condition for the formation of gas hydrate. The water depth ranges from 150 to 3700 m. The QDN basin is characterized by the geothermal gradients with the values of $39\text{--}41^\circ\text{C}/\text{km}$ and high sedimentation rates (up to $1.2 \text{ mm}/\text{yr}$). The average geothermal gradient in the PRM basin is about $36^\circ\text{C}/\text{km}$. However, it goes up to $67.7^\circ\text{C}/\text{km}$ in the gas hydrate drilling zone from the in situ temperature measurement [26].

3. Seismic Data and Methods

3.1. Data. The seismic line A and line C were collected in 2006 with the following a 3000-m long streamer with 240 channels (trace interval 12.5 m) and a tuned airgun source with a total volume of $8 \times 20 \text{ inch}^3$ shooting every 25 m. The seismic processing sequences mainly include prefiltering, true amplitude recovery, noise attenuation, deconvolution, velocity analysis (first), residual statics, velocity analysis (second), multiple attenuation, DMO velocity analysis, DMO stack, and noise attenuation. The seismic line B is one of the 3D seismic data with the same location of seismic line A. The seismic data were acquired by the single-source and single-streamer method using the influence of ocean current on the cable so that the dense 2D seismic data can form one

overlap. As the azimuth angle is narrow and the aim layer is shallow, the processing method is quite different from the traditional 3D seismic processing. The true amplitude, noise attenuation, and deconvolution were used to emphasize the characterization of gas hydrate. The data were processed with a bin spacing in the in-line and cross-line directions of 12.5 m and 25 m, respectively [28].

3.2. Constrained Sparse Spike Inversion (CSSI). Acoustic impedance is obtained from the product of density and seismic velocity, so it can be defined as a layer property and not as an interface property. The acoustic impedance can be directly related to porosity, lithology, and permeability. Although seismic data can be interpreted on its own without inversion, but this does not provide the most detailed view of the subsurface and can be misleading under certain conditions.

Seismic inversion has been used for several decades in the petroleum industry. Seismic inversion methods have progressed from the initial recursive inversion to present software package available to transform band-limited seismic traces to impedance traces. Stochastic seismic inversion combined the seismic and log data to derive the vertical resolution from the log data [29]. Constrained sparse spike inversion (CSSI) is based on seismic data and low-frequency impedance information obtained from well data. Although strictly speaking this technique does not depend on well data, the precision of the results does depend somewhat on the number of wells used. The inversion of seismic data to obtain acoustic impedance for the Baiyun sag was performed with the CSSI package of Jason Geosystems, which involves the following stages.

(1) Wavelet is estimated by using seismic and pseudowell data at the arbitrary CMP. We first create the Ricker wavelet and then we make synthetic seismogram at different locations. The input wavelet was the scaled average wavelet based on different wells. (2) The low-frequency information is constructed by using the EarthModel model generator. The trace gate, solid model created using the interpreted horizons and structural information, and the interpolation method of natural neighbour were chosen to generate the low frequency impedance data. (3) The bandpass P-impedance data are obtained by choosing the sparse spike parameters such as weighting factor in the inversion process. (4) Last, the low-frequency model is merged with the band pass P-impedance.

CSSI determines the acoustic impedance within prescribed constraints by minimizing the objective function

$$F_{\text{obj}} = \sum (r_i)^p + \lambda^q \sum (d_i - s_i)^q \quad (1)$$

at time i , where r_i is the reflection coefficient, d_i the recorded seismic trace, s_i the synthetic trace, p and q empirically determined exponents, and λ the data mismatch weighting factor. The match between output impedance and seismic data is determined by λ . If λ is lower than the “true” value, then the match between the synthetic trace and the recorded seismic data worsens and the output impedance is very approximate. As λ approaches its “true” value, the match improves and the output impedance provides a better

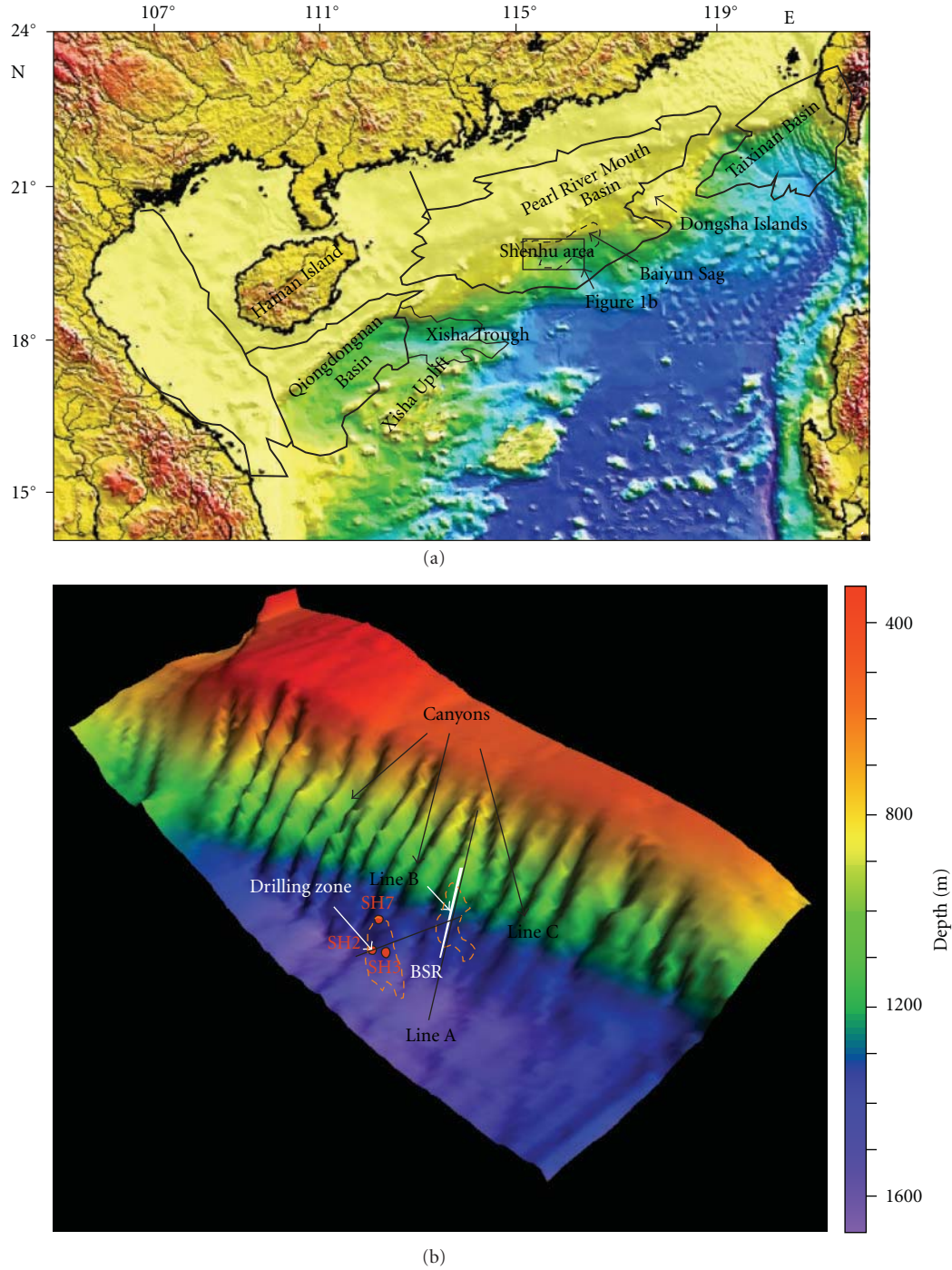


FIGURE 1: (a) Areas of gas hydrate exploration in the northern part of the South China Sea and the gas hydrate drilling zone of Shenhu area, Baiyun sag; (b) Bathymetric map of Baiyun sage that was interpolated by the 2D seismic data in this area. Modern canyons shown by Zhu et al. [23] were also identified. Black lines and white line show seismic line A, line B, and line C used in the paper. The zones surrounded by broken yellow lines show the BSR on the seismic lines and in the gas hydrate drilling zone in 2007 [26].

description of the physical properties of the sediment. The factors p (reflectivity norm) and q (seismic mismatch norm) are 1 and 2 by default, respectively. The value of λ is optimized for signal-to-noise, correlation misfit, seismic misfit, and reflectivity misfit. For the inversion of seismic line, we used $\lambda = 13$, $p = 1$, and $q = 2$.

3.3. Seismic Attributes. Seismic attributes like instantaneous frequency, instantaneous phase, blanking, and reflection strength have been used to identify gas hydrate from seismic data [30–32].

The Variance Cube operation was used to highlight faults and subtle stratigraphic features in a 3D seismic volume.

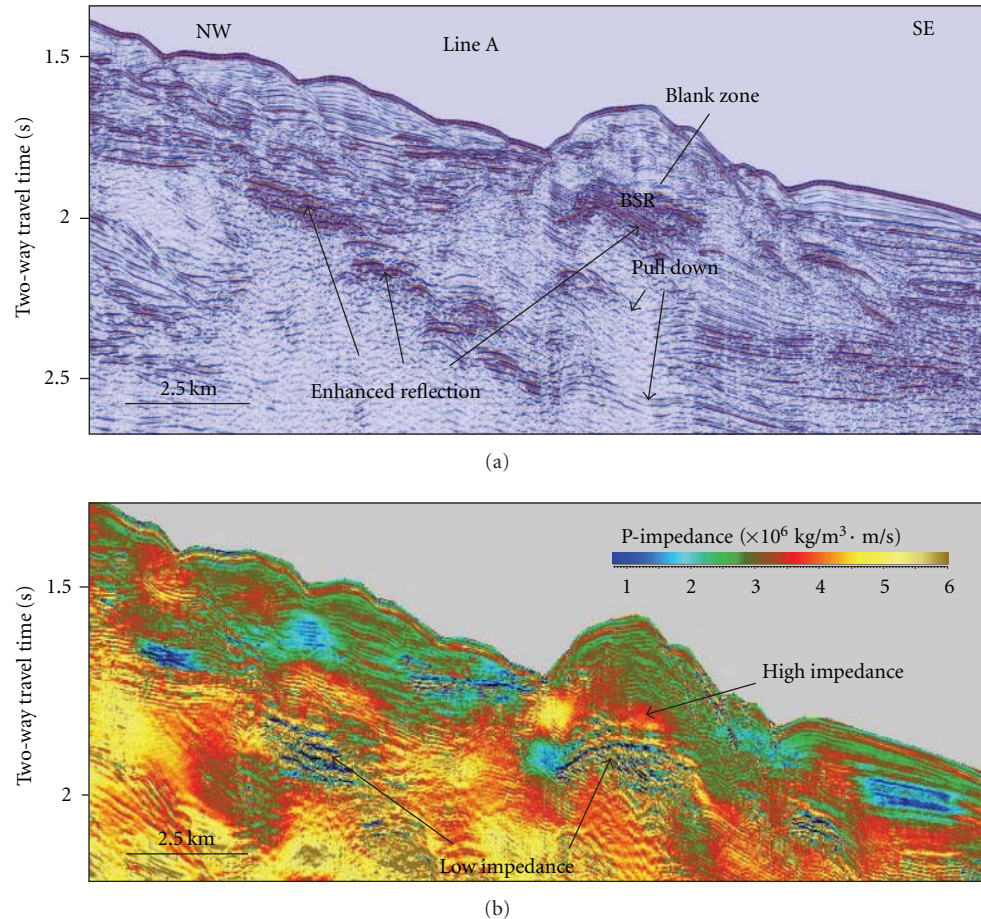


FIGURE 2: In Baiyun sag. (a) The variable-density display of part profile of seismic line A; A strong bottom-simulating reflector and enhanced reflections can be easily identified. (b) The acoustic impedance estimation obtained by CSSI. High acoustic impedance above the BSR is present and low impedance is shown below the BSR.

In the output cube, incoherent (high amplitude) areas are displayed in high contrast (black). In the Seis 3DV, the output variance cube can be shown the inline or crossline profile and compared it with the seismic profile. As the 3D seismic data is pseudo-3D seismic data, we calculated the coherence in larger window length and we compare it with the seismic profile. The output values vary between 0 indicating the worst, and 1 indicating the best.

The instantaneous frequency is a time or depth derivative of the instantaneous phase and a measure of the frequency of the waveform at every sample. It is independent of reflection magnitude, weak events, and noise, which are all equally weighted in display. The minimum and maximum frequencies can be given in the output. The instantaneous frequency attribute is considered a good tool for lateral seismic character correlation. Oil and gas may preferentially attenuate higher frequencies so a low instantaneous frequency anomaly has been used to predict conventional hydrocarbons accumulations in the oil industry.

The reflection strength is simply an expression of the amplitude envelope of the seismic trace and is independent of phase. It shows the total energy of the seismic signal and has the maximum value at point other than the peak or trough

of the real trace, especially when the event is the composite of several reflections [28]. The reflection strength depends on the contrast of acoustic impedance. The strong reflection indicates the apparent changes in the seismic impedance contrast.

4. Results

4.1. Geophysical Attributes. One reflector is located at about 280 ms of two-way travel time below seafloor, which has the reversed polarity compared with the seafloor in seismic line A (Figure 2). Blanking is the reduction of amplitude of the seismic reflection, which appears to be caused by the presence of gas hydrate. Amplitude blanking is identified above this reflector. On the upper slope within the Baiyun sag, this reflector and associated amplitude anomalies are relatively indistinct comparing to the ridge crest. Enhanced reflections are identified in the shallow sediments. Below this reflector of the crest, the down-warped reflectivity may be related to the presence of focused or concentrated gas. This anomaly is interpreted as a reduction of the seismic velocity (pull-down effect) through a gas-charged column. The acoustic impedances above this reflector range from

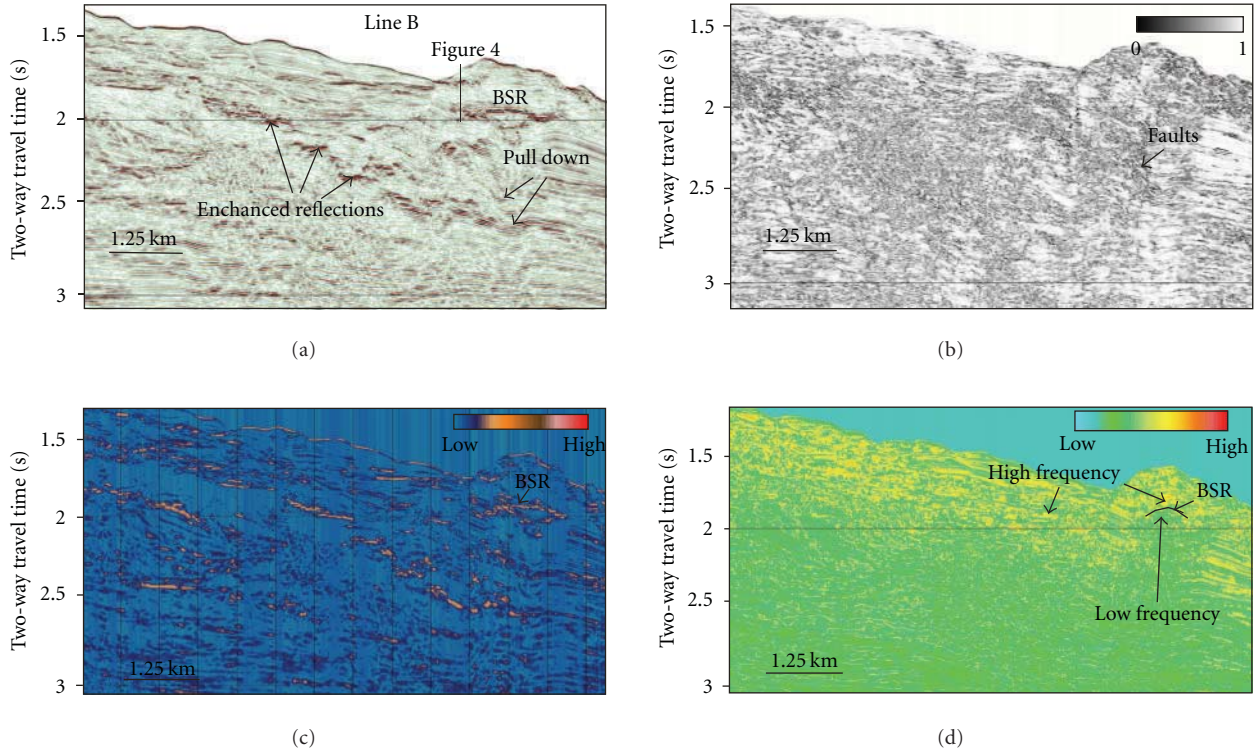


FIGURE 3: (a) Part of seismic line B that is parallel to seismic line A, which can show the continuous reflections of the sediments. Enhanced reflections are identified at the similar locations to seismic line A; (b) Coherence profile for the seismic line B showing the faults and subtle stratigraphic change. (c) Reflection strength profile for the line, showing loss of amplitude above the BSR and the enhanced reflection. (d) Instantaneous frequency profile shows high frequency above the interpreted BSR caused by the presence of gas hydrate and low frequency zone below the interpreted BSR caused by the presence of free gas.

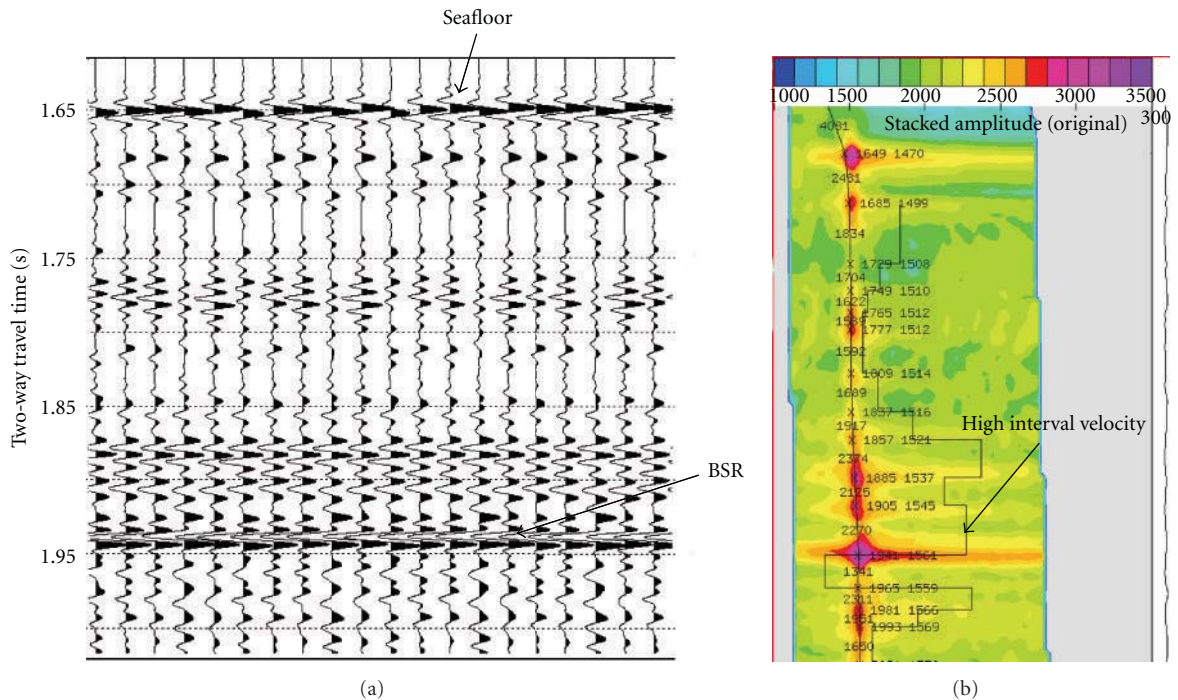


FIGURE 4: CMP gather shows how interval velocities were obtained. (a) Normal-moveout-corrected CMP gather shown in Figure 3(a). (b) shows the semblance plot and the interval velocity calculated from the Dix equation for the crosses locations. Higher interval velocity is shown in the layer of 1.85–1.95 s.

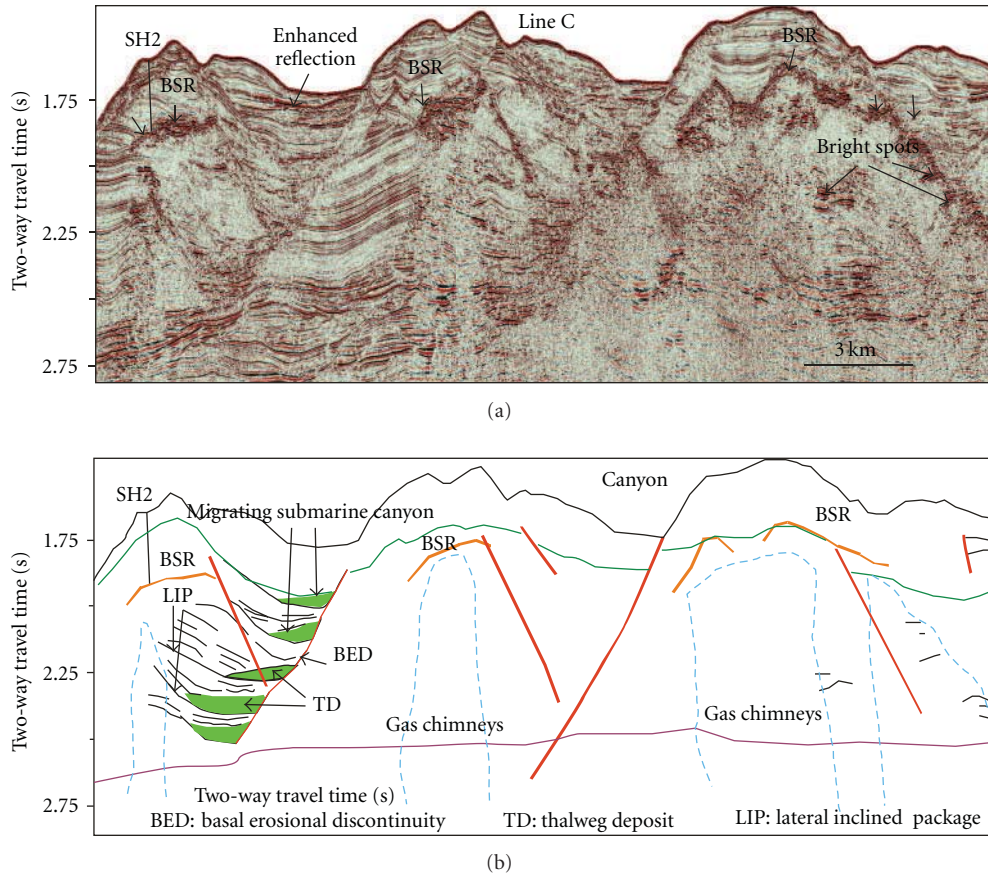


FIGURE 5: Part of seismic line C profile (a) and interpreted profile showing BSR, gas chimneys, and migrating submarine canyons, Baiyun Sag, Pearl River Mouth Basin, South China Sea (b).

3.5×10^6 to 4.5×10^6 $\text{kg/m}^3 \cdot \text{m/s}$, which have higher impedances than the sediments of water-saturated zone indicating the presence of gas hydrate above this reflector. Below it, lower impedance indicates the presence of free gas.

Seismic line B is one of the inline of 3D seismic data which is parallel to seismic line A (Figure 1). We put them together to obtain more seismic attributes and to show the evidence of gas hydrate in this region from seismic profile. The reflector of seismic line B is more continuous than that of seismic line A. Seismic line B shows the reflectors clearly in the several zone where they are wipe-out reflection or lower amplitude in seismic line A. However, the pull-down effect and enhanced reflection below the reflector of reversed polarity to seafloor are more prominent in the seismic line B profile (Figure 3(a)). The coherence profile can show the faults and the chaotic reflection below the bright spots (Figure 3(b)). Figure 3(c) shows the reflection strength for the seismic line B. Blue and red show the amplitude anomalies with low and high amplitudes, respectively. The blanking zone in the seismic profile and the coherence is better, which may be caused by the cementation of gas hydrate. The instantaneous frequency profile in Figure 3(d) shows the high frequencies in red and the low frequencies in green. The lower instantaneous frequency may be caused by the presence of free gas. The frequency indicates that the

attenuation in free gas-bearing sediment is higher than that of gas hydrate-bearing sediments.

4.2. P-Wave Velocity. Geophysical attributes show an indicator of the presence of gas hydrate in seismic lines A and B. The direct indicator of gas hydrate is the study of the anomalies in the P-wave velocity above and below BSR. Higher velocities should be associated with gas hydrate and lower velocities should be associated with free gas. Figure 4 shows the CMP gather in Figure 3(a) location. It shows numerous clear reflections and semblance peaks. The stacking velocity picks were made at the locations where the semblances are high. The interval velocities show anomalously high at 1.85–1.95 s, which range from 1850 to 1900 m/s (Figure 4). The high interval velocity above the strong reflector of the crest indicates a gas hydrate-bearing zone near the drilling area in 2007.

4.3. Seismic Facies of Canyons. Seismic line C passed through site SH2 (Figure 5). BSRs identified in the Baiyun sag are stronger at the ridges of submarine canyons than those of the canyons axes. Seismic profile shows that canyon walls abruptly terminate surrounding sub-parallel-bedded, inclined reflections which are interpreted as progradational deposits.

The submarine canyon near site SH2 was interpreted to show the migration of the canyon. It has been referred that the thalwegs of the submarine canyons are progressively offset toward the northeast from the middle Miocene to present [23], which also was identified in Figure 5. Each cycle of the canyon is marked by a basal erosional discontinuity (BED) at the base. The thalweg deposits (TD) are overlain by a lateral inclined package (LIP) and are marked by lens-shaped, parallel, high amplitude, continuous reflections that onlap basal erosional discontinuities. Canyon margin deposits consist of continuous reflections with high amplitude, and truncated by basal erosional discontinuities. Gas chimneys are identified below crests of submarine canyons and are characterized vertical disturbances in seismic data and low seismic amplitudes, which are interpreted to be associated with the upward migration of free gas (Figure 5). Gas chimneys and the erosion of migrating submarine canyons acted as major pathways for gas migration. Bright spots shown below the base of gas hydrate stability (BGHS) indicate that the occurrence of gas hydrate decrease the permeability of the sediments. Gas was trapped below the gas hydrate stability zone, which has been identified from the low acoustic impedance in seismic line A (Figure 2(b)).

5. Conclusion

Gas hydrates have been identified by the gas hydrate drilling exploration at the Shenhu area, Baiyun sag, Pearl River Mouth basin, South China Sea. Another gas hydrate province was identified at the adjacent canyon by using new seismic data and seismic attributes. Amplitude blanking, high acoustic impedance, high frequency and enhanced reflections identified from the 2D and 3D seismic profiles at about 280 ms of two-way travel time below seafloor were caused by the presence of gas hydrate. The reflector that is subparallel to the seafloor and cuts across the strata is the BSR. The acoustic impedance profile has lower impedance below it. A strong reflection at the BSR was observed in the reflection strength profile, and low frequencies were seen below the BSR from the instantaneous frequency profile. These anomalies suggest the presence of free gas below the BSR. The distribution of BSRs has a close relationship with the submarine canyons and gas chimneys. Prominent and strong BSRs exist in the crests of the migrating submarine canyons in the middle of Baiyun sag. Few BSRs are found in the axes of these canyons, which are controlled by the geological setting in this basin.

Acknowledgments

The authors would like to thank the team of Guangzhou Marine Geological Survey for shooting the seismic data used in this paper. Our research is supported by the International Science and Technology Cooperation Program of China (2010DFA21740), National Basic Research Program (2009CB219505), and Key Laboratory of Marine Hydrocarbon Resources and Environmental Geology, Ministry of Land and Resources (MRE201105).

References

- [1] K. A. Kvenvolden and T. D. Lorenson, "The global occurrence of natural gas hydrates," in *Natural Gas Hydrates: Occurrence, Distribution and Detection*, C. K. Paull and W. P. Dillon, Eds., Geophys Monogr Ser, 124, pp. 3–18, AGU, Washington, DC, USA, 2001.
- [2] B. A. Buffett, "Clathrate hydrates," *Annual Review of Earth and Planetary Sciences*, vol. 28, pp. 477–507, 2000.
- [3] W. P. Dillon and C. Paull, "Marine gas hydrates, II—Geophysical evidence," in *Natural Gas Hydrates: Properties, Occurrences and Recovery*, J. L. Cox, Ed., pp. 73–90, Butter Worths, 1983.
- [4] M. Riedel, T. Collett, and M. Malone, "Expedition 311 scientists," in *Proceedings of the Integrated Ocean Drilling Program, 311*, Ocean Drilling Program, Washington, DC, USA, 2006.
- [5] J. Ashi, H. Tokuyama, and A. Taira, "Distribution of methane hydrate BSRs and its implication for the prism growth in the Nankai Trough," *Marine Geology*, vol. 187, no. 1-2, pp. 177–191, 2002.
- [6] C. C. Lin, A. T.-S. Lin, C. S. Liu, G. Y. Chen, W. Z. Liao, and P. Schnurle, "Geological controls on BSR occurrences in the incipient arc-continent collision zone off southwest Taiwan," *Marine and Petroleum Geology*, vol. 26, no. 7, pp. 1118–1131, 2009.
- [7] A. M. Tréhu, P. E. Long, M. E. Torres et al., "Three-dimensional distribution of gas hydrate beneath southern Hydrate Ridge: constraints from ODP Leg 204," *Earth and Planetary Science Letters*, vol. 222, no. 3-4, pp. 845–862, 2004.
- [8] W. S. Holbrook, H. Hoskins, W. T. Wood, R. A. Stephen, and D. Lizarralde, "Methane hydrate and free gas on the Blake Ridge from vertical seismic profiling," *Science*, vol. 273, no. 5283, pp. 1840–1843, 1996.
- [9] T. S. Collett, C. C. Knapp, A. H. Johnson, and R. Boswell, "Natural gas hydrate: a review," *AAPG Memoir*, vol. 89, pp. 146–219, 2009.
- [10] X. Wang, S. Wu, S. Yuan et al., "Geophysical signatures associated with fluid flow and gas hydrate occurrence in a tectonically quiescent sequence, Qiongdongnan Basin, South China Sea," *Geofluids*, vol. 10, no. 3, pp. 351–368, 2010.
- [11] K. Sain and H. Gupta, "Gas-hydrates: Indian scenario," *Journal of the Geological Society of India*, vol. 72, no. 3, pp. 299–311, 2008.
- [12] I. A. Pecher, S. A. Henrys, W. T. Wood et al., "Focussed fluid flow on the Hikurangi Margin, New Zealand—evidence from possible local upwarping of the base of gas hydrate stability," *Marine Geology*, vol. 272, no. 1-4, pp. 99–113, 2010.
- [13] G. J. Crutchley, A. R. Gorman, I. A. Pecher, S. Toulmin, and S. A. Henrys, "Geological controls on focused fluid flow through the gas hydrate stability zone on the southern Hikurangi Margin of New Zealand, evidenced from multi-channel seismic data," *Marine and Petroleum Geology*. In press.
- [14] S. Lu and G. A. McMechan, "Elastic impedance inversion of multichannel seismic data from unconsolidated sediments containing gas hydrate and free gas," *Geophysics*, vol. 69, no. 1, pp. 164–179, 2004.
- [15] G. K. Westbrook, S. Chand, G. Rossi et al., "Estimation of gas hydrate concentration from multi-component seismic data at sites on the continental margins of NW Svalbard and the Storegga region of Norway," *Marine and Petroleum Geology*, vol. 25, no. 8, pp. 744–758, 2008.
- [16] J. M. Carcione, D. Gei, G. Rossi, and G. Madrussani, "Estimation of gas-hydrate concentration and free-gas saturation

- at the Norwegian-Svalbard continental margin,” *Geophysical Prospecting*, vol. 53, no. 6, pp. 803–810, 2005.
- [17] M. Riedel, G. Bellefleur, S. Mair, T. A. Brent, and S. R. Dallimore, “Acoustic impedance inversion and seismic reflection continuity analysis for delineating gas hydrate resources near the Mallik research sites, Mackenzie Delta, Northwest Territories, Canada,” *Geophysics*, vol. 74, no. 5, pp. B125–B137, 2009.
- [18] H. Q. Zhang, S. X. Yang, N. Y. Wu et al., “Successful and surprising results for China’s first gas hydrate drilling expedition. Fire in the Ice,” *Methane Hydrate Newsletter, National Energy Technology Laboratory, US Department of Energy*, Fall issue 6-9, 2007.
- [19] S. Wu, G. Zhang, Y. Huang, J. Liang, and H. K. Wong, “Gas hydrate occurrence on the continental slope of the northern South China Sea,” *Marine and Petroleum Geology*, vol. 22, no. 3, pp. 403–412, 2005.
- [20] T. M. Guo, B. H. Wu, Y. H. Zhu, S. S. Fan, and G. J. Chen, “A review on the gas hydrate research in China,” *Journal of Petroleum Science and Engineering*, vol. 41, no. 1–3, pp. 11–20, 2004.
- [21] S. Wu, X. Wang, H. K. Wong, and G. Zhang, “Low-amplitude BSRs and gas hydrate concentration on the northern margin of the South China Sea,” *Marine Geophysical Researches*, vol. 28, no. 2, pp. 127–138, 2007.
- [22] G. X. Zhang, Y. Y. Huang, Y. H. Zhu, and B. H. Wu, “Prospect of gas hydrate resources in the South China Sea,” *Marine Geology and Quaternary Geology*, vol. 22, no. 1, pp. 75–81, 2002 (Chinese).
- [23] M. Zhu, S. Graham, X. Pang, and T. McHargue, “Characteristics of migrating submarine canyons from the middle Miocene to present: Implications for paleoceanographic circulation, northern South China Sea,” *Marine and Petroleum Geology*, vol. 27, no. 1, pp. 307–319, 2010.
- [24] K. Ru and J. D. Pigott, “Episodic rifting and subsidence in the South China Sea,” *AAPG Bulletin*, vol. 70, pp. 1136–1155, 1986.
- [25] W. Zhu, B. Huang, L. Mi, R. W. T. Wilkins, N. Fu, and X. Xiao, “Geochemistry, origin, and deep-water exploration potential of natural gases in the Pearl River Mouth and Qiongdongnan Basins, South China sea,” *AAPG Bulletin*, vol. 93, no. 6, pp. 741–761, 2009.
- [26] N. Y. Wu, S. X. Yang, H. Q. Zhang, J. Q. Liang, H. B. Wang, and J. A. Lu, “Gas hydrate system of Shenhu area, northern South China Sea: wire-line logging, geochemical results and preliminary resources estimates,” *OCT 20485*, pp. 1–13, 2010.
- [27] M. J. Higginson, J. R. Maxwell, and M. A. Altabet, “Nitrogen isotope and chlorin paleoproductivity records from the Northern South China Sea: remote vs. local forcing of millennial- and orbital-scale variability,” *Marine Geology*, vol. 201, no. 1–3, pp. 223–250, 2003.
- [28] H. N. Xu, H. Shu, L. Q. Li, M. Zhang, and G. X. Zhang, “3-D seismic data processing techniques for gas hydrate by the single-source and single-cable acquisition method,” *Progress in Geophysics*, vol. 24, no. 5, pp. 1801–1806, 2009 (Chinese).
- [29] G. Robinson, “Stochastic seismic inversion applied to reservoir characterization,” *CSEG Recorder*, pp. 36–40, 2001.
- [30] N. Satyavani, K. Sain, M. Lall, and B. J. P. Kumar, “Seismic attribute study for gas hydrates in the Andaman Offshore India,” *Marine Geophysical Researches*, vol. 29, no. 3, pp. 167–175, 2008.
- [31] M. H. Taylor, W. P. Dillon, and I. A. Pecher, “Trapping and migration of methane associated with the gas hydrate stability zone at the Blake Ridge Diapir: new insights from seismic data,” *Marine Geology*, vol. 164, no. 1–2, pp. 79–89, 2000.
- [32] M. Ojha and K. Sain, “Seismic attributes for identifying gas-hydrates and free-gas zones: application to the Makran accretionary prism,” *Episodes*, vol. 32, no. 4, pp. 264–270, 2009.

Research Article

Assessment of Marine Gas Hydrates and Associated Free Gas Distribution Offshore Uruguay

**Juan Tomasini,¹ Héctor de Santa Ana,¹ Bruno Conti,¹ Santiago Ferro,¹
Pablo Gristo,¹ Josefina Marmisolle,¹ Ethel Morales,¹ Pablo Rodriguez,¹
Matías Soto,¹ and Gerardo Veroslavsky²**

¹ ANCAP, Exploración y Producción, Paysandú s/n y Avenida del Libertador, 6to piso, 11100 Montevideo, Uruguay

² Departamento de Evolución de Cuencas, Facultad de Ciencias, Instituto de Ciencias Geológicas, Iguá 4225, 11400 Montevideo, Uruguay

Correspondence should be addressed to Juan Tomasini, jtomasini@ancap.com.uy

Received 14 June 2011; Revised 29 July 2011; Accepted 2 August 2011

Academic Editor: Xuewei Liu

Copyright © 2011 Juan Tomasini et al. This is an open access article distributed under the Creative Commons Attribution License, which permits unrestricted use, distribution, and reproduction in any medium, provided the original work is properly cited.

Natural gas hydrates are crystalline solids formed by natural gas (mainly methane) and water that are stable under thermobaric conditions of high pressure and low temperature. Methane hydrate is found in polar areas of permafrost and in offshore basins of continental margins. These accumulations may represent an enormous source of methane. Based on global estimations of methane concentration in natural gas hydrates, the methane content may be several times greater than those of technically recoverable, conventional natural gas resources. In the continental margin of Uruguay, seismic evidence for the occurrence of gas hydrate is based on the presence of (bottom simulating reflectors) BSRs in 2D seismic reflection sections. Here we present results regarding gas hydrates and associated free gas distribution assessment offshore Uruguay, based on BSR mapping and applying a probabilistic approach. A mean value of 25,890 km² for the area of occurrence shows a great potential for this nonconventional resource, encouraging further research.

1. Introduction

Natural gas hydrates are crystalline solids formed by natural gas (mainly methane) and water that are stable under thermobaric conditions of high pressure and low temperature [1].

Methane hydrate occurs in sediments within and below thick permafrost in Arctic regions and in the subsurface of most continental margins where water depths are greater than 500 meters [2].

Gas hydrate accumulations may represent an enormous source of methane. Based on global estimations of methane concentrations, the methane content is about 2 to 10 times greater than those of technically recoverable conventional natural gas resources [2]. The existence of such a large methane hydrate resource has provided a strong global research incentive and international interest, which has grown in the last years.

The first acoustic indication of gas hydrate occurrence is given by presence of (bottom simulating reflection) BSR

in seismic sections due to a significant change in acoustic impedance between sediment containing hydrates and sediments containing free gas [3, 4]. The seismic appearance is parallel to seafloor reflection with a polarity reversal with respect to the seafloor.

The BSR is usually a good indication of gas trapped below the base of the gas hydrate stability zone (GHSZ) implying that gas hydrates are present [1]. On the other hand, gas hydrate can exist without creating a well-defined BSR, especially when gas fluxes are directed through faults or comparable permeable fluid pathways [1].

In offshore basins around the world the base of the GHSZ can have different seismic expressions such as continuous, segmented, and high-relief BSRs depending on the stratigraphic, fluid, and geothermal setting [5].

Another seismic response associated with the presence of gas hydrates in marine sediment is the blanking (reduction of the amplitude of seismic reflections). It can be used to identify sediments, in which hydrates have been formed. However, blanking is not a good indicator of the base of

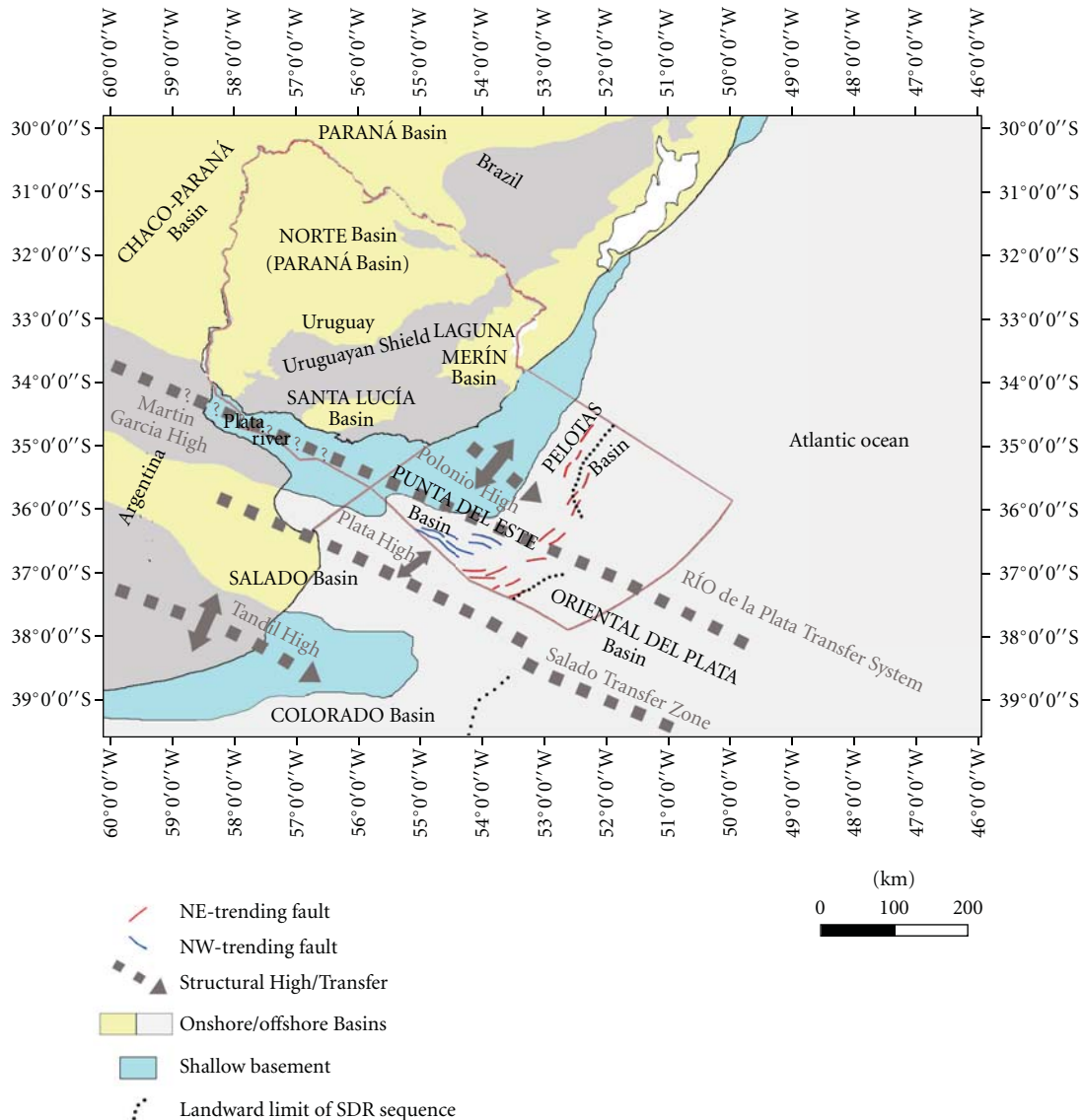


FIGURE 1: Sedimentary basins of Uruguay. After Soto et al. [7].

GHSZ because there are several possibilities leading to signal attenuation, like the original or diagenetic character of strata as well as artifacts produced during seismic processing [1].

The study area for this work is the continental margin of Uruguay. This margin was formed during continental rifting and seafloor spreading, which included strong volcanic activity [6]. Three offshore basins were created during this process: Punta del Este, Pelotas, and Oriental del Plata basins (Figure 1) [7], which have a total extent, within the 200 nautical miles limit, of near 85,000 km² and a maximum volcano-sedimentary fill of 8,000 m based on seismic data [7]. This volcano-sedimentary fill comprises Juro-Cretaceous to recent sequences and is worth to mention the presence of a Paleozoic pririft correlative with Parana Basin records.

These basins are genetically related to the Western Gondwana breakup (~130 Ma ago) and the subsequent

development of the Atlantic Ocean and thus, are part of an important series of depocenters which include offshore hydrocarbon productive basins such as Santos and Campos basins (Brazil) and also the conjugate Orange Basin (South Africa and Namibia) [7].

The Punta del Este Basin is a mainly NW-SE trending aborted rift, perpendicular to the general trend of the continental margin [8]. In contrast, the NE-SW trending Pelotas Basin belongs to the flexural border of a precursor rift structure and continues in the Brazilian margin up to the Florianópolis Platform [7].

The Punta del Este and Pelotas basins are separated in shallow waters by the Polonio High. The distal part of both basins, where the Polonio High is not present and comprises a thick Cenozoic package, is called by some authors the Oriental del Plata Basin (Figure 1) [9, 10], which according to a recent redefinition has been restricted to the

TABLE 1: Offshore Uruguay seismic survey's details.

Survey	Acquisition company	Year	Number of lines	Length (km)
UR70	CGG	1970	12	2571
UR71	CGG	1971	32	2696
UR74	GSI	1974	35	2578
UR75	GSI	1975	28	1897
UR77	GSI	1977	16	1050
UR82	WESTERN	1982	23	1402
UR02	CGG	2002	6	1850
UR07	WAVEFIELD-INSEIS	2007	32	7125
UR08	WAVEFIELD-INSEIS	2008	22	2909

southern region of the continental margin, comprising only transitional and oceanic crust [7].

Different water masses and currents coexisting in the area play a fundamental role in the occurrence of gas hydrates considering temperature, salinity, and pressure conditions as well as sediment erosion and deposition.

Today, the continental margin of Uruguay is characterized by strong contour currents and the important input of huge amounts of sediments from the Río de la Plata river [11].

The area comprises a very complex and dynamic oceanographic regime. At surface level, dense and cold antarctic water masses from the Malvinas/Falkland Current flowing northward converge with the warm and saline Brazil Current flowing towards the South, resulting in the Brazil-Malvinas Confluence [12].

However, the confluence is not confined to surface currents, and also the interaction of intermediate water masses results in a complicated flow pattern. While antarctic intermediate water (AAIW) and circumpolar deep water (CDW) are flowing northward, the southward flowing north atlantic deep water (NADW) separates the CDW into Upper-CDW and Lower-CDW. The deep basins are under the influence of the antarctic bottom water (AABW) [13].

Interaction between these currents strongly affects sedimentary processes as well as margin morphology. The existence of strong contour currents leads to the generation of a large Contouritic Depositional Complex, which at least extends from southern Argentine margin to the margin of Uruguay, including various kinds of erosive and depositional sedimentary features [14].

Although strong deep currents are not favorable for organic matter deposition and preservation, contouritic deposits have been frequently associated both with conventional hydrocarbon reservoirs and with gas hydrate accumulations [15]. Indeed, big hydrate accumulations inferred from BSRs have been found in contouritic deposits along Atlantic margin [15].

In addition, these along-slope processes interact with downslope sedimentary gravitational processes, which have a large impact in the study area. In this way, mainly in the southern region (Punta del Este Basin), a series of submarine channels are developed.

Conventional hydrocarbon reservoirs associated with turbiditic sequences are well known while methane hydrate accumulations in this type of sequences have been reported as drilling targets offshore Japan [16].

First work regarding gas hydrates offshore Uruguay was performed by de Santa Ana et al. [17], where the presence of a BSR was recognized for the first time. Gas hydrate distribution and thickness were afterwards estimated based on the available seismic grid allowing first approximations on resource potential. Initial determination of mineralized area was 5,000 km² resulting in 86 trillion cubic feet (TCF) of natural gas under normal conditions [17], based on seismic information available at that time in nondigital format.

In 2005, the presence of gas hydrates was reported by Neben et al. from the German institute BGR after a 2D seismic survey in the area [18]. In this work, the BSR area was mapped from seismic sections acquired at that survey, resulting in a minimum of approximately 7,000 km².

Even if the BSR represents the most reliable indication of the existence of gas hydrates within the study area, high methane concentrations and (anaerobic oxidation of methane) AOM within the upper few meters of the sediments suggest the existence of methane hydrate in the study area [19].

Hydrocarbon generation and migration offshore Uruguay have been confirmed through fluid inclusion analysis [20], which were recognized in synrift and postrift sequences from two wells drilled in the area [21].

In 2008, oil seeps were identified by satellite images [10, 22], and poststack processing for gas chimney identification [23] was performed on 2D seismic sections, which showed vertical disturbances of the seismic signal. These signal anomalies, reaching into higher depths, were interpreted as hydrocarbon migration pathways and suggest a thermogenic origin of the gases that reach gas hydrate reservoirs [24].

All these evidences of hydrocarbon generation strongly indicate that thermogenic provenance of gas to form gas hydrates in upper sequences, as the only or combined with biogenic gas origin, is very plausible.

In this work, the integration of a dense grid of different 2D seismic surveys acquired offshore Uruguay was done for first time in order to identify the base of the GHSZ and assess gas hydrate and associated free gas distribution within

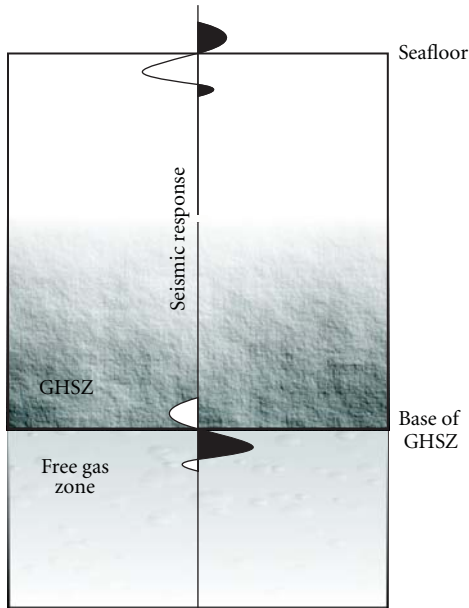


FIGURE 2: Theoretical response of seafloor and base of GHSZ.

the studied area. A probabilistic approach was considered in order to reflect the uncertainty of the interpretation, taking into account both high and low side of the mapped area and reporting a final mean value.

2. Methodology

For this work we used 2D reflection seismic data, acquired during different surveys for hydrocarbon exploration offshore Uruguay between 1970 and 2008.

More than 24,000 km of 2D reflection seismic sections were interpreted (Table 1). Seismic-stratigraphic interpretation was performed using commercial seismic interpretation software, considering reflectors attributable to the base of GHSZ, based on its theoretical response (Figure 2) and known characteristics of BSRs [1, 3, 4].

Once seismic interpretation was performed on available sections, gas hydrate and free gas spatial distribution was mapped and calculated.

3. Results

Interpretation of the base of GHSZ from seismic data in the area shows a widespread distribution of gas hydrate bearing sediments.

Continuous and segmented BSRs were observed while “high relief” BSRs were not identified. In Figure 3 we present an example of seismic wiggle showing the characteristic polarity reverse of the seafloor regarding the seafloor. For some sections, acoustic blanking is observed above a BSR cross-cutting sedimentation strata (Figure 4). In Figure 5 we present a seismic section from UR08 survey shot at Punta del Este Basin; a clear example of BSR is observed while seismic anomalies of enhanced amplitudes are present below it.

BSR was interpreted in UR70, UR71, UR74, UR77, UR82, UR02, UR07, and UR08 surveys. It is present below water

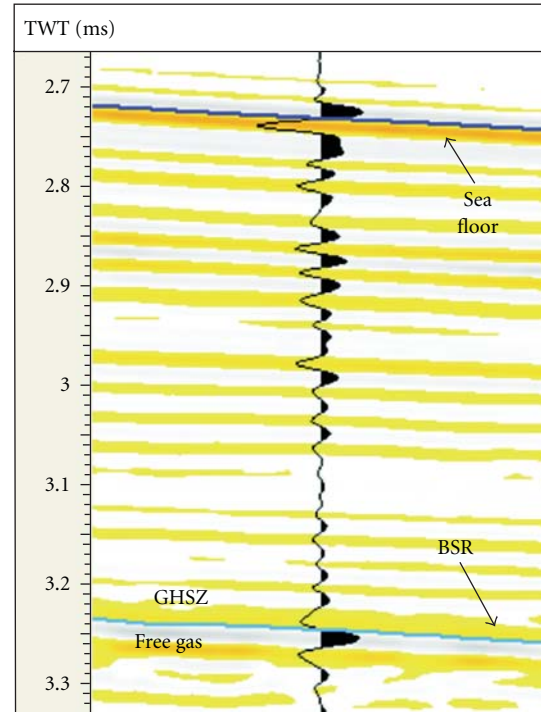


FIGURE 3: Seismic response of seafloor and base of GHSZ in seismic section from the area.

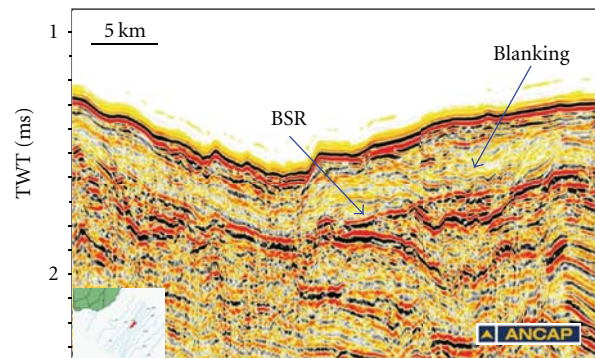


FIGURE 4: Section UR82_004 from Pelotas Basin. BSR present at 1982 survey showing blanking at the hydrate zone.

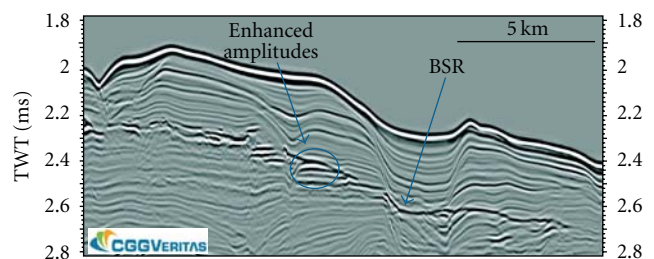


FIGURE 5: Seismic section from Punta del Este Basin showing a BSR at 0.330 sec TWT from the seafloor and enhanced amplitudes below the BGHSZ. Modified from [24]. Courtesy of CGG Veritas.

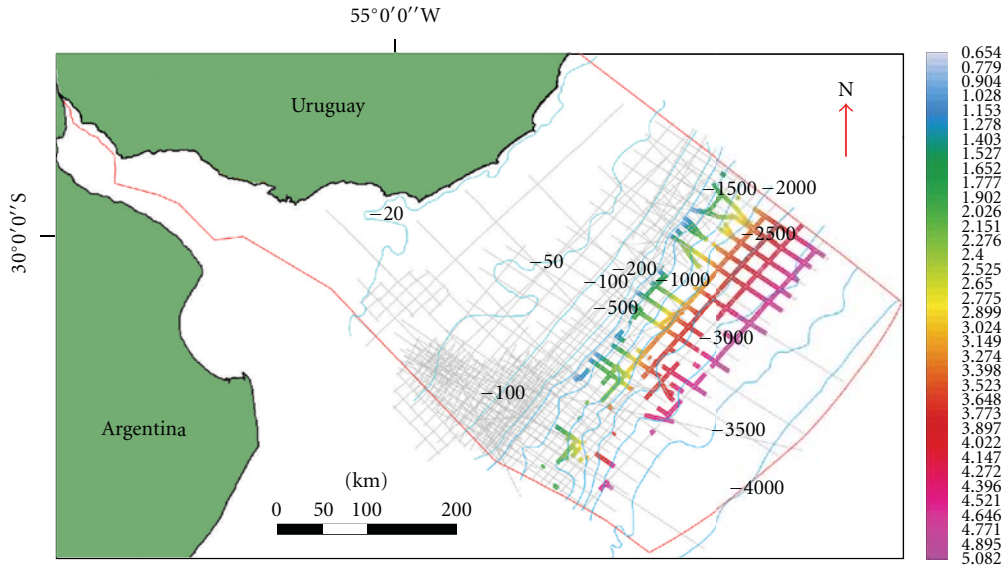


FIGURE 6: Results of BSR interpretation offshore Uruguay, showing a widespread distribution of gas hydrate bearing marine sediments. Color scale represents reflector depth in ms (TWT).

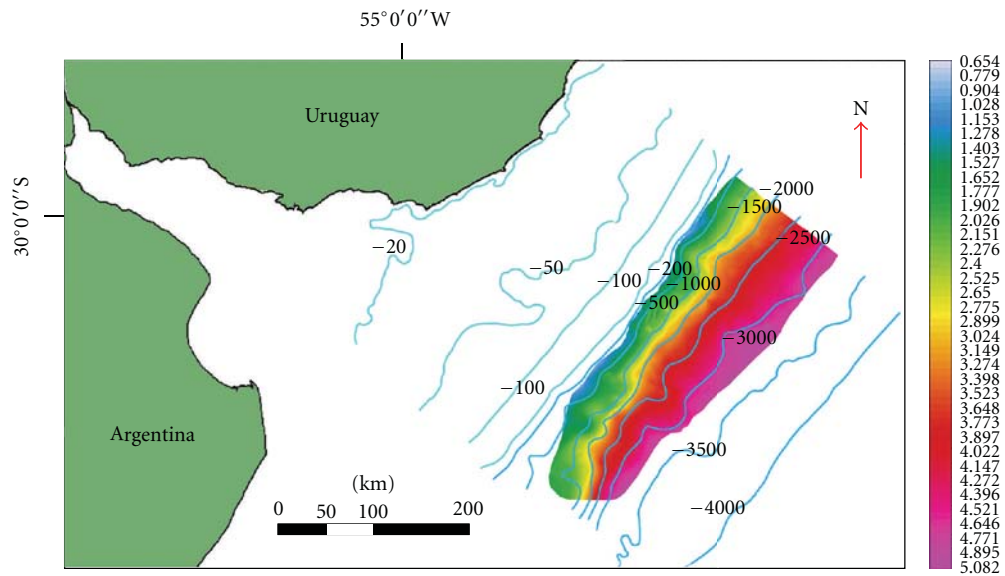


FIGURE 7: Maximum area of gas hydrate and free gas distribution, considering the envelope of BSR interpretations.

depths from 500 to 3,200 m and has high continuity in Pelotas Basin but is more discontinuous at Punta del Este Basin (Figure 6).

BSR interpretations showed in Figure 6 corresponds to 25,000 km² and for probabilistic calculation purposes is considered as the P50 of the occurrence area.

For the high side, we have mapped the total maximum area of sediments that may contain gas hydrates offshore Uruguay considering the envelope of BSR interpretations. The total maximum area corresponds to 32,500 km² (shown in Figure 7) and was considered as a P5 percentile (“larger than” convention).

The distribution chosen for the area assessment was of log-normal type as being the most common followed by nature and in particular for resource area [25]. Considering $\mu = \text{Ln}(P50)$ and truncation for values greater than P1 in order to disregard the extremely high values of the distribution, the resulting mean value for the area is $25.89 \times 10^3 \text{ km}^2$ as shown in Figure 8.

4. Discussion

In Figure 4, acoustic blanking is observed above BSR. As shown by Max et al. [1], this seismic character may have a relation with gas hydrate presence. In this case, the fact of finding

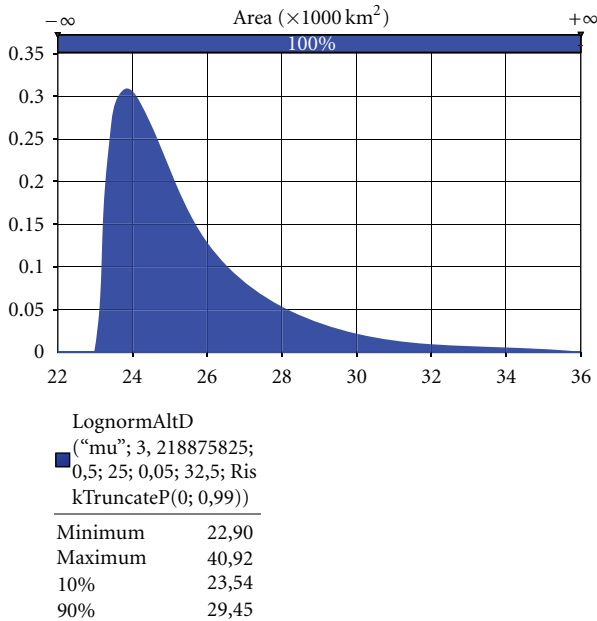


FIGURE 8: Probability density function of the lognormal distribution of gas hydrates occurrence area offshore Uruguay. $P90 = 23.54 \times 10^3 \text{ km}^2$; $P10 = 29.45 \times 10^3 \text{ km}^2$.

blanking associated with BSR supports the interpretation of hydrate occurrence. In Figure 5, seismic anomalies of enhanced amplitudes suggests the presence of free gas below the base of GHSZ opening new opportunities for further research on subhydrate prospects exploration in the area.

At basin scale, as water depth increases, the base of the GHSZ progressively extends farther below the seafloor. This increment in thickness of GHSZ responds to pressure increasing and temperature decreasing at higher water depths as showed by Max et al. [1]. As reported for several offshore basins around the world [2], gas hydrate occurrence offshore Uruguay starts developing at approximately 500 m of water depth (Figure 6). This agrees with the P-T seafloor conditions for phase equilibrium [26] of approximately 4903 KPa, 5°C, and seawater salinity of 35 PSU for a $\text{CH}_4 + \text{NaCl} + \text{H}_2\text{O}$ system [27]. Further studies are needed in order to assess possible gas hydrate formation and destabilization cycles with eustasy and its effects on seafloor stability and geohazards potential.

Towards NE direction, BSR interpretation stops at or close to the end of strike lines, as the available database does not cross the Uruguay-Brazil maritime boundary. Nevertheless, interpreted gas hydrate area offshore Uruguay is probably part of a much greater gas hydrate province, shared with Brazil, extending further north at the Pelotas Basin. This basin has the largest gas hydrate occurrence of the Brazilian coast [28, 29].

At SE direction, BSR was interpreted up to a maximum water depth of 3,200 m. Below this ultradeep water domains, parallelism of sedimentary reflectors makes the identification of BSR difficult. Nevertheless, gas hydrate may be present beyond this range of water depth as found at other locations around the world and reported by Booth et al. [30].

Distribution of gas hydrate deposits offshore Uruguay presents high continuity in the north area (*Pelotas Basin*) but is more discontinuous in the *Punta del Este Basin* (while it cannot be assessed in the *Oriental del Plata Basin* due to limited seismic data; Figure 6). This may be due to various factors, including the presence of submarine channels. The existence of this kind of morphologies associated with sediment transport processes down slope has a special importance in *Punta del Este Basin* and may be the cause of BSR interpretation absence in certain zones, mainly due to complex sedimentary disposition.

In addition, the base of GHSZ has different expressions depending on lithological characteristics of sediments, leading to cases where the BSR may not be evident. In these cases, different relative sand-clay contents may play an important role.

On the other hand, the presence of BSRs indicates the coexistence between Free Gas and Gas Hydrate phases therefore situations may exist where sediments contain hydrates but not enough free gas at the phase boundary as to generate a BSR-like seismic response.

All these different aspects regarding BSR imaging and interpretation support the importance of the probabilistic approach applied to report area of occurrence.

5. Conclusions

Gas hydrate and associated free gas occurrence presents a widespread distribution offshore Uruguay, resulting in a mean value of 25,890 km^2 , being much higher than reported by previous studies. Results show a great potential for this nonconventional resource, encouraging further research.

Further studies are needed about possible gas hydrate formation and destabilization cycles that may take place at the landward limit of the occurrence zone in order to evaluate its effect on seafloor stability and geohazard potential.

Seismic evidence of discrete free gas accumulations below the gas hydrate stability zone through amplitude anomalies was found. Those accumulations could be considered as subhydrate prospects and may play an important role considering future gas field developments offshore Uruguay.

From the exploratory point of view, determination of locations with good reservoir characteristics is critical for a comprehensive resource assessment.

Identification and quantification of high porosity and permeability sand deposits within the mapped area and GHSZ is needed in order to define exploratory targets. This will be the key element for the eventual development of gas hydrate prospects offshore Uruguay, once international research manages to prove that methane from marine gas hydrates can be produced as a technically safe, environmentally compatible, and economically competitive energy resource.

Acknowledgments

This work was performed in the framework of the Project FSE_2009_53 from the ANII. CGGVeritas and ANCAP are acknowledged for the permission to publish figures of seismic sections.

References

- [1] M. D. Max, A. H. Johnson, and W. P. Dillon, *Economic Geology of Natural Gas Hydrate*, Springer, 2006.
- [2] Committee on Assessment of the Department of Energy Methane Hydrate Research and Development Program: Evaluating Methane Hydrate as a Future Energy Resource, *Realizing the Energy Potential of Methane Hydrate for the United States*, 2010.
- [3] E. D. Sloan, *Clathrate Hydrates of Natural Gas*, Marcel Dekker, New York, NY, USA, 1998.
- [4] C. K. Pecher and W. S. Holbrook, "Seismic methods for detecting and quantifying gas hydrates," in *Natural Gas Hydrate in Oceanic and Permafrost Environments*, M. D. Max, Ed., pp. 257–294, Kluwer Dordrecht, 2000.
- [5] B. Shedd, P. Godfriaux, M. Frye, R. Boswell, and D. Hutchinson, *Occurrence and Variety in Seismic Expression of the Base of Gas Hydrate Stability in Gulf of Mexico, USA*, Fire in The Ice, Methane Hydrate Newsletter, 2009.
- [6] D. Franke, S. Neben, S. Ladage, B. Schreckenberger, and K. Hinz, "Margin segmentation and volcano-tectonic architecture along the volcanic margin off Argentina/Uruguay, South Atlantic," *Marine Geology*, vol. 244, no. 1–4, pp. 46–67, 2007.
- [7] M. Soto, E. Morales, G. Veroslavsky, H. de Santa Ana, N. Ucha, and P. Rodríguez, "The continental margin of Uruguay: Crustal architecture and segmentation," *Marine and Petroleum Geology*, vol. 28, pp. 1676–1689, 2011.
- [8] F. A. Stoakes, C. V. Campbell, R. Cass, and N. Ucha, "Seismic stratigraphic analysis of the Punta del Este Basin, offshore Uruguay, South America," *American Association of Petroleum Geologists Bulletin*, vol. 75, no. 2, pp. 219–240, 1991.
- [9] H. de Santa Ana, N. Ucha, and G. Veroslavsky, "Geología y potencial hidrocarburífero de las cuencas offshore de Uruguay," in *Proceedings of the 5th Seminario Internacional: Exploración y Producción de Petróleo y Gas*, Lima, Peru, 2005.
- [10] H. de Santa Ana, G. Veroslavsky, and E. Morales, "Potencial exploratorio del offshore de Uruguay," *Revista de la Industria Petrolera*, no. 12, pp. 48–59, 2009.
- [11] D. A. Giberto, C. S. Bremec, E. M. Acha, and H. Mianzan, "Large-scale spatial patterns of benthic assemblages in the SW Atlantic: the Río de la Plata estuary and adjacent shelf waters," *Estuarine, Coastal and Shelf Science*, vol. 61, no. 1, pp. 1–13, 2004.
- [12] R. G. Peterson and L. Stramma, "Upper-level circulation in the South Atlantic Ocean," *Progress in Oceanography*, vol. 26, no. 1, pp. 1–73, 1991.
- [13] F. J. Hernández-Molina, M. Paterlini, L. Somoza et al., "Giant mounded drifts in the Argentine Continental Margin: origins, and global implications for the history of thermohaline circulation," *Marine and Petroleum Geology*, vol. 27, no. 7, pp. 1508–1530, 2010.
- [14] F. J. Hernández-Molina, M. Paterlini, R. Violante et al., "Contourite depositional system on the Argentine slope: an exceptional record of the influence of Antarctic water masses," *Geology*, vol. 37, no. 6, pp. 507–510, 2009.
- [15] A. R. Viana, "Chapter 23 Economic Relevance of Contourites," *Developments in Sedimentology*, vol. 60, pp. 491–510, 2008.
- [16] T. Saeki, T. Fujii, T. Inamori et al., "Delineation of methane hydrate concentrated zone using 3D seismic data in the eastern Nankai Trough," in *Proceedings of the 6th International Conference on Gas Hydrates (ICGH '08)*, Vancouver, Canada, July 2008.
- [17] H. de Santa Ana, N. Ucha, L. Gutiérrez, and G. Veroslavsky, "Gas hydrates: estimation of the gas potential from reflection seismic data in the continental shelf of Uruguay," *Revista de la Sociedad Uruguaya de Geología*, no. 11, pp. 46–52, 2004.
- [18] S. Neben, B. Schreckenberger, J. Adam et al., *Research Cruise BGR04, ARGURU—Geophysical Investigations Offshore Argentine and Uruguay with Akademik Alexandr Karpinsky. Buenos Aires-Buenos Aires, 19/11/2004–19/12/2004. Cruise Report and Preliminary Results*, Bundesanstalt für Geowissenschaften und Rohstoffe, Hannover, Germany, 2005.
- [19] C. Hensen, M. Zabel, K. Pfeifer et al., "Control of sulfate pore-water profiles by sedimentary events and the significance of anaerobic oxidation of methane for the burial of sulfur in marine sediments," *Geochimica et Cosmochimica Acta*, vol. 67, no. 14, pp. 2631–2647, 2003.
- [20] S. A. Barclay, R. H. Worden, J. Parnell, D. L. Hall, and S. M. Sterner, "Assessment of fluid contacts and compartmentalization in Sandstone reservoirs using inclusions: an example from the magnus oil field, North Sea," *AAPG Bulletin*, vol. 84, no. 4, pp. 489–504, 2000.
- [21] G. F. Tavella and C. G. Wright, "Cuenca del Salado," in *Geología y Recursos Naturales de la Plataforma Continental Argentina*, V. A. Ramos and M. A. Turic, Eds., pp. 95–116, 1996, Relatorio del XIII° Congreso Geológico Argentino y III° Congreso de Exploración de Hidrocarburos, Buenos Aires.
- [22] H. de Santa Ana, G. Veroslavsky, and E. Morales, "Estado exploratorio de la región costa afuera de Uruguay," in *Proceedings of the 7th Congreso de Exploración y Desarrollo de Hidrocarburos*, pp. 649–657, Instituto Argentino del Petróleo y del Gas, Mar del Plata, Argentina, 2008.
- [23] P. Meldahl, R. Heggland, B. Bril, and P. de Groot, "Identifying faults and gas chimneys using multiattributes and neural networks," *Leading Edge*, vol. 20, no. 5, pp. 474–482, 2001.
- [24] J. Tomasini, H. de Santa Ana, and A. Johnson, "Identification of new seismic evidence regarding gas hydrate occurrence and gas migration pathways offshore Uruguay," in *Proceedings of the AAPG 2010 Annual Convention & Exhibition*, New Orleans, La, USA, 2010.
- [25] E. C. Capen, "Probabilistic reserves! Here at last?" *SPE Reservoir Evaluation and Engineering*, vol. 4, no. 5, pp. 387–394, 2001.
- [26] Z. Lu and N. Sultan, "Empirical expression for gas hydrate stability law, its volume fraction and mass-density at temperatures 273.15 K to 290.15 K," *Geochemical Journal*, vol. 42, no. 2, pp. 163–175, 2008.
- [27] J. Tomasini, H. de Santa Ana, P. Gristo et al., "Determination of Hydrate Formation Gases for Marine Gas Hydrates Offshore Uruguay," Project FSE.2009.53, ANII. In preparation.
- [28] S. Oliveira, O. Vilhena, and E. da Costa, "Time-frequency spectral signature of Pelotas Basin deep water gas hydrates system," *Marine Geophysical Researches*, vol. 31, no. 1, pp. 89–97, 2010.
- [29] A. Sad, D. Silveira, S. Silva, R. Maciel, and M. Machado, "Marine gas hydrates along the Brazilian margin," in *Proceedings of the ABGP/AAPG International Conference and Exhibition*, Rio de Janeiro, Brazil, 1998, AAPG Search and Discovery Article #90933.
- [30] J. S. Booth, M. M. Rowe, and K. M. Fischer, "Offshore gas hydrate sample database with an overview and preliminary analysis," Open-File Report 96-272, U.S. Geological Survey, 1996, <http://pubs.usgs.gov/of/1996/of96-272/>.

Research Article

Early Diagenesis Records and Pore Water Composition of Methane-Seep Sediments from the Southeast Hainan Basin, South China Sea

Daidai Wu,^{1,2} Nengyou Wu,^{1,2} Ying Ye,³ Mei Zhang,^{1,2} Lihua Liu,^{1,2}
Hongxiang Guan,^{1,2} and Xiaorong Cong^{1,2}

¹Key Laboratory of Renewable Energy and Gas Hydrate, Guangzhou Institute of Energy Conversion, CAS, Guangzhou 510640, China

²Guangzhou Center for Gas Hydrate Research, CAS, Guangzhou 510640, China

³Department of Ocean Science and Engineering, Zhejiang University, Hangzhou 310028, China

Correspondence should be addressed to Nengyou Wu, wuny@ms.giec.ac.cn

Received 14 April 2011; Revised 4 August 2011; Accepted 4 August 2011

Academic Editor: Umberta Tinivella

Copyright © 2011 Daidai Wu et al. This is an open access article distributed under the Creative Commons Attribution License, which permits unrestricted use, distribution, and reproduction in any medium, provided the original work is properly cited.

Several authigenic minerals were identified by XRD and SEM analyses in shallow sediments from the Southeast Hainan Basin, on the northern slope of South China Sea. These minerals include miscellaneous carbonates, sulphates, and framboidal pyrite, and this mineral assemblage indicates the existence of gas hydrates and a methane seep. The assemblage and fabric features of the minerals are similar to those identified in cold-seep sediments, which are thought to be related to microorganisms fostered by dissolved methane. Chemical composition of pore water shows that the concentrations of SO_4^{2-} , Ca^{2+} , Mg^{2+} , and Sr^{2+} decrease clearly, and the ratios of Mg^{2+} to Ca^{2+} and Sr^{2+} to Ca^{2+} increase sharply with depth. These geochemical properties are similar to those where gas hydrates occur in the world. All results seem to indicate clearly the presence of gas hydrates or deep water oil (gas) reservoirs underneath the seafloor.

1. Introduction

Methane is a major component of cold fluids on the continental shelf and slope [1, 2]. It is also a major hydrocarbon gas source of deep oilgas and gas hydrates. Hydrocarbon gas can escape through the overlying marine sediment column, enter the water column, and form a coldseep [1, 3, 4]. Most of the hydrocarbon gas can generate authigenic carbonates at or under the seafloor via a series of biogeochemical reactions, and a small amount may even be transported into the water column or enter the atmosphere [5, 6]. Hydrocarbon gas seep provides nourishment for Archaea and sulfate-reducing bacteria (SRB) found in benthic sediments. These microorganisms consume sulfate and oxydize methane into HCO_3^- . This process causes changes of pore water chemical composition and results in the precipitation of carbonate [7, 8]. Methane seeps are an important geological phenomenon in marine sediment, and methane-rich cold

seeps are assumed to be the preferential outcrop of oilgas and gas hydrate on the seafloor. Therefore, the knowledge of methane seeps is significant for oil-gas exploration. Furthermore, the greenhouse potential of methane is 24 times of carbon dioxide. Compared to the artificial carbon dioxide, the greenhouse effect of methane discharged by geodynamic and tectonic processes plays a primary role on the global change in the natural environment [9]. Therefore, there has been an increasing interest in methane seepage (gas hydrate) during the past several years.

Southeast Hainan Basin on the northern slope of South China Sea is a potential gas hydrate deposit. Except for direct drilling and sampling of marine gas hydrates, the occurrence of gas hydrates has been identified generally by inference from indirect evidence, derived from geological, geophysical, and geochemical data all over the world. For example, the occurrence of gas hydrate is inferred from seismic profiles, especially the bottom simulating reflector (BSR), although

gas hydrates are also known to occur in the areas without BSR in many locations. In Southeast Hainan Basin, the high-resolution multichannel seismic profiles were collected, and BSR and other seismic indications, such as blanking zone and velocity amplitude anomaly inversions, for gas hydrate occurrences, were observed. However, geochemical studies have been of great help for identification of the occurrence of gas hydrates.

The goal of this research is to study the early diagenesis records and geochemistry of pore waters of shallow sediments from Southeast Hainan Basin. The evidences for gas hydrates or deep water oil (gas) reservoirs and the relationship between authigenic mineral, geochemistry of pore waters, and methane seep in shallow sediments were discussed here.

2. Geological Setting and Sampling

A 4.9 m long sediment core was taken in August 2005 from 1508 m depth in the Southeast Basin (Figure 1) by a gravity piston corer, during the HY4-2005-5 Cruise of R/V Haiyang-4 (Guangzhou Marine Geological Survey, Ministry of Land and Natural Resources). The cored sediment is silty clay with a few foraminifera, yielding strong odor of hydrogen sulfide. The sediment core was stored on board at 4°C. The sampling site T1 (111°4' E, 18°2' N) is located in a flat continental slope, 150 km southeast of Sanya, Hainan Province, China. The geological structural unit belongs to the Songxi Depression Belt, Southeast Hainan Basin.

Oil- and gas-bearing depositional basins on the northern continental slope of the South China Sea were developed during the late Cenozoic [10–12], when a strong extrusion phase followed a period of rift extension and sea-floor spreading 30~24 Ma ago. The area (Figure 1) is characterized by frequent tectonic and magmatic episodes, slope slumps, high heat flux (average about 75 mW/m²), abundant thermogenic gas and biogas in shallow sediments, carbon dioxide and nitrogen-rich gas. Four subareas, including Southwest Taiwan, Northeast Dongsha, Baiyun Sag of Pearl River Mouth Basin, and Southeast Hainan Basin, were identified to be the most favorable for gas seep or gas hydrate presence, showing geological, geochemical, and biological evidences for cold seeps [13–21]. The sediment thickness is reported to be about 12000 m [22], whereas 5000 m thick organic-rich sediments have been accumulated since the Cenozoic [23].

The thick Quaternary organic-rich sediments in Southeast Hainan Basin provide enough sources for hydrocarbons [24]. High geothermal gradient [25] and abnormal high pressure [26] are fitted for hydrocarbons formation, diffusion, and transportation. Methane-rich gas is categorized into three groups: bio-low mature transient gas, normal mature thermogenic gas, and super mature thermogenic gas [23], and the conditions for gas hydrate accumulation were confirmed in previous studies [27]. Some methane-seep-related features, such as mud volcanoes, mud diapirs, and gas chimneys, were discovered in the basin [24, 28]. Unfortunately, there is no similar report at the sampling site, even if the existence of gas hydrates in the Southeast Hainan

Basin has been confirmed by geophysical evidences [24, 28–30]. The existence of gas hydrate in the same site (T1) has also been proved by microbial evidence [31].

3. Materials and Methods

The sediment cores within PVC liners were immediately cut into 80 cm sections after its recovery on deck. The core sections were airtight sealed with plastic cap, gummed typed and stored on board at 4°C. The sealed sections were further splitted longitudinally in a flow-through (N₂) anaerobic chamber at Guangzhou Marine Geological Survey, China. One half of each section was described and archived, while the other half was sampled for pore water and sediment. The external rim of each subsection was removed using sterile tools to avoid contamination. Subsections of freshly cored sediments were removed and placed into special sealed glass bottles. The samples were stored at 4°C for X-ray diffraction (XRD), scanning electron microscope (SEM), and pore water analysis. All analyses were carried out at the Department of Geological Sciences and the Department of Biology, University of Miami.

XRD was employed to analyze mineralogy in the sediments. Samples were oven heated at 60°C for 12 hrs, pestled into less than 200 μ mesh, and X-rayed with a Scintag XGEN-4000 X-ray diffraction system, using Cu radiation in a graphite monochromator, a scintillation counter, with 0.02 two-theta steps from 5 to 70 degrees, for 2 seconds per step, with 0.15406 nm wavelength, 40 kV tube voltage, and 34 mA tube current. Mineral identification was done by a combination of search-match software and comparison with the JCPDS card files.

A Zeiss Supra 35 VP-FEG SEM equipped with EDAX Energy Dispersive X-ray microanalysis system was used to identify minerals and to image their morphologies. In preparation for SEM observations, selected samples were vacuum dried and gold coated. The working distance is 10.3 mm, and voltage is 5 kV.

Sediment pore water samples were collected after centrifugation of about 50 g sediment subsamples (5000 g for 10 minutes). Each sediment subsample could obtain about 13–20 mL water. To measure anions and cations, aliquots of pore water were mixed with 0.1 HCl solutions. The diluted (pore water samples) solutions were then analyzed by high-performance liquid chromatography (HPLC) for anions (IonPacAS14 column 4 × 250 mm) and direct current plasma emission spectrometry (DCP) for cations.

4. Results and Discussions

4.1. Authigenic Minerals and Microstructures of Sediments. XRD results (Figure 2) show that the sediments contain land-derived detrital minerals, that is, quartz, illite, kaolinite, albite, calcite, and a complex suite of authigenic minerals, that is, miscellaneous carbonates, sulphates, and pyrite. Major mineral components and their semiquantification are listed in Table 1. Abundant microstructures were observed by SEM (Figure 3), and the whole crystal form, surface,

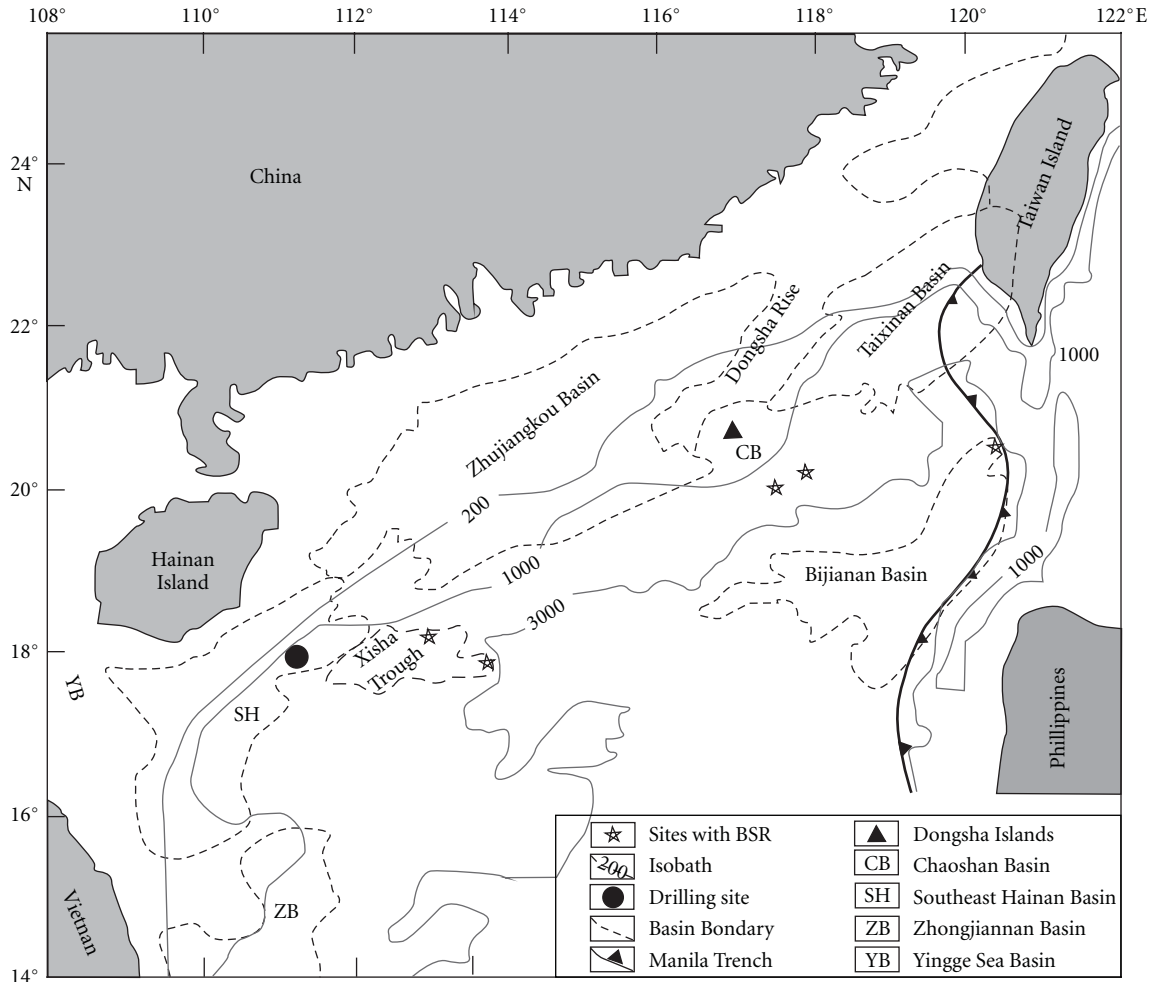


FIGURE 1: Position of the sampling site, Southeast Hainan Sea, South China Sea.

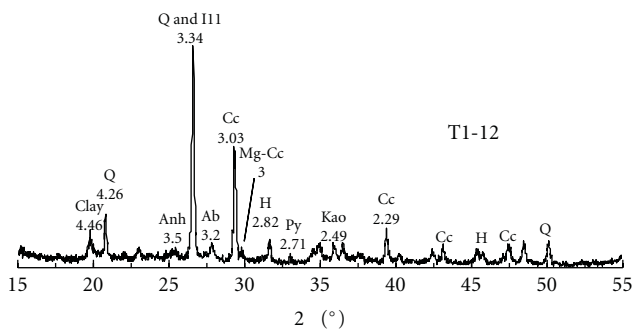


FIGURE 2: XRD pattern of mineral components in sample T1-12 from the Southeast Hainan Basin. Clay, clay minerals; Q, quartz; Anh, anhydrite; Ill, illite; Ab, albite; Cc, calcite; Mg-Cc, Mg-calcite; H, halite; Py, pyrite; Kao, kaolinite.

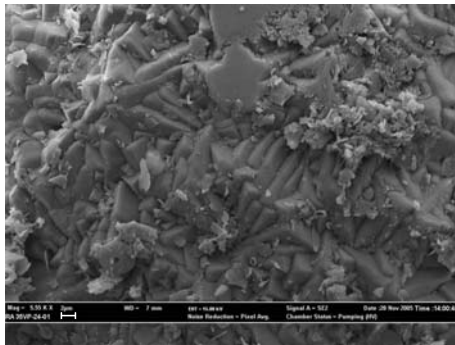
angle, and crystallographic elements are kept intact during the observations. These characters confirm that the minerals are authigenic in situ, without transport and erosion.

Main identified miscellaneous carbonates are calcite, Mg-calcite, nesquehonite, magnesite, siderite, and so forth.

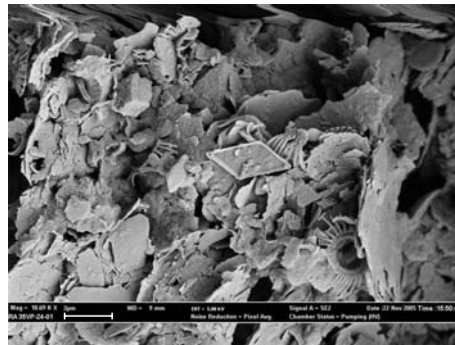
Calcite is one of the major components in the sediment samples, and most part of it is foraminifera shell. Mg-calcite and nesquehonite are common in XRD patterns, but magnesite and siderite are only identified in few subsamples. Part of calcite is aragonite pseudomorph, which looks like an assemblage with acicular, filiform, and ball-shaped carbonates under SEM. The assemblage is identified with calcite by energy dispersive X-ray spectra. However, the crystal form and habit are similar to aragonite (Figures 3(c), 3(d)). There is no identified aragonite peaks in the XRD pattern, which suggests that aragonite was replaced by calcite, and the pseudomorph of aragonite is observed. It evinces that phase transformation of aragonite into calcite has occurred in sediments. The factor leading to formation of acicular, filiform, and ball-shaped aragonite is metabolism of methane-related microorganisms. Sassen et al. found that acicular aragonite, framboidal pyrites, mycelium, and asphalt have symbiotic relationship in cold seep carbonates [5], and the bacterium activity boosting precipitation of authigenic carbonates has been discovered by lab work [32, 33]. Ehrlich observed successfully ball-shaped and dumbbell assemblage of acicular aragonite by bacilli culture in laboratory [34]. Ball-shaped

TABLE 1: Major mineral components and their semi-quantification results in sediments from the Southeast Hainan Basin (%).

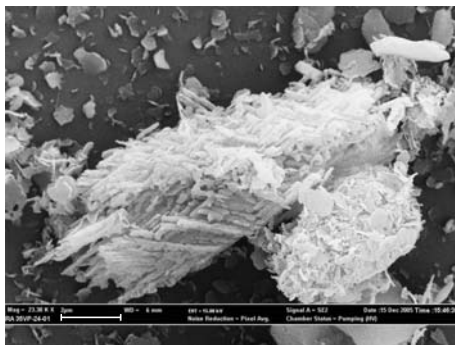
No.	Depth (cm)	Illite	Gypsum	Kaolinite	Brucite	Witherite	Barite	Anhydrite	Quartz	Microcline	Albite	Ba-calcite	Calcite	Mg-calcite	Siderite	Magnesite	Vaterite	Pyrite	Maghemite
T1-44	20	24.2		11.9			22.3		13.1		2.3		7.9			3.5	3.4		11.5
T1-46	35	25.4		13.4	7.0	1.3	22.5	3.5	12.0		2.7		8.9			3.5			
T1-36	85	28.7		14.2			25.9		13.8		2.6	5.8	6.0			3.0			
T1-38	100	25.2		9.1			30.2		14.6		2.5		8.7		1.9	3.3			4.5
T1-28	200	30.3		11.7	9.6		25.0		10.4			4.4	3.7						4.9
T1-30	216	20.8		13.4	3.8		28.0		10.7			5.4	5.9			3.7			8.3
T1-32	230	26.4		13.4	10.0		28.9		9.1			3.0	5.3						3.9
T1-20	320	27.4		16.2			28.2		14.5		4.0		9.6						
T1-22	336	24.5		10.7	11.6		27.1		10.5		2.3		3.7			4.6			5.1
T1-24	355	19.7		11.1	10.4	16.0		2.5	13.4		1.6		11.7	2.3		3.1			3.3
T1-12	380	24.41	3.08	11.37				2.94	26.50		3.27		25.16	2.51					0.76
T1-14	395	43.1		16.7	7.1		15.3		6.4		2.3		3.3	1.8					4.0
T1-16	415			16.6			37.8	6.6	13.5		6.2		7.6	2.7					9.0
T1-2	440	20.8		17.9				2.8	29.4		3.4		19.9	3.1		2.7			
T1-4	450	26.1	4.3	15.0					26.4		3.6		19.0	2.9		2.6			
T1-6	465	20.3		14.8			1.7		30.0	9.9	3.3		18.2						1.8
T1-8	475	22.1		11.3				3.2	29.8	8.0	3.8		15.1	2.3		2.6			1.7



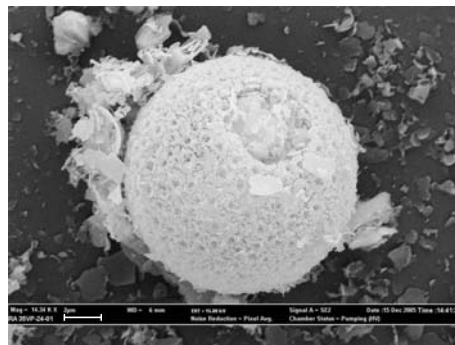
(a) Authigenic carbonates, T1-4



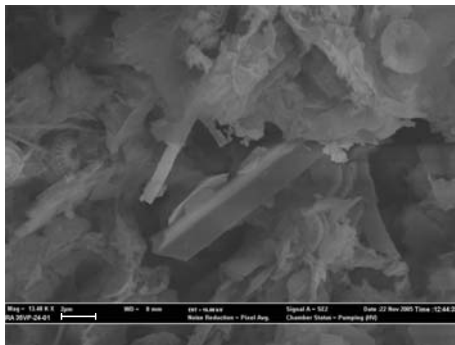
(b) Authigenic dolomite (euhedral rhombus crystal), T1-38



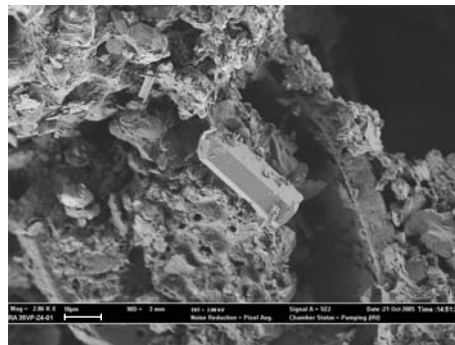
(c) Aragonite assemblage, clay minerals with mycelium, T1-2



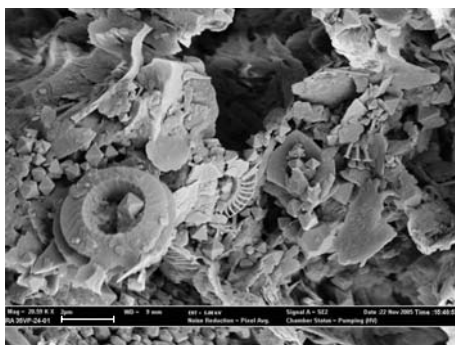
(d) Ball-shaped aragonite assemblage, T1-22



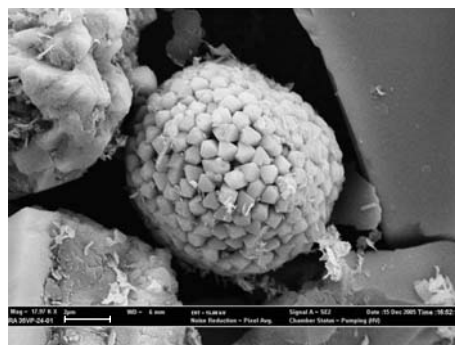
(e) Tabular Ca sulphate (authigenic), T1-30



(f) Authigenic Barite, T1-20



(g) Authigenic pyrite, T1-28



(h) Authigenic framiboidal pyrite, T1-16

FIGURE 3: SEM images of authigenic minerals in sediments from the Southeast Hainan Basin.

carbonates cemented by mycelium were observed under SEM (Figure 3(d)), which further confirmed that there was some cause-effect relationship between carbonates assemblage and microorganism. Mg-calcite and Nesquehonite are authigenic rhombohedral crystals, and usually coat the surface of microorganism shells like coccoliths, diatoms, and so on [5].

Authigenic carbonates deposits have been documented in area near methane seep in both the active and passive continental margin [5, 6]. The carbonates formation relates closely to methane seep or gas hydrate decomposition because of their special microstructure [2, 35]. The Southeast Hainan Basin in South China Sea is a potential area for gas hydrate reservoirs. Methane microseep and its oxidation drive the bicarbonate deposited associating with the available research data although there are no large methane seep found at the sampling site.

Main sulphate minerals identified in the sediments are barite, anhydrite, and gypsum. Gypsum and anhydrite appear as tabular and panidiomorphic textures (Figure 3(e)). The occurrence of authigenic gypsum and anhydrite indicates high concentration of sulphate ion in the pore water. Sulfate reduction is the main pathway of CH₄ oxidation in CH₄-riched anoxic sediments. Although the CH₄-SO₄²⁻ redox cell will decompose and consume sulphate in the sediments, that does not mean there is no SO₄²⁻. On the contrary, SO₄²⁻ originates from the decomposition of organic-rich sediments, and there must be abundant organic matter in gas hydrate reservoirs [36], whereas Ca²⁺ may originate from the decomposition of calcilith or fluids with Ca²⁺ from the gas hydrate present underneath [37]. Therefore, the supersaturated concentration of Ca²⁺, and SO₄²⁻ in pore water drives authigenic gypsum precipitation. Authigenic gypsum has been identified in the sediments from Hydrate Ridge in the northeast Pacific Ocean. That indicates gypsum should be one of the authigenic minerals which have close relation with methane hydrate reservoir [38]. In conclusion, gypsum is one of the markers for hydrate presence similar to other authigenic minerals, carbonates, and barite.

Barite shows a short prismatic and euhedral crystal structure under SEM (Figure 3(f)). Authigenic barite micro-crystals had been identified in sediments from the Peru continental margin (site 684) and Japan Sea (site 799) by the Ocean Drilling Program (ODP), and they contain more ³⁴S than that in the sea water with a δ³⁴S of +84‰. The widespread occurrence of barite indicates high concentration of Ba in pore water. Barite is the major mineral in the cold-seep sediments in Peru and Russian Okhotsk [39, 40]. The source of Ba in the cold seep is assumed to be the barite solution as a result of the sulphate deoxidization at depth [41].

Pyrite was identified in most samples by XRD analysis, and the representative diffraction peaks are 2.709×10^{-10} and 2.423×10^{-10} m. Pyrite is distributed as single granules (Figure 3(g)) or framboidal assemblages (Figure 3(h)); δ³⁴S value of the framboidal pyrite is greatly negative in cold-seep sediments and low-temperature hydrothermal fluid sediments. This indicates that the sulphur of pyrite originates from bacterial reduction of sulphate in sea water [42–44].

Sulphate bacteria mainly depend on sulphate decomposition in the anoxic environment by activity of sulphate redox cell. Meanwhile, the HCO₃⁻ concentration increases in the pore water with decomposition of organic matter. Sulphide forms with free HS⁻ and low-valence iron, and finally sulphide transforms into pyrite [45, 46]. Sassen et al. found many framboidal pyrites, and pyrite granules in sediments from a gas hydrate area in the Gulf of Mexico and suggested that the strong anaerobic methane oxidation (AOM) contributes to pyrite formation in sediments [5]. Liu et al. also believed that AOM is the main reason for sulphide increase in the sediments from the northeastern South China Sea [47]. Therefore, authigenic pyrite is also the major product of AOM process in sediments from a gas hydrate (methane seep) area. High concentration of pyrite in anoxic sediments can indicate the methane abnormality [48] and the occurrence of methane-rich fluids and further show the shallow SMI to a certain degree.

In summary, AOM in the methane seep area results in alkalinity increase in both pore water and sea water [49, 50]. Methane is oxidized to HCO₃⁻ by SO₄²⁻, a process in favor of CO₃²⁻ accumulation. Furthermore, AOM changes the geochemical conditions and results in the rapid deposition of miscellaneous carbonates including aragonite, Mg-calcite, and dolomite [51]. Meanwhile, pyrite formation results from the reaction of H₂S, derived from bacterial sulphate reduction, with reactive iron [45, 46]. Precipitation of aragonite, Mg-calcite, and pyrite is the result of processes related to the presence of methane seep in the northern Black sea [1, 8]. Abundant cold-seep-related minerals, Mg-calcite, dolomite, and framboidal pyrite, precipitate in Monterey Gulf, California [52]. Authigenic minerals including miscellaneous carbonates, sulphate, and sulphide form in gas hydrate-bearing and hydrocarbon seepage in Gulf of Mexico [5]. All these records of authigenic mineral assemblages and fabric features are geological evidences for cool-seep activities, hydrocarbon seeps, and gas hydrate dissociation. The widespread occurrence of authigenic carbonates, pyrite, and sulphate in the sediments of Southeast Hainan Basin, South China Sea is completely similar to reported cases in a typical gas hydrate area. This aspect further indicates gas hydrate existence in the study area.

4.2. Chemical Composition of Pore Waters. Anomalies in the chemical composition of pore water indicating the occurrence of gas hydrates, such as anomalous concentrations of Br, Cl, CH₄, and K, are known in the literature [53, 54].

In pore waters from the Southeast Hainan Basin, NH₄⁺ concentration is close to zero within the upper 320 cm section and increases with depth in lower section (Table 2, Figure 4). That may be due to the zymosis of organic matter via bacteria during gas hydrate formation and dissociation [55]. The concentration of Mg²⁺ decreases slightly with depth, and the Ca²⁺ concentration falls slightly (Table 2, Figure 4). The solubility product of calcium carbonate is less than magnesium, and calcium carbonate deposits easily from the solution. Therefore, Ca²⁺ deposits faster than Mg²⁺ from

TABLE 2: Pore water chemical composition for the analysed core from the Southeast Hainan Basin (mg/dm^3).

Depth (cm)	NH_4^+	K^+	Mg^{2+}	Ca^{2+}	Mn^{2+}	Fe^{2+}	F^-	Br^-	SO_4^{2-}
20	0.0	585.1	1465.9	510.1	17.7	28.8	3.0	71.4	2559.5
35	0.0	561.4	1421.1	529.1	17.2	19.9	2.7	69.3	2496.8
85	0.0	588.1	1448.6	487.3	16.8	45.6	3.0	70.8	2447.2
100	0.0	571.2	1393.3	466.7	15.8	36.6	4.4	69.7	2308.3
200	0.0	592.1	1446.4	469.2	9.0	35.7	4.2	79.1	2423.1
216	0.0	558.9	1342.0	429.9	8.5	30.5	3.2	65.3	2199.2
230	0.0	592.8	1412.7	461.5	8.8	48.7	3.0	68.1	2323.2
320	0.0	674.6	1521.3	431.2	7.5	18.1	4.1	71.5	2014.3
336	10.7	558.5	1412.9	439.9	8.0	27.0	3.5	75.4	2175.8
355	0.0	565.9	1460.6	466.5	8.8	46.9	3.1	78.5	2199.9
380	26.4	552.7	1424.1	429.8	7.8	18.0	3.0	67.8	2170.3
395	22.8	595.4	1415.8	423.2	7.9	28.6	3.2	76.0	2173.7
415	15.7	546.4	1406.7	439.1	8.9	53.2	3.7	71.8	2074.6
440	44.7	537.8	1375.7	412.3	12.0	22.2	3.0	72.7	2085.0
450	55.5	579.6	1421.8	412.7	7.6	9.0	3.8	77.6	2163.3
465	53.6	550.5	1434.4	425.2	8.0	14.4	4.7	79.2	2078.0
475	61.3	595.2	1407.1	363.0	7.3	25.2	4.1	72.6	2153.7

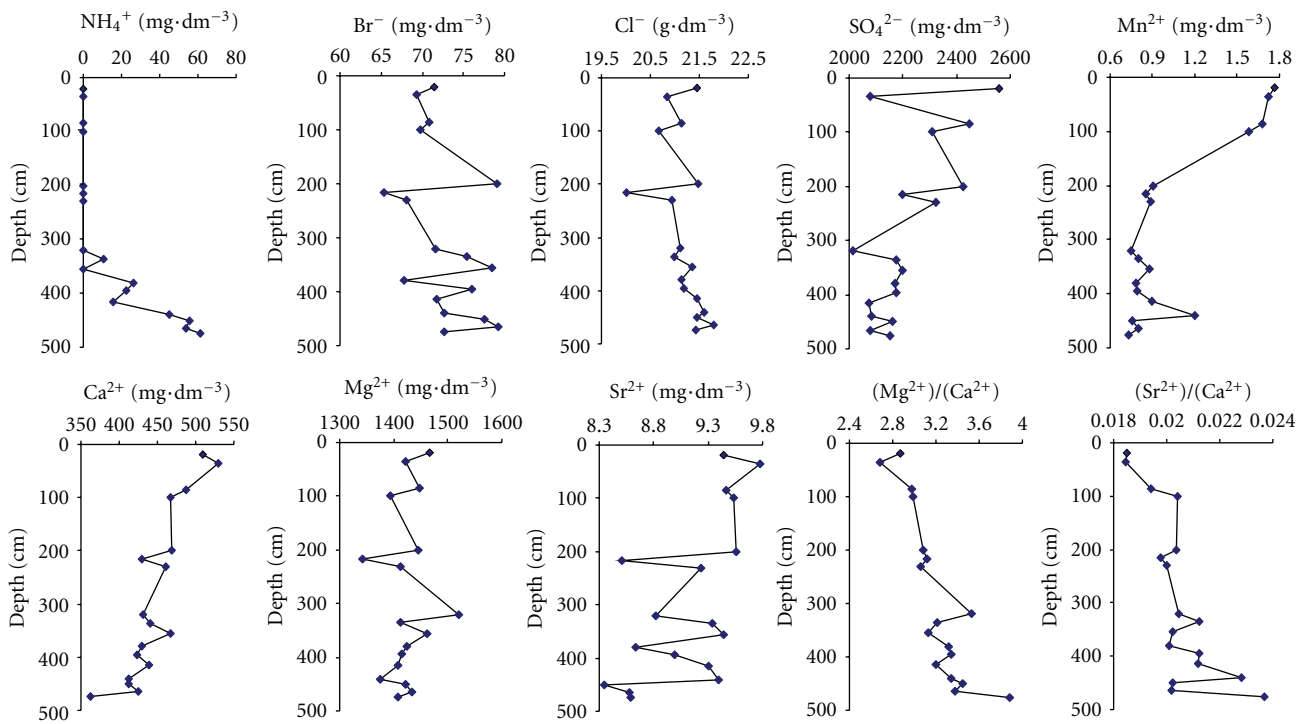


FIGURE 4: Geochemistry of pore waters versus depth of sediments from the Southeast Hainan Basin.

pore water into solid phase. Furthermore, the $\text{Mg}^{2+}/\text{Ca}^{2+}$ ratio increases sharply with depth (Figure 4). The concentrations of Sr^{2+} , and Mn^{2+} go down sharply with depth in the shallow sediments (Table 2). This suggests that Sr^{2+} and Mn^{2+} are removed into the same authigenic phase(s). Also the ratio of Sr^{2+} to Ca^{2+} increases sharply with depth (Figure 4), and the cause may be that Ca^{2+} , Mg^{2+} , Sr^{2+} , and Mn^{2+} cations are easily incorporated within carbonates

deposited at the expense of dissolved carbon dioxide. The consumption of Ca^{2+} , Mg^{2+} , Sr^{2+} , and Mn^{2+} cations in pore water, combined with the authigenic carbonates like calcite (aragonite pseudomorphous), Mg-calcite, and magnesite, indicates that there is supplement of dissolved CO_2 likely originated from AOM in depth during the diagenesis process, then diagenesis is a process affecting AOM and providing cations and dissolved species to pore water for further

reactions. Previous research showed that carbon dioxide could form during gas hydrate decomposition and upper migration in gas hydrate-bearing areas, leading to formation of authigenic carbonates, syngenetic to gas hydrate [56, 57].

The concentrations of Cl^- and Br^- are relatively constant, whereas SO_4^{2-} decreases clearly with depth (Figure 4). These trends, combined with the presence of authigenic carbonates, barite, gypsum, anhydrite, and pyrite, indicate AOM and sulphate reduction



The reaction has affected the shallow sediments at the site T1 of the Southeast Hainan Basin, South China Sea, or the sulphate-methane interface (SMI) has been lifted up to the shallow layer. It means that there is abundance of gas hydrate or gas-oil resource underneath the sampling site. Compared to other methane seep area, the concentration gradient of sulphate in core T1 is smaller. That means sulfate in pore water is not exhausted in sampling depth. So, the depth of SMI should be deeper than the sampling's. Therefore, it is clear that there is a hypogenetic fluid, related to gas hydrate occurrence under the sampling site.

The results of microbial colony research at same site [31] demonstrated that physiological functions of these relatives include Fe(III) and Mn(IV) reduction (*Pelobacter*), sulfate reduction (H_2S production) (*S. kaireitica*), decomposition of complex aromatic hydrocarbons and denitrification (*P. stutzeri*), hydrocarbon degradation (*A. jadensis*), and thio-sulfate/sulfite oxidation (*Sulfitobacter* spp.) in the sediments, similarly to observations of gas hydrate-bearing sediments in the Sea of Okhotsk [58]. The occurrence of microbe suggests hydrocarbon oxidation coupled with sulphate, and Fe (III) reduction is an important process during the early diagenesis in the Southeast Hainan Basin, South China Sea. Oxidation of hydrocarbons may contribute to the increasing alkalinity and carbonate precipitation. The metabolic processes are consistent with the decreasing Mg^{2+} , Ca^{2+} , Sr^{2+} and SO_4^{2-} concentrations in pore water, the precipitation of authigenic carbonates and pyrite in the shallow sediments. These results strongly suggest that there should be gas hydrate reservoirs in the sampling area.

5. Conclusions

Taking together all available mineralogical and geochemical data from the Southeast Hainan Basin, South China Sea, we can draw the following conclusions.

- (1) The shallow sediments from the Southeast Hainan Basin are of a complex suite of authigenic minerals, such as carbonates, sulphates, and framboidal pyrite, indicating clearly the existence of gas hydrates or deep water oil (gas) reservoirs. The assemblage and fabric features of aragonite and mg-calcite could be a result of the activity of microorganisms, which consumes dissolved methane. The miscellaneous authigenic carbonates are the result of abundant HCO_3^- in the pore water, whose source should be related to AOM by microorganisms. Reduction of

sulphate and iron may be coupled with oxidation of methane and hydrocarbons, which causes decreased SO_4^{2-} concentration in pore water and precipitation of authigenic pyrite and carbonates in the sediments.

- (2) Chemical composition of pore waters shows that the concentrations of SO_4^{2-} , Mg^{2+} , Ca^{2+} , Sr^{2+} and Mn^{2+} decrease, and the concentration of NH_4^+ increases with depth. The ratios of $\text{Mg}^{2+}/\text{Ca}^{2+}$, $\text{Sr}^{2+}/\text{Ca}^{2+}$ increase sharply with depth. These geochemical data indicate strongly the presence of gas hydrates or deep water oil (gas) reservoirs beneath the seafloor.

In summary, mineralogical and geochemical data in the shallow sediments and pore waters suggest to us that the Southeast Hainan Basin is one of the promising targets on the northern margin of the South China Sea for further gas hydrate or deep water oil (gas) reservoir exploration. The data allow us to better understand the influence on the methane seep and geochemistry of fluids in shallow sediments exerted by gas hydrates or deep water oil (gas) reservoirs, whose presence could not be determined with certainty until there is further evidence, and the presence of methane seeps on the seafloor needs to be evidenced by swath bathymetry, shallow seismic data, or direct evidence on seafloor images in the future.

Acknowledgments

This study is financially supported by the National Natural Science Foundation of China (No. 41003010 and No.U0933004), National 973 Project (No. 2009CB219506), and Scientific and Technology Program of Guangdong Province (No. 2011A080403021). We sincerely thank the crew and scientific team onboard R/V Haiyang-4 from Guangzhou Marine Geological Survey for their cooperation and highly professional support, two anonymous reviewers for their kind comments and suggestions.

References

- [1] J. Peckmann, A. Reimer, U. Luth et al., "Methane-derived carbonates and authigenic pyrite from the northwestern Black Sea," *Marine Geology*, vol. 177, no. 1-2, pp. 129–150, 2001.
- [2] C. Pierre and J. M. Rouchy, "Isotopic compositions of diagenetic dolomites in the Tortonian marls of the western Mediterranean margins: evidence of past gas hydrate formation and dissociation," *Chemical Geology*, vol. 205, no. 3-4, pp. 469–484, 2004.
- [3] J. Peckmann and V. Thiel, "Carbon cycling at ancient methane-seeps," *Chemical Geology*, vol. 205, no. 3-4, pp. 443–467, 2004.
- [4] D. Wu, N. Wu, Y. Ye, P. Zhang, and X. Chen, "Geochemical characteristics of hydrocarbon compounds in sediments of the eastern South China Sea," *Acta Petrolei Sinica*, vol. 29, no. 4, pp. 516–521, 526, 2008 (Chinese).
- [5] R. Sassen, H. H. Roberts, R. Carney et al., "Free hydrocarbon gas, gas hydrate, and authigenic minerals in chemosynthetic communities of the northern Gulf of Mexico continental slope: relation to microbial processes," *Chemical Geology*, vol. 205, no. 3-4, pp. 195–217, 2004.

- [6] B. M. A. Teichert, G. Bohrmann, and E. Suess, "Chemohermes on Hydrate Ridge—unique microbially-mediated carbonate build-ups growing into the water column," *Palaeogeography, Palaeoclimatology, Palaeoecology*, vol. 227, no. 1–3, pp. 67–85, 2005.
- [7] C. L. Zhang and B. Lanoil, "Geological and biogeochemical dynamics of gas hydrate-hydrocarbon seep systems," *Chemical Geology*, vol. 205, pp. 187–194, 2004.
- [8] J. Reitner, J. Peckmann, M. Blumenberg, W. Michaelis, A. Reimer, and V. Thiel, "Concretionary methane-seep carbonates and associated microbial communities in Black Sea sediments," *Palaeogeography, Palaeoclimatology, Palaeoecology*, vol. 227, no. 1–3, pp. 18–30, 2005.
- [9] G. Etiope, "New directions: GEM—geologic emissions of methane, the missing source in the atmospheric methane budget," *Atmospheric Environment*, vol. 38, no. 19, pp. 3099–3100, 2004.
- [10] S. L. McDonnell and M. Czarnecki, "A note on gas hydrate in the northern sector of the South China Sea," in *Natural Gas Hydrate: In Oceanic and Permafrost Environments*, M. D. Max, Ed., pp. 239–244, Kluwer Academic Publishers, Dordrecht, The Netherlands, 2000.
- [11] T. M. Guo, B. H. Wu, Y. H. Zhu, S. S. Fan, and G. J. Chen, "A review on the gas hydrate research in China," *Journal of Petroleum Science and Engineering*, vol. 41, no. 1–3, pp. 11–20, 2004.
- [12] S. Wu, G. Zhang, Y. Huang, J. Liang, and H. K. Wong, "Gas hydrate occurrence on the continental slope of the northern South China Sea," *Marine and Petroleum Geology*, vol. 22, no. 3, pp. 403–412, 2005.
- [13] D.-F. Chen, Y.-Y. Huang, D. Feng, Z. Su, and G.-Q. Chen, "Seep carbonate and preserved bacteria fossils in the northern of the South China Sea and their geological implications," *Bulletin of Mineralogy Petrology and Geochemistry*, vol. 24, no. 3, pp. 185–189, 2005 (Chinese).
- [14] H. Lu, J. Liu, F. Chen et al., "Mineralogy and stable isotopic composition of authigenic carbonates in bottom sediments in the offshore area of southwest Taiwan, South China Sea: evidence for gas hydrate occurrence," *Earth Science Frontiers*, vol. 12, no. 3, pp. 268–276, 2005 (Chinese).
- [15] Z. Chen, W. Yan, M. Chen et al., "Discovery of seep carbonate nodules as new evidence for gas venting on the northern continental slope of South China Sea," *Chinese Science Bulletin*, vol. 51, no. 10, pp. 1228–1237, 2006.
- [16] D. F. Chen, Y. Y. Huang, X. L. Yuan, and L. M. Cathles, "Seep carbonates and preserved methane oxidizing archaea and sulfate reducing bacteria fossils suggest recent gas venting on the seafloor in the Northeastern South China Sea," *Marine and Petroleum Geology*, vol. 22, no. 5, pp. 613–621, 2005.
- [17] S. Lin, W. C. Hsieh, Y. C. Lim, T. F. Yang, C. S. Liu, and Y. Wang, "Methane migration and its influence on sulfate reduction in the good weather ridge region, South China Sea continental margin sediments," *Terrestrial, Atmospheric and Oceanic Sciences*, vol. 17, no. 4, pp. 883–902, 2006.
- [18] T. F. Yang, P. C. Chuang, S. Lin, J. C. Chen, Y. Wang, and S. H. Chung, "Methane venting in gas hydrate potential area offshore of SW Taiwan: evidence of gas analysis of water column samples," *Terrestrial, Atmospheric and Oceanic Sciences*, vol. 17, no. 4, pp. 933–950, 2006.
- [19] X. Su, F. Chen, S. Wei et al., "Preliminary study on the correlation between microbial abundance and methane concentration in sediments from cold seeps in the northern South China Sea," *Geoscience*, vol. 21, no. 1, pp. 101–104, 2007 (Chinese).
- [20] Y. Y. Huang, E. Suess, N. Y. Wu et al., "Methane and gas hydrate geology of the Northern South China Sea—Sino-German Cooperative," Cruise report SO-177, Geological Publishing House, Beijing, China, 2008.
- [21] X. Han, E. Suess, Y. Huang et al., "Jiulong methane reef: microbial mediation of seep carbonates in the South China Sea," *Marine Geology*, vol. 249, no. 3–4, pp. 243–256, 2008.
- [22] B. Huang, "Gas Potential and its favorable exploration areas in Southeast Hainan Basin," *Natural Gas Industry*, vol. 19, no. 1, pp. 34–40, 1999 (Chinese).
- [23] J. He, B. Xia, D. Sun et al., "Hydrocarbon accumulation, migration and play targets in the Southeast Hainan Basin, South China Sea," *Petroleum Exploration and Development*, vol. 33, no. 1, pp. 53–58, 2006 (Chinese).
- [24] B. Wu, G. Zhang, Y. Zhu et al., "Progress of gas hydrate investigation in China offshore," *Earth Science Frontiers*, vol. 10, no. 1, pp. 177–188, 2003 (Chinese).
- [25] J. Liu and C. Wang, "Thermal fluid in Ying-Qiong Basin and its significance of oil-gas geology," *Natural Gas Exploration and Development*, vol. 27, no. 1, pp. 12–15, 2004 (Chinese).
- [26] M. Wang, "The character of overpressure and its relationship with the distribution of oil and gas Southeast Hainan Basin," *Offshore Oil*, vol. 23, no. 1, pp. 15–21, 2003 (Chinese).
- [27] J. He, "The evolving of gas hydrate and the exploration foreground in the north of South China Sea," *Offshore Oil*, vol. 23, no. 1, pp. 57–64, 2003 (Chinese).
- [28] D. Chen, X. Li, and B. Xia, "Distribution of gas hydrate stable zones and resource prediction in the Southeast Hainan Basin of the South China Sea," *Chinese Journal of Geophysics*, vol. 47, pp. 483–489, 2004 (Chinese).
- [29] S. Jiang, T. Yang, Z. Xue et al., "Chlorine and sulfate concentrations in pore waters from marine sediments in the north margin of the South China Sea and their implications for gas hydrate exploration," *Geoscience*, vol. 19, pp. 45–54, 2005 (Chinese).
- [30] X. Su, F. Chen, X. Yu et al., "A pilot study on Miocene through Holocene sediments from the continental slope of the South China Sea in correlation with possible distribution of gas hydrates," *Geoscience*, vol. 19, pp. 1–3, 2005 (Chinese).
- [31] H. Jiang, H. Dong, S. Ji, Y. Ye, and N. Wu, "Microbial diversity in the deep marine sediment from the Qiongdongnan Basin in China Sea," *Geomicrobiology Journal*, vol. 24, no. 6, pp. 505–517, 2007.
- [32] Y. Van Lith, R. Warthmann, C. Vasconcelos, and J. A. McKenzie, "Microbial fossilization in carbonate sediments: a result of the bacterial surface involvement in dolomite precipitation," *Sedimentology*, vol. 50, no. 2, pp. 237–245, 2003.
- [33] D. T. Wright and D. Wacey, "Precipitation of dolomite using sulphate-reducing bacteria from the Coorong Region, South Australia: significance and implications," *Sedimentology*, vol. 52, no. 5, pp. 987–1008, 2005.
- [34] H. L. Ehrlich, "Microbial formation and degradation of carbonates," in *Geomicrobiology*, pp. 183–228, Marcel Dekker, New York, NY, USA, 4th edition, 2002.
- [35] S. Cavagna, P. Clari, and L. Martire, "The role of bacteria in the formation of cold seep carbonates: geological evidence from Monferrato (Tertiary, NW Italy)," *Sedimentary Geology*, vol. 126, no. 1–4, pp. 253–270, 1999.
- [36] M. V. S. Gupta, "Authigenic gypsum in a deep sea core from southeastern Arabian sea," *Journal of the Geological Society of India*, vol. 21, no. 11, pp. 568–571, 1980.
- [37] E. Suess, M. E. Torres, G. Bohrmann et al., "Gas hydrate destabilization: enhanced dewatering, benthic material turnover and large methane plumes at the Cascadia convergent margin,"

- Earth and Planetary Science Letters*, vol. 170, no. 1-2, pp. 1–15, 1999.
- [38] J. Wang, E. Suess, and D. Rickert, "Authigenic gypsum found in gas hydrate-associated sediments from Hydrate Ridge, the eastern north Pacific," *Science in China D*, vol. 33, no. 5, pp. 433–441, 2003 (Chinese).
- [39] M. E. Torres, H. J. Brumsack, G. Bohrmann, and K. C. Emeis, "Barite fronts in continental margin sediments: a new look at barium remobilization in the zone of sulfate reduction and formation of heavy barites in diagenetic fronts," *Chemical Geology*, vol. 127, no. 1–3, pp. 125–139, 1996.
- [40] J. Greinert, G. Bohrmann, and E. Suess, "Gas hydrate-associated carbonates and methane-venting at Hydrate Ridge: classification, distribution and origin of authigenic lithologies," in *Natural Gas Hydrates: Occurrence, Distribution and Detection*, C. K. Paull and W. P. Dillon, Eds., vol. 124, pp. 99–113, American Geophysical Union, Washington, DC, USA, 2001.
- [41] G. Aloisi, K. Wallmann, S. M. Bollwerk, A. Derkachev, G. Bohrmann, and E. Suess, "The effect of dissolved barium on biogeochemical processes at cold seeps," *Geochimica et Cosmochimica Acta*, vol. 68, no. 8, pp. 1735–1748, 2004.
- [42] M. E. Böttcher and A. Lepland, "Biogeochemistry of sulfur in a sediment core from the west-central Baltic Sea: evidence from stable isotopes and pyrite textures," *Journal of Marine Systems*, vol. 25, no. 3-4, pp. 299–312, 2000.
- [43] R. T. Wilkin and M. A. Arthur, "Variations in pyrite texture, sulfur isotope composition, and iron systematics in the black sea: evidence for late pleistocene to holocene excursions of the O₂-H₂S redox transition," *Geochimica et Cosmochimica Acta*, vol. 65, no. 9, pp. 1399–1416, 2001.
- [44] P. Alfonso, R. M. Prol-Ledesma, C. Canet, J. C. Melgarejo, and A. E. Fallick, "Sulfur isotope geochemistry of the submarine hydrothermal coastal vents of Punta Mita, Mexico," *Journal of Geochemical Exploration*, vol. 78-79, pp. 301–304, 2003.
- [45] S. Lin, K. M. Huang, and S. K. Chen, "Organic carbon deposition and its control on iron sulfide formation of the southern East China Sea continental shelf sediments," *Continental Shelf Research*, vol. 20, no. 4-5, pp. 619–635, 2000.
- [46] M. A. A. Schoonen, "Mechanisms of sedimentary pyrite formation," in *Sulfur Biogeochemistry: Past and Present*, J. P. Amend, K. J. Edwards, and T. W. Lyons, Eds., pp. 117–134, The Geological Society of America, Colo, USA, 2004.
- [47] J. Liu, H. Lu, Z. Liao et al., "Distribution in sulfides in shallow sediments in Dongsha area, South China Sea, and its relationship to gas hydrates," *Earth Science Frontiers*, vol. 12, no. 3, pp. 258–262, 2005 (Chinese).
- [48] H. Lu, F. Chen, J. Liu et al., "Authigenic mineral associated with sedimentary environment of gas hydrate deposit and their occurrence in South China Sea," *Geological Research of South China Sea*, vol. 1, pp. 93–104, 2006 (Chinese).
- [49] S. J. Mazzullo, "Organogenic dolomitization in peritidal to deep-sea sediments," *Journal of Sedimentary Research*, vol. 70, no. 1, pp. 10–23, 2000.
- [50] J. W. Pohlman, C. Ruppel, D. R. Hutchinson, R. Downer, and R. B. Coffin, "Assessing sulfate reduction and methane cycling in a high salinity pore water system in the northern Gulf of Mexico," *Marine and Petroleum Geology*, vol. 25, no. 9, pp. 942–951, 2008.
- [51] S. Ritger, B. Carson, and E. Suess, "Methane-derived authigenic carbonates formed by subduction-induced pore-water expulsion along the Oregon/Washington margin," *Geological Society of America Bulletin*, vol. 98, no. 2, pp. 147–156, 1987.
- [52] D. S. Stakes, D. Orange, J. B. Paduan, K. A. Salamy, and N. Maher, "Cold-seeps and authigenic carbonate formation in Monterey Bay, California," *Marine Geology*, vol. 159, no. 1–4, pp. 93–109, 1999.
- [53] W. S. Borowski, C. K. Paull, and W. Ussler, "Global and local variations of interstitial sulfate gradients in deep-water, continental margin sediments: sensitivity to underlying methane and gas hydrates," *Marine Geology*, vol. 159, no. 1–4, pp. 131–154, 1999.
- [54] S. P. Hesselbo, D. R. Gröcke, H. C. Jenkyns et al., "Massive dissociation of gas hydrate during a Jurassic oceanic anoxic event," *Nature*, vol. 406, no. 6794, pp. 392–395, 2000.
- [55] C. K. Paull, R. Matsumoto, P. J. Wallace et al., *Proceedings of the Ocean Drilling Program*, vol. 164, National Science Foundation and Joint Oceanographic Institutions, College Station, Tex, USA, 1996.
- [56] S. J. Burns, "Early diagenesis in Amazon Fan sediments," in *Proceedings of the Ocean Drilling Program, Scientific Results*, R. D. Flood, D. J. W. Piper, A. Klaus et al., Eds., vol. 155, pp. 497–504, National Science Foundation and Joint Oceanographic Institutions, College Station, Tex, USA, 1997.
- [57] N. M. Rodriguez, C. K. Paull, and W. S. Borowski, "Zonation of authigenic carbonates within gas hydrate-bearing sedimentary sections on the Blake Ridge: offshore southeastern North America," in *Proceedings of the Ocean Drilling Program, Scientific Results*, C. K. Paull, R. Matsumoto, P. J. Wallace et al., Eds., vol. 164, pp. 301–312, National Science Foundation and Joint Oceanographic Institutions, College Station, Tex, USA, 2000.
- [58] F. Inagaki, M. Suzuki, K. Takai et al., "Microbial communities associated with geological horizons in coastal seafloor sediments from the Sea of Okhotsk," *Applied and Environmental Microbiology*, vol. 69, no. 12, pp. 7224–7235, 2003.

Research Article

Gas Hydrate System of Shenhu Area, Northern South China Sea: Geochemical Results

Nengyou Wu,^{1,2,3} Haiqi Zhang,⁴ Shengxiong Yang,³ Guangxue Zhang,³ Jinqiang Liang,³ Jin'an Lu,³ Xin Su,⁵ Peter Schultheiss,⁶ Melanie Holland,⁶ and Youhai Zhu⁷

¹Key Laboratory of Renewable Energy and Gas Hydrate, Guangzhou Institute of Energy Conversion, CAS, Guangzhou 510640, China

²Guangzhou Research Center for Gas Hydrate, CAS, Guangzhou 510640, China

³Guangzhou Marine Geological Survey, Guangzhou 510075, China

⁴China Geological Survey, Beijing 100011, China

⁵School of Marine Sciences, China University of Geosciences, Beijing 100083, China

⁶Geotek, Daventry NN11 8RD, UK

⁷Institute of Mineral Resources, CAGS, Beijing 100026, China

Correspondence should be addressed to Nengyou Wu, wuny@ms.giec.ac.cn

Received 2 April 2011; Revised 3 August 2011; Accepted 3 August 2011

Academic Editor: Michela Giustiniani

Copyright © 2011 Nengyou Wu et al. This is an open access article distributed under the Creative Commons Attribution License, which permits unrestricted use, distribution, and reproduction in any medium, provided the original work is properly cited.

The drilling recovered high-concentration methane hydrates (maximum 26–48%) in a disseminated form in silty clay sediments in Shenhu area of Pearl River Mouth Basin, South China Sea. Combining the geochemical data, the gas hydrate-bearing sediments are 10 m to 43 m in thickness and located just above the base of the gas hydrate stability zone. The methane content is 96.10–99.91% with small amount of ethane and propane. The baseline chlorinity of pore waters shows 10% lower than that of shallow sediments below and inside the gas hydrate zone. The methane/ethane ratios are higher than 1000 above the gas hydrate zone and less than 1000 at the interval of gas hydrate zone. The depth of sulphate methane interface varies from site to site as 17 to 27 mbsf. These results show that the methane of gas hydrate was mainly originated from microbial activity and the upward methane flux is minor. This is evidenced by the $\delta^{13}\text{C}_{\text{CH}_4}$ values of headspace gases from the gravity piston cores and released gases from pressure cores, which range from -74.3‰ PDB to -46.2‰ PDB, with the majority less than -55‰ PDB. The hydrate deposit is a distributed gas hydrate system in Shenhu area.

1. Introduction

Gas hydrate is an ice-like solid substance formed by the combination of low-molecular-weight gases such as methane, ethane, and carbon dioxide with water. Gas hydrate mainly occurs naturally in sediments beneath the permafrost and the sediments of the continental slope in the water depths more than 300 m. The marine gas hydrate is important to the economy and environment due to its enormous inventory and geohazards potential. Gas hydrate and its bearing sediments thus become an important scientific topic.

The stability of gas hydrate depends on temperature, pressure, gas composition, and pore water salinity. Nucleation and growth of gas hydrate also depends on sediment grain size, shape, and minerals [1]. These factors, which control gas hydrate formation and stability, are affected by

a series of physical and chemical processes in the marine sediments and result in a variation of gas hydrate dynamics on different timescales [2–7]. Therefore, gas hydrate is not continuously distributed all over the world in the vertical and horizontal scales [8–10]. Because the geological setting and the factors controlling the gas hydrate formation are different in various locations, scientists have established different geological models based on the formation mechanisms, gas sources, and dynamics. Gas hydrate deposits can be classified into the high-flux gas hydrate deposit and low-flux gas hydrate deposit, based on the mechanisms that control gas transport into the gas hydrate stability zone, although both operate simultaneously in many regions [7].

The northern slope of South China Sea (SCS) is a passive continental margin. Geological, geophysical, and geochemical investigations for gas hydrate have been carried

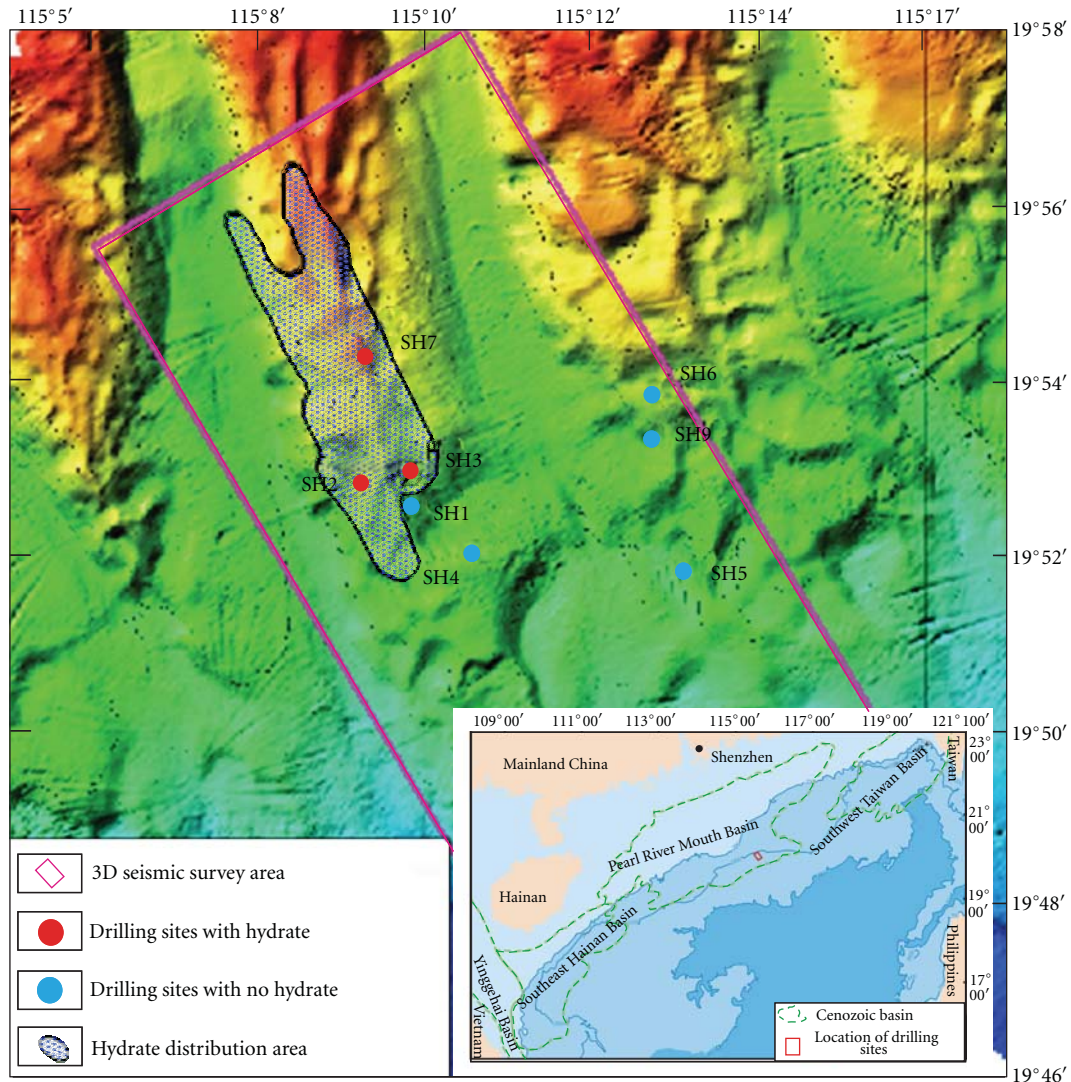


FIGURE 1: Sketch map showing the bathymetry of study area, drilling sites, and the confirmed gas hydrate distribution in Shenhu area. Insert: General location of study area in northern slope of South China Sea.

out and showed great promise for gas hydrates in this region [11–26]. Shenhu area is in the middle of the northern slope of SCS, between Xisha Trough and Dongsha Islands, and tectonically located in the Zhu II Depression, Pearl River Mouth Basin (Figure 1). The thickness of sediments is 1000–7000 m with 0.46–1.9% organic matter [27]. High-resolution seismic investigation shows that most of bottom simulating reflectors (BSRs) are located 150~350 m below seafloor [28]. The heat flow ranges from $74.0 \text{ mW} \cdot \text{m}^{-2}$ to $78.0 \text{ mW} \cdot \text{m}^{-2}$, with an average of $76.2 \text{ mW} \cdot \text{m}^{-2}$, and the geothermal gradient ranges from 45 to $67.7^\circ\text{C}/\text{km}$. This area has already become a large source of oil and natural gas. Therefore, originally, the gas hydrate system was thought to be the high-flux gas hydrate deposit with the thermogenic gas from a deep source in Shenhu area [28].

In order to detect the gas hydrate occurrences and determine the nature and distribution of gas hydrate, a gas hydrate drilling expedition GMGS-1 was initiated by Guangzhou Marine Geological Survey using M/V Bavenit

along with specialized Fugro and Geotek in Shenhu area in 2007. Eight sites were investigated, and a pilot hole was drilled at all sites. A sampling and testing hole was drilled at sites SH1, SH2, SH3, SH5, and SH7. Gas hydrate bearing sediments were recovered at SH2, SH3 and SH7 which the water depth is, respectively, 1230 m, 1245 m, and 1105 m (Figure 1).

From the previous geological investigations and hydrate drilling results, we present a discussion of the geochemical evidence of the gas hydrate system of Shenhu area, based on the pore-water geochemical features of core sediments and their implied gas sources, gas hydrate distribution and concentration of pore volume of sediments, and gas hydrate deposit model in this paper.

2. Methods

The sampling hole was used to determine the concentration, nature, and distribution of gas hydrate in the section, as well

as the temperature gradient, the base of methane gas hydrate stability, the depth of sulphate methane interface (SMI). Both nonpressure and pressure cores were retrieved from the sampling holes with a variety of tools at depths guided by detailed wireline logs and seismic data. Nonpressure cores were sampled for pore water analysis. The results were used to quantify pore water freshening caused by gas hydrate dissociation. Plug samples of sediment were taken from centers of cores and squeezed in a hydraulic press to separate pore water for chemical analyses. Pore water salinity and chloride were measured on board, respectively by refractometry with a precision of ± 0.5 ppt and by silver nitrate titration using a chromate indicator with a repeatability of $\pm 0.5\%$. Sulfate was measured on board by ion chromatography. Baseline chlorinity profiles were constructed by the maximum measured chlorinities from the nonpressure cores and pressure cores. Pore water freshening was calculated from the difference between measured chlorinity and the estimated *in situ* baseline chlorinity. Gas hydrate concentration was calculated from pore water freshening, the density, and water content. The model assumes that pore space can be occupied by either pore water or gas hydrate. Gas hydrate concentration has an estimated error of $\pm 2\%$ of pore volume.

Gas voids in nonpressure cores were sampled light hydrocarbon gases. Headspace samples were taken from near surface cores to determine the depth of SMI. A 5 mL plug of sediment was sealed in a 26 mL glass vial using a teflon-coated septum and an aluminum crimp seal. First added 2 mL saturated NaCl solution to the vial, the sediment was slurred, and the vial was placed in 60°C for two hours. The vials were cool down to room temperature, the headspace gas of the vial was analyzed, and the concentration of hydrocarbon in the pore waters was calculated. Gas composition was measured using an Agilent MicroGC 3000 A gas chromatograph with molecular sieve and PLOT U columns and thermal conductivity detectors. Air contamination during sampling was removed from gas totals.

Most pressure cores were depressurized in a controlled fashion to quantify the total amount of hydrocarbon gas in all phases, including gas hydrate. Gas was collected and analyzed by the on-board gas chromatograph. The released gas volume was determined by the volume of gas and fluid expelled from the system. The gas volumes were used to calculate *in situ* gas concentrations.

3. Results

3.1. The Headspace Methane and Sulfate of Pore Waters in Shallow Sediments. The headspace methane and sulfate concentration of pore waters in shallow sediments is plotted in Figures 2(a)–2(e) for sites SH1, SH2, SH3, SH5, and SH7 as a function of the depth. The decrease of sulfate and the increase of methane at SMI are clear. However, the change pattern of methane and sulfate curves is dissimilar and may show the varied anaerobic methane oxidation (AMO) at different site. According to the methane and sulfate concentration profiles, the depths of SMI were determined to be 17 mbsf to 27 mbsf (Figure 2).

3.2. The Salinity of Pore Waters in Sediments. The salinity, sulfate and chlorinity versus depth at sites SH2, SH3, and SH7 are shown in Figures 3(a)–3(c). The curve is characterized by irregular and anomalous freshening spikes in the gas hydrate zone. These spikes result from the dissociation of gas hydrates during the recovery, because gas hydrates do not contain any salts.

It is clear that the curve shows a background trend towards lower salinities in the gas hydrate zone. The baseline chlorinity of pore waters in gas hydrate zone and below the base of the gas hydrate stability zone (BGHSZ) is about 10% lower than that of shallow sediments. At site SH2, pore water shows a slight decrease of the baseline chlorinity, for example, 570 mM near the surface to 520 mM at a depth of 240 mbsf. Pore water freshening is consistent between 187 mbsf and 230 mbsf, with a gas hydrate concentration over 25% and peaking around 48% (Figure 3(a)). At site SH3, the baseline chlorinity decreases slightly with depth, from 565 mM at the surface to 500 mM at a depth of 212 mbsf. The pore water freshening is identified by pressure cores and shows the gas hydrate zone located between 190 mbsf and 200 mbsf, with the maximum gas hydrate concentration of 26% (Figure 3(b)). At site SH7, pore water baseline chlorinity decreases lightly as well. Pore water freshening is marked between 135 mbsf and 178 mbsf. The maximum gas hydrate concentration is about 43% (Figure 3(c)).

Combining the geochemical data, the gas hydrate-bearing sediments are 10 m to 43 m in thickness and located just above BGHSZ in Shenhu area. The highest gas hydrate volume ratio appears near the base of the gas hydrate stability zone. It is very interesting that the hydrate bearing sediments compose fine grained silty clay and clay silt according to the core sediment description and grain-size analysis [29]. However, the gas hydrate concentration is very high and the maximum is about 48%.

3.3. The Gas Composition and Methane/Ethane Ratio. The gas composition and methane/ethane ratio versus depth is shown in Table 1 and Figures 4(a)–4(c) for sites SH2, SH3, and SH7. The methane content is 96.10–99.91% with small amount of ethane and propane, and hence models for structure I methane hydrate. The methane/ethane ratio slightly decreases with depth above the gas hydrate zone and has a sudden change below and inside the gas hydrate zone. The methane/ethane ratios are higher than 1000 above the gas hydrate zone and less than 1000 at the interval of gas hydrate zone and below BGHSZ.

Methane mass balance analysis of SH2 shows that a single depressurized core inside the hydrate zone is oversaturated with methane. This core released 26.7 L methane during depressurization, and gas hydrate shares 27.1%. Methane is the dominant gas in headspace gas, void gas, and pressure core depressurization experiments. The methane is 96.10–99.82% and with small amount of ethane and propane. The ratio of methane to ethane is greater than 1,205 above 187 mbsf and 330–736 below 187 mbsf (Table 1, Figure 4(a)). At site SH3, methane is undersaturated in the sediment column near the upper resistivity anomaly, but saturated

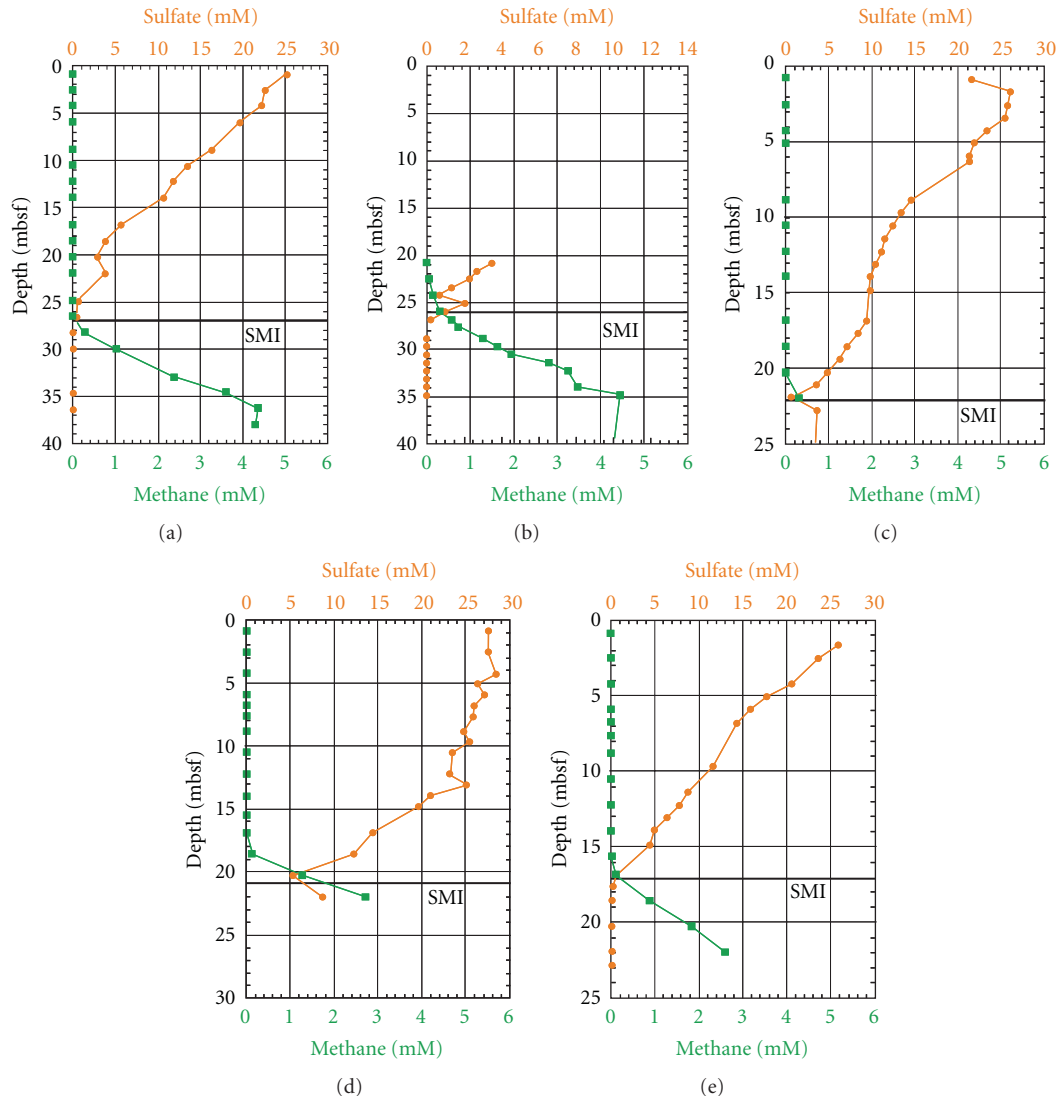


FIGURE 2: Sulfate and methane versus depth in pore waters from shallow sediments showing the decrease of sulfate and the increase of methane at the sulfate-methane interface (SMI). (a) Site SH1, (b) Site SH2, (c) Site SH3, (d) Site SH5, (e) Site SH7.

around the lower resistivity anomaly. Methane was the dominant gas in all gas samples. The average methane/ethane ratio is 1200 (Table 1, Figure 4(b)). At site SH7, one single depressurized core from inside the hydrate zone is saturated in methane. This core released over 18.7 L methane and occupied 27.8% gas hydrate. Methane is also the dominant gas. The average methane/ethane ratio is 4200 (Table 1, Figure 4(c)).

4. Discussions

4.1. Influence of Gas Hydrates on Geochemistry of Fluids. The baseline chlorinity of pore waters shows 10% lower than that of shallow sediments below and inside the gas hydrate zone, and the methane/ethane ratio presents a sudden change below and inside the gas hydrate zone (Figure 3), showing that the gas hydrate is of the influence on the geochemistry of associated fluids. This phenomenon has been noted in the Blake Outer Ridge. Based on the analyses of gases and pore

waters, Thiéry et al. investigated two aspects of the influence of gas hydrates on the geochemistry of fluids [30]. The first aspect is the presence of pore waters less saline than sea waters above and inside the gas hydrate zone because of the upward expulsion of saline waters during the compaction of sediments in the gas hydrate zone; the second one is related to the methane/ethane ratio which shows a sudden change of trend at BGHZ as gas hydrate acts as a concentration barrier for ethane [30]. Unfortunately, the incomplete coring and large spacing interval of sampling probably resulted in the nontypical phenomena in Shenhu area. However, gas hydrates dissociate and release fresh waters and methane gases that should mainly contribute to lowering the salinity of pore waters and methane/ethane ratio at the interval of gas hydrate zone.

4.2. Gas Source of Hydrate. The relative deep SMI (Figure 2) implies that upward methane flux is low, and the highest concentration of gas hydrate is near BGHSZ in Shenhu area.

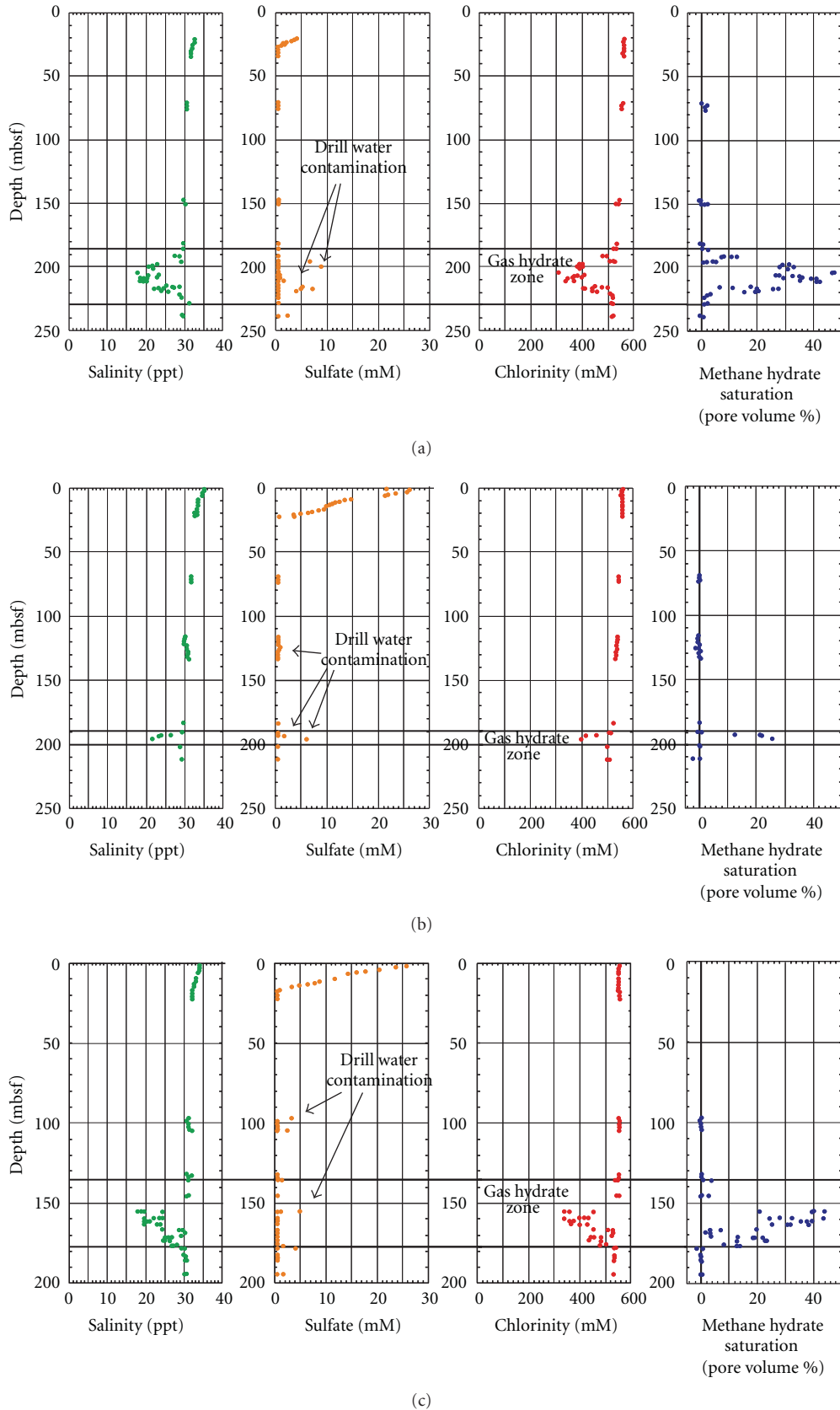


FIGURE 3: Salinity, chlorinity, and sulfate versus depth in pore waters and gas hydrate concentration versus depth at Site SH2 (a), SH3 (b) and SH7 (c). Salinity and chlorinity are corrected for drill water infiltration. Baseline chlorinity used for pore water freshening calculation. The gas hydrate-bearing sediment zone is located within 43, 10, and 40 meters above the BSR, respectively, at SH2, SH3, and SH7.

TABLE 1: Gas composition and methane/ethane ratio in sediments of Shenhu Area, northern slope of SCS.

Sample no.	Depth (mbsf)	Gas composition			C ₁ /C ₂
		CH ₄ (%)	C ₂ H ₆ (ppm)	C ₃ H ₈ (ppm)	
SH2-1	70.73	96.10	440	LD	2185
SH2-2	73.31	96.72	477	LD	2027
SH2-3	146.46	98.49	646	97	1524
SH2-4	146.89	98.02	632	88	1551
SH2-5	150.00	99.53	552	67	1804
SH2-6	150.00	96.60	494	LD	1956
SH2-7	181.65	99.36	675	65	1473
SH2-8	182.07	97.75	533	LD	1833
SH2-9	185.39	99.21	581	61	1708
SH2-10	185.54	99.32	824	53	1205
SH2-11	195.40	99.32	1611	LD	616
SH2-12	197.50	99.82	1737	LD	575
SH2-13	197.50	99.80	1974	LD	506
SH2-14	197.50	99.77	2330	LD	428
SH2-15	197.50	99.72	2778	LD	359
SH2-16	197.50	99.57	3015	LD	330
SH2-17	221.71	99.68	1559	LD	639
SH2-18	228.00	99.70	1653	LD	603
SH2-19	238.58	99.06	1346	LD	736
SH3-1	68.63	99.12	632	ND	1569
SH3-2	71.32	99.78	692	LD	1443
SH3-3	74.55	99.77	640	LD	1560
SH3-4	117.01	99.77	644	LD	1548
SH3-5	117.60	99.80	658	LD	1516
SH3-6	119.85	99.69	618	LD	1613
SH3-7	121.15	99.83	703	LD	1419
SH3-8	125.00	99.91	659	LD	1516
SH3-9	125.00	99.89	695	LD	1438
SH3-10	128.71	99.80	696	LD	1434
SH3-11	129.06	99.73	661	ND	1510
SH3-12	132.34	99.78	726	LD	1374
SH3-13	132.80	99.79	721	LD	1385
SH3-14	190.50	99.87	1241	ND	805
SH3-15	190.50	99.87	1237	ND	807
SH3-16	190.50	99.21	1051	ND	944
SH3-17	192.95	99.21	3587	ND	277
SH3-18	201.31	99.85	1376	ND	718
SH3-19	201.70	99.73	2209	ND	451
SH7-1	97.52	97.52	158	84	6161
SH7-2	99.53	98.19	188	67	5233
SH7-3	100.83	97.40	139	70	6989
SH7-4	104.00	99.86	159	67	6286
SH7-5	131.81	96.44	80	LD	11995
SH7-6	132.84	95.56	102	LD	9377
SH7-7	135.00	99.68	88	55	11315
SH7-8	135.00	99.47	124	61	8009
SH7-9	155.00	99.89	1066	ND	937
SH7-10	155.00	99.85	1042	ND	958
SH7-11	155.00	99.84	1017	ND	981
SH7-12	155.00	99.81	1137	ND	878

TABLE 1: Continued.

Sample no.	Depth (mbsf)	Gas composition			C ₁ /C ₂
		CH ₄ (%)	C ₂ H ₆ (ppm)	C ₃ H ₈ (ppm)	
SH7-13	155.00	99.74	1078	ND	925
SH7-14	168.67	99.55	2912	ND	342
SH7-15	176.12	99.21	7621	ND	130
SH7-16	185.00	99.76	2182	ND	457
SH7-17	185.00	99.54	2277	LD	437

Note. Mbsf: meters below seafloor; % of original gas, mole percent of each gas in the original sample; depressurization samples and void gas samples; ethane and propane (ppm), detection limit 50 parts per million; LD means lower than detection limit; ND means not detectable; C₁/C₂ is the molecule ratio of methane to ethane.

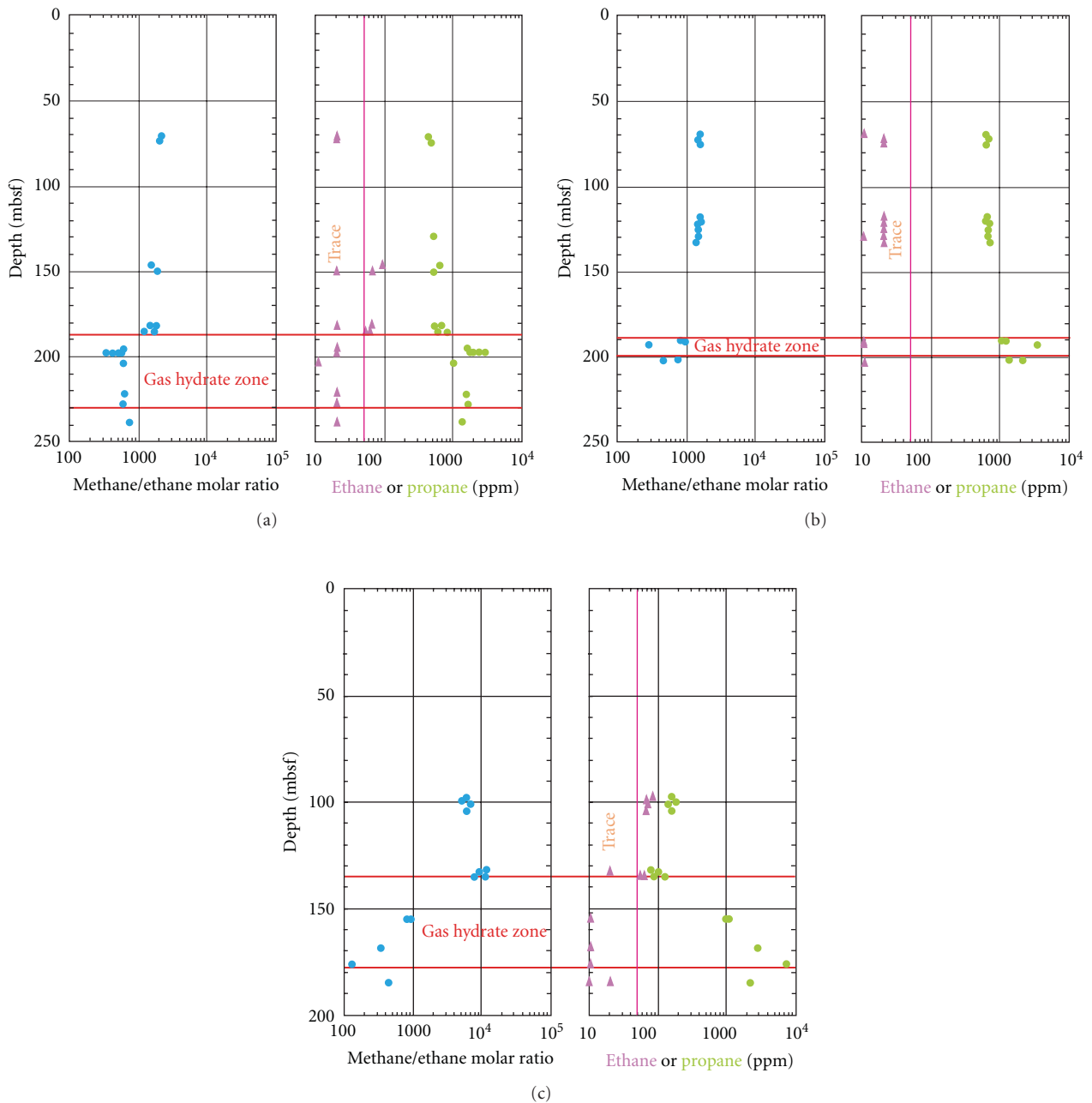


FIGURE 4: Methane/ethane versus depth at Site SH2 (a) SH3 (b), and SH7 (c). Vertical line is detection limit.

TABLE 2: $\delta^{13}\text{C}_{\text{CH}_4}$ data of headspace gases from the gravity piston cores and released gases from pressure cores of Shenhu area, northern slope of SCS.

Sample no.	$\delta^{13}\text{C}_{\text{CH}_4}$ (‰, PDB)
HS-23PC-1/7	-57.0
HS-23PC-2/7	-62.4
HS-23PC-3/7	-64.9
HS-23PC-4/7	-62.1
HS-23PC-5/7	-61.7
HS-23PC-6/7	-59.5
HS-23PC-7/7	-69.5
HS-4PC-1/7	-60.7
HS-4PC-2/7	-62.1
Sample no.	$\delta^{13}\text{C}_{\text{CH}_4}$ (‰, PDB)
HS-4PC-3/7	-74.3
HS-4PC-4/7	-46.2
HS-4PC-5/7	-56.9
HS-4PC-6/7	-63.8
HS-4PC-7/7	-51.0
SH2B-12R	-56.7
SH3B-7P	-62.2
SH5C-11R	-54.1
SH3B-13P	-60.9

This is similar to the gas hydrate distribution features of Blake Ridge [31] and Hydrate Ridge [8]. However, fluid advection may still be a key factor for the migration of methane-bearing fluid to the gas hydrate stability zone, if the *in situ* microbial methane gas production is more than our general thought. This fluid diffusion is very low, and it is not fast enough to form thick gas hydrate in reasonable geologic time scale.

There are two gas sources for the formation of gas hydrate, biogenic gas, and thermogenic gas. Biogenic methane derived anywhere organic matter and microbial populations occur [32]. AOM is the main reason for the zone of methane depletion from seafloor to SMI in marine sediments. The depth of SMI is a significant indication for methane flux in diffusion-type gas hydrate system [33, 34]. However, hydrate can also be found on the seafloor or near the seafloor [33–37]. The formation gas hydrate on seafloor surface requires high methane fluxes and geochemical property that gas from the deeper below seafloor [7].

The current paradigm for distinguishing between microbial and thermogenic sources of methane is one that uses the relative amounts of low-molecular-weight hydrocarbon gases and $\delta^{13}\text{C}_{\text{CH}_4}$ values [38]. Microbial methane typically has $\delta^{13}\text{C}_{\text{CH}_4}$ values that range from -90‰ to -55‰ (PDB) and methane/ethane ratios of $>1,000$, while thermogenic methane typically has $\delta^{13}\text{C}_{\text{CH}_4}$ values more positive than -55‰ and methane/ethane ratios of <100 [38]. The $\delta^{13}\text{C}_{\text{CH}_4}$ values of headspace gases from the gravity piston core sediments and released gases from the pressure cores at site SH2, SH3, and SH5 range from -74.3‰ PDB to -46.2‰ PDB, with the majority less than

-55‰ PDB (Table 2). Two gas samples from hydrate dissociation (SH2B-12R and SH3B-13P) measured, respectively, the $\delta^{13}\text{C}_{\text{CH}_4}$ value of -56.7‰ PDB and -60.9‰ PDB. The methane/ethane ratio are high, greater than 1000 above the gas hydrate zone, and less than 1000 at the interval of gas hydrate zone and below BGHSZ.

Therefore, the methane forming the gas hydrate is mainly from the microbially produced methane, not thermogenic gas from a deep source in Shenhu area, northern slope of SCS.

4.3. Gas Hydrate Distribution and Accumulation Model. GMGS-1 drilling expedition in Shenhu area shows that the thickness of hydrate-bearing sediments is 10–43 m with the maximum gas hydrate concentration around 48%, but the depth and thickness of the gas hydrate-bearing sediments varied in different sites with similar distribution features. (i) Vertically, the gas hydrate occurs deep, and the gas hydrate-bearing sediment zone is near the bottom of BGHSZ (Figure 3), (ii) horizontally, not all BSR regions have gas hydrate, but the gas hydrate was drilled and discovered in the regions with strong BSR reflection (Figure 1), and (iii) the gas hydrate-bearing sediments are composed of fine grained silty clay or clay silt.

Gas hydrate can be classified into two categories, (i) focused, high flux gas hydrate (FHF) and (ii) distributed, low-flux gas hydrate (DLF) according to the control mechanism of gas entering the gas hydrate stability zone [7]. FHF system always forms massive gas hydrate near the seafloor, and DLF system forms the decentralized gas hydrate and in deep sediments. Shenhu area has the features of a stable tectonic setting, relatively even fine grained sediments and lower penetration rate. Clearly, the gas hydrate system may be a distributed, low-flux gas hydrate reservoir in Shenhu area, northern slope of SCS.

5. Conclusions

The geochemical data collected during GMGS-1 drilling expedition help us to better understand the gas hydrate system in Shenhu area of Pearl River Mouth Basin, SCS. The influence of gas hydrates on geochemistry of fluids, gas source, gas hydrate distribution and concentration of pore volume of sediments, and gas hydrate deposit model have been discussed here. The presence of less saline pore waters and sudden change of methane/ethane ratios below and inside the gas hydrate zone shows the influence of gas hydrate on the geochemistry of associated fluids. The disseminated gas hydrate in silty clay is just located above the base of the gas hydrate stability zone, with the thickness of 10–43 m and the concentration up to 48%. The methane content is 96.10–99.91% with small amount of ethane and propane. The methane/ethane ratios are higher than 1000 above the gas hydrate zone and less than 1000 at the interval of gas hydrate zone. Most of the methane gases in these fine grained sediments have been mainly produced biogenically. This is evidenced by the $\delta^{13}\text{C}_{\text{CH}_4}$ values of headspace gases from the gravity piston cores and released gases from pressure cores,

which range from -74.3% PDB to -46.2% PDB, with the majority less than -55% PDB. Thus, the hydrate deposit is a distributed gas hydrate system in Shenhu area.

Acknowledgments

The gas hydrate drilling expedition aboard M/V Bavenit was planned, coordinated, and carried out by China Geological Survey. This study is financially supported by the National Natural Science Foundation of China (no. U0933004), National Basic Research Program of China (973 Program) (no. 2009CB219506), the Scientific and Technology Program of Guangdong Province (no. 2011A080403021), and Ministry of Land and Resources of China (no. 200811014). The authors wish to thank all individuals for their input and support.

References

- [1] M. B. Clennell, M. Hovland, J. S. Booth, P. Henry, and W. J. Winters, "Formation of natural gas hydrates in marine sediments 1. Conceptual model of gas hydrate growth conditioned by host sediment properties," *Journal of Geophysical Research B*, vol. 104, no. 10, pp. 22985–23003, 1999.
- [2] G. R. Dickens, J. R. O'Neil, D. K. Rea, and R. M. Owen, "Dissociation of oceanic methane hydrate as a cause of the carbon isotope excursion at the end of the Paleocene," *Paleoceanography*, vol. 10, no. 6, pp. 965–971, 1995.
- [3] J. P. Kennett, K. G. Cannariato, I. L. Hendy, and R. J. Behl, *Methane Hydrates in Quaternary Climate Change: The Clathrate Gun Hypothesis*, American Geophysical Union, Washington, DC, USA, 2003.
- [4] K. Kvenvolden, "Methane hydrates and climate change," *Global Biogeochemical Cycles*, vol. 2, no. 3, pp. 221–229, 1988.
- [5] C. K. Paull and R. Matsumoto, "Leg 164 overview," in *Proceedings of the Ocean Drilling Program, Scientific Results*, C. K. Paull, R. Matsumoto, and P. J. Wallace, Eds., vol. 164, pp. 3–10, Ocean Drilling Program, College Station, Tex, USA, 2000.
- [6] B. Buffett and D. Archer, "Global inventory of methane clathrate: sensitivity to changes in the deep ocean," *Earth and Planetary Science Letters*, vol. 227, no. 3-4, pp. 185–199, 2004.
- [7] A. M. Tréhu, C. Ruppel, M. Holland et al., "Gas hydrates in marine sediments: lessons from scientific drilling," *Oceanography*, vol. 19, no. 4, pp. 124–142, 2006.
- [8] A. M. Tréhu, G. Bohrmann, F. R. Rack, and M. E. Torres, *Proceedings of the Ocean Drilling Program, Initial Reports*, vol. 204, Texas A&M University, College Station (Ocean Drilling Program), Tex, USA, 2003.
- [9] S. Bünz, J. Mienert, and C. Berndt, "Geological controls on the Storegga gas-hydrate system of the mid-Norwegian continental margin," *Earth and Planetary Science Letters*, vol. 209, no. 3-4, pp. 291–307, 2003.
- [10] X. Su, "Marine gas hydrate distribution and gas-water-sediments dynamic system—inspiration of ODP Leg 204 preliminary result," *Science in China Series D*, vol. 34, no. 12, pp. 1091–1099, 2004.
- [11] B. H. Wu, G. X. Zhang, Y. H. Zhu, Z. Q. Lu, and B. Chen, "Progress of gas hydrate investigation in China offshore," *Frontiers of Earth Science*, vol. 10, pp. 177–189, 2003.
- [12] H. B. Song, N. Y. Wu, S. G. Wu, and W. W. Jiang, "data processing and its BSR character of line 973 in the northeastern South China Sea," in *The Evolution of China Margin Seas and Its Resource Response*, J. B. Li and S. Gao, Eds., pp. 182–185, China Ocean Press, Beijing, China, 2004.
- [13] E. Suess, Y. Y. Huang, N. Y. Wu, X. Q. Han, and X. Su, *IFM-GEOMAR Report, FS Sonne Cruise Report SO177*, Leibniz Institute of Marine Sciences, Kiel, Germany, 2005.
- [14] D. F. Chen, Y. Y. Huang, X. L. Yuan, and L. M. Cathles, "Seep carbonates and preserved methane oxidizing archaea and sulfate reducing bacteria fossils suggest recent gas venting on the seafloor in the Northeastern South China Sea," *Marine and Petroleum Geology*, vol. 22, no. 5, pp. 613–621, 2005.
- [15] S. Wu, G. Zhang, Y. Huang, J. Liang, and H. K. Wong, "Gas hydrate occurrence on the continental slope of the northern South China Sea," *Marine and Petroleum Geology*, vol. 22, no. 3, pp. 403–412, 2005.
- [16] S. Y. Jiang, T. Yang, L. Ge et al., "Geochemical evidences for gas hydrate occurrence in the northern margin of the South China Sea," in *Proceedings of the Western Pacific Geophysics Meeting*, vol. 87, Eos Transactions of American Geophysical Union, 2006, Abstract, OS44B-01.
- [17] S. Y. Jiang, T. Yang, L. Ge et al., "Geochemistry of pore waters from the Xisha Trough, northern South China Sea and their implications for gas hydrates," *Journal of Oceanography*, vol. 64, no. 3, pp. 459–470, 2008.
- [18] N. Y. Wu, H. L. Dong, E. Suess et al., "Mineralogical features and C-O isotope composition of methane-derived carbonate build-up found in the northeastern South China Sea," in *Proceedings of the Western Pacific Geophysics Meeting*, vol. 87, Eos Transactions of American Geophysical Union, 2006, Abstract, OS41F-01.
- [19] N. Y. Wu, S. Y. Fu, E. Suess, B. Domeyer, Y. Y. Huang, and Y. H. Zhu, "Pore-water geochemistry of surface sediments from Haiyang 4 Area of the northeastern South China Sea," in *Proceedings of the Western Pacific Geophysics Meeting*, vol. 87, Eos Transactions of American Geophysical Union, 2006, Abstract, OS31A-0098.
- [20] T. Yang, S. Y. Jiang, J. H. Yang et al., "Dissolved inorganic carbon (DIC) and its carbon isotopic composition in sediment pore waters from the Shenhu area, northern South China Sea," *Journal of Oceanography*, vol. 64, no. 2, pp. 303–310, 2008.
- [21] T. F. Yang, C. S. Liu, J. C. Chen, and C. Y. Huang, "Preface to the special issue on gas hydrate research around the South China Sea and Taiwan," *Terrestrial, Atmospheric and Oceanic Sciences*, vol. 17, no. 4, pp. I–VI, 2006.
- [22] T. F. Yang, P. C. Chuang, S. Lin, J. C. Chen, Y. Wang, and S. H. Chung, "Methane venting in gas hydrate potential area offshore of SW Taiwan: evidence of gas analysis of water column samples," *Terrestrial, Atmospheric and Oceanic Sciences*, vol. 17, no. 4, pp. 933–950, 2006.
- [23] C. S. Liu, P. Schnürle, Y. Wang, S. H. Chung, S. C. Chen, and T. H. Hsiuan, "Distribution and characters of gas hydrate offshore of southwestern Taiwan," *Terrestrial, Atmospheric and Oceanic Sciences*, vol. 17, no. 4, pp. 615–644, 2006.
- [24] S. Lin, W. C. Hsieh, Y. C. Lim, T. F. Yang, C. S. Liu, and Y. Wang, "Methane migration and its influence on sulfate reduction in the good weather ridge region, South China Sea continental margin sediments," *Terrestrial, Atmospheric and Oceanic Sciences*, vol. 17, no. 4, pp. 883–902, 2006.
- [25] P. C. Chuang, T. F. Yang, S. Lin et al., "Extremely high methane concentration in bottom water and cored sediments from offshore southwestern Taiwan," *Terrestrial, Atmospheric and Oceanic Sciences*, vol. 17, no. 4, pp. 903–920, 2006.
- [26] X. Han, E. Suess, Y. Huang et al., "Jiulong methane reef: microbial mediation of seep carbonates in the South China Sea," *Marine Geology*, vol. 249, no. 3-4, pp. 243–256, 2008.

- [27] P. Wang, W. L. Prell, and P. Blum, "Ocean drilling program leg 184 scientific prospectus South China Sea, site 1144," in *Proceedings of the Ocean Drilling Program, Initial Reports*, P. Wang, W. L. Prell, and P. Blum, Eds., vol. 184, pp. 1–97, Ocean Drilling Program, College Station, Tex, USA, 2000.
- [28] N. Y. Wu, H. Q. Zhang, S. X. Yang et al., "Preliminary discussion on natural gas hydrate reservoir system of Shenhu area, north slope of South China Sea," *Natural Gas Industry*, vol. 27, no. 9, pp. 1–6, 2007.
- [29] N. Y. Wu, H. Q. Zhang, X. Su et al., "High concentrations of hydrate in disseminated forms found in very fine-grained sediments of Shenhu area, South China Sea," *Terra Nostra*, vol. 1-2, pp. 236–237, 2007.
- [30] B. B. Bernard, J. M. Brooks, and W. M. Sackett, "Light hydrocarbons in recent Texas continental shelf and slope sediments," *Journal of Geophysical Research*, vol. 83, pp. 4053–4061, 1978.
- [31] T. D. Lorenson and Leg 164 Shipboard Scientists, "Graphic summary of gas hydrate occurrence by proxy measurements across the Blake Ridge," in *Proceedings of the Ocean Drilling Program, Scientific Results*, C. K. Paull, R. Matsumoto, and P. J. Wallace, Eds., vol. 164, pp. 247–252, Ocean Drilling Program, College Station, Tex, USA, 2000.
- [32] M. K. Davie and B. A. Buffett, "Sources of methane for marine gas hydrate: inferences from a comparison of observations and numerical models," *Earth and Planetary Science Letters*, vol. 206, no. 1-2, pp. 51–63, 2003.
- [33] W. S. Borowski, C. K. Paull, and W. Ussler, "Marine pore-water sulfate profiles indicate in situ methane flux from underlying gas hydrate," *Geology*, vol. 24, no. 7, pp. 655–658, 1996.
- [34] W. S. Borowski, C. K. Paull, and W. Ussler, "Global and local variations of interstitial sulfate gradients in deep-water, continental margin sediments: sensitivity to underlying methane and gas hydrates," *Marine Geology*, vol. 159, no. 1, pp. 131–154, 1999.
- [35] J. M. Brooks, M. C. Kennicutt, R. R. Fay, T. J. McDonald, and R. Sassen, "Thermogenic gas hydrates in the Gulf of Mexico," *Science*, vol. 225, no. 4660, pp. 409–411, 1984.
- [36] E. Suess, M. E. Torres, G. Bohrman et al., "Sea floor methane hydrate at hydrate Ridge, Cascadia Margin," in *Natural Gas Hydrates: Occurrence, Distribution, and Detection*, C. K. Paul and W. P. Dillon, Eds., pp. 87–98, American Geophysical Union, Washington, DC, USA, 2001.
- [37] N. R. Chapman, J. W. Pohlman, R. B. Coffin, J. P. Chanton, and L. Lapham, "Thermogenic gas hydrates in the northern Cascadia Margin," *EOS Transactions, American Geophysical Union*, vol. 85, no. 38, pp. 361–365, 2004.
- [38] R. Thiéry, R. Bakker, C. Monnin, and The ODP Leg 164 shipboard scientific party, "Geochemistry of gas hydrates and associated fluids in the sediments of a passive continental margin: Preliminary results of the ODP Leg 164 on the Blake Outer Ridge," in *Gas Hydrates Relevance to World Margin Stability and Climate Change*, I. R. Henriot and J. Mienert, Eds., vol. 137, pp. 161–165, Geological Society, London, UK, 1998.

Research Article

Basal and Frontal Accretion Processes versus BSR Characteristics along the Chilean Margin

I. Vargas-Cordero,¹ U. Tinivella,² F. Accaino,² F. Fanucci,³ M. F. Loreto,² M. E. Lascano,⁴ and C. Reichert⁵

¹Barcelona Center for Subsurface Imaging, Instituto de Ciencias del Mar, CSIC, Passeig Marítim de la Barceloneta 37-49, 08003 Barcelona, Spain

²Istituto Nazionale di Oceanografia e di Geofisica Sperimentale (OGS), Borgo Grotta 42C, Trieste, 34010 Sgonico, Italy

³Dipartimento di Scienze Geologiche, Ambientale e Marine, Università degli Studi di Trieste, C. San Giovanni, Via E. Weiss 2, 34127 Trieste, Italy

⁴International Centre for Theoretical Physics (ICTP), Strada Costiera 11, 34014 Trieste, Italy

⁵Federal Institute for Geosciences and Natural Resources (BGR), Stilleweg 2, 30655 Hannover, Germany

Correspondence should be addressed to I. Vargas-Cordero, ivargas@ub.edu

Received 1 December 2010; Accepted 13 July 2011

Academic Editor: Ingo Pecher

Copyright © 2011 I. Vargas-Cordero et al. This is an open access article distributed under the Creative Commons Attribution License, which permits unrestricted use, distribution, and reproduction in any medium, provided the original work is properly cited.

Multichannel seismic reflection data recorded between Itata (36°S) and Coyhaique offshores (43°S) were processed to obtain seismic images. Analysis of the seismic profiles revealed that weak and discontinuous bottom simulating reflectors were associated to basal accretion processes, while strong and continuous bottom simulating reflectors were associated to frontal accretion processes. This can be explained considering that during basal accretion processes, extensional tectonic movements due to uplifting can favour fluid escapes giving origin to weaker and most discontinuous bottom simulating reflectors. During frontal accretion processes (folding and thrusting), high fluid circulation and stable tectonic conditions however can be responsible of stronger and most continuous bottom simulating reflectors. Along the Arauco-Valdivia offshores, steep accretionary prisms, normal faults, slope basins, and thicker underplated sediment bed were associated to basal accretion, while along the Itata, Chiloe and Coyhaique offshores, small accretionary prisms, folding, and thinner underplated sediment bed were associated to frontal accretion.

1. Introduction

In marine seismic records, the Bottom Simulating Reflector (BSR) is a good indicator of gas hydrate presence. The BSR has allowed defining the distribution of gas hydrate [1–4] along several continental margins. The BSR is associated with the acoustic interface between overlying sediment containing gas hydrate, which increases compressional seismic velocity, and underlying sediment containing free gas, which decreases compressional seismic velocity [2, 5]. The BSR has been identified in seismic sections in accretionary complexes along both convergent and passive margin settings [1]. Along the Chilean continental margin, the BSR is well reported by several geophysical cruises. In particular, the BSR is recognized along the accretionary prism [6–11].

Along the Chilean margin, two main tectonic processes are recognized. The first one is associated with frontal accretion and the second one with basal accretion [11–14].

This study is aimed at identifying the main morphostructures on the continental margin, in particular on oceanic trench and continental slope. In this way, by interpreting six stacked and poststack time-migrated sections, relationships between BSR characteristics and tectonic processes can be identified (Figure 1).

2. Tectonic and Geological Setting

The study area is located along the Central Chile, between 35° and 45°S including Itata, Arauco, Toltén, and Valdivia

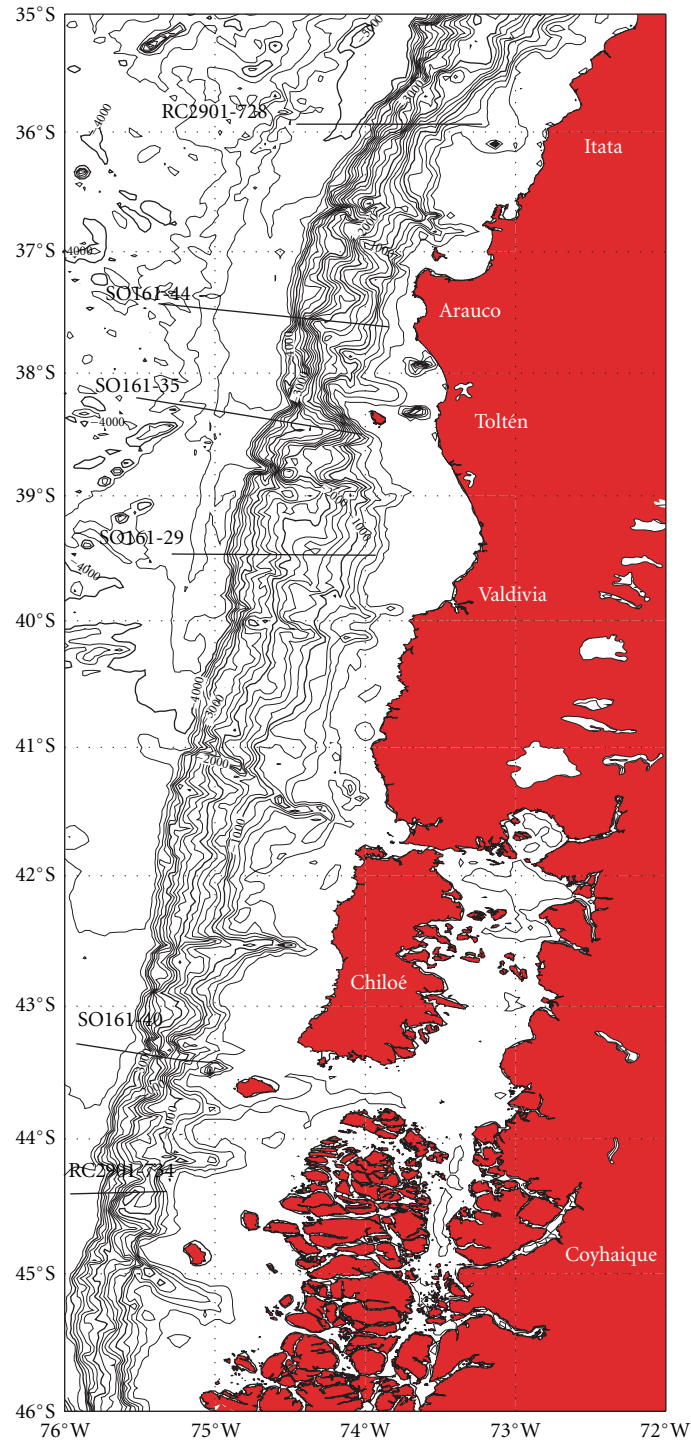


FIGURE 1: Map of study area.

offshores (from 36° to 40°S) and Chiloé and Coyhaique offshores (from 43° to 45°S) (Figure 1).

The central and south Chile (34°–46°S) is limited northwards the Juan Fernandez ridge and southwards the Chile rise. The Juan Fernandez ridge is characterized by Pampean flat-slab segment, which presents a lack of volcanism and foreland uplift (*Sierras Pampeanas*) the highest mountains

of the Andes, such as the Aconcagua massif (6989 m). South of Pampean flat-slab segment, the Andean margin is characterized by normal subduction (dips 30°) extending from 34° to 46°S up to the Chile triple junction. The convergence between the Nazca and South American plates occurs at an average rate of 6.4 cm/yr [15]. In this area (from 34° to 45°S) the entire margin is characterized by an oblique

vector of convergence (N78°E) and reaches an orthogonal direction in the austral segment.

The continental slope consists of a lower and an upper slope. The lower slope is associated with the accretionary prism that is built by turbidites that are incorporated from trench fill to the lower slope as accreted sediments [12, 16], while the upper slope is associated with an important volume of terrigenous sediments from Andean arc volcanic rocks [17], deposited onto a continental metamorphic basement [18].

The oceanic trench is filled by sediments of partly more than 2 km thickness locally appearing rather as a flat plain than as a bathymetric depression [12]. The trench infill is composed of interbedded turbiditic and hemipelagic strata, which show certain cyclicity in their seismic reflection pattern that is interpreted as the influence of global climate cycles on sedimentation [16, 19]. The oceanic basement represents the Nazca Plate subducting beneath the South-America Plate and is constituted by pelagic sediments and oceanic basalts.

3. Data and Seismic Processing

In this study six seismic lines are analyzed. Four of them (SO161-44, SO161-35, SO161-29, and SO161-40; see Figure 1) were acquired by the RV SONNE cruise (January-February 2001) as part of the project “*Subduction Processes Off Chile (SPOC)*,” and the other two (RC2901-728 and RC2901-734; see Figure 1) were acquired by RV CONRAD cruise (January-February 1988), as part of the project “*Mid-Ocean Spreading Ridge (Chile Ridge)*” of the Ocean Drilling Program (ODP). Prestack seismic data of four seismic lines (RC2901-728, SO161-44, SO161-29, and RC2901-734) were used, while only the stacked seismic data are available for the other two lines (SO161-35 and SO161-40). Seismic data were acquired during the RV SONNE cruise using a 3000 m long 132-channel digital streamer with 12.5 m between the first 24 channels and 25 m between the other channels. The seismic source was a tuned array of 20 air guns, providing a total volume of 54.1 l, with a shot spacing of 50 m. Seismic data acquired during RV CONRAD cruise used a 3000 m long digital streamer, with 240 channels and intertrace of 12.5 m. The seismic source was a tuned array of 10 air guns with a total volume of 61.3 l, with a shot spacing of 50 m.

The seismic processing was performed by using the open source Seismic Unix (SU) software [20]. In order to obtain an accurate seismic image, a standard processing [21] was performed on the Prestack seismic data followed by the poststack time migration (Phase Shift and Stolt methods). In order to evaluate the seismic attributes of the stacked section, a true-amplitude processing was performed. In fact, in each processing step, the preservation of the amplitude spectrum was checked. In the case of SO161-35 and SO161-40 seismic lines, for which only stacked seismic data were available, a phase shift migration by using the water seismic velocity (1480 m/s) was performed.

The first step of the standard processing was to convert the data from SEG Y to SU format. Once converted in SU format, a checking of the minimum offset was done by using

the first arrival (direct wave). In fact, assuming the seismic water velocity equal to 1480 m/s (from direct wave analysis), a time shift of 0.12 s was identified in the SO161-44 seismic line. It was corrected shifting in 0.12 s all seismic data.

The next step was to define the geometrical arrangement of the prestack data. In this study, the source-receiver coordinates were defined arbitrarily without considering the geographic coordinates, and the offset and common midpoint (CMP) were calculated by using the source-receiver coordinates previously calculated. In the case of the SO161-44 and SO161-29 seismic lines, two different streamers were considered: the first one of 24 channels spaced every 12.5 m and the second one of 108 channels spaced every 25 m. The setting geometry was assigned separately and, then, integrated as a single streamer. CMP distances of 6.25 m (for RC2901-728 and RC2901-734 seismic lines) and 12.5 m (for SO161-44 and SO161-29 seismic lines) were defined.

To attenuate noise and correct the effects on amplitude due to wavefront spherical divergence, a band-pass filter (15–70 Hz) and a gain were applied, respectively.

In the SO161-44 seismic line, strong noises associated with out-of-plane reflections (sideswipe), probably due to the irregular morphology, were recognized. In order to attenuate this noise, a dip filter (slope ranging $8\text{--}5.5 \cdot 10^{-4}$) in the F-K domain was applied.

A stacking velocity analysis every 100 CMP (i.e., every 1250 m for the SO161-44 and SO161-29 seismic lines and every 625 m for the RC2901-728 and RC2901-734 seismic lines) was performed. Consequently, stacking velocity models were used to perform the stacking [21]. In order to obtain an accurate seismic image, a poststack time migration was performed; thus, the stacking velocity models were converted into interval velocity models. Moreover, different tests of poststack time migration (Stolt and phase shift methods) were performed. The best results were obtained by using the phase shift method. Finally, to obtain the final poststack-migrated sections, a band-pass filter (15–70 Hz), mixing traces, AGC gain (800 ms window), and muting were applied.

4. Results

4.1. RC2901-728. RC2901-728 time-migrated section, located offshore Itata (36°S), is characterized by a regular oceanic basement top, with a small number of structures in the westernmost part, while in depth underthrust structures are evident.

At the base of lower slope, an anticline ramp was recognized. Upslope several thrusts define an imbricated complex (approximately 15 km width). At about 8 s, high-amplitude reflections are interpreted as a decollement surface (Figure 2). Below this level, another reflector with high amplitude can be associated with the oceanic basement top. An uplifted slope basin behind a subvertical is characterized by divergent and continuous reflectors (Figure 2). Downwards and upwards of the slope basin chaotic reflections with low instantaneous amplitude (see insert in the Figure 2) can be related to slump deposits (CDPs 8000 and 9500, resp.). From CDPs 8000 to 13000, a strong and continuous BSR

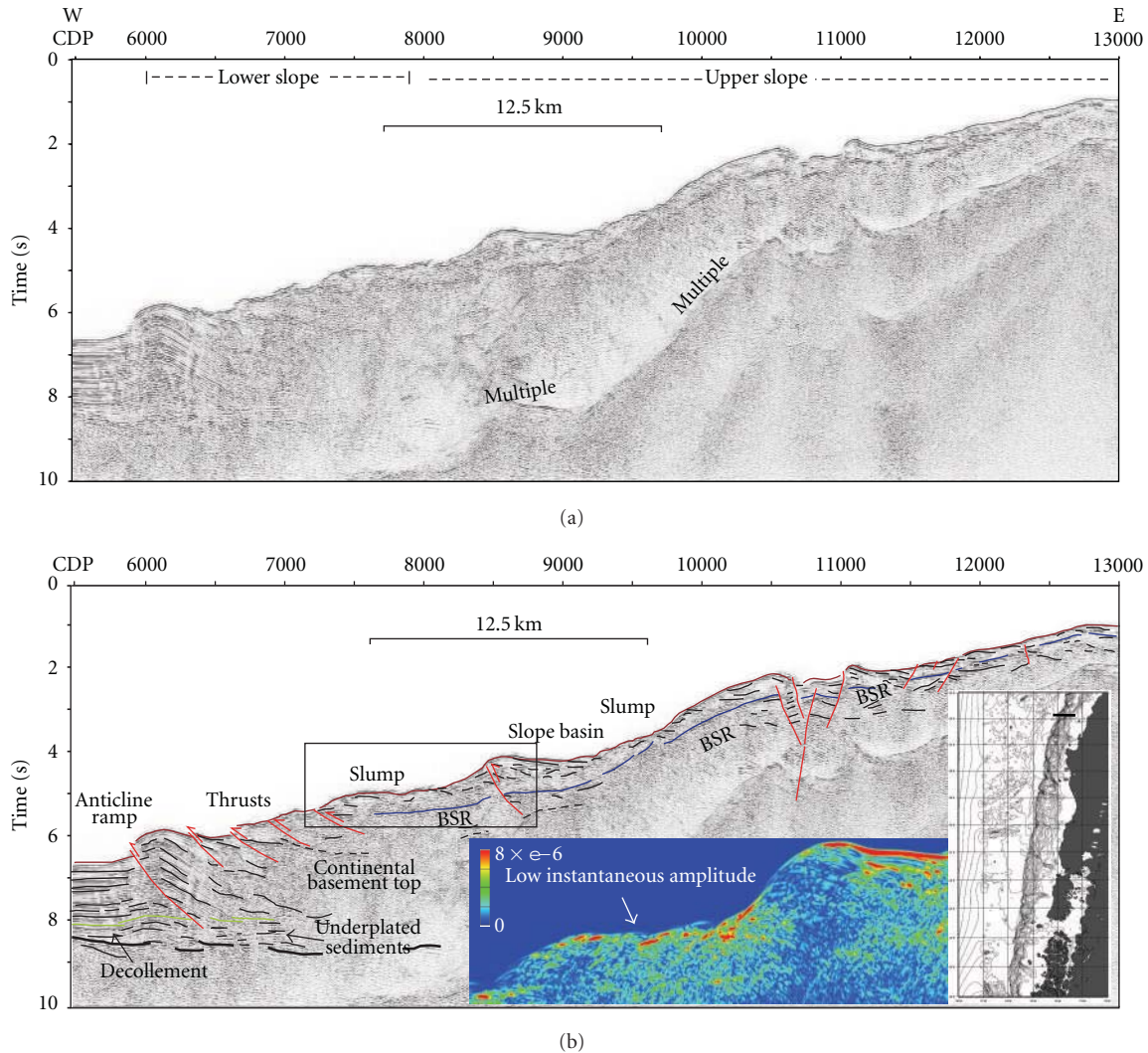


FIGURE 2: RC2901-728 seismic profile. Poststack time-migrated (a) and poststack time-migrated (b) sections with superimposed line drawing section. The box indicates the location of the instantaneous section reported in the insert.

was identified and can be associated to gas hydrate presence. From CDPs 10500 to 11500, a negative flower structure was recognized (Figure 2). In depth, reflections with high amplitude were associated to the continental basement top.

4.2. SO161-44. SO161-44 time-migrated section (Figure 3) located offshore Arauco (close to 38°S) shows different features compared to the previous section. Several faults at top of oceanic basement were recognized.

At the base of the slope, slightly deformed reflectors, thrusts, and underthrusts affect the trench fill. The top of an acoustically semitransparent level (about 7 s) can be associated with a decollement surface.

The lower slope is wide about 15 km and is steeper than the section SO161-44. At the base of the lower slope, slightly deformed sediments are recognized, which involve only the shallowest bed of the sedimentary trench fill (about 0.8 s of

thickness; Figure 3). The decollement surface and the oceanic basement top (about 6 s and 7.5 s) show pull-up features (Figure 3). From CDPs 5700 to 6600, a thrust sequence shapes a steep-dipping lower slope. Eastward, a normal fault scarp with offset of about 1 s (close to CDP 7000) was recognized. Here, chaotic reflections were observed. Note that fault scarp marks the boundary between lower slope and upper slope.

The upper slope shows an irregular topography disrupted by two main thrusts (at CDPs 7000 and 8000). Chaotic reflections, observed in the shallow and deep part, are evident (Figure 3). From CDPs 7200 to 7600 (5 km of width) a depressed zone characterized by morphological highs and a graben structure was imaged. Some slope basins on the top of seaward verging thrusts were recognized. At about 3.2 s, a discontinuous and strong BSR was identified. Reflections with high amplitude at about 4 s can be interpreted as the continental basement top.

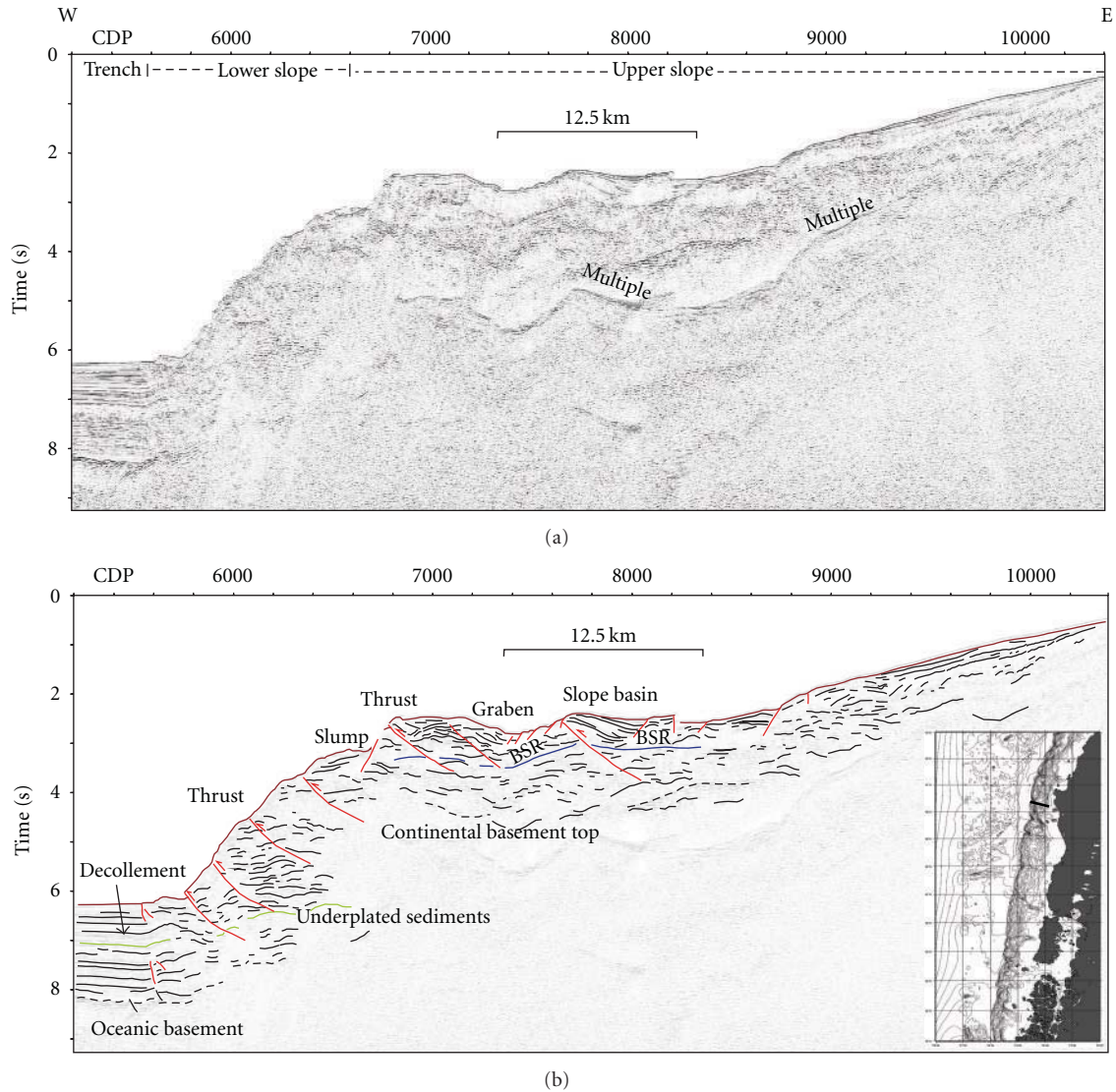


FIGURE 3: SO161-44 seismic profile. Poststack time-migrated (a) and poststack time-migrated (b) sections with superimposed line drawing section.

4.3. *SO161-35*. SO161-35 poststack time-migrated section, located south of Mocha Island close to 38.5°S shows an irregular oceanic basement top.

The lower slope is characterized by an irregular topography, which is disrupted by a morphological high (about CDP 9000). Downslope a closely spaced thrust section was recognized, while upslope two main widely spaced thrusts shape the accretionary prism (Figure 4). At about 7 s and 8 s, high-amplitude reflections and pull-up features were associated with the top of the underplated sediment bed and to the oceanic basement top. From CDPs 9200 to 10000 a weak and discontinuous BSR was recognized (Figure 4). The sea bottom is characterized by anomalous morphological highs, which can be associated with possible mud volcanoes. From CDPs 10200 to 11500, two main slope basins were recognized. Note that these basins are affected mainly by the displacement of normal and inverse faults (see Figure 4). On

the right side of the basins, normal faults configuring “half-graben” structures were recognized (Figure 4). At about 5 s, reflections with high amplitude associated with the continental basement top were recognized.

4.4. *SO161-40*. SO161-40 poststack time-migrated section (Figure 5), located at south of Chiloe island (43.5°S), is characterized by a regular oceanic basement top. The trench sediments are affected by thrusts and normal faults.

At the base of the lower slope, a thrust structure forms an anticline ramp. In depth, chaotic reflections and inactive faults affect the sedimentary sequence; here, the underplated bed and oceanic basement tops are less clear, but some high-amplitude reflections can be recognized at 6 s and 7 s, respectively (Figure 5). From CDPs 7800 to 10000, scarps are evident and can be associated to normal faults. In depth, from CDPs 8000 to 9000, a strong and continuous BSR

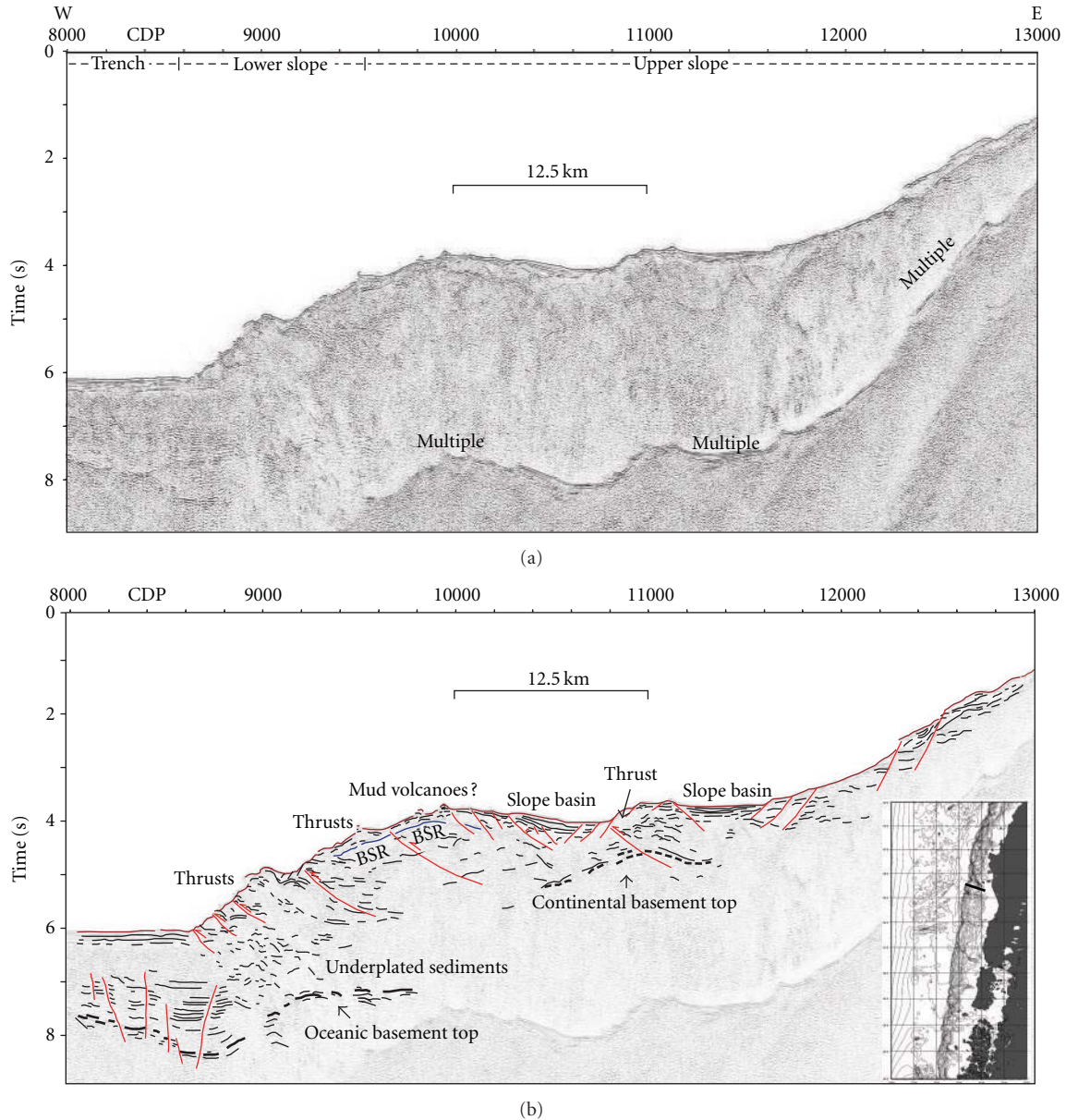


FIGURE 4: SO161-35 seismic profile. Poststack time-migrated (a) and poststack time-migrated (b) sections with superimposed line drawing section.

was recognized. Note that upslope the BSR is interrupted by active faults that configure a possible flower structure (Figure 5). At about 3 s, high-amplitude reflections, affected by faults, were associated to the continental basement top. Upslope from CDPs 9000 to 10000, a morphological high and a submarine channel (3 km width), controlled by normal faults was recognized (Figure 5).

5. Discussions and Conclusions

Two main accretion processes can be recognized along the Chilean margin: the first one is related to frontal accretion and the second one to basal accretion [12]. Both processes, frontal and basal accretions, were recognized in all seismic

sections. In particular, areas characterized by regular oceanic basement top, morphological highs, and thrusting across the continental slope (RC2901-728, SO161-40, and RC2901-734; Figure 6) can be associated to frontal accretion, while areas characterized by irregular oceanic basement top, absence of morphological highs, and wide and steep continental slopes can be associated to basal accretion. Moreover, relationships between the thickness of the underplated sediment bed and the morphology of lower slope can be described. Thus, thicker underplated sediment bed contributes to the formation of steeper slopes, while thinner underplated sediment bed contributes to the formation of rougher slopes. In RC2901-728 and SO161-40 sections, a thin underplated sediment bed (0.5 s) is in agreement with a rougher slope,

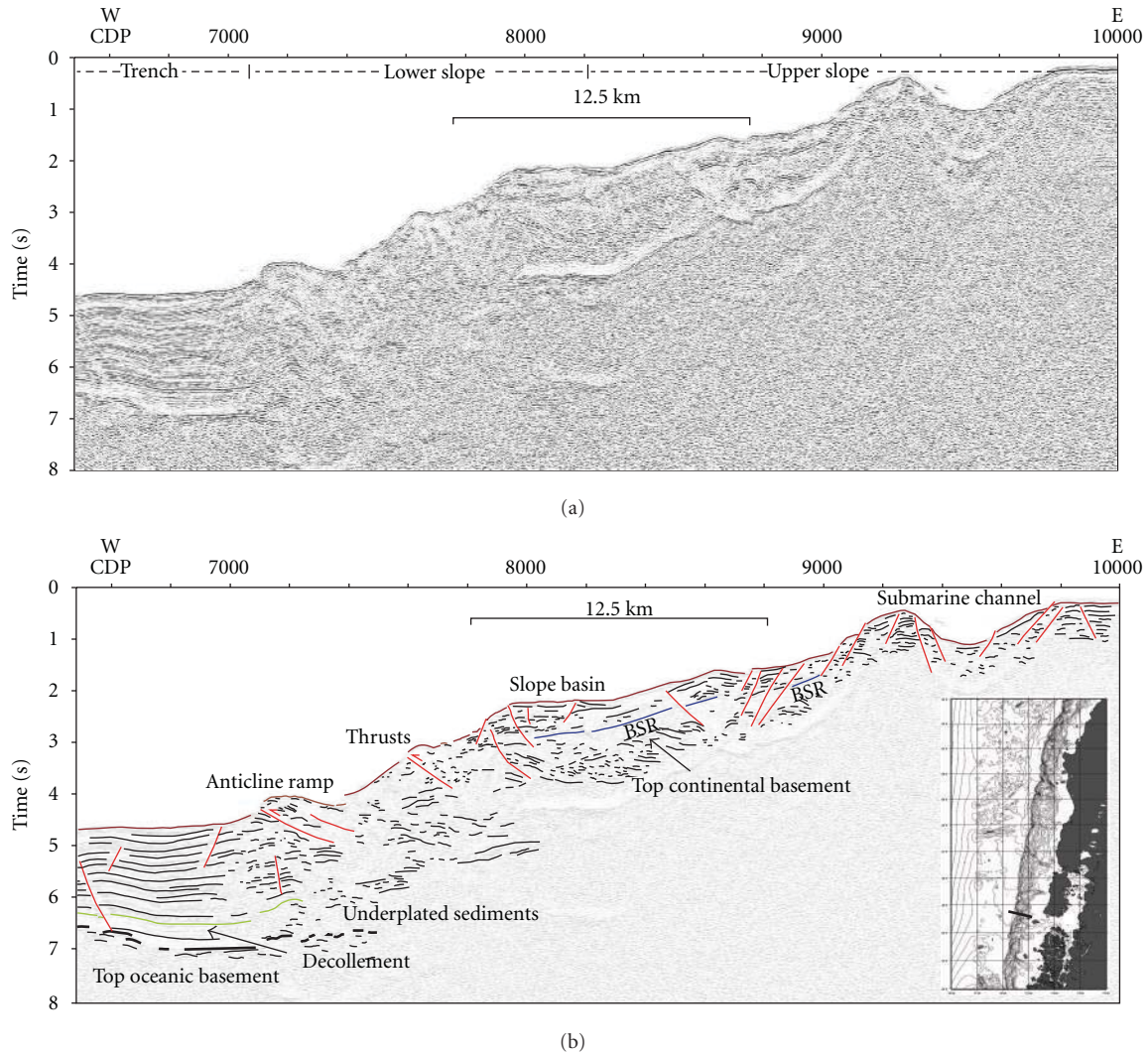


FIGURE 5: SO161-40 seismic profile. Poststack time-migrated (a) and poststack time-migrated (b) sections with superimposed line drawing section.

while in the SO161-44 and SO161-35 sections (Figure 6(b)) a thicker underplated sediment bed (1.2 s) evidences a steeper and smoother slope. In this way, a greater amount of underplated sediments can determine the formation of duplexes below the accretionary prism affecting accreted sediments and uplifting the internal prism, as evidenced in SO161-44, SO161-35, and SO161-29 sections. It seems that the off-scraped material provides movement accommodations along the thrusts during uplifting generating subhorizontal thrusts. Lateral and vertical growth of accretionary prisms associated to basal accretion has been reported by several authors on different continental margins (i.e, 8, 22, 23, 24, and 25). On the contrary, in areas where a thinner underplated sediment bed is recognized, the accretionary prism shows thrusts with high offset, which are related to an episodic frontal accretion [8, 12]. In this case, the underplated material plays a minor role influence. In this way, the evolution for these prisms will be similar to the prisms shown in the previous analyzed sections.

BSRs observed on seismic sections are often considered as indicators of the existence of free gas, delineating the base of the gas hydrate stability zone. Southwards of Juan Fernandez ridge, the BSR was recognized on the internal prism in all sections. In the northernmost part (RC2901-728, SO161-40) and southernmost part (SO161-40 and RC2901-734), the BSR is strong and continuous (Figures 6(a) and 6(b)), while in the central part (SO161-44, SO161-35, and SO161-29) a weak and discontinuous BSR was recognized (Figure 6(b)). So relationships between the BSR characteristics and the accretion processes can be observed; in particular, the BSR is strong and continuous in correspondence with the frontal accretion processes, whereas it is weak and discontinuous in presence of the basal accretion processes. During frontal accretion, tectonic movements seem to affect the frontal prism, but not affecting the internal prism favoring fluid accumulation conditions and consequently formation of strong and continuous BSRs (see right on Figures 6(a) and 6(c)). Meanwhile the uplifting by basal accretion generates

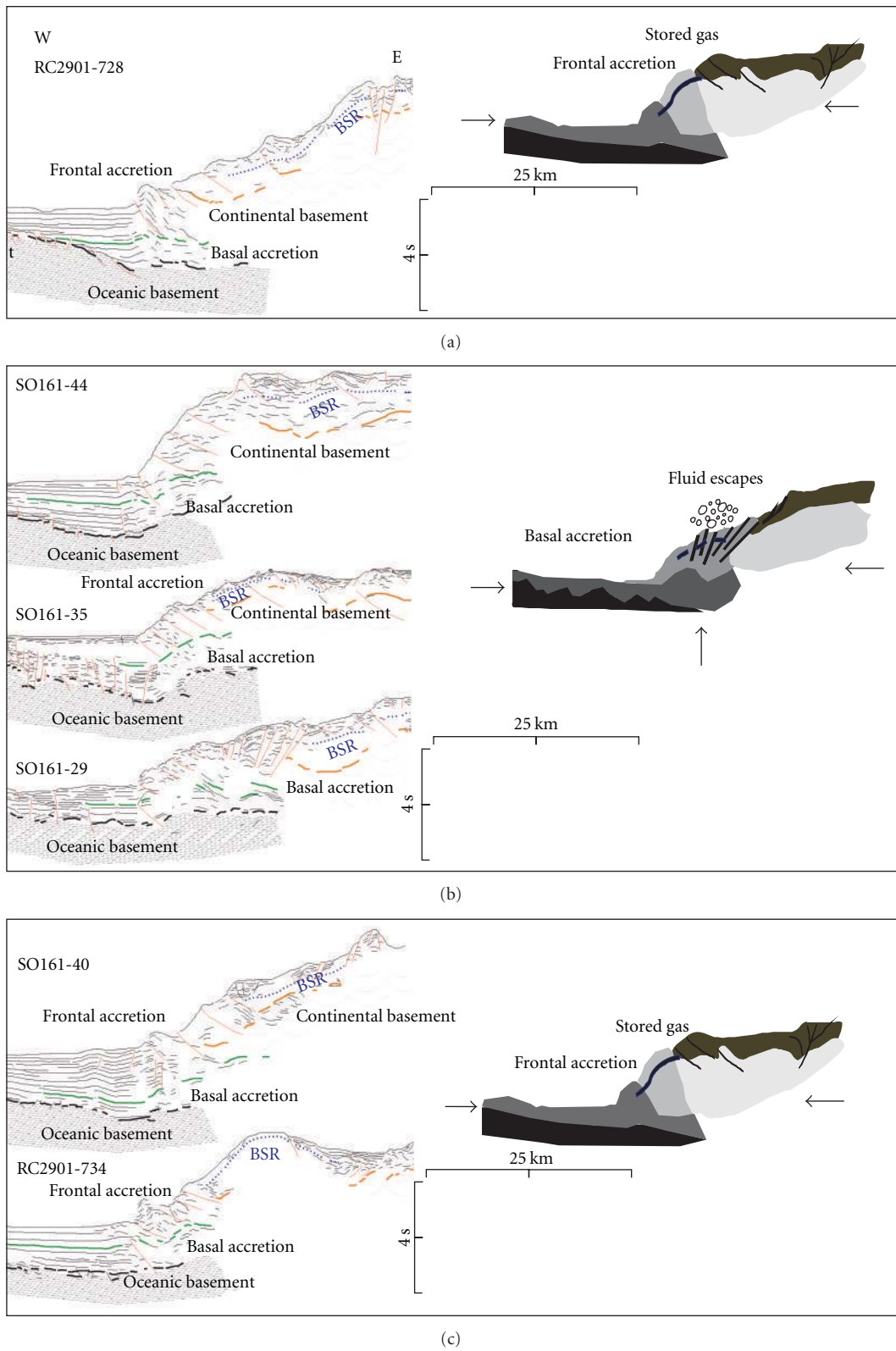


FIGURE 6: (a) Left: RC2901-728 line drawing profile. Right: frontal accretion diagram. (b) Left: SO161-44, SO161-35, and SO161-29 line drawing profiles. Right: basal accretion diagram. (c) Left: SO161-40 and RC2901-734 line drawing profiles. Right: frontal accretion diagram.

extensional tectonic movements on the internal prism, which can favour fluid escapes (see right on Figure 6(b)) and, consequently, the change of temperature. So the depth of the gas hydrate stability zone is strongly variable along the seismic line and, consequently, the BSR disappears or becomes weaker. Moreover, a lower geothermal gradient (30°C/km) [22] in the northern sector (SO161-44 section) is in agreement with an older oceanic crust (35 Ma) [23], where a reduced fluid circulation can be expected. Whereas, in the southern sector (RC2901-734 section), a higher and variable geothermal gradient (50–95°C/km) [24] is in agreement with a younger oceanic crust (15 Ma) [23], where the increased fluid circulation can be expected. Note that the BSR features might be explained considering several factors. Thus, it is possible to associate a weak and discontinuous BSR mainly to a reduced circulation and an active tectonic. However, in the northernmost part (Itata offshore), a strong and continuous BSR is in disagreement with an older oceanic crust. Even if a reduced circulation from oceanic crust is expected, stable tectonic conditions and methane biogenic sources [25] can explain a strongest and continuous BSR in this area. In fact, in Itata offshore from bathymetric data, a smoother continental slope can be recognize, which can be related to steady tectonic regime, while southwards (Arauco and Valdivia offshore) an irregular continental slope characterized by submarine canyons, erosive areas, and structural lineaments can be related to unsteady tectonic regime [26].

Acknowledgments

The authors are very grateful to Joyce Alsop and Volkmar Damm for seismic data provided by the Lamont Doherty Earth Laboratory (LDEO), USA and the Federal Institute for Geosciences and Natural Resources (BGR), Germany, respectively. This work was partially supported by International Centre for Theoretical Physics (Trieste).

References

- [1] T. H. Shipley, M. H. Houston, R. T. Buffler et al., "Seismic reflection evidence for the widespread occurrence of possible gas hydrate horizons on continental slopes and rises," *AAPG Bulletin*, vol. 63, pp. 2204–2213, 1979.
- [2] R. D. Hyndman and G. D. Spence, "A seismic study of methane hydrate marine bottom simulating reflectors," *Journal of Geophysical Research*, vol. 97, no. 5, pp. 6683–6698, 1992.
- [3] U. Tinivella and F. Accaino, "Compressional velocity structure and Poisson's ratio in marine sediments with gas hydrate and free gas by inversion of reflected and refracted seismic data (South Shetland Islands, Antarctica)," *Marine Geology*, vol. 164, no. 1-2, pp. 13–27, 2000.
- [4] C. Berndt, S. Bünz, T. Clayton, J. Mienert, and M. Saunders, "Seismic character of bottom simulating reflectors: examples from the mid-Norwegian margin," *Marine and Petroleum Geology*, vol. 21, no. 6, pp. 723–733, 2004.
- [5] M. E. Mackay, R. D. Jarrard, G. K. Westbrook, and R. D. Hyndman, "Origin of bottom-simulating reflectors: geophysical evidence from the Cascadia accretionary prism," *Geology*, vol. 22, no. 5, pp. 459–462, 1994.
- [6] N. L. B. Bangs, D. S. Sawyer, and X. Golovchenko, "Free gas at the base of the gas hydrate zone in the vicinity of the Chile triple junction," *Geology*, vol. 21, no. 10, pp. 905–908, 1993.
- [7] K. M. Brown, N. L. Bangs, P. N. Froelich, and K. A. Kvenvolden, "The nature, distribution, and origin of gas hydrate in the Chile Triple Junction region," *Earth and Planetary Science Letters*, vol. 139, no. 3-4, pp. 471–483, 1996.
- [8] J. Diaz-Naveas, *Sediment subduction and accretion at the Chilean convergent margin between 35° and 40°S*, Dissertation, University of Kiel, Kiel, Germany, 1999.
- [9] E. Morales, "Methane hydrates in the Chilean continental margin," *Electronic Journal of Biotechnology*, vol. 6, no. 2, pp. 3–7, 2003.
- [10] I. Grevemeyer, J. L. Diaz-Naveas, C.R. Ranero, and H. W. Villenger, "Heat Flow over the decensing Nazca plate in Central Chile, 32°S to 41°S: observations from ODP Leg 202 and the occurrence of natural gas hydrates," *Earth and Planetary Sciences Letters*, vol. 213, pp. 285–298, 2003.
- [11] I. Vargas-Cordero, *Gas hydrate occurrence and morphostructures along Chilean margin*, Ph.D. thesis, University of Trieste, Trieste, Italy, 2009.
- [12] N. L. Bangs and S. C. Cande, "Episodic development of a convergent margin inferred from structures and processes along the southern Chile margin," *Tectonics*, vol. 16, no. 3, pp. 489–503, 1997.
- [13] J. Glodny, H. Echter, O. Figueroa et al., "Long-term geological evolution and mass-flow balance of the South-Central Andes," in *the Andes—Active Subduction Orogeny*, O. Oncken, G. Chong, G. Franz et al., Eds., vol. 1 of *Frontiers in Earth Science Series*, pp. 401–428, Springer, Berlin, Germany, 2006.
- [14] C. M. Krawczyk, J. Mechie, S. Lüth et al., "Geophysical signatures and active tectonics at the south-central Chilean margin," in *the Andes—Active Subduction Orogeny*, O. Oncken, G. Chong, G. Franz et al., Eds., vol. 1 of *Frontiers in Earth Science Series*, pp. 171–192, Springer, Berlin, Germany, 2006.
- [15] D. Angermann, J. Klotz, and C. Reigber, "Space-geodetic estimation of the Nazca-South America Euler vector," *Earth and Planetary Science Letters*, vol. 171, no. 3, pp. 329–334, 1999.
- [16] D. Völker, M. Wiedicke, S. Ladage et al., "Latitudinal variation in sedimentary processes in the Peru-Chile trench off Central Chile," in *the Andes—Active Subduction Orogeny*, O. Oncken, G. Chong, G. Franz et al., Eds., vol. 1 of *Frontiers in Earth Science Series*, pp. 193–216, Springer, Berlin, Germany, 2006.
- [17] K. Strand, "SEM microstructural analysis of a volcanogenic sediment component in a trench-slope basin of the Chile margin," in *Proceedings of the Ocean Drilling Program, Scientific Results*, S. D. Lewis, J. H. Behrmann, R. J. Musgrave, and S. C. Cande, Eds., vol. 141, pp. 169–180, 169–180, 1995.
- [18] C. Mordojovich, "Sedimentary basins of Chilean Pacific offshore," in *Energy Resources of the Pacific Region*, M. T. Halbouty, Ed., vol. 12, pp. 63–82, American Association of Petroleum Geologists Studies in Geology, 1981.
- [19] K. Rauch, "Cyclicity of Peru-Chile trench sediments between 36° and 38°S: a footprint of paleoclimatic variations?" *Geophysical Research Letters*, vol. 32, no. 8, pp. 1–4, 2005.
- [20] J. K. Cohen and J. W. Stockwell, "CWP/SU: seismic Unix release 35: a free package for seismic research and processing," Center for wave phenomena, Colorado school of Mines, 2001.
- [21] O. Yilmaz, *Seismic Data Analysis: Processing, Inversion and Interpretation of Seismic Data*, Society of Exploration, Tulsa, Okla, USA, 2001.
- [22] I. Vargas Cordero, U. Tinivella, F. Accaino, M. F. Loreto, F. Fanucci, and C. Reichert, "Analyses of bottom simulating

- reflections offshore Arauco and Coyhaique (Chile),” *Geo-Marine Letters*, vol. 30, no. 3-4, pp. 271–281, 2010.
- [23] R. D. Müller, W. R. Roest, J. Y. Royer, L. M. Gahagan, and J. G. Sclater, “Digital isochrons of the world’s ocean floor,” *Journal of Geophysical Research*, vol. 102, no. 2, pp. 3211–3214, 1997.
- [24] I. Vargas-Cordero, U. Tinivella, F. Accaino, M. F. Loreto, and F. Fanucci, “Thermal state and concentration of gas hydrate and free gas of Coyhaique, Chilean Margin (44°30′ S),” *Marine and Petroleum Geology*, vol. 27, no. 5, pp. 1148–1156, 2010.
- [25] T. Treude, J. Niggemann, J. Kallmeyer et al., “Anaerobic oxidation of methane and sulfate reduction along the Chilean continental margin,” *Geochimica et Cosmochimica Acta*, vol. 69, no. 11, pp. 2767–2779, 2005.
- [26] C. Rodrigo, A. González-Fernández, and E. Vera, “Variability of the bottom-simulating reflector (BSR) and its association with tectonic structures in the Chilean margin between Arauco Gulf (37°S) and Valdivia (40°S),” *Marine Geophysical Researches*, vol. 30, no. 1, pp. 1–19, 2009.

Research Article

Natural Gas Production from Methane Hydrate Deposits Using CO₂ Clathrate Sequestration: State-of-the-Art Review and New Technical Approaches

Annick Nago and Antonio Nieto

The John and Willie Leone Family Department of Energy and Mineral Engineering, The Pennsylvania State University, University Park, PA 16802, USA

Correspondence should be addressed to Annick Nago, abn113@psu.edu

Received 21 March 2011; Revised 27 June 2011; Accepted 1 July 2011

Academic Editor: Michela Giustiniani

Copyright © 2011 A. Nago and A. Nieto. This is an open access article distributed under the Creative Commons Attribution License, which permits unrestricted use, distribution, and reproduction in any medium, provided the original work is properly cited.

This paper focuses on reviewing the currently available solutions for natural gas production from methane hydrate deposits using CO₂ sequestration. Methane hydrates are ice-like materials, which form at low temperature and high pressure and are located in permafrost areas and oceanic environments. They represent a huge hydrocarbon resource, which could supply the entire world for centuries. Fossil-fuel-based energy is still a major source of carbon dioxide emissions which contribute greatly to the issue of global warming and climate change. Geological sequestration of carbon dioxide appears as the safest and most stable way to reduce such emissions for it involves the trapping of CO₂ into hydrocarbon reservoirs and aquifers. Indeed, CO₂ can also be sequestered as hydrates while helping dissociate the in situ methane hydrates. The studies presented here investigate the molecular exchange between CO₂ and CH₄ that occurs when methane hydrates are exposed to CO₂, thus generating the release of natural gas and the trapping of carbon dioxide as gas clathrate. These projects include laboratory studies on the synthesis, thermodynamics, phase equilibrium, kinetics, cage occupancy, and the methane recovery potential of the mixed CO₂-CH₄ hydrate. An experimental and numerical evaluation of the effect of porous media on the gas exchange is described. Finally, a few field studies on the potential of this new gas hydrate recovery technique are presented.

1. Introduction

Since their initial discovery by Sir Davy Humphrey in 1810, natural gas hydrates have graduated from a laboratory oddity to a hydrocarbon production nuisance as seen forming inside the chamber bell used to cap the spill in the deep water horizon oil well, and so forth, before being considered as a potential energy resource for the future. For many decades, countries such as the USA, Canada, Japan, India, and China have funded major research projects to get a better understanding and knowledge of natural gas hydrates [1]. Resource assessment studies have demonstrated the huge potential of gas hydrate accumulations as a future energy resource [2].

World energy demand is steadily rising due to global population and economic growth. World energy consumption is expected to increase from 472 quadrillion Btu to 678

quadrillion Btu in 2030, that a total increase of 44% from 2006 to 2030 [3]. China and India are currently the fastest growing non-OECD economies, and their combined energy consumption is expected to represent 28% of the world energy consumption in 2030 [4]. Despite recent progress in obtaining energy from nonfossil fuels, nearly 80% of the world energy supply will still be generated from oil, natural gas, and coal. The combustion of these fuels is a major source of carbon dioxide emissions. Unfortunately, a perceived change in the global climate has been attributed to the increasing concentration of Green House Gases such as CO₂ in the atmosphere. Geological sequestration of CO₂ is a potential solution to this problem. Typical geological sequestration consists in capturing and storing the gas in a geological setting such as active and depleted oil/gas reservoir, deep brine formations, deep coal seams, and coal-bed methane formation [5]. Sequestration of CO₂ in marine

and arctic hydrates is considered as an advanced geologic sequestration concept, which needs further investigation [6].

Gas hydrates are found in nature, in permafrost and marine environments. They contain mixtures of gases such as methane and ethane, with carbon dioxide and hydrogen sulfide as trace. Methane is the predominant component of natural gas hydrates, which is the reason they are simply called methane hydrates. Gas hydrates form under specific conditions: (1) the right combination of pressure and temperature (high pressure and low temperature), (2) the presence of hydrate-forming gas in sufficient amounts, and (3) the presence of water. CO₂ and CH₄ hydrates are of interest with CO₂ being a preferential hydrate guest former when compared to CH₄. In addition, CO₂ hydrates are more stable than CH₄ hydrates, and the exposition CH₄ hydrates to carbon dioxide has resulted in the release of methane, while carbon dioxide remained trapped. Thus, the use of carbon dioxide to recover natural gas from hydrate deposits has gained more and more relevance in the industry.

Other techniques are being explored in the area of production from hydrate deposits. However, the resource is still not commercially viable due to technical, environmental, and economic issues. Any further investigation of the mixed CO₂-CH₄ gas hydrate properties could lead to major breakthroughs in the fields of unconventional resource production and carbon sequestration.

2. What Are Methane Hydrates?

Natural gas hydrates, commonly called methane hydrates, are crystalline compounds, which are constituted of gas and water molecules. The water molecules or host molecules form a hydrogen-bonded lattice, in which gas molecules or guest molecules are entrapped. The presence of guest molecules stabilizes the lattice due to the sum of the attractive or repulsive forces between molecules known as the Van der Waals forces. There is no bonding between the host molecules and the guest molecules, that is, the gas molecules are free to rotate inside the lattice [2, 7-9]. Gas hydrate formation and dissociation are described by the following equations:

$$G + N_H H_2O \rightarrow G \cdot N_H H_2O \text{ and } G \cdot N_H H_2O \rightarrow G + N_H H_2O,$$

where N_H is the hydration number and G is the guest molecule. Gas hydrate formation is an exothermic process while gas hydrate dissociation is endothermic.

Gas hydrates come under three distinguishable structures: type I, type II, and type H. All structures involve a network of interconnected cages. Structure I (sI) hydrates display unit cells that are constituted of 46 water molecules organized into 2 small cavities and 6 large cavities. The small cavities are dodecahedral cages with 12 pentagonal faces. They are usually denoted as 5¹² cages. The large cavities are 14-sided polyhedra (tetrakaidecahedron), which are usually denoted as 5¹²6². The unit cells of Type II hydrates (sII) contain 136 water molecules. They are organized into 16 small cavities and 8 large cavities. The small cavities are of the same kind as the small cavities in sI hydrates. However, the large cavities are hexacaidecahedra (5¹²6⁴) with

12 pentagonal faces and 4 hexagonal faces [9]. In 1987, a new hydrate structure was discovered and called structure H (sH). This structure contains 34 water molecules in its unit cell, forming a hexagonal lattice. Type H hydrates display three types of cavities: three 5¹² cages, two 4³5⁶6³ cages, and one large 5¹²6⁸ [9, 10].

Because of the size difference between the cages, the three types of hydrates tend to trap different kinds of molecules. Type I hydrates are usually formed with smaller molecules such as ethane and hydrogen sulfide. Type II clathrates are formed by larger molecules such as propane and isobutane. Type H hydrates require the presence of a small molecule such as methane and a type H gas former like 2-methylbutane and cycloheptane to be created. They are less common in nature than the other types of gas hydrates [9, 10]. Figure 1 illustrates the different sorts of hydrate structures and some of their gas-forming molecules. These structures have been observed with X-ray diffraction.

Methane and carbon dioxide both form type I hydrates. The comparison of their hydrate phase equilibrium conditions suggests the occurrence of a transition zone between both hydrate equilibrium curves where CO₂ hydrates can exist while CH₄ hydrates dissociate into methane gas and water. The hydrate phase diagrams of both compounds are presented in Figure 2. In addition, the heat of formation of carbon dioxide hydrate (-57.98 kJ/mole) is greater than the heat of dissociation of methane hydrate (54.49 kJ/mole). The heat released from the formation of carbon dioxide hydrate in the presence of methane hydrate should be sufficient to dissociate the methane hydrate and recover methane gas [11]. Thirdly, it has been experimentally proven that carbon dioxide is preferentially trapped over methane in the hydrate phase [12]. These observations fuel the growing interest in the use of carbon dioxide for natural gas recovery from gas hydrate deposits.

Gas hydrates can be naturally found in permafrost areas and subsea environments. The temperature and pressure gradients which are at play underneath the Earth help define specific hydrate occurring zones, when associated to the thermodynamic hydrate equilibrium conditions. These zones are called hydrate stability zones [8]. Figure 3 displays the hydrate stability zones in permafrost and marine environments.

Assessment methods for gas hydrates include seismic studies (bottom simulating reflectors), pore water salinity measurements, well-logging, and direct observations from core samples [13]. So far, 89 hydrate locations have been discovered all over the world [14]. These locations are presented in Figure 4.

3. Current Research Status

Three main production methods have so far been explored for the recovery of natural gas from hydrate deposits: depressurization, thermal stimulation, and inhibitor injection [8, 15, 16]. These methods aim at thermodynamically destabilizing the reservoir environment to provoke the release of the entrapped gas [17, 18]. They have been investigated

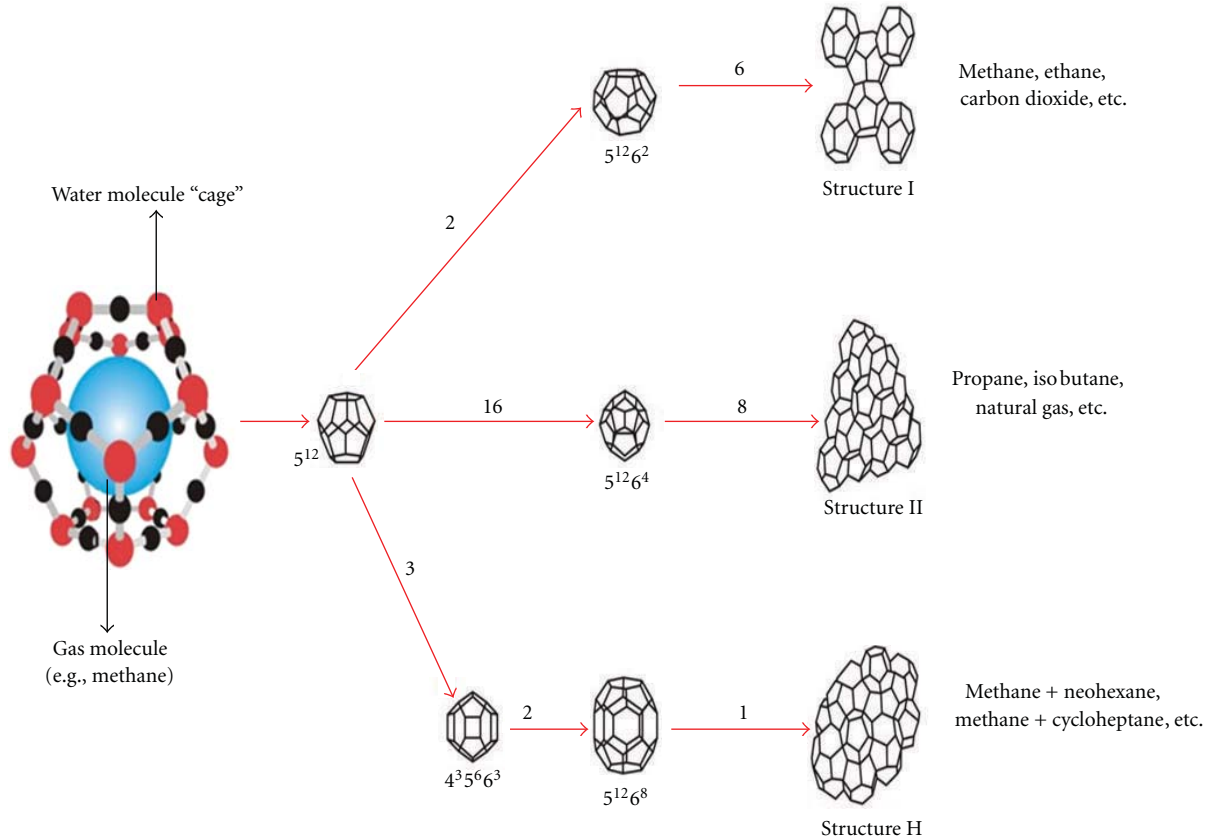


FIGURE 1: Different types of clathrate hydrates [9].

experimentally, numerically, and in the field. However, they have not yet been used for commercial production of natural gas hydrates due to remaining technical and economic issues. A fourth method was introduced a few years ago and is based on the concept of hydrate guest molecule exchange between methane and carbon dioxide in the hydrate phase.

In 1996, Ohgaki et al. [12] examined the possible interactions between these two hydrates by injecting carbon dioxide (gas) into an aqueous-gas hydrate system containing methane. CO_2 displays a higher chemical affinity than CH_4 in the hydrate structure since it has a higher heat of formation and equilibrium temperature; that is, at 1000 psi, the equilibrium temperature of CH_4 hydrate is approximately 283.15 K while the equilibrium temperature of CO_2 hydrate is around 286.15 K. Ohgaki et al.'s experiments resulted in the synthesis of a mixed CO_2 - CH_4 hydrate. The equilibrium concentrations obtained for CO_2 were greater in the hydrate phase than those of CH_4 and less than the concentrations of CH_4 in the gas phase. Nakano et al. (1998) [19] performed a similar study using carbon dioxide and ethane and obtained comparable results. Smith et al. (2001) [20] inquired the feasibility of exchanging carbon dioxide with methane in geologic accumulations of natural gas hydrates. They numerically investigated the effect of the pore size distribution on the conversion of CH_4 hydrate to CO_2 hydrate. It was demonstrated that the guest molecule exchange between CO_2 and CH_4 , in porous media was less thermodynamically favored, as the pore size decreased. They recommended these

numerical results be validated by laboratory experiments. Seo et al. (2001) [21] experimentally investigated hydrate phase equilibrium processes for mixtures of CO_2 and CH_4 . They determined the existing conditions of quadruple points ($\text{H-L}_w\text{-L}_{\text{CO}_2}\text{-V}$) in order to examine the hydrate stability. It was noted that the equilibrium curves of the mixed hydrates lied between those of simple carbon dioxide and methane hydrates. For a given mixture, the concentration of CO_2 in the hydrate phase decreased as the pressure was lowered. In 2003, Lee et al. [22] published the results of their study on the thermodynamics and kinetics of the conversion of CH_4 hydrate to CO_2 hydrate. They analyzed the distribution of guest molecules over different cavities for pure methane hydrates and different mixtures of CO_2 - CH_4 hydrates, using solid state NMR methods. It was observed that the cage occupancy ratio of CH_4 in the pure methane hydrate decreased as the concentration of CO_2 in the mixture increased. This was explained by the fact that CO_2 preferentially occupied large $5^{12}6^2$ cages in the mixed hydrate. In terms of kinetics, it was noticed that the conversion of CH_4 hydrate to CO_2 hydrate happened much more quickly than the formations of pure CO_2 and CH_4 hydrates. The amount of CH_4 that could be recovered from the gas hydrate of composition $\text{CH}_4 \cdot 6.05\text{H}_2\text{O}$ was limited to 64% of the original entrapped gas, even with a CO_2 concentration of 100 mol%. Ota et al. (2004) [23] focused on the gas exchange process using liquid CO_2 . They performed laboratory measurements using the Raman spectroscopy and

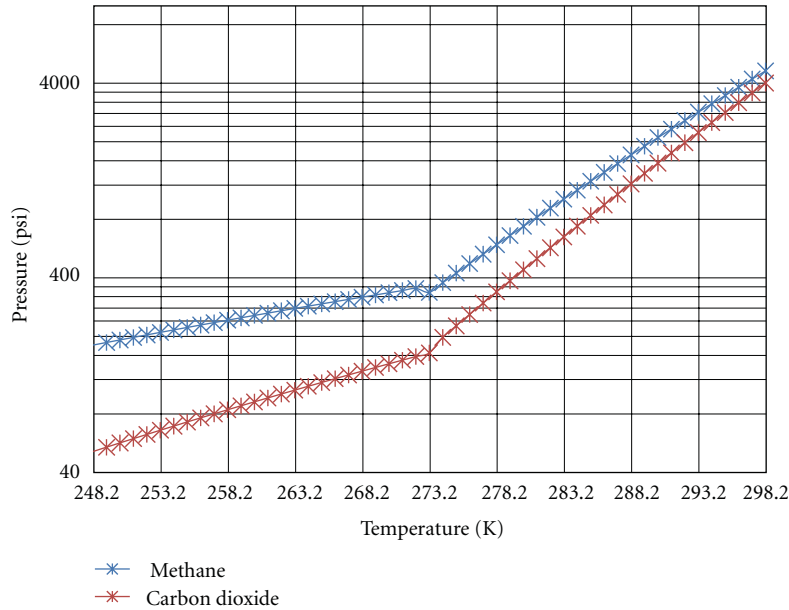


FIGURE 2: CH₄ and CO₂ hydrate phase diagrams [2].

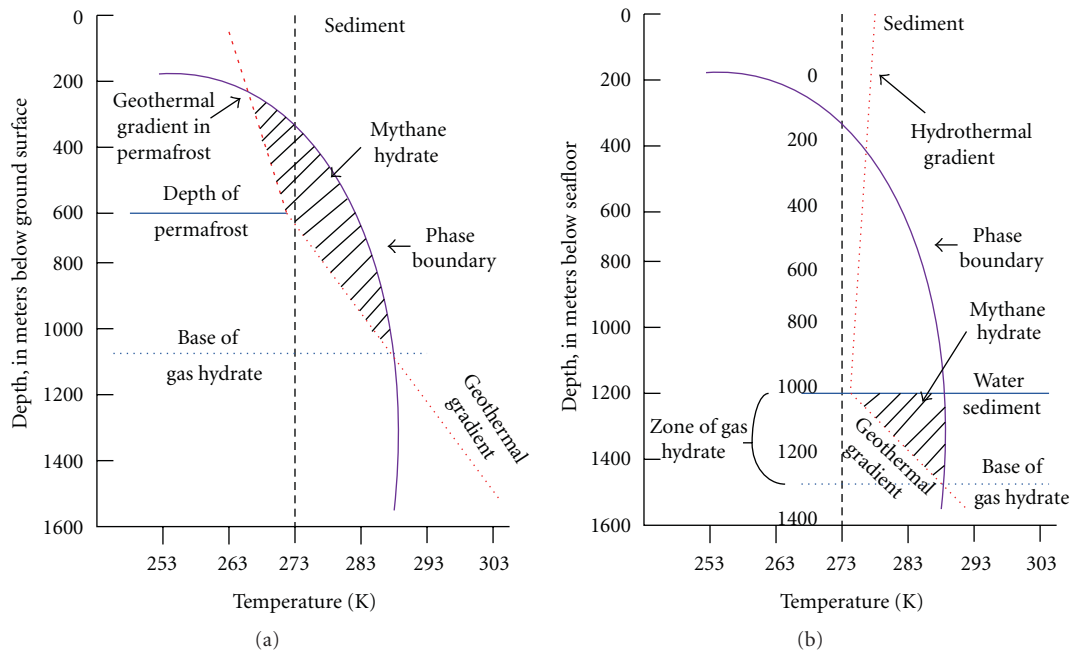


FIGURE 3: Hydrate stability zones in permafrost and marine environments [2].

numerical simulations, and they found similar results in terms of feasibility of the molecular gas exchange. Stevens et al. (2008) [24] took the studies on this topic one step further by publishing his work on the gas exchange between CO₂ and CH₄ in hydrates formed within sandstone core samples. He used a MRI to analyze the samples and realized there was formation of CO₂ hydrate at the expense of the initial CH₄ hydrate. Diffusion seemed to be the main driving force behind the conversion from CH₄ hydrate to CO₂ hydrate. A considerable amount of CH₄ was released during the process, which was judged as rapid and efficient. There

was no free water present. The permeability of the core was reduced during CH₄ hydrate formation. This reduced permeability was maintained constant during the CH₄-CO₂ exchange, and the permeability levels were considered sufficient for gas transportation. In 2008, Youngjune et al. [25] made a major discovery while they were inquiring the effect of the injection of a binary mixture of N₂ and CO₂ on methane hydrate recovery. They found out that the injection of a binary mixture of N₂ and CO₂, instead of the traditional pure CO₂, increased the percentage of methane recovered from 64% to 85% for type I gas hydrates. They

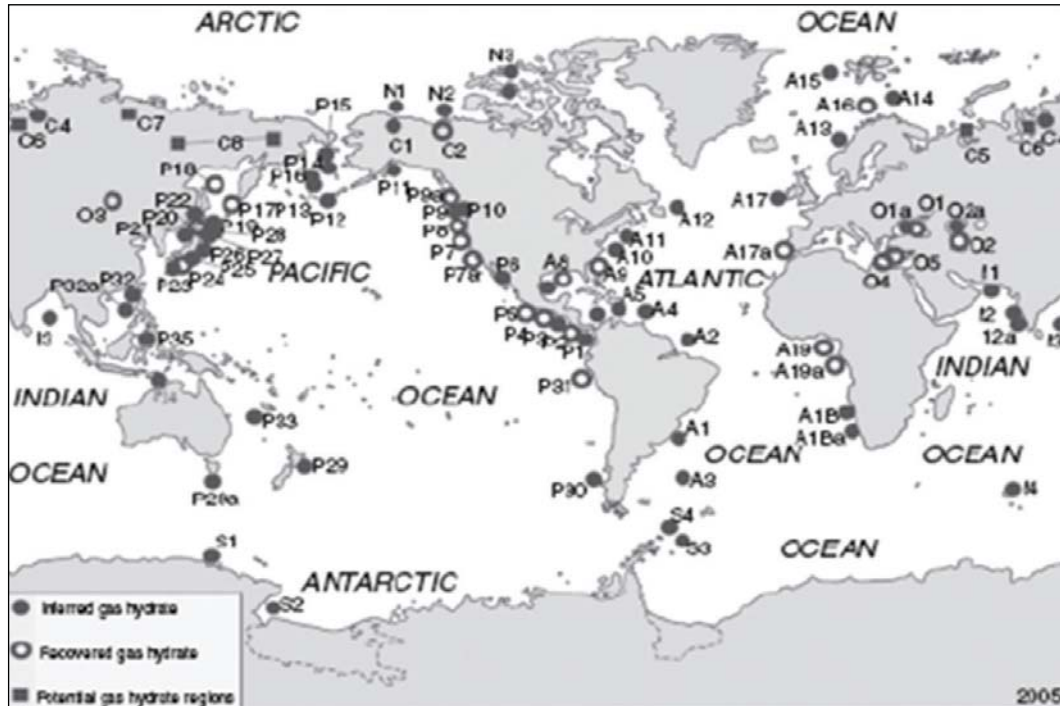


FIGURE 4: World gas hydrate locations [13].

also looked at the potential influence of structural transition by forming a type II $\text{CH}_4\text{-C}_2\text{H}_6$ hydrate and injecting CO_2 and a mixture of CO_2 with N_2 . It was determined that the hydrate structure changed from type II to type I during the gas injection, thus increasing the gas recovery to more than 90% for CH_4 . Besides these major thermodynamically related numerical and laboratory investigations, several studies were conducted to evaluate the potential of this new concept as a field scale production method for methane hydrate deposits. In 2003, Rice [26] proposed a scheme for methane recovery from marine hydrate accumulations. In this scheme, the produced methane would be converted into hydrogen and carbon dioxide; then, the carbon dioxide would be reinjected into the ocean to be converted into CO_2 hydrates and finally the produced hydrogen would be used as fuel. Methane would be recovered from hydrates using depressurization combined with thermal stimulation. No direct molecular gas exchange between CH_4 and CO_2 was inferred in this production scheme. In 2004, McGrail et al. [27] investigated Ohgaki et al.'s method to determine the rate of CO_2 gas penetration in the bulk methane hydrate, using the Raman spectroscopy. They discovered that the rates of CO_2 gas penetration were too low for this method to be useful for gas hydrate production. Then, they performed a preliminary study on a new enhanced gas hydrate recovery concept based on the injection of a microemulsion of CO_2 and water in the methane hydrate core samples. The technique was validated through laboratory experiments and numerical simulation, using a custom model based on STOMP- CO_2 . Finally, Castaldi et al. (2006) [28] examined the technical feasibility of applying a down-hole combustion method for gas recovery from hydrate accumulations, while

sequestering CO_2 as hydrates. The gas molecular exchange between CH_4 and CO_2 was not directly mentioned, but they suggested there should be equality between the rates of CO_2 hydrate formation and CH_4 hydrate dissociation, during the process. In 2006, Goel [11] released a review of the status of research projects and issues related to methane hydrate production with carbon dioxide sequestration. It was concluded that although several studies had been performed on the topic, additional experimental data was needed on the topic of $\text{CH}_4\text{-CO}_2$ molecular gas exchange in hydrate-bearing sediments. He emphasized the importance of fully knowing the thermodynamics and kinetics of the formation and dissociation of this mixed hydrate and of the conversion process, in porous media. He also pointed out the essence of understanding the equilibrium conditions of the mixed hydrate in sediments as a function of pressure, temperature, mole fraction of CO_2 and CH_4 in the mixture, pore size, porous material, and flow properties.

4. Conclusions

This paper is a brief review of the studies that have been performed on the gas molecular exchange between CO_2 and CH_4 within the hydrate phase. As this paper highlights, such studies are even more essential in this day and age, as we need to quickly discover and exploit new sources of energy in a sustainable and energy-efficient manner. An emphasis is put here on experimental, numerical, and field investigations of the gas hydrate recovery process using CO_2 , clathrate sequestration. All studies present positive outcomes and further research on the topic is encouraged to make this new recovery technique commercially viable.

References

- [1] Committee to Review the Activities Authorized Under the Methane Hydrate Research and Development Act of 2000, *Charting the Future of Methane Hydrate Research in the United States*, The National Academies Press, Washington, DC, USA, 2004.
- [2] S. E. Dendy and C. A. Koh, *Clathrate Hydrates of Natural Gas*, CRC Press, Boca Raton, Fla, USA, 2008.
- [3] Exxon Mobil Corporation, *The Outlook for Energy: A View to 2030*, 2009.
- [4] EIA, Energy Information Administration-Official Energy Information Administration website, 2009, <http://www.eia.gov/>.
- [5] D. A. Voormeij and G. J. Simandl, "Geological, ocean, and mineral CO₂ sequestration options: a technical review," *Geoscience Canada*, vol. 31, no. 1, pp. 11–22, 2004.
- [6] DOE's Office of Fossil Energy and Office of Science, "Carbon sequestration research and development," US Department of Energy, 1999.
- [7] M. R. Prado, A. Pham, R. E. Ferazzi, K. Edwards, and K. C. Janda, "Gas clathrate hydrates experiment for high school projects and undergraduate laboratories," *Journal of Chemical Education*, vol. 84, no. 11, pp. 1790–1791, 2007.
- [8] Y. F. Makogon, *Hydrates of Hydrocarbons*, Pennwell Publishing Company, Tulsa, Okla, USA, 1997.
- [9] "Center for gas hydrate research," Herriot-Watt University, Institute of Petroleum Engineering, 2010, <http://www.pet.hw.ac.uk/research/hydrate/index.cfm>.
- [10] J. Carroll, *Natural Gas Hydrate: A Guide for Engineers*, Gulf Professional Publishing, 2003.
- [11] N. Goel, "In situ methane hydrate dissociation with carbon dioxide sequestration: current knowledge and issues," *Journal of Petroleum Science and Engineering*, vol. 51, no. 3-4, pp. 169–184, 2006.
- [12] K. Ohgaki, K. Takano, H. Sangawa, T. Matsubara, and S. Nakano, "Methane exploitation by carbon dioxide from gas hydrates-phase equilibria for CO₂-CH₄ mixed hydrate system," *Journal of Chemical Engineering of Japan*, vol. 29, no. 3, pp. 478–483, 1996.
- [13] G. J. Moridis, T. S. Collett, R. Boswell et al., "Toward production from gas hydrates: current status, assessment of resources, and simulation-based evaluation of technology and potential," *SPE Reservoir Evaluation and Engineering*, vol. 12, no. 5, pp. 745–771, 2009.
- [14] K. A. Kvenvolden and B. W. Rogers, "Gaia's breath-global methane exhalations," *Marine and Petroleum Geology*, vol. 22, no. 4, pp. 579–590, 2005.
- [15] H. A. Phale, T. Zhu, M. D. White, and B. P. McGrail, "Simulation study on injection of CO₂-microemulsion for methane recovery from gas-hydrate reservoirs," in *Proceedings of the 2006 SPE Gas Technology Symposium*, pp. 369–380, Society of Petroleum Engineers, Calgary, Canada, May 2006.
- [16] M. D. Max and M. J. Cruickshank, "Extraction of methane from oceanic hydrate system deposits," in *Proceedings of the Offshore Technology Conference*, Houston, Tex, USA, 1999.
- [17] C. P. Thomas, "Methane hydrates: major energy source for the future of wishful thinking?" in *Proceedings of the 2001 SPE Annual Technical Conference and Exhibition*, New Orleans, La, USA, 2001.
- [18] M. D. White, S. K. Wurstner, and B. P. McGrail, "Numerical studies of methane production from Class 1 gas hydrate accumulations enhanced with carbon dioxide injection," *Marine and Petroleum Geology*, vol. 28, no. 2, pp. 546–560, 2011.
- [19] S. Nakano, K. Yamamoto, and K. Ohgaki, "Natural gas exploitation by carbon dioxide from gas hydrate fields-high-pressure phase equilibrium for an ethane hydrate system," *Proceedings of the Institution of Mechanical Engineers, Part A*, vol. 212, no. 3, pp. 159–163, 1998.
- [20] D. H. Smith, K. Seshadri, and J. W. Wilder, "Assessing the thermodynamic feasibility of the conversion of methane hydrate into carbon dioxide hydrate in porous media," *Journal of Energy and Environmental Research*, pp. 101–117, 2001.
- [21] Y.-T. Seo, H. Lee, and J. H. Yoon, "Hydrate phase equilibria of the carbon dioxide, methane, and water system," *Journal of Chemical and Engineering Data*, vol. 46, no. 2, pp. 381–384, 2001.
- [22] H. Lee, Y.-T. Seo, I. L. Moudrakovski, and J. A. Ripmeester, "Recovering methane from solid methane hydrate with carbon dioxide," *Angewandte Chemie*, vol. 42, no. 41, pp. 5048–5051, 2003.
- [23] M. Ota, K. Morohashi, Y. Abe, M. Watanabe, R. Lee Smith Jr., and H. Inomata, "Replacement of CH₄ in the hydrate by use of liquid CO₂," *Energy Conversion and Management*, vol. 46, no. 11-12, pp. 1680–1691, 2005.
- [24] J. C. Stevens, J. J. Howard, B. A. Baldwin, G. Ermland, J. Husebo, and A. Graue, "Experimental hydrate formation and gas production scenarios based on CO₂ sequestration," in *Proceedings of the 6th International Conference on Gas Hydrates (ICGH '08)*, Vancouver, Canada, 2008.
- [25] P. Youngjune et al., "Swapping carbon dioxide for complex gas hydrate structures," in *Proceedings of the 6th International Conference on Gas Hydrates (ICGH '08)*, Vancouver, Canada, 2008.
- [26] W. Rice, "Proposed system for hydrogen production from methane hydrate with sequestering of carbon dioxide hydrate," *Journal of Energy Resources Technology*, vol. 125, no. 4, pp. 253–257, 2003.
- [27] B. P. McGrail, T. Zhu, R. B. Hunter, M. D. White, S. L. Patil, and A. S. Kulkarni, "A new method for enhanced production of gas hydrate with CO₂," in *Proceedings of the AAPG Hedberg Conference*, Vancouver, Canada, 2004.
- [28] M. J. Castaldi, Y. Zhou, and T. M. Yegulalp, "Down-hole combustion method for gas production from methane hydrates," *Journal of Petroleum Science and Engineering*, vol. 56, no. 1–3, pp. 176–185, 2007.

Research Article

Analysis of Water Features in Gas Leakage Area

Liu Huaishan, Wang Fengfan, Tong Siyou, Li Gaolin, and Zhang Haiyan

Key Lab of Submarine Geosciences and Prospecting Techniques, Ministry of Education, Ocean University of China, Qingdao 266100, China

Correspondence should be addressed to Liu Huaishan, lhs@ouc.edu.cn and Li Gaolin, gaolin666li@163.com

Received 13 April 2011; Accepted 16 May 2011

Academic Editor: Xuewei Liu

Copyright © 2011 Liu Huaishan et al. This is an open access article distributed under the Creative Commons Attribution License, which permits unrestricted use, distribution, and reproduction in any medium, provided the original work is properly cited.

In a certain frequency range, gas is an effective absorber and scatterer of sound, which changes the compressibility of water, and then changes the speed and frequency of sound. Gas continues rising, deforming, and dissolving. The same bubble of natural gas has different radii at different depths. By analyzing these changes, the resonance frequency of gas bubble, and its impacts on sound wave, characteristics of the influences of gas at different depths on the incident sound wave can be obtained. The main sound features of gas are relevant to the gas size, gas content, velocity, attenuation, resonance frequency, the scattering cross-section, and so forth. Sound models with hydrate and free gas in the water and sediment are established. Through the practical application to actual data, the sound characteristics yielded when the gas (or gas hydrate dissociation) escaped the water of seismic data are very clear.

1. Introduction

There are various forms of marine gas, they may be generated by ocean waves, fish's swim bladder, submarine wake, shallow gas leak, hydrate decomposition, and so forth, they have a wide range of effects on sound signal used in marine seismic exploration, such as changing the speed of sound and attenuating signal energy. Various phenomena caused by natural gas have been found in the sea shallow gas and gas hydrates area, for example, speckled reflection "flame-shaped" reflection, and so forth. These phenomena do not exist in an area without shallow gas and gas hydrates.

Carstensen and Foldy [1] proceeded with theoretical study of bubble scattering effects on sound propagation ignoring the relevance of the spatial distribution of bubbles. They obtained the bubble's radius by measuring the frequency of the sound generated by bubble, combined with the relationship between resonant frequency and bubble radius, and also obtained experimental data of the transmission and reflection coefficient of sound in the mixture. Experiments show that when the same bubble radius, and the incident wave frequency and the bubble resonance frequency are the same, the sound attenuates most, which is consistent with the theoretical value. Fox et al. [2] and others got the

sound phase velocity and the sound absorption coefficient when the frequency is between 10 ~ 390 kHz through incident continuous wave on the bubbly water. Keller and Kolodner incident sound with frequency 15 ~ 100 kHz into the mixed-phase medium with the bubble (the radius of the 0.16–0.5 mm), the result confirmed the Foldy theory once again. Silberman [3] measured the velocity and the attenuation coefficient of bubbly liquid in the static wave tube, the bubble radius is 0.08 ~ 0.26 inches, and bubble volume fraction of 0.03 to 1.0%, sound frequency is 60 Hz ~ 20 kHz. Xiaoliang et al. first proposed the concept of mixed media, obtained the sound wave equation in bubbly mixed media [4]. The researchers also found that the vibration characteristics of the bubble should be included in dynamic equations of mixed body. Prosperetti [5] linearized the vibration of air bubbles under the action of sound, studied heat conduction effects on the attenuation of sound, and found that the polytropic index and thermal conductivity were related to sound frequency. Kameda and Matsumoto [6] gave the mathematical model of nonlinear vibration of the bubble, and gave accurate description of the scope and characteristics of the effective equation. From his study we can find that Foldy theory and Van Wijngaarden equations are applicable in the case of lower volume fraction of

bubbles that the interaction between bubbles can be ignored. Commamder [7, 8] and Prosperitti developed this theory based on Porsperetti's and others' accurate description of the dynamics on the bubble, and discussed the linear pressure wave propagation in bubbly water.

Li et al. [9] discussed the influences of the relevance of the spatial distribution of bubbles to sound propagation in bubbly water with consideration of Twersky's theory and sound absorption of bubble. The results show that when considering the relevance of the spatial distribution of bubbles, the attenuation coefficient of the peak moves backward and the peak is lower and flatter than ignoring the relevance. With the increasing of bubbles' volume fraction, the relevance of their spatial distribution increases, the resonant frequency of the bubble increases, and its scattering amplitude becomes smaller when resonating. Yonghui [10] used ultrasonic testing method to measure sound transmission loss and velocity ratio of the gas-water miscible media, the used sound frequencies were 0.5 MHz, 1.25 MHz, 2 MHz, and 2.5 MHz. Xiaoliang et al. [4] and others developed a series of analytical formulas that calculate the sound propagation characteristics in bubbly water and the nonlinear parameters of media for the fact that the actual bubble size always exists distribution. They studied the sound wave propagation features such as velocity and attenuation in bubbly water.

All the studies above are based on analysis of the impact extent of bubbles on the water, there are no studies on the sound characteristics of sediments and water containing hydrate and free gas in the gas leakage area. This paper studies the influence of gas on the effective sound absorber and scatter in a certain frequency range, natural gas radius at different depths when the gas continues to rise, deformation, or dissolved in the sea water. Then this paper analyzes that when these processes occur, how the resonance frequency of natural gas and the sound characteristics of it change. This paper established sound models with hydrate and free gas in the water and sediment through the analysis of gas leakage area (including hydrate and free gas) and real seismic data.

2. The Rising Velocity and Track of Gas

The rising of natural gas in water is a very complex process, and its rising velocity and track are related to the diameter and shape of natural gas. When calculating the rising process of natural gas, in order to simplify the calculation process, in theory, the diameter of natural gas is considered as the volumetric spherical to calculate, ignoring the internal activity and driven from setting velocity of solid particle in water.

The resultant force of natural gas in water equals to buoyancy force minus resistance force;

$$F_1 - F_2 = \frac{\pi}{6} d^3 (\rho_w - \rho_a) g - \frac{\pi}{2} C_D \rho_w \frac{v_0^2 d^2}{4}. \quad (1)$$

In (1), d is the diameter of natural gas, ρ_w is the density of water, ρ_a is the density of air, g is the acceleration of gravity, C_D is resistance coefficient, and $v_0^2 d^2 / 4$ is the projected area of natural gas in vertical direction.

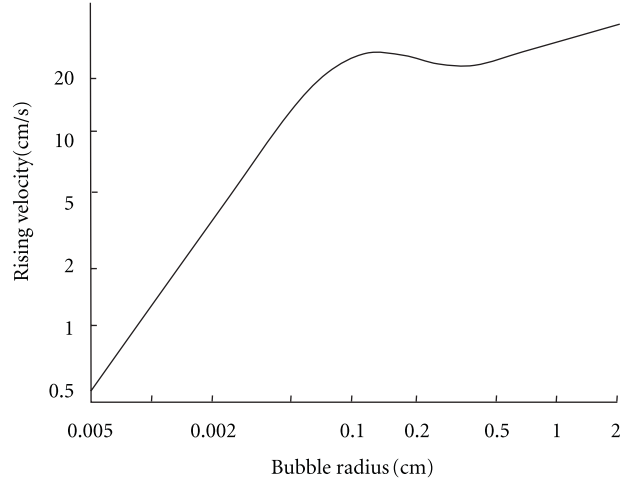


FIGURE 1: Curve between the rising velocity and diameter of natural gas.

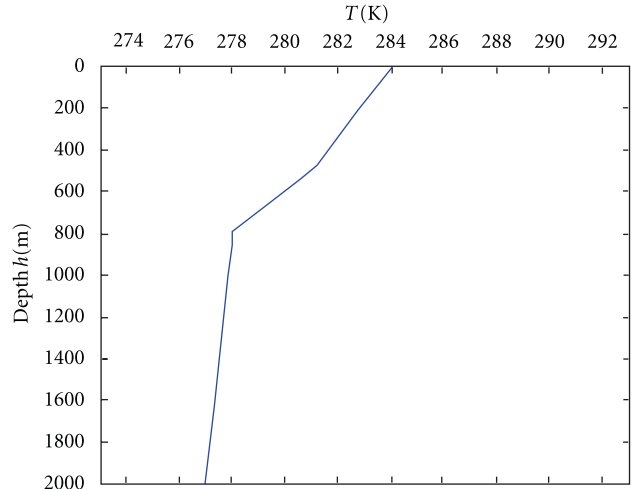


FIGURE 2: Curve of longitudinal temperature of seawater.

According to Newton's second law, we can know that $F = ma$, $m = \pi d^3 \rho_a / 6$, $a = dv_a / dt$, v_a is the rising velocity of natural gas, if we put it into (1), we can get that

$$\frac{dv_a}{dt} = \frac{(\rho_w - \rho_a)g}{\rho_a} - \frac{3C_D \rho_w v_a^2}{4\rho_a d}. \quad (2)$$

When $dv_a / dt = 0$, v_a is the ultimate velocity;

$$v_0^2 = \frac{4gd(\rho_w - \rho_a)}{3\rho_w C_D}. \quad (3)$$

From hydromechanics knowledge, we can know that resistance coefficient C_D can be determined by Reynolds number Re ;

$$Re = \frac{v_a d}{\nu} = \frac{\rho_w v_a d}{\mu}. \quad (4)$$

In (4), ν is motion viscosity coefficient and μ is dynamic viscosity coefficient, respectively. According to the difference

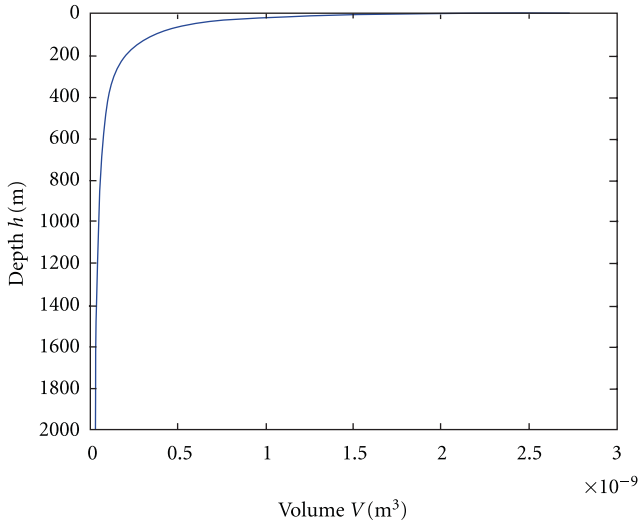


FIGURE 3: The relationship between the balance volume of natural gas and depth.

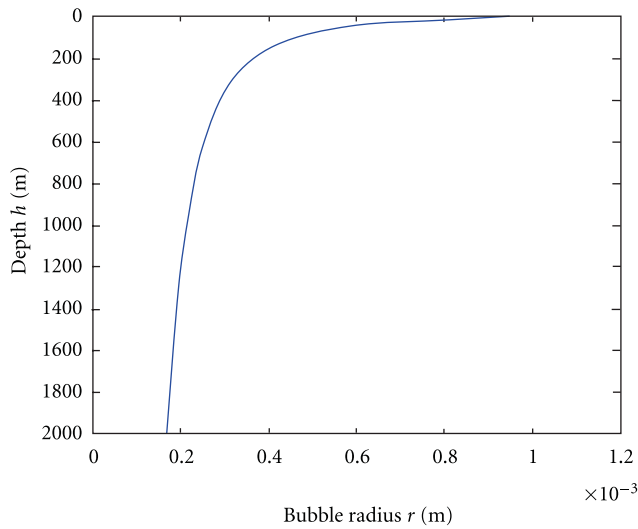


FIGURE 4: Curve of the balance radius of natural gas with depth.

of Reynolds number, the value of C_D can be divided into three areas: laminar flow, transition, and turbulence. The velocity formula calculated from this is also different.

According to hypothetical conditions, (3) has a small range of application and usually is suitable to bubble whose diameter is less than $150 \mu\text{m}$ in static water.

While in the rising process of moderate natural gas, there are two forms of motions [5]: (1) Rolling motion of rigid body, zigzag or spiral motion. (2) Changes in shapes and expanding, which is oscillation of natural gas. These forms of motion often exist at the same time, and movement of moderate natural gas is very complicated. But we can simplify its model to a perfect ellipsoidal and then consider its additional motions.

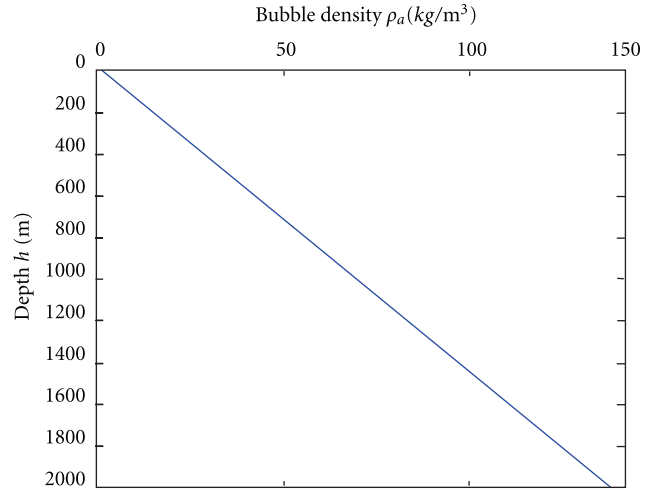


FIGURE 5: Curve of the density of natural gas with depth.

While with regard to big natural gas, its shape can only be acquired from observation and the expression of its velocity is considerably complex.

Therefore, the rising velocity of natural gas in static water is closely related to its linear density. According to huge amounts of experimental data and theoretical analysis, we can get the relation curve between the rising velocity and diameter of natural gas which is shown in Figure 1. It can be seen from Figure 1 that the velocity of natural gas reaches a maximum value when the diameter is about 0.1 cm , and then changes very little with the increasing of diameter while the shape of natural gas changes from spherical to ellipsoidal. With regard to small natural gas, its characteristics of motion are linear. And for big natural gas, its characteristics of motion is approximate to linear, but its shape usually becomes distorted and not spherical any more. When the diameter is greater than $1000 \mu\text{m}$, the motion of natural gas is not stable anymore and is not the function of diameter, so it is hard to calculate the velocity of natural gas. In experimental observation, its rising velocity is approximate to 30 cm/s .

In fact, in the rising process of natural gas, the volume will increase with the decrease of pressure and its shape will also change. The formation of water vapor in its interior changes the density of natural gas. And because of the existence of surface tension, the gas in natural gas will dissolve in the water. Experiments show that the natural gas whose diameter is 0.1 cm can completely dissolve in water within about 20 min .

From the above analysis, we can see that the big natural gas in sea water will rise to the sea surface quickly, and tiny natural gas mainly exists in sea water. The minimum stable diameter in sea water is about $1 \mu\text{m}$. Although this natural gas is still subjected to the influence of buoyancy force and gas diffusion to dissolve and rise constantly, amounts of measuring results in sea show that the densities of tiny natural gases in sea water will keep a dynamic balance state and diameters of natural gases are all less than $500 \mu\text{m}$ [11].

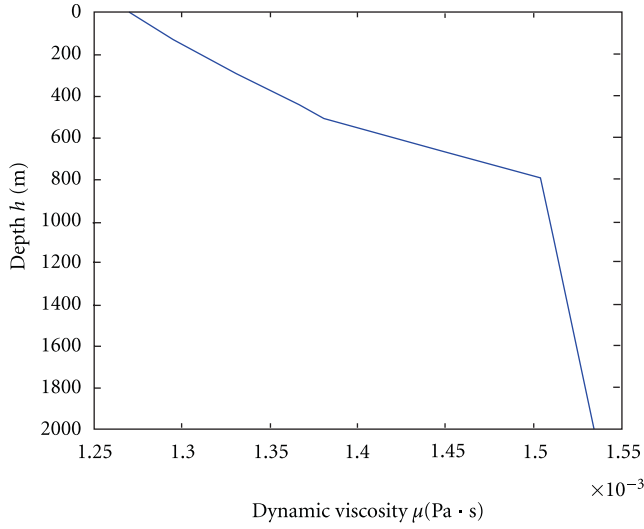


FIGURE 6: Curve of seawater viscosity coefficient with depth.

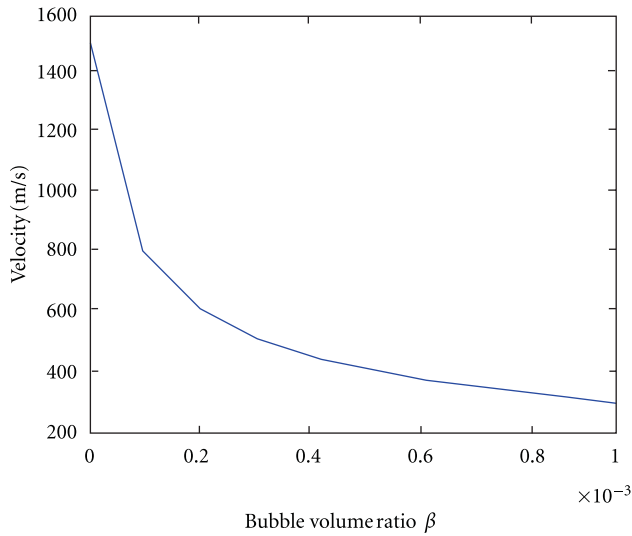


FIGURE 7: The curve of relation between sound velocity and the ratio of gas volume.

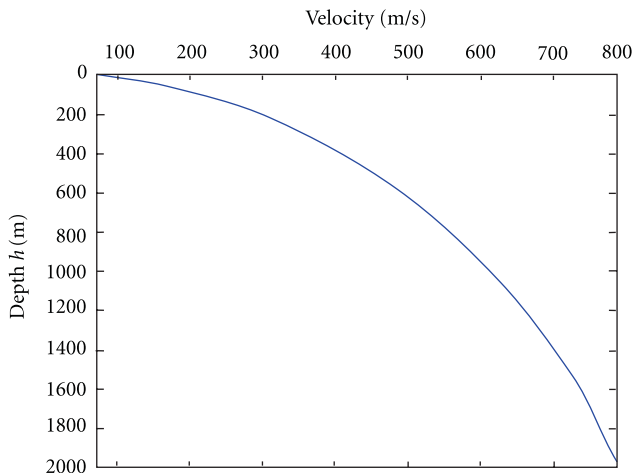


FIGURE 8: Sound velocity changing with depth in the gas layer.

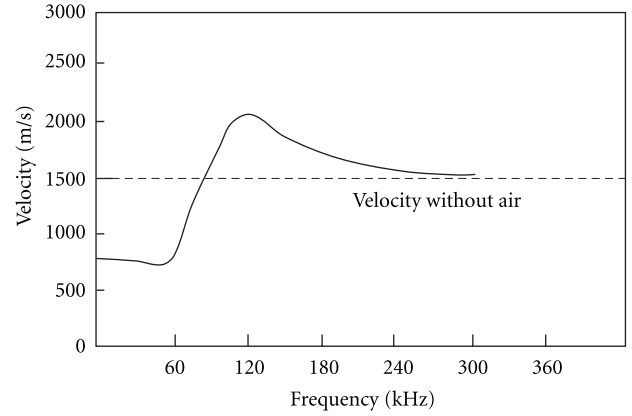


FIGURE 9: Curve of sound velocity measured in the gas of same size (diameter is 0.011 cm) under wide frequency range [2].

2.1. The Rising Feature of Natural Gas in Water. Assuming that there is some natural gas in marine, its shape always remained spherical in the process of rising in static water, the radius in sea level is 1 mm, and the volume is $V_0 = 4.1888 \times 10^{-9} \text{ m}^3$, which is full of methane gas.

The pressure in the sea level is one standard atmospheric pressure, and the seawater pressure in the depth of h is $P_1 = P_0 + \rho_w g h$. Suppose the seawater is incompressible fluid, $\rho_w = 1026 \text{ kg/m}^3$ is the average density of seawater, and the gravity acceleration is $g = 9.81 \text{ m/s}^2$. The temperature in sea surface is 284 K. The change of temperature is shown in Figure 2.

The molar mass of methane gas M is 16 g/mol, according to the equation of state of ideal gas:

$$\frac{P_0 V_0}{T_0} = \frac{P_1 V_1}{T_1} = nR, \quad (5)$$

$R = 8.31 \text{ J} \cdot \text{mol}^{-1} \cdot \text{K}^{-1} = 0.082 \times 10^{-3} \text{ m}^3 \cdot \text{atm} \cdot \text{K}^{-1} \cdot \text{mol}^{-1}$.

We can obtain that the amount of substance of this natural gas is $n = 1.7987 \times 10^{-7} \text{ mol}$, its quality is $m = n \times M = 2.8779 \times 10^{-9} \text{ kg}$, and the density in the surface is $\rho_a = m/V_0 = 0.68705 \text{ kg/m}^3$, then the relationship between volume of gas and depth can be obtained:

$$V_1 = \frac{P_0 V_0}{P_0 + \rho_w g h} \frac{T_1}{T_0}. \quad (6)$$

In the equation, T_0 is the temperature in the sea surface, and T_1 is the temperature in the depth of h .

Assume that the internal gas composition and quality of the natural gas do not change in different depths of ocean water, then according to (6) and the given data, we can obtain the change curve of gas volume with depth (Figure 3).

At the same time, the change of radius r with depth h can be found by formula $r = (3V/4\pi)^{1/3}$ (Figure 4). As shown in the figure, at the beginning, the change of volume and radius of the bubble in the water depth of several hundred meters is very rapid, but along with the increase of depth, the change rates of volume and radius become smaller and smaller. According to the relationship between the quality m

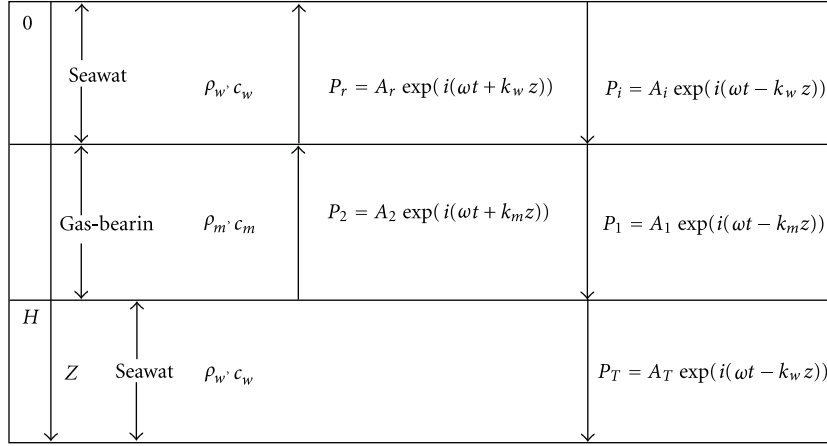


FIGURE 10: Reflection and transmission of sound wave in gas reservoir.

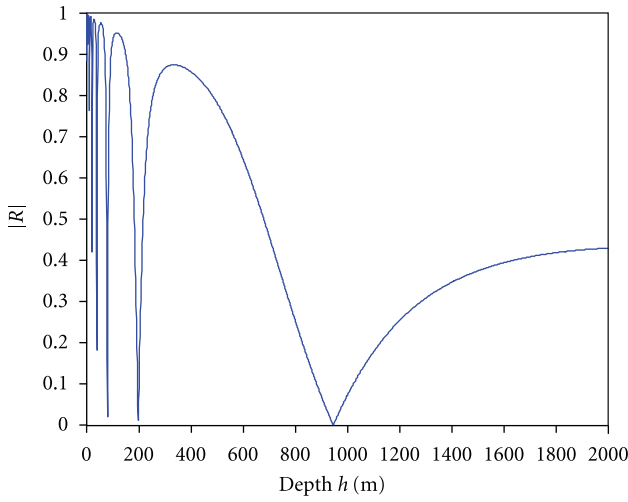


FIGURE 11: Curve of |R| changed with depth h .

of natural gas and volume V , the change curve of the density of natural gas can be worked out (Figure 5).

Without considering the composition change of natural gas, there is a linear relationship between the density of natural gas and depth:

$$\rho_a = \frac{mT_0}{P_0 V_0 T_1} (\rho_w g h + P_0). \quad (7)$$

We can calculate that the volume of natural gas is $V = 2.05 \times 10^{-2} \text{ mm}^3$ and the radius is $r = 0.16966 \text{ mm}$ in the depth of 2000 m.

Thus we can assume that there is a methane gas with balance radius of 0.16966 mm in the depth of 2000 m below the sea surface, which rises freely in the case of static seawater.

Because the maximal radius of this natural gas is only 1 mm, according to the actual observation data and calculation results, its maximal Reynolds number in seawater is far less than 1000.

As known from the fluid mechanics, the object moves relative to the fluid in the fluid whose surface has a

“boundary layer.” The microregiment near objects in the layer is static relative to the object, and the fluid micro regiment on the outside of the layer has the same speed as fluid. So there are velocity grads and viscous force in the boundary layer, which can serve as resistance to the object.

According to the given conditions, the dynamic viscosity coefficients μ of different depths are calculated using water and steam properties (Figure 6).

Smaller objects move slowly in the fluid with large stickiness, which means, in the case of small Reynolds numbers, the resistance, called viscous resistance, is the main factor. The famous Stokes formula describes the viscous resistance of spherical objects: $F = 6\pi\mu vr$, r is the sphere radius, v is the velocity of sphere, and μ is viscosity. This formula is correct as the condition that Reynolds number is much smaller than 1. That means when $Re \leq 1$, it fits the conditions of Stokes resistance formula, $C_D = 24/Re$, combined (4):

$$\frac{dv_a}{dt} = \frac{(\rho_w - \rho_a)g}{\rho_a} - \frac{18\mu v_a}{\rho_a d^2}. \quad (8)$$

While $1 \leq Re \leq 1000$, resistance coefficient C_D is calculated by corrected White experience formula:

$$C_D = \frac{24}{Re} + \frac{6}{\sqrt{Re}} + 0.4. \quad (9)$$

Take formula (9) into formula (8):

$$\frac{dv_a}{dt} = \frac{(\rho_w - \rho_a)g}{\rho_a} - \frac{3\rho_w v_a^2}{4\rho_a d} \left(\frac{24\mu}{\rho_w v_a d} + 6\sqrt{\frac{\mu}{\rho_w v_a d}} + 0.4 \right). \quad (10)$$

Using formula (10) can calculate the transient acceleration of bubble in the process of rising, and making $dv_a/dt = 0$ can obtain the final speed when the force is balance.

2.2. *The Velocity of Natural Gas in Water.* It is measured that the air dissolved in fluid (liquid) has no influence on the velocity of sound, even the air in the liquid is

saturated. But if there is small gas saturated suspended in the water, even very little, it may decrease the sound velocity. The sound velocity is related to the proportion of the gas in liquid and the frequency. Because the gas has a better compression than water, the compressibility of the water will change as the increasing of the proportion of the air. According to the formula $c = \sqrt{1/\rho_0\beta_s}$ ($\beta_s = -(dV/V)/dP$ is the adiabatic volume compressibility), the sound velocity changes apparently.

When the air's volume is smaller than the resonance bubbles, that means the frequency of sound is less than the resonance frequency, according to the theory of mixed liquid, we can get the sound velocity through the resonance of the water and air and the density. We can suppose k, k_a, k_w to represent the compressibility of mixed liquid, air, and water separately, and presume ρ, ρ_a, ρ_w are the corresponding density, when β (the proportion of the air) in the water is very little, because the $k_a \gg k_w, \rho_a \ll \rho_w$, and $\beta \ll 1$, we can get the velocity:

$$\begin{aligned} v &= \left(\frac{1}{\rho k}\right)^{1/2} \\ &= \left\{ \frac{1}{[\beta\rho_a + (1-\beta)\rho_w][\beta k_a + (1-\beta)k_w]} \right\}^{1/2} \\ [5pt] &= \left[\frac{1}{\rho_w k_w (1 + \beta k_a/k_w)} \right]^{1/2} = v_0 \left[\frac{1}{1 + \beta k_a/k_w} \right]^{1/2} \\ &= v_0 \left(\frac{1}{1 + 2.5 \times 10^4 \beta} \right)^{1/2} \end{aligned} \quad (11)$$

In (11), v_0 is the sound velocity of water without air. We can get that when the ratio of the gas in the mixed liquid is 0.01, the velocity is about the 53.5% of that without air. Supposing the velocity is $v_0 = 1500$ m/s when there is no air, the curve is shown in Figure 7.

Conversely, when the frequency is higher than the resonance frequency of the mixed liquid with least air, which means that the frequency is higher than all the resonance frequency of the air, the influence of suspension gas can be ignored.

If the single bubbles distributing inside an area changed to be uniform, supposing the starting volume ratio is 0.01%, the sound velocity varies following the depth, as in Figure 8. Through calculating, near the sea level, the velocity of sound in the layer is only 5% of that without gas.

When the frequency of sound approximately equals the air frequency, the velocity of sound wave has relations with not only the gas content but also the frequency of sound wave. If the frequency is approaching the resonance frequency, the speed of sound has a big change. Figure 9 is the smoothing speed curve of a group of homogeneous gas drawn by Fox et al. [2] under the conditions as these, the average diameter is 0.011 cm, and the density $V_a = 2 \times 10^{-4}$. When the frequency is resonant frequency, the speed of sound is the same as the velocity without air.

From Figure 9 we can see that when the frequency of sound wave is less than the resonant frequency of gas, the sound speed decreases because of the air; conversely, when the frequency of sound wave is higher than the resonant frequency of gas, the gas has little infection on the sound velocity; when the frequency of sound wave is approaching to the resonant frequency of gas, the sound velocity changes largely as the change of frequency.

When the frequency of the sound wave is almost the same as the resonant frequency of gas, and the diameter of sphere bubble distributed evenly far less than the wave length of sound, the accurate speed c and reduction α under the effects of gas resonance is expressed as

$$\begin{aligned} \left(\frac{c_0}{c}\right)^2 &= \frac{1+AX}{2} \left\{ 1 \pm \left[1 + \left(\frac{AY}{1+AX} \right)^2 \right]^{1/2} \right\}, \\ \alpha &= \frac{c\pi fAY}{c_0^2}. \end{aligned} \quad (12)$$

In the equation, $A = \rho c_0^2/p_0\gamma$, γ is the adiabatic exponent, c_0 is the speed of water without bubble, p_0 is the pressure of static water, ρ depends the density of gas and water mixture, and the parameters X and Y are presented as

$$X = \frac{\beta(1-f_*^2)}{(1-f_*^2)^2 + \delta_*^2}, \quad Y = \frac{\beta\delta_*}{(1-f_*^2)^2 + \delta_*^2}. \quad (13)$$

Among (13), $f_* = f/f_0$, $\delta_* = \delta/f_*^2$. f is the frequency of the sound wave, f_0 is the resonant frequency of gas bubble, and the δ is the damping constant.

2.3. Reflection and Transmission of Sound Wave. When the distance between the gases is less than the sound wavelength, the gas medium can be regarded as homogeneous medium, because the gas in the sea water changes its compressibility, making the average density and velocity changed, the interface between gas-bearing water and seawater is the wave impedance interface. Therefore, the gas reservoir can be seen as an intermediate of the sea water medium at this time. If the wavelength is much longer than the radius of the gas ($r \ll \lambda/2\pi$), suppose that a plane wave normally incident to a gas reservoir with the thickness of H , and the gas in it has the uniform size and uniform distributed (Figure 10), then the incident sound pressure is $P_i = A_i \exp(i(\omega t - k_w z))$, where A_i is amplitude of the incident sound pressure; $P_r = A_r \exp(i(\omega t + k_w z))$ is the reflection sound pressure, where A_r is amplitude of the reflection sound pressure; the transmission wave sound pressure is $P_T = A_T \exp(i(\omega t - k_w z))$, where A_T is amplitude of the sound pressure; the layer transmission wave sound pressure is $P_1 = A_1 \exp(i(\omega t - k_m z))$, where A_1 is amplitude of the sound pressure; the reflection sound pressure is $P_2 = A_2 \exp(i(\omega t + k_m z))$, where ω is the sound harmonic vibration circular frequency, ρ_w and ρ_m are the density of sea water and gasbearing, and c_w and c_m are the sound speed of sea water and gas-bearing, and $k_w = \omega/c_w$ and $k_m = \omega/c_m$ are the sound wave number of sea water and gas-bearing. The plane wave particle velocity is $v = v_0 \exp(\omega t - kx)$, and the velocity amplitude is $v_0 = p_0/c\rho$.

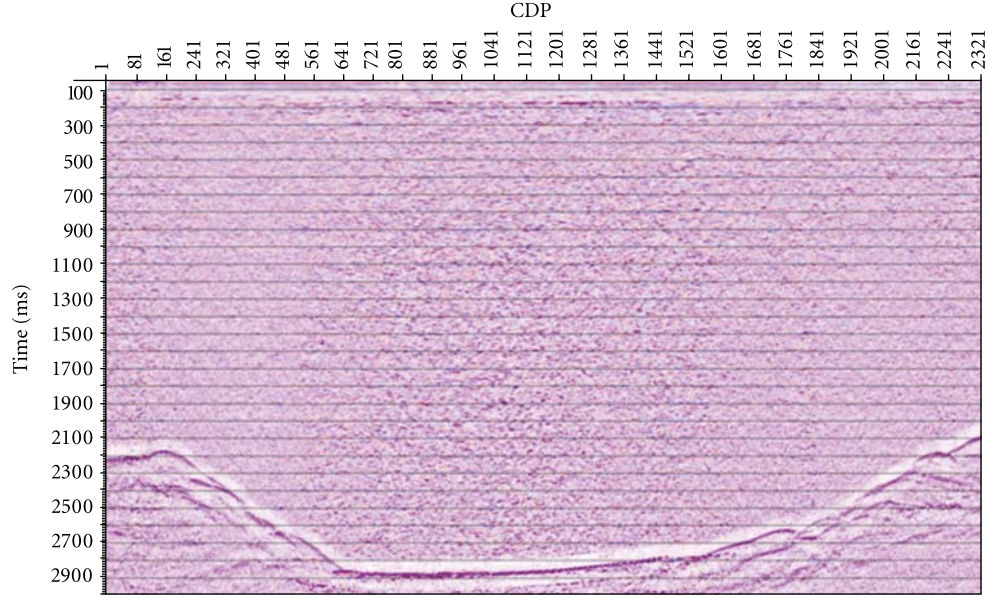


FIGURE 12: Characteristics of water bodies which appear in the high-resolution seismic profile of gas hydrate leakage area in the South China Sea.

Let $Z = c\rho$, then Z_w and Z_m are wave impedances of sea water and gas-bearing.

The velocity and pressure on interface between sea water and gasbearing are continuous, so the boundary conditions are as follows

(1) when $z = 0$, pressure: $P_i + P_r = P_1 + P_2$, that is,

$$A_i + A_r = A_1 + A_2, \quad (14)$$

velocity: $(P_i - P_r)/Z_w = (P_1 - P_2)/Z_m$, that is,

$$\frac{A_i - A_r}{Z_w} = \frac{A_1 - A_2}{Z_m}, \quad (15)$$

(2) when $z = H$, pressure: $P_1 + P_2 = P_T$, that is,

$$A_1 \exp(-ik_m H) + A_2 \exp(ik_m H) = A_T \exp(-ik_w H), \quad (16)$$

velocity: $(P_1 - P_2)/Z_m = P_{T1}/Z_w$, that is,

$$\frac{A_1 \exp(-ik_m H) - A_2 \exp(ik_m H)}{Z_m} = \frac{A_T \exp(-ik_w H)}{Z_w}. \quad (17)$$

Simultaneous equations (14), (15), (16), and (17), and making $R = A_r/A_i$, $T = A_T/A_i$, $B_1 = A_1/A_i$, $B_2 = A_2/A_i$, then

$$\begin{aligned} R &= \frac{(Z_w^2 - Z_m^2)[1 - \exp(i2k_m H)]}{(Z_m + Z_w)^2 \exp(i2k_m H) - (Z_w - Z_m)^2}, \\ T &= \frac{4Z_m Z_w \exp[i(k_m + k_w)H]}{(Z_m + Z_w)^2 \exp(i2k_m H) - (Z_m - Z_w)^2}, \\ B_1 &= \frac{2Z_m(Z_m + Z_w) \exp(i2k_m H)}{(Z_m + Z_w)^2 \exp(i2k_m H) - (Z_m - Z_w)^2}, \\ B_2 &= \frac{2Z_m(Z_w - Z_m)}{(Z_m + Z_w)^2 \exp(i2k_m H) - (Z_m - Z_w)^2}. \end{aligned} \quad (18)$$

The particle displacement is $\xi = (v_0/i\omega) \exp(i(\omega t - kx))$ for plane wave, and the displacement amplitude is $\xi_0 = v_0/i\omega$, at the point of $x = 0$, $R = A_r/A_i = v_{r0}/v_{i0} = \xi_{r0}/\xi_{i0}$ is the ratio of the displacement amplitude of incident and reflected waves on the interface. Similarly, T is the ratio of the amplitude of incident and wave transmission through the gas, B_1 is the ratio of the amplitude of incident and wave transmission of the above interface, B_2 is the ratio of the amplitude of incident and wave transmission of the following interface.

Assuming a floating gas layer, in which the size of the gas is uniform distribution, with the thickness of $H = 0.01$ m remaining unchanged, the size of the gas at the depth of 2000 m is the size of gas assumed in this paper. The volume ratio is $\beta = 0.01\%$. When a plane wave with the frequency of 30 kHz normal incident, the amplitude ratio R of incident and reflection is shown as Figure 11.

As can be seen from Figure 11, $|R|$ has certain cyclical changes. When $k_m H = n\pi$ ($n = 0, 1, 2, \dots$), the thickness of the bubble layer is an integer multiple of half wavelength, then $|R|$ is minimum, for example, at the point of $h = 947$ m, the wave is almost the transmission sound. When $k_m H = (2n-1)\pi/2$, the thickness of the gas layer is an odd multiple of the quarter wavelength, then $|R|$ is maximum, for example, at the point of $h = 338$ m, almost all the sound wave reflects back.

2.4. Scattering Effect of Natural Gas. The attenuation yielded by sound absorption needs to be considered in the actual gas. While the gas is forced to vibrate, some sound energy is burned because of the system's internal friction and distributed to the surrounding water in the form of heat, but the large vibration attenuation prevented the temperature balance in every moment. When the gas is compressed,

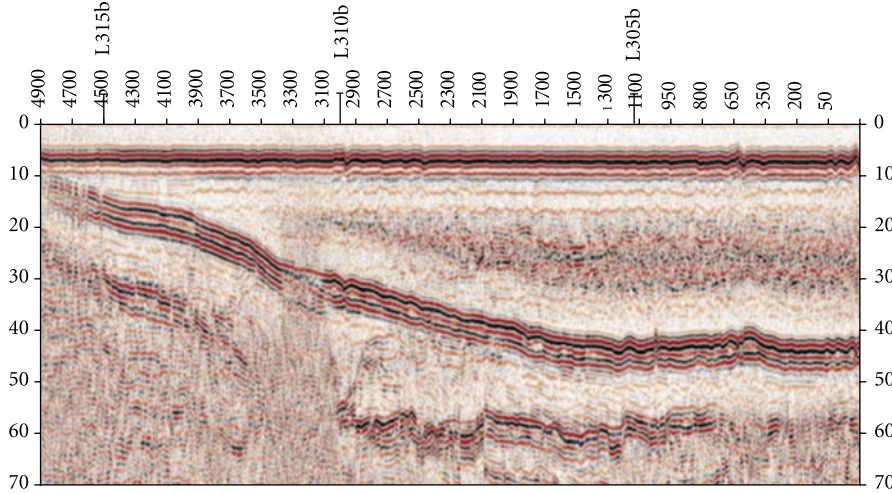


FIGURE 13: Characteristics of water bodies which appear in the high-resolution seismic profile of shallow gas hydrate leakage area in the Bohai Sea.

the heat is diffused along with the increasing temperature, so the bubble began to cool prior to the expansion. When the volume of gas is compressed to a minimum, the temperature is slightly reduced because of the heat shed to the water. The same is true when the expansion. Therefore, the process carried out in the gas is the procession between adiabatic process and isothermal process. Taking all these circumstances into account, the scattering cross-section expression of real gas is

$$\sigma_s = \frac{4\pi r^2}{(f_0^2/f^2 - 1)^2 + \delta^2}, \quad (19)$$

in (19), δ is total damping value, of which expression is

$$\delta = \frac{f_0^2}{f^2}\beta + \eta + \frac{C_1}{c\rho\eta}, \quad (20)$$

in (20), β is normal number; $\beta \ll 1$, C_1 is constant, to represent friction effect.

From (19), can obtain the ration of scattering cross-section and geometric cross section:

$$\frac{\sigma_s}{\pi r^2} = \frac{4}{(f_0^2/f^2 - 1)^2 + \delta^2}. \quad (21)$$

When the sound frequency is closed to resonance frequency, $\sigma_{s0}/\pi r^2 = 4/\delta_0^2$, δ_0 is called the total damping constant.

For the real gas, the absorption of sound energy must be considered. The sum of scattering energy and absorption energy is called dissipation energy while the dissipation section is

$$\sigma_e = \sigma_s + \sigma_a = \frac{4\pi r^2(\delta/\eta)}{(f_0^2/f^2 - 1)^2 + \delta^2}. \quad (22)$$

So the absorption cross-section can be calculated as

$$\sigma_a = \frac{4\pi r^2(\delta/\eta - 1)}{(f_0^2/f^2 - 1)^2 + \delta^2}. \quad (23)$$

It can be seen that the relationship of dissipation section and scattering cross-section is $\sigma_e/\sigma_s = \delta/\eta$.

3. Effect of Actual Data

Deep -ea high-resolution multichannel seismograph system developed by Ocean University of China was used in March 2009. It is an all new digital marine seismic hydrophone and the most advanced new marine seismic hydrophone all-digital instrument system in the world. Compared with the current analog seismic hydrophone system, its domestic applicability is stronger, and its resolution and SNR are higher. Each hydrophone has 24 channels and can be combined into a system of 24 ~ 1940 channels. The diameter of hydrophone is only 38 mm and the wall thickness is 1/8 inch. That is easy for transport and delivery and is durable. Using 6.25 m group interval and 1/16 ~ 4 ms broadband technology, it can be applied in oil exploration, marine engineering, and stratigraphic section measurement to obtain high-resolution seismic data. The high-resolution seismic data acquisition was firstly used in gas hydrates area near Dongsha Islands in the South China Sea. Record length of survey line is 3 s, the sampling interval is 1 ms, and the number of coverage is 6 times.

For feature of study areas that have a wide range of leakage area (including hydrate and free gas) in favor gas hydrate [12, 13], various gas hydrate leakage areas (including gas hydrate and free gas) distributions have been found through the geological survey studies. With the recent increase in understanding and investigating instrument performance improvement, we can further understand the distribution of gas hydrate leakage area (including gas hydrate and free gas) and seismic character (Figure 12), through the study on gas hydrate leakage area (including hydrate and free gas) according to seismic survey data.

For further research on the seismic character in shallow gas leakage area (including hydrate and free gas), according

to the research and experimental observation of water body features (Figure 13) on high-resolution seismic profile in the Bohai Sea shallow gas leakage area, the following sound properties of sediments and water that contains gas have been found. (1) The nature of the sound parameters of the gas. (2) The sound characteristics in the water contains natural gas (gas in shallow water, and the vibration process, resonance frequency, sound velocity, attenuation, reflection, and transmission). (3) The sound characteristics of sediments contain natural gas (resonant frequency, bubble damping, sound velocity, and attenuation).

In recent years seismic reflection characteristics of gas hydrates in deep water (Figure 12) and shallow gas in shallow water (Figure 13) leakage area (including hydrate and free gas) were summarized. Thus the seismic characteristics of the natural gas leakage area (containing gas hydrate and free gas) is divided into three categories according to spatial location. (1) The seismic characteristics in the formation: sound blanket, sound curtains, sound disturbances, irregular strong reflecting surface interface, and phase-down on both sides. (2) Features in the seabed surface: submarine pockmark and large collapse pit. (3) Features in water layer: sound plumes, cloud-like move, and dash-dot reflection. Combination of theory and case analysis shows that (1) there exists gas escaped from buried natural gas area in the sound plumes, cloud-like disturbance, and dash-dot reflection areas in seawater; (2) the region of sound blanket space represents areas of high gas concentration, a variety of sound disturbances represents areas with low gas concentration, and the gas concentration in sound curtains between the front two conditions.

4. Conclusions

The following conclusions can be obtained by the study of features of bubbly water in gas leakage area (including hydrate and free gas) through the study of characteristics of elastic parameters of deposition in the gas leakage area (including hydrate and free gas), and the use of sound theory of water and sediment containing hydrate and free gas.

- (1) We get the changes of the volume and radius when the gas rises at different depths, and also get the expression of acceleration in the static water. Besides, since the dynamic viscosity becomes smaller when the gas rises, the force gas suffered and the velocity keeps increasing until it arrives at the surface. Radius and volume of gas changes with depth with different velocities, in the context of 400 m below sea level, the velocity changes very fast, and as the depth increases the changes become smaller.
- (2) We also give the expression of reflection coefficient of gas, the size of the reflection coefficient not only related to impedance of both sides of the interface, but also related to the product of wave number and thickness of the gas, the reflection coefficient shows a certain periodicity. The gas becomes bigger when rising, volume ratio grows and sound is attenuated

faster, Theoretically, there are only 5% of no gas medium reaching sea level.

- (3) The size of the cross-section represents the gas range of the sound scattering, When the pressure is constant, scattering cross-section reaches the maximum near the resonance frequency, these conditions are changing as the gas rises, and the maximum of the scattering cross-section is only one-tenth of its geometric cross-section. Sound energy endure losses through internal friction and thermal conduction when the actual gas vibrates. This loss of performance for the scattering and absorption of air bubbles, absorption cross-section is less than the scattering cross section.
- (4) The main sound features of gas are relevant to gas size, gas content, velocity, attenuation, resonance frequency and the scattering cross-section, and other conditions. We can clearly see the sound characteristics of seismic data that yielded when the gas (or gas hydrate dissociation) escaped the water.

Acknowledgments

This paper is supported by the National Basic Research Program (973) subjects (2009CB219505) and Natural Science Foundation of Shandong Province (ZR2010DM012).

References

- [1] E. L. Carstensen and L. L. Foldy, "Propagation of sound through a liquid containing bubbles," *Journal of Acoustical Society of America*, vol. 19, no. 3, pp. 481–501, 1947.
- [2] F. E. Fox, S. R. Curley, and G. S. Larson, "Phase velocity and absorption measurements in water containing bubbles," *Journal of the Acoustical Society of America*, vol. 27, no. 3, p. 534, 1955.
- [3] E. Silberman, "Sound velocity and attenuation in bubbly mixtures measured in standing wave tubes," *Journal of Acoustical Society of America*, vol. 29, no. 8, pp. 925–933, 1957.
- [4] Z. Xiaoliang, Z. Zhemin, and Z. Lin, "Analytical description of sound wave propagation in a bubbly liquid and its strong nonlinearity," *Applied Sounds*, vol. 18, no. 6, pp. 18–23, 1999.
- [5] A. Prosperetti, "Thermal effects and damping mechanisms in the forced radial oscillations of gas bubbles in liquids," *Journal of Acoustical Society of America*, vol. 61, no. 1, pp. 17–27, 1977.
- [6] M. Kameda and Y. Matsumoto, "Nonlinear oscillation of a spherical gas bubble in acoustic fields," *Journal of the Acoustical Society of America*, vol. 106, no. 6, pp. 3156–3166, 1999.
- [7] K. W. Commander and A. Prosperetti, "Linear pressure waves in bubbly liquids: comparison between theory experiments," *Journal of the Acoustical Society of America*, vol. 85, no. 2, pp. 732–746, 1989.
- [8] A. Prosperetti, L. A. Crum, and K. W. Commander, "Nonlinear bubble dynamics," *Journal of the Acoustical Society of America*, vol. 83, no. 2, pp. 502–514, 1988.
- [9] F. Li, J. Sun, and J. Huang, "Study on propagation of sound wave in a bubbly liquid," *Journal of Northwestern Polytechnical University*, vol. 16, no. 2, pp. 241–245, 1998.

- [10] G. Yonghui, "Concentration of entrained air in air-water mixture as measured by sound transmission loss," *Applied Sounds*, vol. 18, no. 1, pp. 32–35, 1999.
- [11] S. Vagle and M. F. David, "The measurement of bubble-size distribution by soundal backscatter," *Journal of Atmos-Pheric and Oceanic Technology*, vol. 9, pp. 630–644, 1992.
- [12] L. Huaishan and Z. Zhengyun, "Seismic data processing approaches for the study of gas hydrates in the East China Sea," *Journal of Ocean University of Qingdao*, vol. 1, no. 1, pp. 87–92, 2002.
- [13] H. Liu, G. Huang, Y. He, S. Tong, S. Cui, and J. Zhang, "AVO character research of natural gas hydrates in the East China Sea," *Journal of Ocean University of Qingdao*, vol. 8, no. 3, pp. 270–276, 2009.

Research Article

Possible Relationships between Seep Carbonates and Gas Hydrates in the Miocene of the Northern Apennines

Stefano Conti and Daniela Fontana

Department of Earth Sciences, University of Modena and Reggio Emilia, Via S. Eufemia 19, 41100 Modena, Italy

Correspondence should be addressed to Daniela Fontana, daniela.fontana@unimore.it

Received 12 April 2011; Accepted 13 June 2011

Academic Editor: Umberta Tinivella

Copyright © 2011 S. Conti and D. Fontana. This is an open access article distributed under the Creative Commons Attribution License, which permits unrestricted use, distribution, and reproduction in any medium, provided the original work is properly cited.

In the Miocene of the northern Apennines, a widespread carbonate precipitation was induced by the expulsion of methane-rich fluids. Numerous outcrops of carbonate masses share sedimentological, textural and geochemical features with present-day gas hydrate-associated carbonates. We hypothesize the contribution of paleo-gas hydrate destabilization on the base of the heavy oxygen isotope signature, the presence of distinctive sedimentary features (breccias, pervasive nonsystematic fractures, and soft sediment deformation), the close association between seep carbonates and sedimentary instability, and the huge dimensions of seep carbonates bearing brecciated structures.

1. Introduction

Authigenic ^{13}C depleted carbonates have actually been described to form within or in proximity to gas hydrates, and gas hydrate-associated carbonates have been sampled from present-day settings in direct contact with the sea-floor or a few meters below it [1–3]. These seep carbonates, called clathrites [4, 5], show peculiar lithologies and structures such as vacuolar or vuggy-like structures resembling the shape of gas hydrate bubbles, monogenic and polygenic breccias, resulting from the rapid destabilization of gas hydrates. Highly brecciated structures are usually reported and restricted to large chemoherm complexes [1, 6, 7].

It is well known [8] that gas hydrate stability depends on temperature, pressure, and availability of gas and water. Different geologic processes, such as sea-level drop, tectonic uplift, climate changes, and hot fluid rise, can induce the destabilization of gas hydrates. Their destabilization causes the release of huge amounts of fluids (gas and water), thus triggering large-scale continental slope instability: slumps, slides, mud diapirism and seafloor collapses. Gas hydrate destabilization can also affect the oxygen isotope composition due to the release of ^{18}O -enriched water (see [9] and references therein).

Very few examples of seep carbonate-rich rocks recording the formation of gas hydrates within the sedimentary column have been documented [10–14]. Gas hydrates cannot survive for long geological times either because buried sediments are submitted to increasing geothermal conditions or are tectonically uplifted. In fossil sediments, the study of the interaction between seep carbonates, hydrate destabilization, and sediment instability is particularly difficult, owing to the lack of a direct recognition of fluid seepages and to the absence of precise quantifications of paleoenvironmental factors (pressure, temperature, and paleodepth) conditioning hydrate stability conditions.

Following present-day analogues, the only means to infer a possible role of gas hydrates in fossil seep carbonates are geochemical (oxygen isotope signature) and textural (presence of distinctive sedimentary features such as breccias, pervasive nonsystematic fractures, and soft sediment deformation) described in clathrites. Additional evidences can derive from the close association between seep carbonates and sedimentary instability, and the large dimensions of seep carbonate masses bearing brecciated structures.

Cold seep carbonates and associated lithologies were discovered in various geological settings of the northern Apennines during the Miocene [15–18] (Figure 1). Many

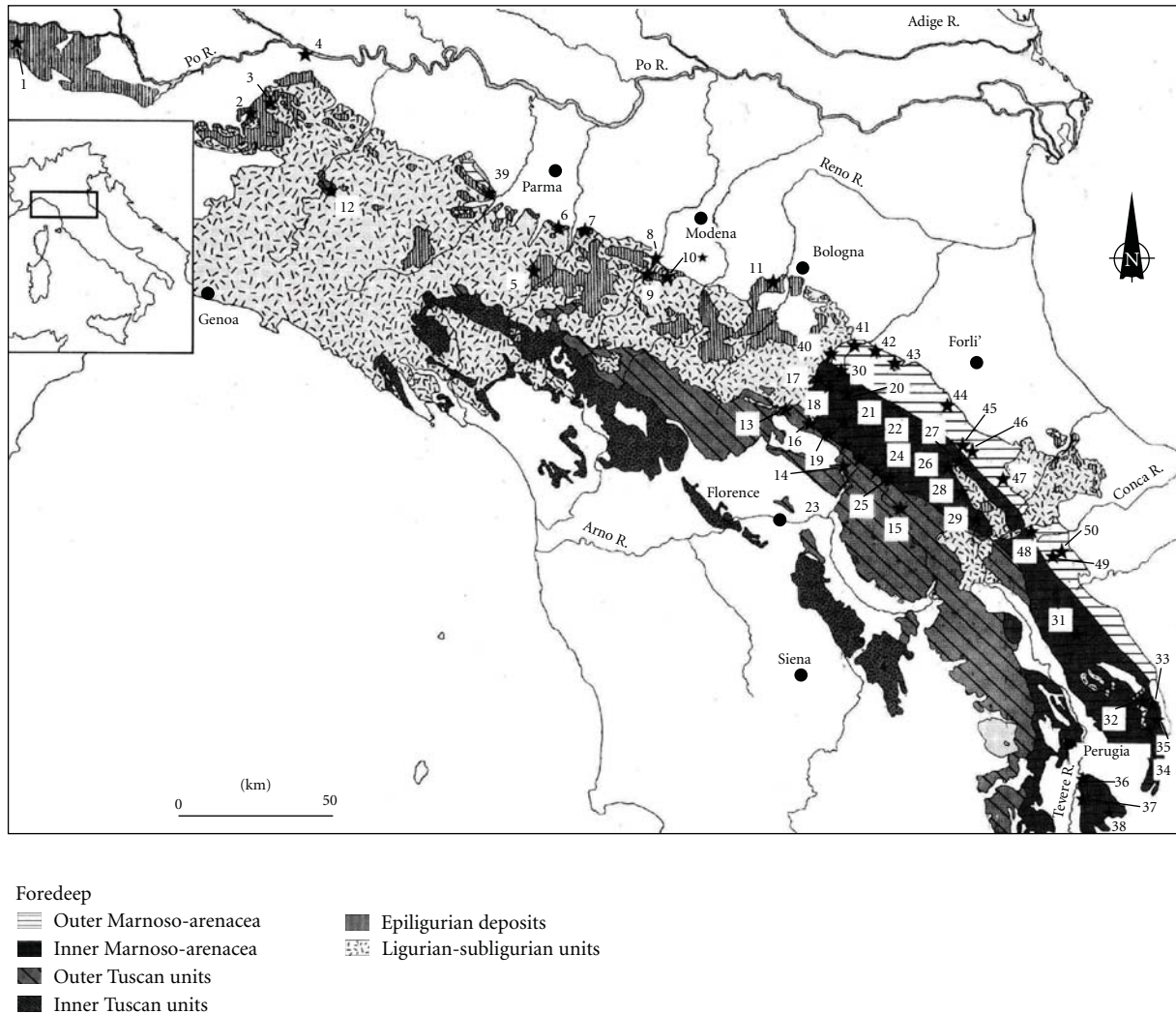


FIGURE 1: Seep carbonates of the northern Apennines (stars). Numbers 1–11 refer to outcrops enclosed in the Epiligurian deposits, 12–15 in the Tuscan Units, and 16–50 in the Marnoso-arenacea and related slope mudstones. The outcrops considered in this work are 10 referring to Sasso Streghe, Le Prade, Montandone; 25 to Castagno d'Andrea; 47 to Montepetra and 48 to Poggio delle Campane (modified from [15]).

seep carbonates are characterized by negative $\delta^{13}\text{C}$ and positive $\delta^{18}\text{O}$ values, by various types of brecciated structures and fluid-flow conduits, and are associated with intense sediment instability such as slumps, intraformational breccias, and olistostromes. In this paper, we report the results of 12 years of studies on seep carbonates, obtained from field work, facies analysis, geochemistry, and biostratigraphy, focussing on structures and clues highlighting the seepage activity and the possible relationships with gas hydrate destabilization.

2. Geological Setting

The northern Apennines is a thrust and fold belt characterized by the stacking of several structural units of oceanic and continental origin (Figures 1 and 2). The complex structure of the chain is the result of the convergence and collision between the European and the Adria plates from the Mesozoic to the present. Starting from the Early Cretaceous, an intraoceanic accretionary prism caused the progressive

consumption of the Piedmont-Ligurian Ocean, a portion of the Tethys ([20] and references therein). The complete closure of the ocean during Middle-Late Eocene caused the rapid uplift and erosion of the Alpine orogenic wedge and the inception of the continental collision. During the collision (late Oligocene to Recent) the internal oceanic units (Ligurian units), which were deformed and accreted during the Alpine orogenesis, were placed over the western continental margin of Adria while the thrust system migrated toward the foreland involving the Tuscan and Umbrian units, which were deposited on the Adria plate (Figure 2) [21–23]. Foredeep basins have developed and migrated easterly and northeasterly in response to the advancing Apenninic fronts which progressively have accreted the foredeep deposits (Figure 2). Starting from late Oligocene, the migration of the thrust belt was coupled with the counterclockwise rotation of the Corsica-Sardinia block and of the northern Italian peninsula [24, 25].

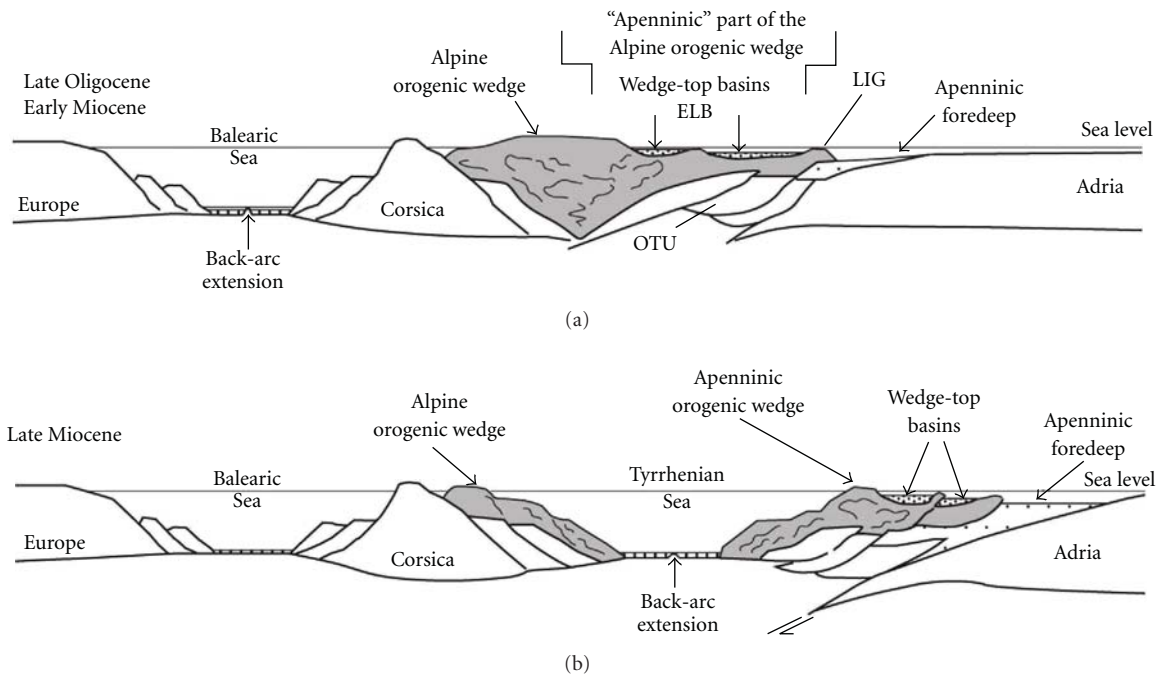


FIGURE 2: Schematic sketch of the migration of the Apennine thrust-belt foredeep system. (a) From the Late Oligocene to Early Miocene. (b) In the Late Miocene, ELB: Epiligurian basin, OUT: outer Tuscan Units, LIG: Ligurian Units (modified from [19]).

At present, the Apenninic orogenic wedge is framed by two superposed structural levels. The upper, allochthonous structural level is made up of the accreted Ligurian units. These comprise Mesozoic oceanic and forearc deposits derived from the closure of the Ligurian-Piedmont ocean and its continental margins [26]. On top of the Ligurian units, the Epiligurian wedge-top basins are characterized by a middle Eocene-early Messinian succession [27–29]. The lower structural level (Tuscan-Umbrian Units) consists of metamorphic basement and Mesozoic to Paleogene carbonate successions folded and segmented by thrusts.

The Miocene paleogeography of the northern Apennine orogenic wedge and associated foredeep basin is depicted in Figure 2. The foredeep depocenters and Epiligurian wedge-top basin migrated in response to the advancing orogenic leading edges. At the same time, the external ramp was migrating and flexing toward outer areas of the foreland basin. The foredeep depocenters were mainly filled by sheet-like turbiditic deposits derived from fluvial and deltaic systems draining the Alps. By contrast, the Epiligurian clastic deposits testify to local Apenninic sources [30]. Deltaic turbiditic systems are mainly located on the orogenic wedge and wedge-top basins; mixed turbiditic systems are at the leading edges of the orogenic wedge and inner foredeep; deep marine turbiditic systems are situated in axial foredeep depocenters and on the foreland external ramp.

In the northern Apennines, mass-wasting products (slumps, slides, block falls, and debris and flows), also known as olistostromes, are common [31, 32]. They occur either in the Epiligurian wedge-top basin, or close to the toe of the orogenic wedge [33, 34], and even in the inner part of the foredeep basins [35]. They might be related to instability



FIGURE 3: Castagno d'Andrea carbonates (number 25 of Figure 1), the basal part of the body is severely brecciated.

caused by fluid seepage [36]. They form complex units of various sizes, from a few meters to hundreds of meters, and derive from masses of both foredeep deposits and Ligurian units slid off submarine slopes.

3. Apennine Seep Carbonate Distribution and Characters

Authigenic seep carbonates in the northern Apennines are concentrated in Middle-Late Miocene pelitic successions in two different geological settings: in the foredeep and in Epiligurian wedge-top basins (Figures 1 and 2) [15, 37]. In the foredeep, seep carbonates (Figure 3) occur in marly and clayey hemipelagites and fine-grained turbidites, located in the inner slope (closure facies), and in intrabasinal highs in the inner side of the foredeep



FIGURE 4: Sasso Streghe carbonates (number 10 of Figure 1): note the large pinnacle in the middle, and the lateral extension of the body on the left. On the right the diapiric mélange of Montardone crops out (argillaceous badlands).

(pelitic intervals of [38]). Closure facies are essentially slope deposits, Langhian-early Messinian in age, thinning laterally and capping huge arenaceous turbiditic bodies (Monte Cervarola and Marnoso-arenacea Fms). Pelitic intervals are Langhian-early Serravallian in age, intercalated within Monte Cervarola and Marnoso-arenacea Fms; they are composite bodies, including intraformational and subordinate extraformational sediments, with a lateral extent of 10–30 km. The intraformational sediments are basin plain and slope lithofacies, partly involved in spectacular megaslumps. The extraformational are Ligurian, Subligurian, Epiligurian, or Tuscan deposits, derived from the migrating thrust front.

In the Epiligurian basins, seep carbonates occur in the lower part (Serravallian-early Tortonian) of the pelitic Termina Marls Formation (Figure 4).

In the field, seep carbonates occur in a variety of morphologies: lenticular-amygdaloid or scattered irregular bodies, pinnacles, irregularly thickened levels ranging in diameter from a few centimeters to several decameters (Figures 3 and 4). The maximum thickness is about 30 m. They are commonly poorly stratified and strongly bioturbated (as indicated by burrows, mottled structures, and trace fossils), but some seep carbonates show a clear stratification. The marly and fine calcarenitic lithofacies are typically associated with abundant fossil remains, consisting of thick recrystallized closed shells and moulds of lucinid and vesicomid-like clams, thin shells of modioloid-like mussels, and small gastropod shells. The fossil preservation shows unabraded condition; lucinid-like shells can be very large (up to 25 cm), thick and articulated, and so densely packed as to represent a striking feature of the deposit. In contrast, coarser facies are markedly impoverished in fossil content; bivalve coquina is abundant and valves, when articulated, are generally isolated or more often packed but disarticulated.

Seep carbonate dominant rock types are calcilitic/marly limestones, calcareous marls, and calcarenites. Enclosing sediments are hemipelagic/turbiditic mudstones, muddy sandstones, and marlstones, characterized by low permeability but severely fractured.

4. Evidence of Paleo-Gas Hydrates in Seep Carbonate Formation

Following present-day analogues (described in great detail by [1]), the only means to infer a possible role of gas hydrates in fossil seep carbonates are (1) the heavy oxygen isotope signature, (2) the presence of distinctive sedimentary features (breccias, nonsystematic fractures, and soft sediment deformation) linked to clathrites, (3) the close association between seep carbonates and sedimentary instability, and (4) the huge dimensions of seep carbonate deposition bearing brecciated structures.

Among seep carbonates of the northern Apennines, numerous outcrops show the peculiar features listed above, that could suggest relationships with gas hydrate destabilization.

In this paper we have selected four significant outcrops covering a wide area from Modena to Tuscan-Marchean Apennines (Figure 1). Three are in the foredeep: Montepetra (47 of Figure 1) and Poggio delle Campane (48) enclosed in the inner slope hemipelagites (closure facies), and Castagno d'Andrea (25) in the pelitic intervals of the foredeep. Sasso Streghe (10 of Figure 1, which includes several bodies) is located in the Epiligurian wedge-top basins.

These outcrops are made of large carbonate bodies characterized by negative $\delta^{13}\text{C}$ and positive $\delta^{18}\text{O}$ values, by various types of brecciated structures and fluid-flow conduits, and are associated with intense sediment instability such as slumps, intraformational breccias, and mud diapirs. In the following section we report data from field work, facies analysis, petrography, geochemistry, and biostratigraphy, focussing on features indicating possible relationships with gas hydrate destabilization.

4.1. Clathrite-Like Structures

4.1.1. Dimensions. In the field, the examined carbonates consist of huge isolated lenticular-amygdaloid, stratiform bodies and pinnacles ranging in extension from 10 to 100 m and with a maximum thickness up to 30 m (Figures 3 and 4). They can be laterally repeated with a close distribution and disposed in irregular thickened levels as long as 200–300 m. The lateral distribution of levels is conformable with the stratification of the enclosing mudstones, and the lateral contact with host sediments varies from sharp to transitional.

4.1.2. Seepage-Induced Breccias. Monogenic, and polygenic breccias are abundant and generally restricted to the basal portion of carbonate bodies. Monogenic breccias (Figure 5) are made of heterometric angular clasts, ranging in size from few millimeters to 5–10 centimeters, composed of the authigenic micrite from the seep carbonates. Clasts are chaotically dispersed in a micritic matrix or in a fine to medium-grained sandy matrix. Larger clasts derive from the coalescence of heterometric smaller clasts, testifying various cycles of cementation and fragmentation. In many cases, monogenic breccias pass gradually to a dense network of nonsystematic carbonate-filled veins and microfractures,



FIGURE 5: Monogenic breccias and irregular network of veins, Poggio delle Campane (number 48 of Figure 1).

irregularly connected to a larger vein network. Fossils are commonly reworked and disarticulated; they occur as isolated shells or are organized in discontinuous levels; layers of shell detritus are also present. Lateral extension is decimetric to metric.

Polygenic breccias (Figure 6) are characterized by a complex framework of carbonate, arenitic, and pelitic clasts of various provenance (both extraformational and intraformational) and dimensions, chaotically floating in the micritic matrix. Clasts are heterometric (from some millimeters to 50 centimeter in diameter), generally very angular, rarely subangular; sometimes clast size gradually decreases from the base to the top of carbonate masses. Intraformational clasts are made of carbonates from the various facies, or are supplied by lithotypes of the host turbidites and hemipelagites. Extraformational clasts derive from various sources such as Ligurian, sub-Ligurian, Epiligurian or foredeep arenaceous turbidites (Tuscan units) older than those including seep carbonates. Allochthonous clasts can also derive from the Ligurian nappe front and are now intercalated within foredeep or Epiligurian sequences. Fossils are scarce to absent and commonly disarticulated or represented by bivalve coquina in packstones or grainstones. In few cases, polygenic breccias are clast-supported. They form units ranging in thickness from some centimeters to a few meters, randomly distributed and often interdigitated with fine-grained carbonate cemented sediments. Pseudofluidal textures are observed.

4.1.3. Textures. Examined seep carbonates show many structures similar to those reported by [1] in the Hydrate Ridge gas hydrate-associated carbonates. Micritic-marly limestones and fine calcarenites show vacuolar and vuggy-like fabrics, and stromatactis-like structures resembling drusy crystals. Vuggy structures are often associated with irregular patches of monogenic carbonate breccias and irregular network of carbonate-filled veins (Figures 7, 8, and 9).

Void infillings are made up of carbonate cements and/or coarser sediments (calcarenites, microbreccias, and coquina debris). The abundance of veins and fractures of centimetric dimension give the carbonate masses the appearance of megabreccias. In thin section the micritic groundmass is crosscut by an intertwined network of irregular fissures.



FIGURE 6: Polygenic breccias: clast dimensions vary from some mm to about 20 cm. Sasso Streghe (number 10 of Figure 1).



FIGURE 7: Micritic limestones with dense network of carbonate-filled veins and conduits. Maximum diameter of conduits is 2 cm. Colline, near Castagno d'Andrea (number 25 of Figure 1).

Vein diameter ranges from 1-2 millimeters to 2 centimeters, they are not systematic and show a sinuous to irregular distribution; in most cases they can join forming veins of major dimensions (1-2 cm) containing abundant black iron sulfides. In some cases, veins and rims are lined by acicular or botryoidal aragonite. The vein infillings can also contain coquina debris.

4.1.4. Sediment Instability. The examined seep carbonates occur in deposits associated with intense sediment instability, such as intraformational slumps, soft-sediment deformation structures, and mud diapirs. Slumps and slides predominate in the foredeep (Montepetra, Poggio delle Campane,



FIGURE 8: Micritic limestones with extensive vuggy and spongy fabric; maximum dimension of cavities is 1 cm, Sasso Streghe (number 10 of Figure 1).



FIGURE 9: Vuggy structures associated with monogenic breccias and irregular network of carbonate-filled veins (diameter 3-4 mm), Castagno d'Andrea (number 25 of Figure 1).

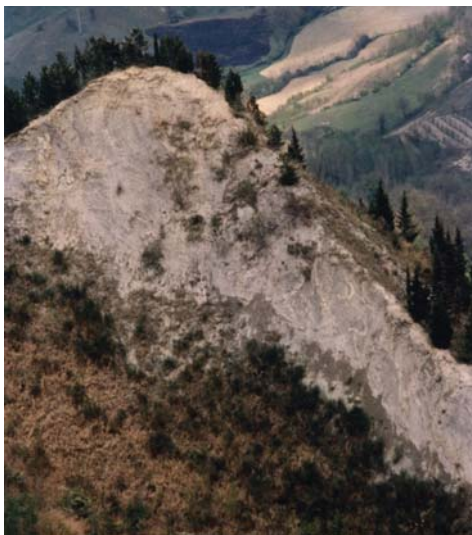


FIGURE 10: Intraformational slump in closure pelites of the foredeep, near Montepetra (number 47 of Figure 1).

Castagno d'Andrea; Figure 10), where carbonates are hosted in pelitic successions deposited in intrabasinal structural highs. The formation of structural highs is linked to synsedimentary thrust activity, related to blind thrusts. Intrabasinal highs are developed very close, some tens of kilometers, to the front of the paleo-Apennine wedge represented by the allochthonous Ligurian nappe. They formed during the closure stage of the foredeep, generally related to the synsedimentary growth of anticlines. Field analyses suggest that detachment folding was the leading mechanism of anticline growth and of synsedimentary instability along the anticline flanks. In this structural setting, the fold geometry can deflect and confine the mass transport deposits sourced from the Ligurian nappe (olistostromes). The occurrence of sediment sliding sourced both from intraformational and extraformational sediments, and the ascent of blocks of already compacted rocks and clasts from the underlying basin-plain turbidites of the Marnoso-arenacea Fm, in some cases seem to indicate a contribution from diapiric rising of fluids [17, 18]. In the Epiligurian basins, seep carbonates are lateral to a huge sedimentary *mélange* (Montardone *mélange*; Figure 4) recently interpreted as a diapir on the basis of the distribution and geometry of the *mélange*, the vertical abrupt contact with the hosting Termina marls, the occurrence of huge seep carbonates associated with the *mélange*, and the presence of polygenic breccias at the base of carbonates.

The marginal portion of the diapir is characterized by diffuse slope instability with the emplacement of coalescent debris flows involving blocks of authigenic carbonates. Minor lens-like bodies of chaotic deposits are present in seep carbonates at different levels, resembling sill-like intrusions of diapiric material.

4.1.5. Isotopes. The $\delta^{13}\text{C}$ and $\delta^{18}\text{O}$ analyses indicate that examined seep carbonates are depleted in ^{13}C and slightly but significantly enriched in ^{18}O compared to carbonates of surrounding sediments. The ^{13}C depletion and ^{18}O enrichment reach the maximum values in the brecciated portions of the larger seep carbonates. In Sasso Streghe outcrops the carbon value has an average = -37‰ , and the $\delta^{18}\text{O}$ value range from 0.1 to 5.4 ‰ relative to the PDB standard [19, and unpublished data]. In enclosing pelites values vary narrowly in most samples, showing a slight depletion in ^{18}O ($\delta^{18}\text{O}$ from -3.11 to -4.47‰) that suggests derivation of oxygen from seawater. The Montepetra carbonates (MP5 and FC bodies, [17]) show negative carbon values (from -36.02 to -52.68‰) associated with enriched values of ^{18}O ($\delta^{18}\text{O}$ from 2 to 5.97 ‰). The Castagno d'Andrea carbonates constituting the main massive micrite portion of the body show an average $\delta^{13}\text{C} = -24\text{‰}$ [16] and carbonates in the brecciated units have an average = -36.0‰ PDB. The ^{18}O values ($\delta^{18}\text{O} = +1.2\text{‰}$ PDB) show a slight but significant enrichment in $\delta^{18}\text{O}$ for chemoherms when compared to values of carbonate phases present in enclosing pelites. In samples from Poggio Campane the carbon values reach -32.2‰ and $\delta^{18}\text{O} +2.21\text{‰}$.

5. Discussion

In fossil Apenninic seep carbonates, we found structures that are very similar to “gas-hydrate related rock structures” reported by [1] in present-day carbonates of the Hydrate ridge in the Cascadia margin. In the Hydrate Ridge, the authors recognized a direct relationship between gas hydrates and sediment fracturing: carbonates show layered megapores and veins as relict of the original gas hydrate fabric, and different types of breccias formed by growing and decomposing gas hydrate near the sediment surface. In addition carbonates are involved in sedimentary instability processes. The heavy oxygen isotopic signatures are also a peculiar feature.

In the Miocene Apenninic seep carbonates, vacuolar and vuggy-like structures of irregular shape (Figures 7, 8, and 9) look similar to hydrate layers observed in modern sediments. Monogenic breccias (Figure 5) share many characters with mudclast breccias and intraformational breccias “chemoherm-typical,” described in [1], and to “irregular edifices” reported in [39], due to ascending bubbles and growing gas hydrate that caused sediment brecciation. We do not exclude that part of these features are collapse breccia, related to the rapid destabilization of gas hydrates in the sediment pore spaces. Both recent and fossil breccias have very angular clasts, a similar irregular clast-supported fabric, and abundant pores. Polygenic breccias (Figure 6) in studied sediments are also similar to polymictic lithologies of [1]. The large dimensions of Miocene carbonate edifices (Figures 3 and 4) bearing brecciated structures, as well as the close association with sedimentary instabilities (Figures 4 and 10) are also reported in modern hydrate-associated settings. Geochemistry provides an additional evidence. Apenninic seep carbonates show negative carbon values ($\delta^{13}\text{C}$ up to -52.68‰) associated with enriched values of ^{18}O ($\delta^{18}\text{O}$ up to 5.97‰) that could be likely due to decomposition of gas hydrates.

All these elements seem to indicate that the decomposition of gas hydrates played a role in the precipitation of methane-derived carbonates in wedge-top and foredeep basins of the northern Apennines, during the Miocene. The gas hydrate destabilization was not substitutive but contributory to surface microbial methanogenesis and could permit a large amount of fluids to be released in a short time.

In the northern Apennines inferred paleobathymetric data are compatible with gas hydrate stability field [40], as estimated on the basis of benthic foraminiferal fauna characteristics, indicating intermediate water depth (upper slope) for the seep carbonates [17, 18].

We hypothesized different mechanisms in the foredeep and in wedge-top basins, resulting in geological responses largely dependent on rate and duration of fluid expulsion processes.

Carbonates in the foredeep (Castagno d’Andrea, Montepetra, Poggio delle Campane) are related to intrabasinal highs where methane accumulation in the hinge zone may form a hydrate seal, trapping methane in underlying strata. Tectonic movements could have disrupted the underlying gas hydrate stability zone, as a consequence of upward movement of the base of gas-hydrate stability field due to uplift

of the structural highs (cf. [41]), and/or anomalous heating by waters moving up along faults [42, 43]. Seal rupture by tectonic activity allowed methane seepage that sustained chemosynthetic biota and consented carbonate precipitation. Gas hydrate dissociation produced large amount of gas and water released in a short time, thus favouring more intense fluid activity triggering mass wasting deposits, such as sliding and slumping, and sand/mud diapirism.

Decomposition of gas hydrates and weakening of the mechanical strength of sediments encouraged failure along low-angle slopes producing more slides and some slumps rather than debris flows, as indicated by [44] in modern geological settings. The lack of turbidity deposits at the foot of the slumps could be a further clue to their gas-hydrate dissociation-related origin. Fluid overpressures was probably facilitated by the tectonic loading of Apennine thrust-sheets, related to underthrust foredeep deposits dewatering. The occurrence of extraformational deposits (olistostromes) within pelitic intervals testifies a close position of the deformational front. This intense activity could also explain the ascent of blocks of already compacted rocks and clasts from the underlying basin-plain turbidites.

In epiligurian wedge-top basins we hypothesize mud diapirism due to the tectonic loading by overthrusting, and the generation of a large amount of methane-rich fluid for gas-hydrate destabilization. The occurrence of methane-rich fluids, testified by authigenic carbonates, contributed to generate overpressured shales ascending along sin-sedimentary faults. The fine-grained nature of the matrix of buried debris flow deposits, common in epiligurian succession but absent in the foredeep, incorporated in the accreted terranes of the Apenninic thrusts, favoured the build-up of the excess pore pressure necessary for the evolution of mud diapirs. In our opinion, the polygenic extraformational breccias in epiligurian seep carbonates originated not only from hydrofracturing and erosion of the country rocks during gas hydrate destabilization and mud eruption, but also from the reworking of buried slides and debris flows, common in the epiligurian succession (sedimentary mélanges). The surface expression of the mud diapir is affected by diffuse slope-instability with the emplacement of coalescent debris flows also involving blocks of authigenic carbonates.

6. Conclusions

Authigenic seep carbonates in the northern Apennines are concentrated in Middle-Late Miocene pelitic successions in two different geological settings: in the foredeep and in epiligurian wedge-top basins.

By comparison with present-day analogues, we infer a possible role of gas hydrates in the precipitation of fossil seep carbonates of the Apennines. The factors that have allowed us to hypothesize the paleo occurrence of gas hydrates are the heavy oxygen isotope signature, the presence of distinctive sedimentary features (breccias, soft sediment deformation) related to clathrites, the close association between seep carbonates and sedimentary instabilities, and

the large dimensions of seep carbonate deposition bearing brecciated structures.

Carbonates in the foredeep are related to intrabasinal highs where methane accumulation in the hinge zone formed a hydrate seal, trapping methane in underlying strata. Seal rupture by tectonic activity induced gas hydrate dissociation, resulting in carbonate precipitation and triggering mass wasting deposits. Decomposition of gas hydrates and weakening of the mechanical strength of sediments encouraged failure along low-angle slopes producing more slides and some slumps rather than debris flows.

In epiligurian wedge-top basins, carbonates are associated with a diapiric mélange, generated by overpressured shales ascending along sin-sedimentary faults, related to gas hydrate dissociation. We assumed that the fine-grained nature of the matrix of buried debris flow deposits, common in epiligurian succession but absent in the foredeep, favoured the build-up of the excess pore pressure necessary for the evolution of mud diapir. The polygenic extraformational breccias in epiligurian seep carbonates originated not only from hydrofracturing and erosion of the country rocks during gas hydrate destabilization and mud eruption, but also from the reworking of buried slides and debris flows.

Acknowledgments

The authors are grateful for all the suggestions of the editor, and the careful revisions of the anonymous reviewers who greatly improved the original paper.

References

- [1] J. Greinert, G. Bohrmann, and E. Suess, "Gas hydrate-associated carbonates and methane-venting at Hydrate Ridge: classification, distribution, and origin of authigenic lithologies," in *Natural Gas Hydrates: Occurrence, Distribution and Detection*, C. K. Paull and W. P. Dillon, Eds., Geophysical Monograph 124, pp. 99–113, 2001.
- [2] L. L. Mazurenko and V. A. Soloviev, "Worldwide distribution of deep-water fluid venting and potential occurrences of gas hydrate accumulations," *Geo-Marine Letters*, vol. 23, no. 3–4, pp. 162–176, 2003.
- [3] A. Mazzini, H. Svensen, M. Hovland, and S. Planke, "Comparison and implications from strikingly different authigenic carbonates in a Nyegga complex pockmark, G11, Norwegian Sea," *Marine Geology*, vol. 231, no. 1–4, pp. 89–102, 2006.
- [4] J. P. Kennett and B. N. Fackler-Adams, "Relationship of clathrate instability to sediment deformation in the upper Neogene of California," *Geology*, vol. 28, no. 3, pp. 215–218, 2000.
- [5] G. Bohrmann, K. Heeschen, C. Jung et al., "Widespread fluid expulsion along the seafloor of the Costa Rica convergent margin," *Terra Nova*, vol. 14, no. 2, pp. 69–79, 2002.
- [6] H. H. Roberts, "Fluid and gas expulsion on the Northern Gulf of Mexico continental slope: mud-prone to mineral-prone responses," in *Natural Gas Hydrates: Occurrence, Distribution and Detection*, C. K. Paull and W. P. Dillon, Eds., Geophysical Monograph 124, pp. 145–161, 2001.
- [7] X. Han, E. Suess, Y. Huang et al., "Jiulong methane reef: microbial mediation of seep carbonates in the South China Sea," *Marine Geology*, vol. 249, no. 3–4, pp. 243–256, 2008.
- [8] G. Bohrmann and M. E. Torres, "Gas hydrates in marine sediments," in *Marine Geochemistry*, H. D. Schulz and M. Zabel, Eds., pp. 481–512, Springer, Berlin, Germany, 2006.
- [9] B. M. A. Teichert, N. Gussone, A. Eisenhauer, and G. Bohrmann, "Clathrites: archives of near-seafloor pore-fluid evolution ($\delta^{44/40}\text{Ca}$, $\delta^{13}\text{C}$, $\delta^{18}\text{O}$) in gas hydrate environments," *Geology*, vol. 33, no. 3, pp. 213–216, 2005.
- [10] F. F. Krause, "Genesis and geometry of the Meiklejohn Peak lime mud-mound, bare mountain quadrangle, Nevada, USA: ordovician limestone with submarine frost heave structures—A possible response to gas clathrate hydrate evolution," *Sedimentary Geology*, vol. 145, no. 3–4, pp. 189–213, 2001.
- [11] C. Pierre and J. M. Rouchy, "Isotopic compositions of diagenetic dolomites in the Tortonian marls of the western Mediterranean margins: evidence of past gas hydrate formation and dissociation," *Chemical Geology*, vol. 205, no. 3–4, pp. 469–484, 2004.
- [12] M. J. Bojanowski, "Oligocene cold-seep carbonates from the Carpathians and their inferred relation to gas hydrates," *Facies*, vol. 53, no. 3, pp. 347–360, 2007.
- [13] F. D. Pierre, L. Martire, M. Natalicchio, P. Clari, and C. Petrea, "Authigenic carbonates in upper miocene sediments of the tertiary piedmont basin (NW Italy): vestiges of an ancient gas hydrate stability zone?" *Bulletin of the Geological Society of America*, vol. 122, no. 7–8, pp. 994–1010, 2010.
- [14] L. Martire, M. Natalicchio, C. C. Petrea, S. Cavagna, P. Clari, and F. D. Pierre, "Petrographic evidence of the past occurrence of gas hydrates in the Tertiary Piedmont Basin (NW Italy)," *Geo-Marine Letters*, vol. 30, no. 3–4, pp. 461–476, 2010.
- [15] S. Conti and D. Fontana, "Miocene chemoherts of the northern Apennines, Italy," *Geology*, vol. 27, no. 10, pp. 927–930, 1999.
- [16] S. Conti, D. Fontana, A. Gubertini et al., "A multidisciplinary study of middle Miocene seep-carbonates from the northern Apennine foredeep (Italy)," *Sedimentary Geology*, vol. 169, no. 1–2, pp. 1–19, 2004.
- [17] S. Conti, D. Fontana, S. Mecozzi, G. Panieri, and G. A. Pini, "Late Miocene seep-carbonates and fluid migration on top of the Montepetra intrabasinal high (Northern Apennines, Italy): relations with synsedimentary folding," *Sedimentary Geology*, vol. 231, no. 1–2, pp. 41–54, 2010.
- [18] G. Panieri, A. Camerlenghi, S. Conti, G. A. Pini, and I. Cacho, "Methane seepages recorded in benthic foraminifera from Miocene seep carbonates, Northern Apennines (Italy)," *Palaeogeography, Palaeoclimatology, Palaeoecology*, vol. 284, no. 3–4, pp. 271–282, 2009.
- [19] S. Conti and D. Fontana, "Anatomy of seep-carbonates: ancient examples from the Miocene of the northern Apennines (Italy)," *Palaeogeography, Palaeoclimatology, Palaeoecology*, vol. 227, no. 1–3, pp. 156–175, 2005.
- [20] W. Cavazza, F. M. Roure, W. Spackman, G. M. Stampali, and P. A. Ziegler, *The TRANSMED Atlas. The Mediterranean Region from Crust to Mantle*, Springer, Berlin, Germany, 2004.
- [21] C. Doglioni, F. Monelli, and G. Pialli, "Boudinage of the Alpine belt in the Apenninic back-arc," *Memorie Della Societa' Geologica Italiana*, vol. 52, pp. 457–468, 1998.
- [22] E. Gueguen, C. Doglioni, and M. Fernandez, "On the post-25 Ma geodynamic evolution of the western Mediterranean," *Tectonophysics*, vol. 298, no. 1–3, pp. 259–269, 1998.
- [23] A. Argnani and F. Ricci Lucchi, "Tertiary silicoclastic turbidite systems of the Northern Apennines," in *Anatomy of an Orogen: The Apennines and Adjacent Mediterranean Basins*, I. P. Martini and G. B. Vai, Eds., pp. 327–350, Kluwer Academic, London, UK, 2001.

- [24] G. Muttoni, L. Lanci, A. Argnani et al., "Paleomagnetic evidence for a neogene two-phase counterclock wise tectonic rotation in the Northern Apennines (Italy)," *Tectonophysics*, vol. 326, no. 3-4, pp. 241–253, 2000.
- [25] J. Ferrandini, J. Gattacceca, M. Ferrandini, A. Deino, and M. C. Janin, "Chronostratigraphy and paleomagnetism of Oligo-Miocene deposits of Corsica (France): geodynamic implications for the liguro-provençal basin spreading," *Bulletin de la Societe Geologique de France*, vol. 174, no. 4, pp. 357–371, 2003.
- [26] M. Marroni, G. Molli, A. Montanini, G. Ottria, L. Pandolfi, and R. Tribuzio, "The external Ligurian units (Northern Apennine, Italy): from rifting to convergence of a fossil ocean-continent transition zone," *Ofioliti*, vol. 27, pp. 119–131, 2002.
- [27] A. Amorosi, M. L. Colalongo, and S. C. Vaiani, "Le unità epiliguri mioceniche nel settore emiliano dell'Appennino settentrionale. Biostratigrafia, stratigrafia sequenziale e implicazioni litostratigrafiche," *Palaeopelagos*, vol. 3, pp. 209–240, 1993.
- [28] E. Mutti, L. Papani, D. Di Biase et al., "Il bacino terziario epimesoalpino e le sue implicazioni sui rapporti tra Alpi ed Apennino," *Memorie di Scienze Geologiche, Università di Padova*, vol. 47, pp. 217–244, 1995.
- [29] G. Ottria, R. Catanzariti, and A. C. Feroni, "The Ranzano unit boundaries in the type area: lower Oligocene events in the epi-Ligurian Succession (northern Apennines, Italy)," *Eclogae Geologicae Helvetiae*, vol. 94, no. 2, pp. 185–196, 2001.
- [30] U. Cibin, E. Spadafora, G. G. Zuffa, and A. Castellarin, "Continental collision history from arenites of episutural basins in the Northern Apennines, Italy," *Bulletin of the Geological Society of America*, vol. 113, no. 1, pp. 4–19, 2001.
- [31] S. Conti and R. Gelmini, "Miocene-Pliocene tectonic phases and migration of foredeep-thrust belt system in Northern Apennines," *Memorie Della Societa' Geologica Italiana*, vol. 48, pp. 261–274, 1994.
- [32] G. A. Pini, "Tectosomes and olistostromes in the argille scagliose of Northern Apennines," *Geological Society of America*, pp. 1–70, 1999, Special Paper 335.
- [33] G. Papani, C. Tellini, L. Torelli, L. Vernia, and S. Iaccarino, "Nuovi dati stratigrafici e strutturali sulla Formazione di Bismantova nella "sinclinale" Vetto-Carpinetti (Appennino reggiano-parmense)," *Memorie Della Societa' Geologica Italiana*, vol. 39, pp. 245–275, 1987.
- [34] A. Artoni, G. Papani, F. Rizzini et al., "The salsomaggiore structure (Northwestern Apennine foothills, Italy): a Messinian mountain front shaped by mass-wasting products," *GeoActa*, vol. 3, pp. 107–127, 2004.
- [35] C. C. Lucente and G. A. Pini, "Anatomy and emplacement mechanism of a large submarine slide within a miocene foredeep in the Northern Apennines, Italy: a field perspective," *American Journal of Science*, vol. 303, no. 7, pp. 565–602, 2003.
- [36] C. C. Lucente and M. Taviani, "Chemosynthetic communities as fingerprints of submarine sliding-linked hydrocarbon seepage, Miocene deep-sea strata of the Tuscan-Romagna Apennines, Italy," *Palaeogeography, Palaeoclimatology, Palaeoecology*, vol. 227, no. 1–3, pp. 176–190, 2005.
- [37] F. Ricci Lucchi and G. B. Vai, "A stratigraphic and tectonofacies framework of the "calcari a Lucina" in the Apennine Chain, Italy," *Geo-Marine Letters*, vol. 14, no. 2-3, pp. 210–218, 1994.
- [38] S. Conti and D. Fontana, "Sediment instability related to fluid venting in Miocene authigenic carbonate deposits of the northern Apennines (Italy)," *International Journal of Earth Sciences*, vol. 91, no. 6, pp. 1030–1040, 2002.
- [39] L. D. Kulm and E. Suess, "Relationship between carbonate deposits and fluid venting: oregon accretionary prism," *Journal of Geophysical Research*, vol. 95, no. 6, pp. 8899–8915, 1990.
- [40] G. R. Dickens and M. S. Quinby-Hunt, "Methane hydrate stability in seawater," *Geophysical Research Letters*, vol. 21, no. 19, pp. 2115–2118, 1994.
- [41] K. Sain, T. A. Minshull, S. C. Singh, and R. W. Hobbs, "Evidence for a thick free gas layer beneath the bottom simulating reflector in the Makran accretionary prism," *Marine Geology*, vol. 164, no. 1-2, pp. 3–12, 2000.
- [42] A. Y. Golmshtok, A. D. Duchkov, D. R. Hutchinson, and S. B. Khanukaev, "Heat flow and gas hydrates of the Baikal rift zone," *International Journal of Earth Sciences*, vol. 89, no. 2, pp. 193–211, 2000.
- [43] M. D. Tryon, K. M. Brown, M. E. Torres, A. M. Tréhu, J. McManus, and R. W. Collier, "Measurements of transience and downward fluid flow near episodic methane gas vents, Hydrate Ridge, Cascadia," *Geology*, vol. 27, no. 12, pp. 1075–1078, 1999.
- [44] B.U. Haq, "Natural gas hydrates: searching for the long-term climatic and slope-stability records," in *Gas Hydrates: Relevance To World Marginn Stability And Climate Change*, J. P. Henriot and J. Mienert, Eds., Special Publication No.137, pp. 303–318, Geological Society, London, UK, 1998.

Research Article

BSR versus Climate Change and Slides

U. Tinivella, M. Giustiniani, and D. Accettella

Istituto Nazionale di Oceanografia e di Geofisica Sperimentale, 34010 Sgonico, Italy

Correspondence should be addressed to U. Tinivella, utinivella@ogs.trieste.it

Received 29 March 2011; Accepted 7 June 2011

Academic Editor: Xuewei Liu

Copyright © 2011 U. Tinivella et al. This is an open access article distributed under the Creative Commons Attribution License, which permits unrestricted use, distribution, and reproduction in any medium, provided the original work is properly cited.

We investigate the relationship between climate change and hydrate stability in two peri-Antarctic areas: Antarctic Peninsula and South Chile. We consider these areas because the polar and subpolar areas are the most sensitive about global change. The zone, where the methane can be easily released by hydrate melting, is the shallow water, that is, in proximity of the intersection between the BSR and the sea bottom. In order to simulate the effect of climate change on hydrate stability, we consider the following seven scenarios for both areas: present environmental condition; sea bottom temperature increase/decrease of 1°C water depth increase/decrease of 100 m; sea bottom temperature and water depth increase/decrease of 1°C and 100 m, respectively. On the basis of our result, we can draw the conclusion that the modeling is a useful tool to understand the effect of the climate change on hydrate stability. Moreover, in these areas where the sea bottom temperature is influenced by temperature increase, slides could be easily triggered by hydrate dissociation.

1. Introduction

Submarine slides are global phenomena that can occur on slopes that may be considerably less inclined than their terrestrial equivalents due to the presence of excess water [1, 2]. They can displace huge amounts of material over great distances. For example, the Storegga slide of Norway had a total run-out distance of about 800 km, with a total displaced volume of sediments estimated to be in the order of 5500 km³ [3]. Slope failures occur when the downslope driving forces due to gravity and other factors exceed the resisting forces that are inherited from the sediment strength. During the last decades, a debate was started regarding the relationship among gas hydrate, climate change, and slope stability. In fact, gas hydrates represent a significant geohazard that is of immediate importance to near and offshore developments. Human activities and installations in regions of gas hydrate occurrence must take into account the presence of gas hydrate and deal with the consequences of its presence [4].

The hydrate stability zone in marine environments is a function of the water depth, the seafloor temperature and the geothermal gradient. Any changes to the temperature and/or pressure, both at the surface and in the area adjacent to the hydrate, affect the thickness of the stability zone.

Although temperature and pressure are the main controls in the formation of gas hydrates and the thickness of the hydrate stability zone, other factors such as gas chemistry and gas availability will also alter the thickness and location of the hydrate stability zone [5]. Dissociation of hydrate may trigger the sudden release of large amounts of methane through the ocean into the atmosphere, leading to accelerated climate warming. Hydrate dissociation and gas release in the atmosphere have been proposed as a significant mechanism to explain the rapid and significant climate change during the Palaeocene-Eocene Thermal Maximum [6–9]. This hypothesis has been challenged by different studies, which suggest that methane from dissociating hydrate may never have reached the atmosphere [10, 11]. Alternatively it has been proposed that methane release may follow, rather than lead, climate change [12].

The association between gas hydrates and submarine slope failure has been widely documented (e.g., [2, 3, 13–16]). As is well known, gas hydrates have been found to be a significant constituent of seafloor sediment in many continental shelf-slope environments around the world [17, 18]. There are many examples of a possible connection between gas hydrates and submarine slope failures. Kvenvolden [9, 10] summarized slope failures on the continental slope and rise of the west coast of Africa, on the US Atlantic continental

slope, in the fjords of British Columbia, and on the Alaskan Beaufort Sea continental margin. Several researchers have performed in-depth analyses of the Norwegian continental margin [19–23], and all have suggested that gas hydrates may have triggered one or more large submarine slides in this area. The other famous examples of coincident gas hydrate distribution and slope failure include the Cape Fear slide on the continental slope and of the rise southeast of Cape Fear, North Carolina [15], the Humboldt slide zone near the Mendocino triple junction on the Northern California continental margin [14], and the submarine slope failure in offshore Fiordland [2].

In the last years, several authors (i.e., [22–24]) have investigated the relationship between the gas hydrate dissociation and the increase of pore fluid pressure below the bottom simulating reflector (BSR), which is the seismic indication of the base of the gas hydrate stability zone. In fact, dissociation of gas hydrates at the BSR, in response to a change in the physical environment (i.e., temperature and/or pressure regime), can liberate excess gas and elevate the local pore fluid pressure in the sediment [24, 25]. The increase in pore fluid pressure has the effect of decreasing the effective normal stress on any assumed failure surface, so that less shear stress is required to initiate failure. Whether free gas liberation by gas hydrate dissociation can singularly cause a slide, rather than just being a contributing load or the final trigger, is dependent on various factors. These include rate of dissociation, sediment permeability, depth below sea level, and depth below the seafloor [26].

For decomposing gas hydrates to be a widespread cause of slope failure, three criteria must be met [28]: (1) gas hydrates must not only be present, but must be widespread as well; (2) slides must have originated in areas that are within the gas hydrate phase boundaries; (3) soils of low permeability must be common at the base of the hydrate zones (to permit the buildup of excess pore pressure that could lead to unstable slopes during sea-level falls).

In this paper, we focus our attention on the slides that occur in area where the BSR is shallow and, consequently, in the area where the hydrate stability is influenced by climate change, that is, temperature and pressure changes. In order to quantify the effects of gas hydrate dissociation, a numerical analysis has been undertaken in two areas: Antarctic Peninsula and South Chile (Figure 1). The first area is chosen because the polar regions are more sensitive to climate change. In fact, the climate change signals are particularly amplified in transition zones, such as the peri-Antarctic regions [29]. On the other hand, the high amount of gas hydrate present in the South Chile plays an important geohazard related to intense seismicity affecting the region [30, 31] and shallow BSR locally present [32]. In this contest, we plan to study the relationship between the shallow hydrate/BSR depth and the pressure/temperature changes.

2. The Study Areas

2.1. Antarctic Peninsula. A strong BSR was identified on multichannel seismic reflection and ocean bottom seismometer (OBS) data acquired during the Austral summers 1989/1990

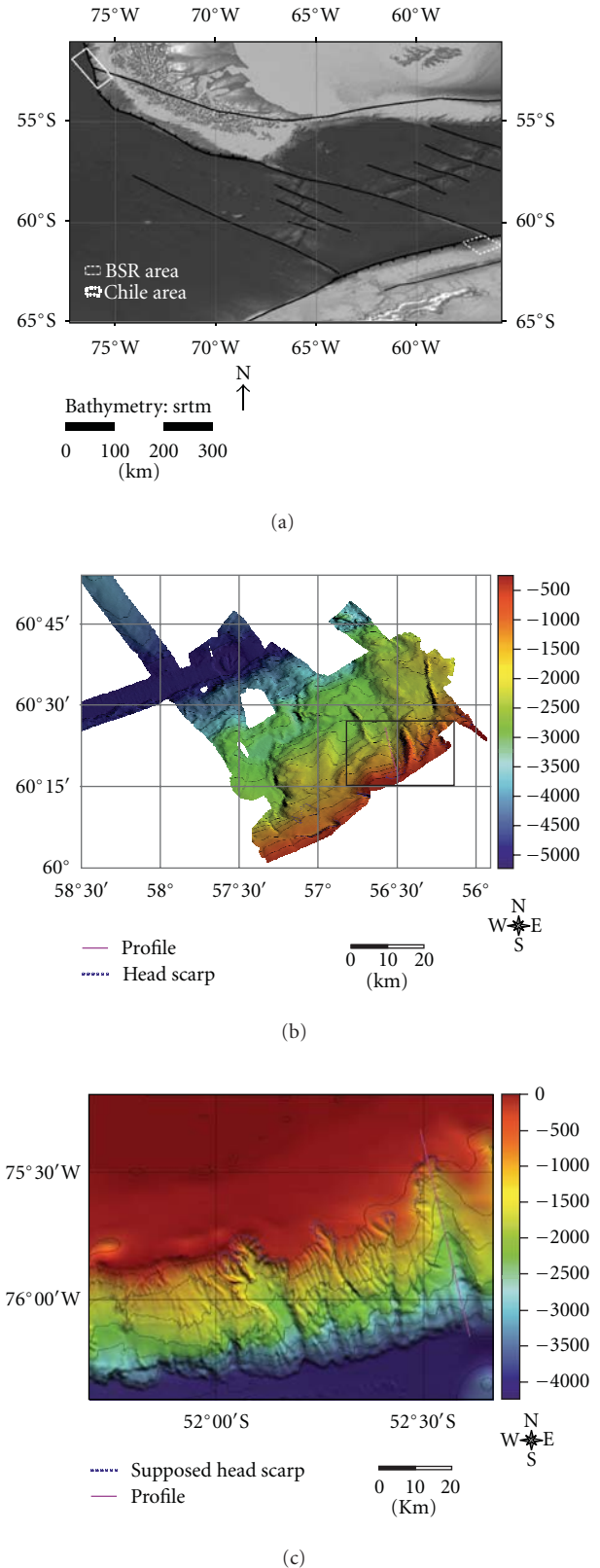


FIGURE 1: (a) Location map of investigated areas. (b) Multibeam map of the Antarctic area. The pink solid line represents the analyzed profile, while the black block represents the analyzed area reported in Figure 2. (c) Multibeam map of the Chile area. The pink solid line represents the analyzed profile.

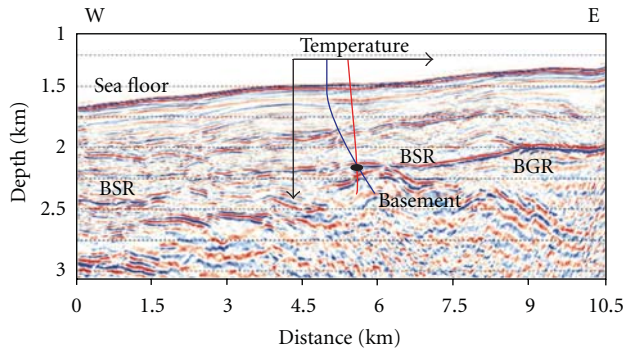


FIGURE 2: Example of prestack depth migrated section from Antarctic Peninsula with a clear BSR (austral summer 1996/1997, line IT213). See location map and details in [27]. BGR: base of free gas reflector. Insert: blue line: geothermal curve. Red line in the insert: gas hydrate stability curve. The intersection between the two curves indicates the BSR depth.

[33], 1996/1997 [27] on the South Shetland margin. Example of the seismic data acquired in this area with a clear BSR was reported in Figure 2. In the prestack depth migrated section the presence of the base of the free gas reflector (BGR; [33]) is clearly detected. To better characterize the area where the BSR is very strong and continuous, another cruise was carried out to acquire detailed bathymetric data (12 kHz was the acoustic frequency used), subbottom profile data, two gravity cores, and seismic data with a short hydrophone streamer (600 m) during the Austral summer 2003/2004 [29]. The multibeam bathymetric data, collected using a Reson multibeam echo sounding system (Reson SeaBat 8150), cover an area of about 4,500 km² [29, 34]. The data were calibrated using water column velocity profiles, reconstructed from conductivity-temperature-density measurements (CTD) acquired in four representative sites. The new bathymetry map was generated in the form of a shaded digital elevation model, using the processing software PDS2000 and based on a cell grid size of 100 × 100 m (Figure 1). The bathymetric map of the study area provides evidence of mud volcanoes, collapse troughs, and recent slides [29].

The geothermal gradient of the area was estimated analyzing the seismic data, in particular comparing the BSR depth extracted by seismic data analysis and the theoretical BSR depth evaluated considering different geothermal gradient [34]. The analysis indicated that the regional geothermal gradient is 38°C/km, considering the sea bottom temperature equal to 0.4°C, as indicated by OBS [27] and CTD data [34].

2.2. South Chile. The second study area is located along the south Chilean margin on the continental slope (Figure 1). BSRs have been detected during several geophysical cruises. In particular, BSR has been recognized along the accretionary prism by several authors [32, 35–40]. Unfortunately, in this area data from Global Multi-Resolution Topography compilation [41] were available (<http://media.marine-geo.org/category/bathymetry>), which contain multibeam

data from NBP0602 Project (Simrad EM120; Figure 1). Consequently, the resolution is about 600 m/node, and it is difficult to recognize evidences of slides at relative shallow depth. In the literature, no information about slide related to gas hydrate in the southern Chilean margin can be found. Moreover, on the basis of bathymetric data, we focused our attention on a slide located in the northern part of the investigated area.

The geothermal gradient is very variable along this margin (see, e.g., [32]). For this reason, we considered a constant geothermal gradient equal to 38°C/km as in Antarctic Peninsula. The sea bottom temperature was considered equal to 2.2°C, as reported in [42].

3. The Modeling

Our objective is to verify if the climate change (i.e., sea level and bottom temperature changes) can be responsible of slides because of gas hydrate dissociation. As is well known, the most crucial zone is the area where there is the intersection of the base of the gas hydrate stability zone with the seabed. This area is affected by a bottom-water temperature increase more than the deeper parts on the hydrate stability zone [19]. In the first condition, gas hydrates are close to their stability limit and will respond quickly to the anticipated warming of the polar region because thermal diffusion times through any overlying sediment are short. Recent models have shown that shallow and cold deposit can be very unstable and release significant quantities of methane under the influence of as little as 1°C of seafloor temperature increases [43].

For this reason, we model the effect of climate change on the intersection between the base of the gas hydrate stability field and the seafloor. By using bathymetric data, sea bottom temperature, geothermal gradient and considering that the natural gas is methane, we evaluate the theoretical BSR [34]. It was calculated considering the intersection between the geothermal curve (evaluated from sea bottom temperature and geothermal gradient) and the hydrate stability curve, considering the Sloan formula [5]. Figure 2 indicates the geothermal (blue line in the insert) and the gas hydrate stability (red line in the insert) curves, and their intersection is in correspondence to the BSR depth. The bathymetric data are translated in pressure considering the average water density equal to 1046 kg/m³, as reported in the literature [44].

In order to simulate the effect of climate change on BSR depth, we consider small temperature variation (equal to 1°C) in order to verify how slight climate change can influence hydrate stability, as suggested recently by several authors (i.e., [43]). Regarding the sea level change, several models have suggested that the sea level dropped of almost 100 m during the Last Glacial Maximum [45]. For this reason, we adopt this sea level variation in our modeling. On the base of these considerations, we consider the following seven scenarios for both areas: (S0) present environmental condition from measurements; (S1) sea bottom temperature increase of 1°C with respect to the present temperature (interglacial period scenario); (S2) sea bottom temperature

decrease of 1°C with respect to the present temperature (glacial period scenario); (S3) water depth increase of 100 m with respect to the present bathymetry (interglacial period scenario); (S4) water depth decrease of 100 m with respect to the present bathymetry (glacial period scenario); (S5) sea bottom temperature and water depth increases of 1°C and 100 m, respectively, with respect to the present environmental conditions (interglacial period scenario); (S6) sea bottom temperature and water depth decreases of 1°C and 100 m, respectively with respect to the present environmental conditions (glacial period scenario).

In Antarctic Peninsula, the seismic BSR depth is affected by an error of about 5%, while the bathymetric data present an error of about 1.5% [34]. Consequently, we consider that the theoretical BSR, evaluated by using the geothermal gradient extracted from seismic and bathymetric data, is affected by an error of about 6.5%. So, we consider that the BSR crosses the seafloor if the difference between the bathymetry and the theoretical BSR depth is less than the bathymetry multiplied by 6.5%. Because not more detailed information is available in the South Chile, we suppose the error considered in the first dataset for coherence.

The results of the modeling are shown in Figure 3 for both analyzed areas. The grids representing each scenario are reported with different colors superimposed on multibeam data. In order to understand the effect of climate change on the slope stability, we evaluate the relationship between the considered scenarios and the identified slides, indicated by solid line in Figure 1.

In Figure 4, we show the results of our modeling for both analyzed profiles. The solid line indicates the present situation, that is, the intersection between the BSR and the seafloor. The dashed lines represent the scenarios (S2, S3), in which the hydrate is more stable. On the contrary, the dissociation of the gas hydrate is represented by dotted lines for scenarios S1, S4, and S6. Scenario S5 affects very weakly the depth of the intersection between the base of the hydrate stability and the seafloor.

4. Discussion and Conclusions

Our modeling clearly shows the relationship between the gas hydrate and the slope stability. In fact, the lines in Figure 4, representing the intersection between the gas hydrate stability and the seafloor for each scenario, are located in proximity of the main head scarp (see Figure 1). This result confirms the hypothesis that the hydrate can influence the slope stability causing important slides. It is important to underline that direct measurements of sedimentary sequence are not available; so, consideration about the age of the slides and the climate change is just a speculation.

As already mentioned, we extract profiles, which cross two slides, to better evaluate the effect of climate change on the intersection between the hydrate stability and the seafloor. Note that the results of the two models are in agreement. Note that the two datasets have a different resolution and, for this reason, we perform a qualitative analysis of the model results.

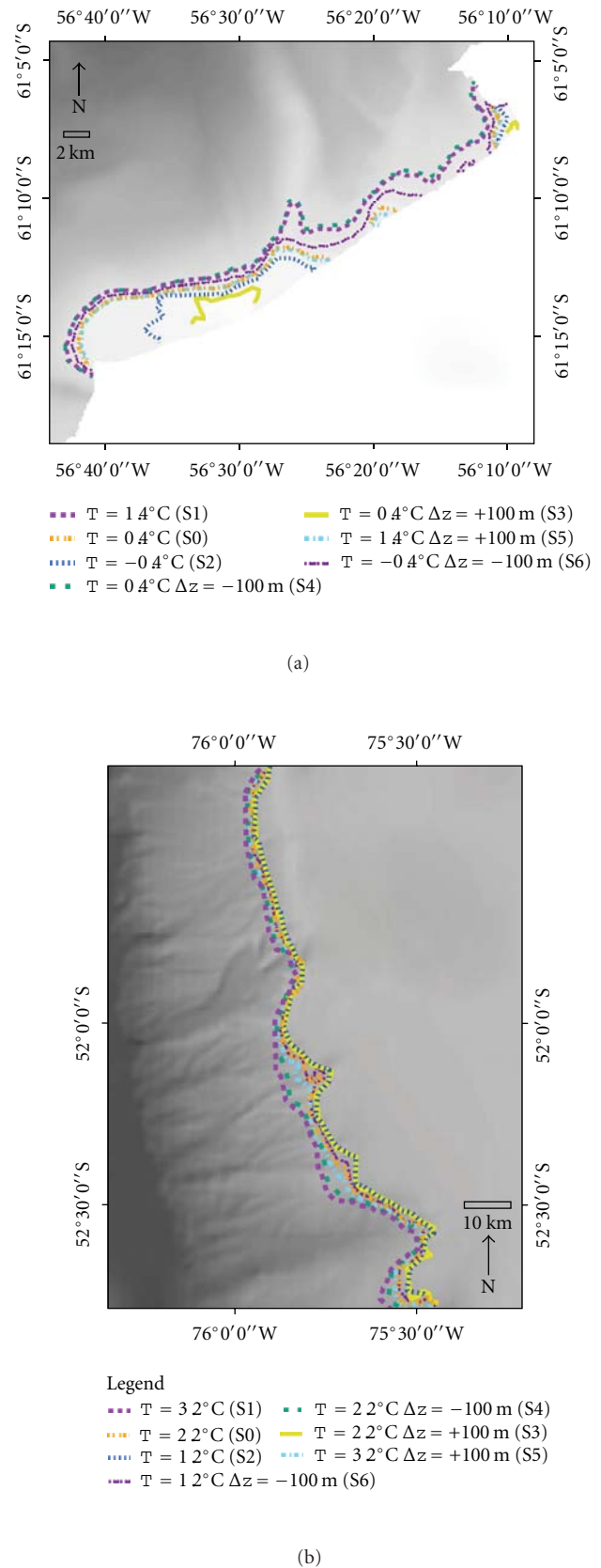


FIGURE 3: The colored lines indicate the intersection between the seafloor and the BSR in Antarctic (a) and the Chile (b) areas. The different scenarios are indicated according to the text.

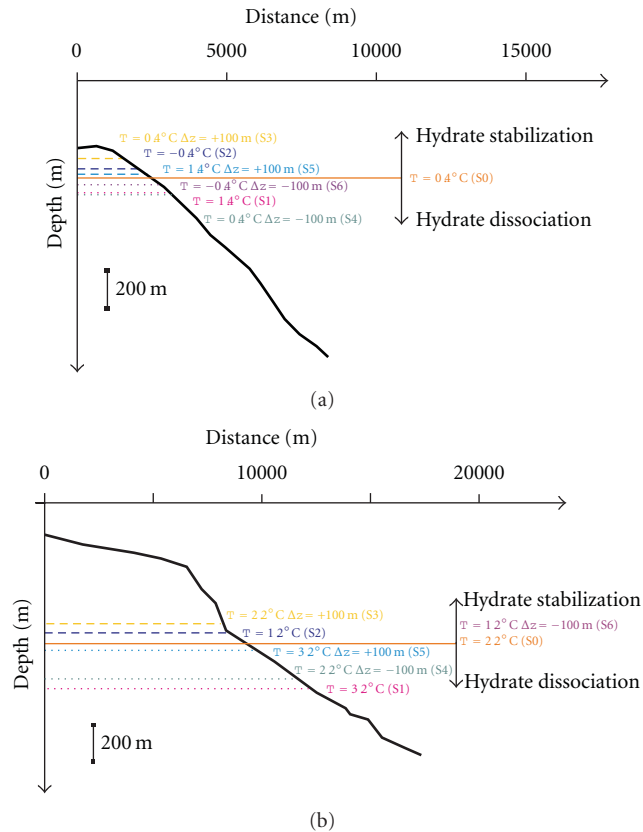


FIGURE 4: The colored lines indicate the intersection between the seafloor and the BSR along the analyzed profiles in Antarctic (a) and the Chile (b) areas. The different scenarios are indicated according to the text.

Let us consider the glacial period, in which we have the decrease of temperature and decrease of pressure. At the beginning, we suppose just a decrease of the temperature (scenario S2), and the result indicates a positive feedback. On the contrary, when the cooling produces a pressure decrease (scenarios S4 and S6), the negative feedback is observed. In this case, gas is released in the seawater, and consequently in the atmosphere, reducing the cooling.

In the interglacial period, the first effect is the temperature increase (scenario S1). As expected, the modeling indicates gas hydrate dissociation (positive feedback). So, the methane released can reach the atmosphere, contributing to the global warming. If we consider a case in which the seafloor temperature is not affected by global warming and the water depth increases (scenario S3), the feedback is negative, that is, the hydrate is stable. If we consider the joint effect of temperature and pressure increase, the effect of hydrate stability is negligible. Resuming, the hydrate influences the slope stability and the climate change during the interglacial period only at the beginning of the warming and only if sea bottom is influenced by temperature variation.

In conclusion, our modeling points out the strong relationship between gas hydrate presence and climate change. So, it is very important to perform a modeling in the areas where gas hydrate is present in order to simulate the effect

of climate change on hydrate and slope stabilities. It is clear that, in these areas, where the sea bottom temperature is influenced by temperature increase, slides could be easily triggered by hydrate dissociation.

References

- [1] M. A. Hampton, H. J. Lee, and J. Locat, "Submarine landslides," *Reviews of Geophysics*, vol. 34, no. 1, pp. 33–59, 1996.
- [2] G. J. Crutchley, A. R. Gorman, and M. Fohrmann, "Investigation of the role of gas hydrates in continental slope stability west of Fiordland, New Zealand," *New Zealand Journal of Geology and Geophysics*, vol. 50, no. 4, pp. 357–364, 2007.
- [3] S. Bouriak, M. Vanneste, and A. Saoutkine, "Inferred gas hydrates and clay diapirs near the Storegga Slide on the southern edge of the Vøring Plateau, offshore Norway," *Marine Geology*, vol. 163, no. 1–4, pp. 125–148, 2000.
- [4] K. A. Kvenvolden, "Gas hydrate and humans," *Annals of the New York Academy of Sciences*, vol. 912, pp. 17–22, 2000.
- [5] E. D. Sloan Jr., *Clathrate Hydrates of Natural Gases*, Marcel Dekker, New York, NY, USA, 1998.
- [6] D. E. Archer and B. Buffett, "Time-dependent response of the global ocean clathrate reservoir to climatic and anthropogenic forcing," *Geochemistry, Geophysics, Geosystems*, vol. 6, no. 3, Article ID Q03002, 2005.
- [7] G. R. Dickens, "The blast in the past," *Nature*, vol. 401, pp. 752–753, 1999.
- [8] J. P. Kennett, K. G. Cannariato, I. L. Hendy, and R. J. Behl, "Carbon isotopic evidence for methane hydrate instability during quaternary interstadials," *Science*, vol. 288, no. 5463, pp. 128–133, 2000.
- [9] K. A. Kvenvolden, "Gas hydrates—geological perspective and global change," *Reviews of Geophysics*, vol. 31, no. 2, pp. 173–187, 1993.
- [10] K. A. Kvenvolden, "Potential effects of gas hydrate on human welfare," *Proceedings of the National Academy of Sciences of the United States of America*, vol. 96, no. 7, pp. 3420–3426, 1999.
- [11] T. Sowers, "Late quaternary atmospheric CH_4 isotope record suggests marine clathrates are stable," *Science*, vol. 311, no. 5762, pp. 838–840, 2006.
- [12] E. G. Nisbet, "Have sudden large releases of methane from geological reservoirs occurred since the last glacial maximum, and could such releases occur again?" *Philosophical Transactions of the Royal Society*, vol. 360, no. 1793, pp. 581–607, 2002.
- [13] G. B. Carpenter, "Coincident sediment slump/clathrate complexes on the U.S. Atlantic continental slope," *Geo-Marine Letters*, vol. 1, no. 1, pp. 29–32, 1981.
- [14] M. E. Field and J. H. J. Barber, "A submarine landslide associated with shallow seafloor gas and gas hydrates off Northern California," in *Submarine Landslides: Selected Studies in the U.S. Exclusive Economic Zone*, W. C. Schwab, H. J. Jee, and D. C. Twichell, Eds., pp. 971–972, U.S. Geological Survey, Reston, Va, USA, 1993.
- [15] P. Popenoe, E. A. Schmuck, and W. P. Dillon, "The Cape Fear landslide: slope failure associated with salt diapirism and gas hydrate decomposition," in *Submarine Landslides-Selected Studies in the U.S. Exclusive Economic Zone*, W. C. Schwab, H. J. Lee, and D. C. Twichell, Eds., pp. 40–53, U.S. Geological Survey, Reston, Va, USA, 2002.
- [16] M. F. Nixon and J. L. H. Grozic, "A simple model for submarine slope stability analysis with gas hydrates," *Norwegian Journal of Geology*, vol. 86, no. 3, pp. 309–316, 2006.

- [17] K. A. Kvenvolden, "Methane hydrates and global climate," *Global Biogeochemical Cycles*, vol. 2, pp. 221–229, 1988.
- [18] B. A. Buffett, "Clathrate hydrates," *Annual Review of Earth and Planetary Sciences*, vol. 28, pp. 477–507, 2000.
- [19] J. Mienert, M. Vanneste, S. Bünz, K. Andreassen, H. Hafli-dason, and H. P. Sejrup, "Ocean warming and gas hydrate stability on the mid-norwegian margin at the Storegga Slide," *Marine and Petroleum Geology*, vol. 22, no. 1-2, pp. 233–244, 2005.
- [20] W.-Y. Jung and P. R. Vogt, "Thermal models for post-glacial evolution of the gas hydrate stability zone: Storegga Slide, Norwegian Margin," in *Proceedings of the AAPG Annual Meeting*, Naval Research Laboratory, Salt Lake City, Utah, USA, 2004.
- [21] P. R. Vogt and W.-Y. Jung, "Holocene mass wasting on upper non-Polar continental slopes—due to post-glacial ocean warming and hydrate dissociation?" *Geophysical Research Letters*, vol. 29, no. 9, pp. 55-1–55-4, 2002.
- [22] N. Sultan, P. Cochonat, M. Canals et al., "Triggering mechanisms of slope instability processes and sediment failures on continental margins: a geotechnical approach," *Marine Geology*, vol. 213, no. 1–4, pp. 291–321, 2004.
- [23] N. Sultan, P. Cochonat, J. P. Foucher, and J. Mienert, "Effect of gas hydrates melting on seafloor slope instability," *Marine Geology*, vol. 213, no. 1–4, pp. 379–401, 2004.
- [24] M. J. Hornbach, D. M. Saffer, and W. S. Holbrook, "Critically pressured free-gas reservoirs below gas-hydrate provinces," *Nature*, vol. 427, pp. 142–144, 2004.
- [25] M. J. Hornbach, W. S. Holbrook, A. R. Gorman, K. L. Hackwith, D. Lizarralde, and I. Pecher, "Direct seismic detection of methane hydrate on the Blake Ridge," *Geophysics*, vol. 68, no. 1, pp. 92–100, 2003.
- [26] W. Xu and L. N. Germanovich, "Excess pore pressure resulting from methane hydrate dissociation in marine sediments: a theoretical approach," *Journal of Geophysical Research*, vol. 111, Article ID B01104, 12 pages, 2006.
- [27] U. Tinivella and F. Accaino, "Compressional velocity structure and Poisson's ratio in marine sediments with gas hydrate and free gas by inversion of reflected and refracted seismic data (South Shetland Islands, Antarctica)," *Marine Geology*, vol. 164, no. 1-2, pp. 13–27, 2000.
- [28] W. P. Dillon and M. D. Max, "Oceanic gas hydrates," in *Natural Gas Hydrate in Oceanic and Polar Environments*, M. Max, Ed., chapter 6, pp. 61–76, Kluwer Academic Publishers, Dodrecht, The Netherlands, 2000.
- [29] U. Tinivella, F. Accaino, and B. D. Vedova, "Gas hydrates and active mud volcanism on the South Shetland continental margin, Antarctic Peninsula," *Geo-Marine Letters*, vol. 28, no. 2, pp. 97–106, 2007.
- [30] I. Grevemeyer, N. Kaul, and J. L. Diaz-Naveas, "Geothermal evidence for fluid flow through the gas hydrate stability field off Central Chile—transient flow related to large subduction zone earthquakes?" *Geophysical Journal International*, vol. 166, no. 1, pp. 461–468, 2006.
- [31] D. Lange, *The south chilean subduction zone between 41° and 43.5° S: seismicity, structure and state of stress*, Dissertation, University of Potsdam, Potsdam, Germany, 2008.
- [32] I. V. Cordero, U. Tinivella, F. Accaino, M. F. Loreto, F. Fanucci, and C. Reichert, "Analyses of bottom simulating reflections offshore Arauco and Coyhaique (Chile)," *Geo-Marine Letters*, vol. 30, no. 3-4, pp. 271–281, 2009.
- [33] U. Tinivella, E. Lodolo, A. Camerlenghi, and G. Boehm, "Seismic tomography study of a bottom simulating reflector off the South Shetland Islands (Antarctica)," *Geological Society*, vol. 137, pp. 141–151, 1998.
- [34] M. Giustiniani, D. Accetella, U. Tinivella, M. F. Loreto, and F. Accaino, "Geographic information system: an application to gas hydrate reservoir," *Advances in Geosciences*, vol. 18, pp. 213–222, 2008.
- [35] N. L. Bangs, D. S. Sawyer, and X. Golovchenko, "Free gas at the base of the gas hydrate zone in the vicinity of the Chile triple junction," *Geology*, vol. 21, no. 10, pp. 905–908, 1993.
- [36] K. M. Brown, N. L. Bangs, P. N. Froelich, and K. A. Kvenvolden, "The nature, distribution, and origin of gas hydrate in the Chile triple junction region," *Earth and Planetary Science Letters*, vol. 139, no. 3-4, pp. 471–483, 1996.
- [37] J. Diaz-Naveas, *Sediment subduction and accretion at the Chilean convergent margin between 35° and 40°S*, Dissertation zur Erlangung des Doktorgrades, Christian-Albrechts-Universität zu Kiel, Kiel, Germany, 1999.
- [38] E. G. Morales, "Methane hydrates in the Chilean continental margin," *Electronic Journal of Biotechnology*, vol. 6, no. 2, pp. 3–7, 2003.
- [39] I. Grevemeyer, J. L. Diaz-Naveas, C. R. Ranero, and H. W. Villinger, "Heat flow over the decensing nazca plate in central Chile, 32°S to 41°S: observations from ODP leg 202 and the occurrence of natural gas hydrates," *Earth and Planetary Science Letters*, vol. 213, pp. 285–298, 2003.
- [40] I. V. Cordero, U. Tinivella, F. Accaino, M. F. Loreto, and F. Fanucci, "Thermal state and concentration of gas hydrate and free gas of coyhaique, Chilean margin (44°30'S)," *Marine and Petroleum Geology*, vol. 27, no. 5, pp. 1148–1156, 2010.
- [41] W. B. F. Ryan, S. M. Carbotte, J. O. Coplan et al., "Global multi-resolution topography synthesis," *Geochemistry, Geophysics, Geosystems*, vol. 10, no. 3, Article ID Q03014, 2009.
- [42] I. Grevemeyer and H. Villinger, "Gas hydrate stability and the assessment of heat flow through continental margins," *Geophysical Journal International*, vol. 145, no. 3, pp. 647–660, 2001.
- [43] M. T. Reagan and G. J. Moridis, "Dynamic response of oceanic hydrate deposits to ocean temperature change," *Journal of Geophysical Research*, vol. 113, Article ID C12023, 21 pages, 2008.
- [44] A. Giorgetti, A. Crise, R. Laterza, L. Perini, M. Rebesco, and A. Camerlenghi, "Water masses and bottom boundary layer dynamics above a sediment drift of the Antarctic Peninsula pacific margin," *Antarctic Science*, vol. 15, no. 4, pp. 537–546, 2003.
- [45] M. J. Bentley, "Volume of Antarctic ice at the last glacial maximum, and its impact on global sea level change," *Quaternary Science Reviews*, vol. 18, no. 14, pp. 1569–1595, 1999.